Spatially Resolved Spectroscopy on the Preparation of $CoMo/Al_2O_3$ Hydrodesulphurization Catalysts

Plaats-opgeloste Spectroscopie in de Bereiding van $CoMo/Al_2O_3$ Ontzwavelingskatalysatoren

(met een samenvatting in het Nederlands)

Proefschrift

ter verkrijging van de graad van doctor aan de Universiteit Utrecht
op gezag van de rector magnificus, prof. dr. W. H. Gispen,
ingevolge het besluit van het college voor promoties in het openbaar te verdedigen
op maandag 19 maart 2007 des middags te 2.30 uur

door

Jacob Arie Bergwerff

geboren op 30 juli 1979 te Schiedam

Promotores:	prof. dr. ir. B. M. Weckhuysen prof. dr. ir. K. P. de Jong
Co-promotor:	dr. T. Visser

Spatially Resolved Spectroscopy on the Preparation of $CoMo/Al_2O_3$ Hydrodesulphurization Catalysts

Voor mijn ouders

The research described in this thesis was financially supported by Albemarle Catalysts

ISBN-10: 90-902-1647-8
ISBN-13: 978-90-902-1647-8

Cover lay-out by Fred van Eeden

Drukkerij Ponsen en Looijen, Wageningen

Contents

Chapter 1

Introduction

Supported catalysts

Heterogeneous catalysts are functional materials with tremendous economical and societal importance, as they are essential in oil refining, environmental applications (e.g. automotive catalysts) and the manufacturing of bulk and fine chemicals as well as pharmaceuticals [1]. Supported catalysts form an important class of solid catalysts. In these systems, the catalytically active sites are dispersed on a porous support with high surface area to maximize the number of active sites per unit volume of material. When the reaction proceeds on a metal surface, as is for instance the case in hydrogenation (e.g. Ni, Pt and Pd) and Fischer-Tropsch (e.g. Co) reactions, small metal particles are created to maximize the metal surface area. The support acts as a spacer to separate the metal-particles and prevent the thermodynamically favored growth of larger metal-particles [2]. Supported transition metal-oxides are frequently applied as catalysts, due to the ability of the metal-oxide phase to adopt different oxidation states and coordination environments. Reactions take place on individual surface sites or metal-oxide domains, in which the metal-surface complexes often undergo a redox cycle. In this case, the support acts as a genuine ligand that determines the nature and hence reactivity and selectivity of the active sites [2]. Metal-sulfide systems constitute a third class of supported catalysts [3]. MoS_2 and WS_2 slabs provide sites for the adsorption of sulphur-containing organic molecules and their consecutive reaction into H_2S and hydrocarbons. In all cases the pore-system of the support, which generally consists of an oxide, such as SiO_2, Al_2O_3, TiO_2 or some form of carbon material, enables the transport of reactants and products to and from the active sites. When the reaction is carried out in an industrial fixed bed reactor, the catalyst needs to be in the shape of mm-scale particles to facilitate the gas flow and to prevent the occurrence of a pressure drop in the reactor [4]. Hence, supported catalysts are highly complicated systems with molecularly engineered active sites in pores with a diameter of several nanometers inside mm-sized support bodies [5-7].

Preparation of supported catalyst bodies

Although the nature of the active sites in supported metal, metal-oxide and metal-sulfide catalysts is entirely different, the methods that are employed for their industrial preparation and the challenges that are attached to it show large similarities [4,8]. The catalyst is often applied in the shape of cylindrical pellets or extrudates. For maximum dispersion, a homogenous distribution of the active phase in these bodies is generally desired. However, the occurrence of mass-transfer limitations and the use of expensive metals can create situations in which it is advantageous to concentrate all active sites in the outer part of the catalyst bodies. By the use of these so-called egg-shell catalysts, the reaction can exclusively take place in the outer shell of the catalyst bodies, diffusion distances for reactants are minimized, and most effective use is made of the metal. Another strategy to prevent mass-transfer limitations is the use of catalyst bodies with enhanced surface-to-volume ratio, such as trilobal and quadrulobal extrudates. Schematic presentations of different types of extrudates and metal-distribution profiles inside catalyst bodies, including the less-common egg-white and egg-yolk distributions, are presented in Fig. 1 [4,8].

As a first step in the industrial preparation of supported catalysts, pore volume impregnation of pre-shaped support bodies is usually carried out with an aqueous solution of a soluble metal-ion precursor, for instance a metal-nitrate salt [9-11]. After impregnation, the solution

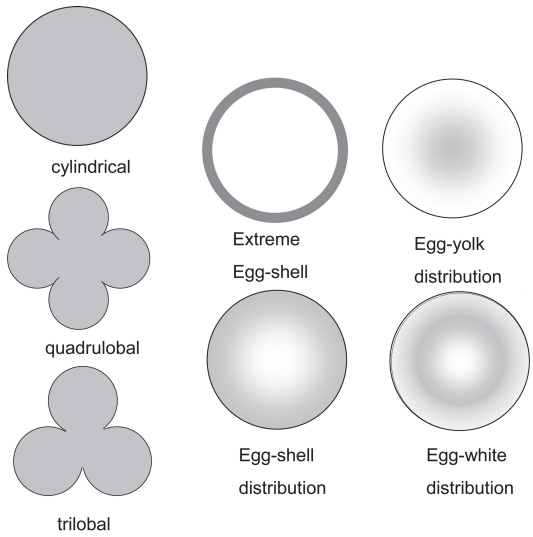

Figure 1. Schematic presentation of the cross-sections of supported catalyst bodies with different shapes and metal-distribution profiles.

is almost instantaneously taken up by the support through capillary forces. Compounds dissolved in the impregnation solution will be transported throughout the support bodies with this capillary flow. However, when a strong interaction exists between the metal-ion complexes and the support, their transport may fall behind that of the solution and a higher concentration of these complexes is created near the edges of the support bodies [12,13]. This situation is schematically depicted in Fig. 2. The thus established concentration gradient generates a driving force for diffusion of the complexes towards the center of the support bodies. However, desorption of the adsorbed metal-ion complexes is required. As a result, diffusion can be slow and it may take considerable time before the equilibrium situation, in which a homogeneous distribution of all solutes is established throughout the catalyst bodies, is reached. An inhomogeneous distribution of active components in the catalyst bodies is obtained when the impregnated material is dried before equilibration is complete. This strategy can be employed for the synthesis of egg-shell type catalysts [12-15]. However, when a homogeneous distribution of the active phase is desired, an ageing step is required. After ageing, a situation is often obtained, where the metal-ion complexes are homogeneously distributed throughout the support bodies, either adsorbed onto the support or free in solution inside the pores, as depicted in Fig. 2. The strength of the interaction between metal-ion precursor and the support surface depends on the nature of the metal-ion complexes and the pH of the impregnation solution. Organic complexing agents are sometimes added to the impregnation solution to alter the interaction between the metal-ion complexes and the support surface.

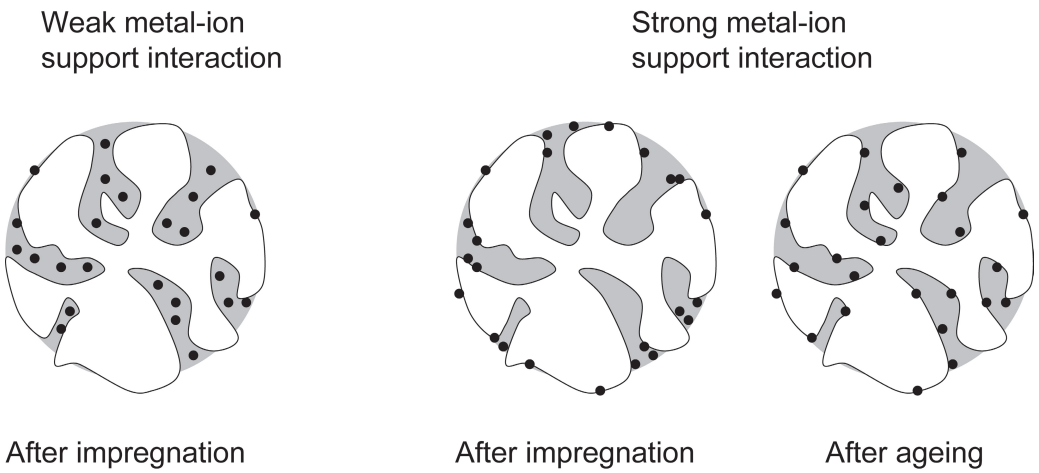

Figure 2. Schematic presentation of the distribution of metal-ion complexes (represented by black dots) inside support bodies after impregnation.

Subsequently, the material is dried and all metal-ion complexes inside the pores are deposited onto the support surface. Drying of wet mm-size extrudates is an extremely complex process [12,13,16-19]. In first instance, evaporation of water will take place at the external surface of the catalyst bodies and pores start to be emptied, as shown in Fig. 3A. Large pores are preferentially emptied, due to the higher vapor pressure that exists above the water-gas interface in these pores. Small pores at the exterior surface of the support bodies will remain filled as redistribution of the solution takes place by a convective flow, in which larger pores are constantly emptied into smaller ones. Large pores in the interior of the extrudates are emptied, which are completely surrounded by smaller pores that remain filled (Fig. 3B,C). This phenomenon results in a net convective flow of the solution from the center of the extrudates towards the outer surface, where evaporation takes place. In the absence of any interaction between metal-ion complexes and the support surface, these complexes will travel with this convective flow of the solution. As a result, evaporation of water at the exterior surface leads to an increase in the concentration of metal-ion complexes at this position. When the concentration of super-saturation is exceeded at this stage of the drying process, precipitation of the metal-salts takes place specifically at the periphery of the catalyst bodies. However, back-diffusion of metal-ion complexes towards the center of the extrudates will also occur due to the concentration gradient that is established. When a certain fraction of the pores is emptied, filled pores are no longer interconnected and diffusion of metal-ion complexes to the center of the extrudates is no longer possible (Fig. 3D). Isolated domains with small pores remain

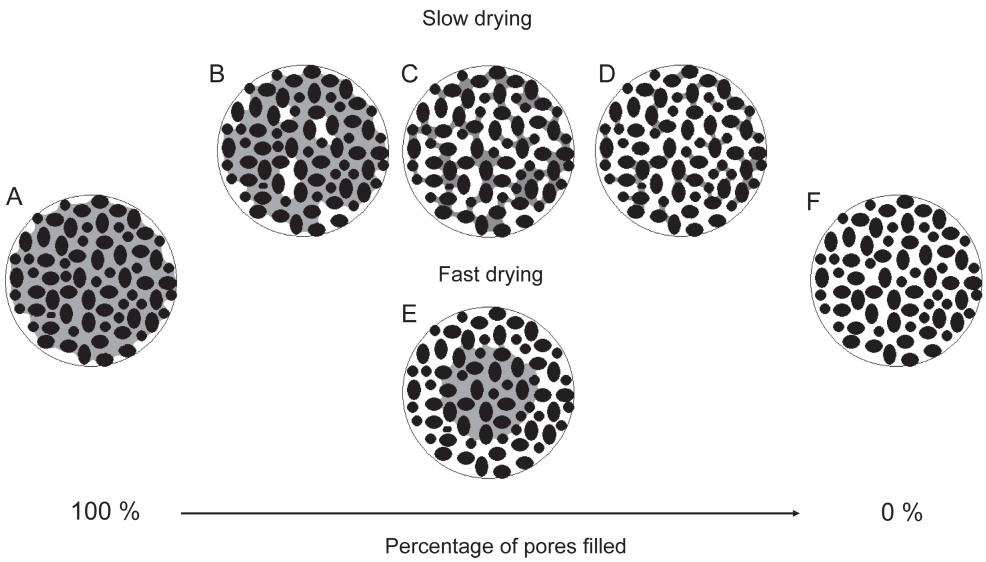

Figure 3. Schematic presentation of the distribution of liquid inside the pores of support bodies at various stages of the drying process.

filled with solution, which will dry independently in this last drying stage. Hence, in general, an egg-shell distribution of metal-complexes inside the dried catalyst bodies is obtained when back-diffusion of metal-ion complexes towards the center of the catalyst bodies is not sufficiently fast.

In some cases, redistribution of the solution through capillary flow is not fast enough and all pores at the exterior surface are completely emptied, before they can be replenished from the interior part of the support bodies. A drying front, where evaporation of the water takes place, moves towards the center of the extrudates (Fig. 3E). When precipitation is avoided and interaction of metal-ion complexes with the support is absent, these components may travel with this drying front, leading to a high concentration of metal-ion complexes near the center of the extrudates. When precipitation finally takes place, an egg-yolk distribution of precipitated metal-complexes can be the result. In general, when a strong interaction exists between the metal-ion complexes and the support, the drying procedure is less critical, since the adsorbed metal-ion complexes are less likely to be transported with the convective flow of the solution and a homogeneous distribution is retained after drying [12,17,18].

To remove carbon- and nitrogen-containing components, a high temperature treatment in air is usually applied after drying. Ideally, a well-dispersed metal-oxide phase is obtained on the support after this calcination. In this way, a good dispersion of the active phase is obtained after reduction (metal catalysts) or sulphidation (metal-sulfide catalysts). The dispersion of the metal-oxide phase can be influenced in the calcination step as well. The formation of volatile metal-complexes at elevated temperatures may lead to a redistribution of these compounds and their agglomeration. The formation of mixed oxides is sometimes observed when calcination is carried out at (too) high temperatures. A fraction of the metal-ions applied to the support may form solid solutions with the oxidic support material and can therefore not participate in catalysis. In conclusion, the macro distribution and dispersion of the active phase in supported catalyst bodies are influenced by a manifold of parameters in the different steps of the preparation procedure. For the characterization of the material that is obtained after drying and calcination, a number of analytical techniques are available. Transmission electron microscopy (TEM) can be applied to gain information on the dispersion of the metal-oxide phase. Scanning electron microscopy (SEM) in combination with the energy dispersive analysis of X-rays (EDX) allows one to obtain quantitative distribution profiles of the metal-precursor inside catalyst bodies. X-ray diffraction (XRD) can be applied to monitor the formation of crystalline material, while X-ray fluorescence (XRF) is a standard technique to verify the metal loading in supported catalysts.

Metal-ion support interactions

As explained in the previous paragraph, the interaction between metal-complexes in the impregnation solution and the support surface is a key parameter in the preparation of supported catalysts. Both the dispersion of the metal-oxide phase and its macroscopic distribution inside calcined catalyst bodies are determined by the strength of this interaction. Insight into the adsorption of metal-ion complexes onto the support surface is therefore of high importance if one aims at preparing supported catalysts in a controlled manner. It is difficult to obtain a detailed description of the interface of support surfaces in contact with impregnation solutions. For crystalline materials, such as TiO_2 or α-Al_2O_3, an impression of the surface can be obtained by investigation of preferentially exposed crystal planes. Exposure of these surfaces to an aqueous solution leads to the conversion of exposed oxygen atoms into hydroxyl groups. Density Functional Theory (DFT) calculations may be applied to obtain the energetically most favorable configuration of such a surface [20-22]. However, since different surfaces are likely to be exposed in crystalline supports and often amorphous materials, such as SiO_2, are being applied, a simplified model for the support surface is generally used in fundamental catalyst preparation studies [23]. In most models, the surface is represented by a collection of hydroxyl groups that can be protonated or deprotonated as a function of pH, as described in Eq. 1 and 2. Hence, the net charge of the surface varies from positive at low pH to negative at high pH. Depending on the model, the presence of a single type, or a number of different hydroxyl groups can be assumed. The point of zero charge (PZC) of a support material defines the pH at which there is no net protonation and the total charge of the surface is zero.

$$S\text{-}OH + H^+ \leftrightarrow S\text{-}OH_2^+ \qquad \text{(Eq. 1)}$$

$$S\text{-}OH + OH^- \leftrightarrow S\text{-}O^- + H_2O \qquad \text{(Eq. 2)}$$

When the support is contacted with a solution of a specific pH, (de-) protonation of the surface leads to a pH shift in this solution. Hence, the PZC of support materials can be determined through potentiometric mass titrations [24,25]. In catalyst preparation, (de-) protonation of the surface also implies that the pH of the impregnation solution will be affected. This buffering effect of the support will be stronger when the number of hydroxyls per volume of impregnation solution increases, and can be expected to play an important role when no excess solution is applied to the support. In fact, for solutions without any buffering capacity,

the pH inside the pores was found to shift to the PZC of the support after incipient wetness impregnation [24].

Different modes of interaction between metal-ion complexes and the support surface exist. These different adsorption mechanisms were recently discussed in a review article on the role of the liquid solid interface in the preparation of supported catalysts by Bourikas et al. [26], which was used as the guideline for this paragraph. Binding of complexes to specific surface sites may take place in which adsorption of the metal-ion complexes is of a chemical nature. Surface oxygens are incorporated in the first coordination sphere of the metal-ion and an inner-sphere surface complex is formed. Highly charged metal ions, such as Mo(VI) attract oxygen ligands strongly, and oxomolybdate anions with strong Mo-O bonds, such as MoO_4^{2-}, are formed in aqueous solution. Interaction of this anion with a support surface may lead to the formation of surface complexes containing covalent support-O-Mo bonds. The adsorption of these anions is accompanied with the release of OH^- from the surface.

Metal ions with lower positive charge, such as Ni(II) and Co(II), form $[M(H_2O)_6]^{2+}$ complexes in solution. Upon interaction with the support, coordinating water molecules can be exchanged for support oxygen groups leading to inner-sphere surface complexes, as evidenced for $[Co(H_2O)_6]^{2+}$ on γ-Al_2O_3 surfaces [27,28] and Ni(II)-complexes with several organic amine ligands on SiO_2 surfaces [29-31]. In this case, deprotonation of the surface hydroxyls is required for the formation of the inner-sphere complexes and protons are released upon adsorption. Alternatively, metal-complexes may be chemically bound to the support surface through hydrogen bonds, as was for instance shown for CrO_4^{2-} anions on a TiO_2 surface at high pH. A schematic representation of the different adsorption modes of metal-ions on a support surface is presented in Fig. 4 [26].

Besides these specific interactions, adsorption can take place through electrostatic attraction between a charged support surface and metal-complexes in solution [32,33]. Non-specific adsorption of cations can for instance take place on a negatively charged surface when the pH of the impregnation solution that is applied is lower than the PZC of the support. Exchange of ligands does not take place in this case and merely outer-sphere surface complexes are formed. This adsorption mechanism is dominant when inert complexes are present in the impregnation solution. A well-known example is the strong electrostatic adsorption of relatively inert low-spin octahedral $PtCl_6^{2-}$ complexes [34] and square planar $Pt(NH_3)_4^{2+}$ complexes [35] onto charged oxidic surfaces. These metal complexes were found to be adsorbed with their first hydration sphere intact. In this type of adsorption, the ionic strength of the impregnation

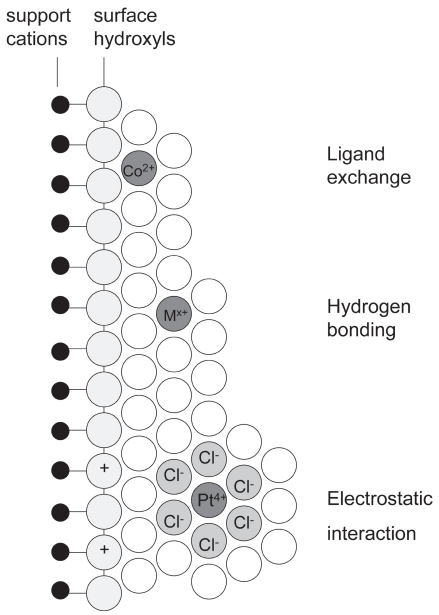

Figure 4. Schematic presentation of different types of metal-ion support interactions [25].

solution is an important parameter. A high concentration of ions in the impregnation solution results in the shielding of metal-ion complexes from the surface charge.

A third example of interaction between metal-ion complexes and surfaces is the so-called ligand-promoted dissolution of the support. This general term is used to describe the incorporation of dissolved support ions, such as Al(III) and SiO_4^{4-}, into mixed metal complexes after impregnation. A low pH of the impregnation solution can result in the dissolution of an Al_2O_3 surface layer and the formation of Al(III) ions in solutions. These Al(III) ions can be incorporated into heteropolyanions, such as $Al(OH)_6Mo_6O_{18}^{3-}$ Anderson-type [36] and $Al_{1,2}W_{10,11}$ Keggin-type complexes [37], when impregnation is carried out with acidic molybdate or tungstate solutions. Alternatively, the formation of mixed Co-Al and Ni-Al hydrotalcite phases showing no contact with the support surface was observed when Al_2O_3 was contacted with basic Co- and Ni-solutions [38,39]. In both cases, the dissolution of the support is enhanced due to the formation of these mixed complexes.

Finally, the buffering effect of the support, described above, may lead to the precipitation of metal-hydroxides after impregnation. Protonation of the surface results in an increase of the pH of the solution inside the pores of the support. Impregnation of basic supports may result in the precipitation of metal-hydroxides.

For the elucidation of these different modes of interaction, several experimental procedures may be applied. As described above, chemisorption of metal-ion complexes on support surfaces generally leads to a pH shift in the impregnation solution and can thus be evidenced by potentiometric titration experiments. Adsorption experiments in which the amount of metal-ion complexes adsorbed on a specific support is determined after contact with different impregnation solutions can yield valuable information. Such measurements can for instance be used to determine the strength of the metal-ion support interaction as a function of the PZC of the support, or the pH and ionic strength of the impregnation solution.

Molecular spectroscopic techniques, such as Raman [40-43], Ultraviolet-Visible-Near Infrared (UV-Vis-NIR) [30,44,45], nuclear magnetic resonance (NMR) [46], electron paramagnetic resonance (EPR) [47] and extended X-ray absorption fine structure (EXAFS) [48,49] spectroscopy are powerful techniques for the direct characterization of the (surface) metal-ion complexes in the impregnated support [50-53]. Bar the odd exception [14], the application of the abovementioned techniques has mostly been limited to the analysis of impregnated powder supports or crushed extrudates. At the same time, information on the distribution of metal-ion complexes inside catalyst bodies is usually only obtained after completion of the preparation process, through SEM-EDX analysis. The application of molecular spectroscopy in a spatially resolved mode during the preparation process of catalyst bodies, should allow one to gain more insight in both the molecular interaction between metal-ion complexes and the support surface and the macroscopic transport of these compounds inside catalyst bodies. In this way, the genesis of the active phase in supported catalyst bodies can be monitored in the course of the preparation process.

Hydroprocessing catalysts

Hydroprocessing is the common term for the catalytic treatment of fuel streams with hydrogen, in which sulphur, nitrogen and other impurities are removed and hydrogenation of aromatics takes place [3]. In modern refineries, hydrotreating units serve different purposes. At an early stage, a large fraction of the heteroatoms needs to be removed from the feed-stream to prevent poisoning of down-stream cracking and reforming catalysts. Furthermore, the stringent legislation on the maximum amount of sulphur in transportation fuels requires that a deep hydrodesulphurization step is carried out at some stage. Despite the development of different types of catalysts (e.g. bulk catalysts and supported metal phosphides) and alternative desulphurization methods (e.g. different adsorption methods) supported Co/Ni promoted MoS_2 and WS_2 catalysts are still predominantly used for this purpose. Since their

introduction in the 1930's their efficiency has gradually been improved, where the introduction of phosphate and chelating agents, such as citrate and nitrilotriacetic acid, to the impregnation solution has lead to remarkable improvements. These catalysts are applied in high-pressure trickle-bed reactors, in which the catalyst is present in a packed bed of catalyst bodies with a diameter of 1-3 mm and a length of several mm. Trilobal and quadrulobal shaped extrudates are predominantly used to prevent mass-transfer limitations.

The mechanism for hydrodesulphurization, and the molecular structure and genesis of the active phase in supported (Co/Ni)MoS_2 catalysts have been the topic of extensive research and intense debate over the years. Fuel streams in refineries are mixtures of a large number of different hydrocarbons. Sulphur-containing molecules are mainly present in the form of thiols, thiophenes and (substituted) dibenzothiophenes. In general, it was found that two different reaction pathways exist for the hydrodesulphurization of sulphur-containing aromatics. For the reaction of thiophene, an often-used model feed, direct cleavage of the C-S is reported to be the dominant pathway. However, for the cleavage of substituted dibenzothiophenes, hydrogenation of the aromatic rings is a prerequisite for steric reasons [54]. In unpromoted MoS_2 catalysts, the active sites for the C-S bond cleavage are reported to be located on sulphur vacancies on the edges of MoS_2 slabs. For this reason, H_2S was found to act as an inhibitor in this reaction. The presence of Co is reported to lead to the decoration of the MoS_2 slabs by these atoms and the formation of highly active sites. The formation of this so-called CoMoS-phase was evidenced by scanning tunneling microscopy on model catalysts [55].

Research has also been dedicated to determining links between the nature of the oxidic phase obtained after calcination and the structure and activity of the sulfided catalyst. The formation of bulk phases, such as MoO_3 and Co_3O_4, is generally to be avoided after calcination for a good dispersion of the active phase and the formation of the mixed CoMoS-phase. Furthermore the formation of interaction compounds, such as $CoAl_2O_4$ and $NiAl_2O_4$, after calcination was found to be detrimental for the final activity of the catalyst [56]. The sulphidation of the oxidic Mo- and Co/Ni surface complexes is influenced by their nature. The complexation of Ni by complexing agents, such as nitrilotriacetic acid and citrate, was found to lead to an increase in the sulphidation temperature of the promotor metal, and an increase in its dispersion after sulphidation [57,58]. In general, it can be stated that the nature of the metal-oxide phase obtained on the support surface before sulphidation is of considerable influence on the activity of the final catalysts.

Scope and outline of the PhD thesis

In this PhD-thesis, an attempt has been made to unravel the physical and chemical processes in the preparation of supported catalyst bodies. For this purpose, methodologies have been developed that allow one to employ molecular spectroscopic techniques in a spatially resolved mode. Through the analysis of bisected catalyst bodies by Raman and UV-Vis-NIR micro-spectroscopy it is possible to record spectra at different positions in the sample. In this way, both the nature and distribution of metal-ion complexes and other components in the impregnation solution, such as complexing agents, inside catalyst bodies can be determined. Magnetic resonance imaging (MRI) proved to be a powerful technique to study the dynamics of pore volume impregnation. By combining these techniques, the effect of parameters, such as the composition of the impregnation solution and the ageing time that was applied after impregnation, on the molecular structure of the oxidic catalyst could be examined in great detail.

The micro-spectroscopic techniques can be used to study the preparation of a wide range of different supported catalyst systems. In the studies described in this PhD-thesis they have been applied to study the preparation of cylindrical (Co)Mo/Al_2O_3 extrudates. Special attention was paid to the influence of the addition of citrate and phosphate as complexing agents to CoMo-impregnation solutions on the speciation of metal-ion complexes in impregnation solutions, impregnated support bodies and dried and calcined samples.

In order to gain fundamental insight into the interaction between metal-ion complexes and the support surface, it is important to know the nature of metal-ion complexes in the impregnation solution. In **chapter 2**, the speciation of Mo- and Co-complexes in CoMo impregnation solutions was investigated. Formation constants for these complexes reported in literature were used to derive the theoretical speciation of different complexes in solution. Raman spectroscopy was applied to monitor the distribution of Mo-complexes in the absence and presence of citrate and phosphate as complexing agents. UV-Vis-NIR spectroscopy was applied to study the interaction of $[Co(H_2O)_6]^{2+}$ complexes with Mo-anions and to determine the speciation of Co-citrate complexes in solution. The molecular structure of the latter complexes is discussed on the basis of a vibrational spectroscopy study on citrate and Co(II)-citrate solutions. Multivariate curve resolution (MCR) was used to derive the speciation of relevant Mo(VI)- and Co(II)-complexes in solution and obtain their reference spectra.

In the work described in **chapter 3,** Raman micro-spectroscopy was used to study the

impregnation of Al_2O_3 pellets with different Mo(VI)-solutions. Spectra were recorded on bisected pellets (∅ 3 mm) at several points in time during the ageing process to monitor the transport of Mo(VI)-complexes after impregnation. The interaction between Mo(VI)-complexes with the Al_2O_3 surface through ligand exchange, electrostatic interaction and ligand-promoted dissolution processes was envisaged. In **chapter 4**, it is shown that the same technique can be applied to follow the preparation of industrial-type Mo/Al_2O_3 catalyst extrudates (∅ 1.5 mm) throughout their preparation process. Through spectroscopic measurements on impregnated, dried and calcined samples, the formation of bulk oxidic phases in the calcined catalyst could be traced back to the formation of an $Al(OH)_6Mo_6O_{18}^{3-}$ precipitate during impregnation and the redistribution of Mo(VI)-complexes during drying. The detrimental influence of the formation of these bulk phases on the activity of the catalysts in HDS was demonstrated.

In **chapter 5**, UV-Vis-NIR micro-spectroscopy is introduced as a new technique to study the preparation of supported catalyst bodies. The technique is applied in combination with Raman micro-spectroscopy to monitor the distribution of Mo- and Co-complexes inside Al_2O_3 pellets after impregnation with different CoMo-solutions. The disintegration and formation of a $CoMo_{11}P$ heteropolyanion is envisaged inside the Al_2O_3 pore-system during the ageing process. **Chapter 6** is dedicated to the application of MRI as a non-invasive technique to monitor the preparation of supported catalyst bodies. The use of direct imaging of ^{13}C and ^{31}P nuclei to determine the distribution of complexing agents, such as phosphate and citrate, inside extrudates is discussed. An indirect imaging technique, which exploits the detrimental effect of paramagnetic cations on the ^{1}H-NMR signal of the water inside the Al_2O_3 extrudates, is employed to monitor the distribution of $[Co(H_2O)_6]^{2+}$. Likewise, the distribution of diamagnetic components can be determined through their influence on the T_1 relaxation time of water protons. In the experiments described in **chapter 7**, MRI is used as the main technique to monitor the distribution of Co(II)-complexes inside Al_2O_3 extrudates after impregnation with Co(II)-citrate solutions. By varying the pH and Co:citrate ratio in these solutions, it proved to be possible to change the interaction of Co(II)-complexes with the Al_2O_3 surface and control the distribution of Co inside the extrudates after impregnation. The main conclusions derived in the preceding chapters are summarized in **chapter 8.** This chapter also contains some perspectives for future research. The prospects of the use of X-ray tomography as a new technique to study the distribution of metal-ion complexes and crystalline phases inside catalyst bodies is discussed in more detail, on the basis of some preliminary results.

References

1 G. Ertl, H. Knozinger, J. Weitkamp *(Eds.)*, *Handbook of Heterogeneous Catalysis*, Wiley-VCH, Weinheim, 1997.

2 G. C. Bond, *Active Phase-Support Interactions* in *Handbook of Heterogeneous Catalysis* (G. Ertl, H. Knozinger, J. Weitkamp, *Eds.)*, Wiley-VCH, Weinheim, 1997.

3 H. Topsoe, B. S. Clausen, F. E. Massoth *(Eds.)*, *Hydrotreating Catalysis*, Springer-Verlag, Berlin, 1996.

4 J. Hagen *(Eds.)*, *Industrial Catalysis: A Practical Approach*, Wiley-VCH, Weinheim, 1999.

5 K. P. de Jong, *CatTech* **1998**, *3*, 87.

6 R. Schlogl, S. B. Abd Hamid, *Angew. Chem. Int. Ed.* **2004**, *43*, 1628.

7 A. T. Bell, *Science* **2003**, *299*, 1688.

8 G. Ertl, H. Knozinger, J. Weitkamp *(Eds.)*, *Preparation of Solid Catalysts*, Wiley-VCH, Weinheim, 1999.

9 C. Louis, M. Che, *Supported catalysts. Deposition of active component. Anchoring and grafting of coordination metal complexes onto oxide surfaces* in *Preparation of Solid Catalysts* (G. Ertl, H. Knözinger, J. Weitkamp, *Eds.)*, Wiley-VCH, Weinheim, 1999.

10 M. Che, O. Clause, C. Marcilly, *Supported catalysts. Deposition of active component. Impregnation and ion exchange* in *Preparation of Solid Catalysts* (G. Ertl, H. Knözinger, J. Weitkamp, *Eds.)*, Wiley-VCH, Weinheim, 1999.

11 J. W. Geus, J. A. R. van Veen, *Preparation of Supported Catalysts* in *Catalysis: An Integrated Approach*, *Second, Revised and Enlarged Edition* (R. A. van Santen, P. W. N. M. van Leeuwen, J. A. Moulijn, B. A. Averill, *Eds.*), Elsevier, Amsterdam, 1999.

12 A. V. Neimark, L. I. Kheifez, V. B. Fenelonov, *Ind. Eng. Chem. Prod. Res. Dev.* **1981**, *20*, 439.

13 S. Y. Lee, R. Aris, *Catal. Rev. Sci. Eng.* **1985**, *27*, 207.

14 T. Mang, B. Breitscheidel, P. Polanek, H. Knozinger, *Appl. Catal. A-General* **1993**, *106*, 239.

15 C. Galarraga, E. Peluso, H. de Lasa, *Chem. Eng. J.* **2001**, *82*, 13.

16 P. J. van den Brink, *The Selective Oxidation of Hydrogen Sulfide on Supported Iron-Based Catalysts* PhD thesis, Utrecht University, 1992.

17 A. Lekhal, B. J. Glasser, J. G. Khinast, *Chem. Eng. Sci.* **2004**, *59*, 1063.

18 A. Lekhal, B. J. Glasser, J. G. Khinast, *Chem. Eng. Sci.* **2001**, *56*, 4473.

19 L. M. Knijff, *The application of active components into catalyst support bodies,* PhD thesis, Utrecht University, 1993.

20 M. Digne, P. Sautet, P. Raybaud, P. Euzen, H. Toulhoat, *J. Catal.* **2002**, *211*, 1.

21 M. Digne, P. Sautet, P. Raybaud, P. Euzen, H. Toulhoat, *J. Catal.* **2004**, *226*, 54.

22 C. Arrouvel, M. Digne, M. Breysse, H. Toulhoat, P. Raybaud, *J. Catal.* **2004**, *222*, 152.

23 K. Bourikas, C. Kordulis, A. Lycourghiotis, *Adv. Colloid Interface Sci.* **2006**, *121*, 111.

24 J. Park, J. R. Regalbuto, *J. Colloid Interface Sci.* **1995**, *175*, 239.

25 J. Vakros, C. Kordulis, A. Lycourghiotis, *Chem. Commun.* **2002**, 1980.

26 K. Bourikas, C. Kordulis, A. Lycourghiotis, *Catal. Rev. Sci. Eng.* **2006**, *48*, 363.

27 K. Bourikas, C. Kordulis, J. Vakros, A. Lycourghiotis, *Adv. Colloid Interface Sci.* **2004**, *110*, 97.

28 J. Vakros, K. Bourikas, S. Perlepes, C. Kordulis, A. Lycourghiotis, *Langmuir* **2004**, *20*, 10542.

29 K. Q. Sun, E. Marceau, M. Che, *Phys. Chem. Chem. Phys.* **2006**, *8*, 1731.

30 S. Boujday, J. F. Lambert, M. Che, *ChemPhysChem* **2004**, *5*, 1003.

31 F. Negrier, E. Marceau, M. Che, D. de Caro, *C. R. Chim.* **2003**, *6*, 231.

32 J. R. Regalbuto, A. Navada, S. Shadid, M. L. Bricker, Q. Chen, *J. Catal.* **1999**, *184*, 335.
33 W. A. Spieker, J. R. Regalbuto, *Chem. Eng. Sci.* **2001**, *56*, 3491.
34 W. A. Spieker, J. Liu, X. Hao, J. T. Miller, A. J. Kropf, J. R. Regalbuto, *Appl. Catal. A-General.* **2003**, *243*, 53.
35 M. Schreier, J. R. Regalbuto, *J. Catal.* **2004**, *225*, 190.
36 X. Carrier, J. F. Lambert, M. Che, *J. Am. Chem. Soc.* **1997**, *119*, 10137.
37 X. Carrier, J. B. D. de la Caillerie, J. F. Lambert, M. Che, *J. Am. Chem. Soc* **1999**, *121*, 3377.
38 J. B. D. Delacaillerie, M. Kermarec, O. Clause, *J. Am. Chem. Soc.* **1995**, *117*, 11471.
39 J. L. Paulhiac, O. Clause, *J. Am. Chem. Soc.* **1993**, *115*, 11602.
40 M. A. Banares, I. E. Wachs, *J. Raman Spectros.* **2002**, *33*, 359.
41 I. E. Wachs, *Catal. Today* **1996**, *27*, 437.
42 M. A. Vuurman, I. E. Wachs, *J. Phys. Chem.* **1992**, *96*, 5008.
43 G. Mestl, T. K. K. Srinivasan, *Catal. Rev. Sci. Eng.* **1998**, *40*, 451.
44 S. Boujday, J. Lehman, J. F. Lambert, M. Che, *Catal. Lett.* **2003**, *88*, 23.
45 B. M. Weckhuysen, R. A. Schoonheydt, *Catal. Today* **1999**, *49*, 441.
46 M. Hunger, J. Weitkamp, *Nuclear magnetic resonance* in *In-Situ Spectroscopy of Catalysts* (B. M. Weckhuysen, *Ed.)*, American Scientific Publishers, Stevenson Range, CA, USA, 2004.
47 K. Dyrek, M. Che, *Chem. Rev.* **1997**, *97*, 305.
48 S. Vijay, E. E. Wolf, J. T. Miller, A. J. Kropf, *Appl. Catal. A-General* **2004**, *264*, 125.
49 J. H. Yang, J. D. Henao, C. Costello, M. C. Kung, H. H. Kung, J. T. Miller, A. J. Kropf, J. G. Kim, J. R. Regalbuto, M. T. Bore, H. N. Pham, A. K. Datye, J. D. Laeger, K. Kharas, *Appl. Catal. A-General* **2005**, *291*, 73.
50 B. M. Weckhuysen *(Ed.)*, *In-situ Spectroscopy of Catalysts*, American Scientific Publishers, Stevenson Ranch, 2004.
51 X. Carrier, E. Marceau, M. Che, *Pure Appl. Chem.* **2006**, *78*, 1039.
52 M. Hunger, J. Weitkamp, *Angew. Chem. Int. Ed.* **2001**, *40*, 2954.
53 J. M. Thomas, *Chem. Eur. J.* **1997**, *3*, 1557.
54 R. Prins, A. Egorova, A. Rothlisberger, Y. Zhao, N. Sivasankar, P. Kukula, *Catal. Today* **2006**, *111*, 84.
55 J. V. Lauritsen, S. Helveg, E. Laegsgaard, I. Stensgaard, B. S. Clausen, H. Topsoe, E. Besenbacher, *J. Catal.* **2001**, *197*, 1.
56 C. Papadopoulou, J. Vakros, H. K. Matralis, G. A. Voyiatzis, C. Kordulis, *J. Colloid Interface Sci.* **2004**, *274*, 159.
57 R. Cattaneo, F. Rota, R. Prins, *J. Catal.* **2001**, *199*, 318.
58 L. Coulier, V. H. J. de Beer, J. A. R. van Veen, J. W. Niemantsverdriet, *J. Catal.* **2001**, *197*, 26.

Chapter 2

Spectroscopic Investigation of the Molecular Structure of Mo(VI)- and Co(II)-Complexes in Aqueous Solution in the Absence and Presence of Complexing Agents

General introduction

A key parameter in the preparation of supported metal and metal-oxide catalysts by means of incipient wetness impregnation is the interaction between the support material and metal-ion complexes. As explained in chapter 1, the distribution of metal-ion complexes inside catalyst bodies after their preparation is partly determined by the strength of this interaction [1-6]. A strong interaction may lead to an egg-shell distribution of metal-ion complexes after impregnation, while a weak interaction can result in their redistribution during the drying process. In this context, the charge of metal-ion complexes in the impregnation solution is an important property, as interactions between these complexes and the support surface are often electrostatic. Furthermore, their reactivity defines whether covalent bonds can be formed with the support surface during catalyst preparation. Finally, the transport rate of metal complexes inside the porous support after impregnation is likely to be influenced by their size. Hence, for characterization studies on the preparation of CoMo/Al_2O_3 catalyst bodies, insight into the nature of the different Mo(VI)- and Co(II)-complexes that can be formed in solution is essential to design sensible experiments and explain experimental results.

Throughout this thesis, Raman and UV-Vis-NIR spectroscopy are applied as the main techniques for the characterization of Mo(VI)- and Co(II)-complexes in Al_2O_3 support bodies. In this chapter, the application of these techniques to discriminate between different complexes in aqueous solutions is evaluated. The extensive

literature that exists on the formation of Mo(VI)- and Co(II)-complexes in solution [7-21] is used for the interpretation of the spectroscopic data. In these references, the stoichiometry, formation constants and, in some cases, crystal structures of the different metal-ion complexes are presented. However, reports on Raman and UV-Vis-NIR spectroscopic studies of these metal-ion complexes in solution are scarce. Therefore, with the aid of chemometric techniques, an attempt is made to obtain reliable reference spectra of the Mo(VI) and Co(II)-complexes that can be formed in aqueous solution. In the following chapters, these reference spectra are used to determine the nature of Mo(VI) and Co(II)-complexes in impregnation solutions and inside the Al_2O_3 pores after impregnation.

Complexing agents are frequently added to industrial CoMo-impregnation solutions for a number of reasons [22-31]. Through complex formation, the solubility of metal-ion complexes can be enhanced, yielding a higher metal loading in the final catalyst. The presence of organic acids may lead to a more disperse deposition of the metal-oxide phase on the support [6,26,28] and was found to delay the sulphidation of Co, yielding a more effective $CoMoS_2$-phase [25,30]. Phosphate is often regarded as a second promotor in these systems, although its exact function is still a topic of debate [27,31].

This chapter is divided into three sections. In chapter 2A, the nature of Mo(VI)- and Co(II)-complexes in solution, in the absence of complexing agents, is evaluated with the aid of Raman and UV-Vis-NIR spectroscopy. A vibrational study of citrate and a spectroscopic investigation into the complexation of citrate with Co(II) and Mo(VI) in aqueous solution are reported in chapter 2B. The formation of phosphomolybdate complexes in MoP-solutions in the presence and absence of Co(II) is elucidated in chapter 2C.

Chapter 2A

Spectroscopic Investigation of the Molecular Structure of Mo(VI)-anions in $(NH_4)_6Mo_7O_{24}$ Solutions and their Interaction with Co(II)

Abstract

A Raman spectroscopic study was carried out to elucidate the formation of Mo(VI)-anions in $(NH_4)_6Mo_7O_{24}$ solutions. Reference spectra of MoO_4^{2-}, $Mo_7O_{24}^{6-}$, $HMo_7O_{24}^{5-}$ and $H_2Mo_7O_{24}^{4-}$ anions in aqueous solution were derived. The formation of mixed CoMo-complexes with $Co_2Mo_7O_{24}^{2-}$ as a tentative structure was evidenced by Raman and UV-Vis-NIR spectroscopy.

Introduction

$(NH_4)_6Mo_7O_{24}$ (AHM) is the most common precursor salt for the synthesis of Mo(VI)-containing impregnation solutions. The speciation of Mo(VI)-complexes in AHM solutions is therefore extensively studied and well established [9,13,16,32,33]. It was found that tetrahedral MoO_4^{2-} anions are present at low Mo-concentrations and high pH. Formation of isopolyanions takes place at higher concentrations in acidic solutions. $H_xMo_7O_{24}^{(6-x)-}$complexes are found to be dominant in solutions of pH 3-6. At lower pH the formation of larger clusters, such as $H_xMo_8O_{26}^{(4-x)-}$ is reported as well. In industrial catalyst preparation, impregnation solutions with high Mo-concentrations (typically exceeding 1.0 M Mo) are used to obtain high Mo-loadings in the final catalyst. However, at these concentrations, formation of larger Mo(VI)-clusters at low pH results in the precipitation of Mo(VI)-salts. Hence, for the spectroscopic investigations described in this section, 0.10 M Mo AHM-solutions were used to study the speciation of Mo(VI)-complexes in a broad pH range. Using Raman spectroscopy, the formation of Mo(VI)-complexes was studied as a function of pH. With the aid of multivariate curve resolution (MCR), the speciation of the different isopolymolybdate complexes and their reference spectra were derived. The results are discussed in the context of the available literature.

Mo(VI)-isopolyanions are known to react with various cations in solution to form so-called heteropolyanions. The complexation of trivalent cations, such as Al(III) [33,34], Cr(III) [35] and Co(III) [36] by Mo(VI)-anions is reported to result in the formation of Anderson-type complexes in acidic environment. Murase et al. reported on the formation of complexes with $NiMo_6$ stoichiometry in acidic NiMo solutions, for which they propose a similar structure [32]. It seems therefore sensible to check whether interaction exists between Co(II)-cations and Mo(VI)-anions in CoMo-solutions in the absence of complexing agents.

Experimental

The compositions of the solutions used for spectroscopic studies are listed in Table 1. $(NH_4)_6Mo_7O_{24}$ (Acros, p.a.) and $Co(NO_3)_2{\cdot}6\ H_2O$ (Acros, p.a.) were used for the preparation of these solutions. For Raman measurements on Mo-solutions (series 1), NH_4NO_3 (Acros, p.a.) was added to serve as an internal standard. Concentrated NaOH (Merck, p.a.) and HCl (Merck, p.a.) solutions were used for pH adjustment. Care was taken that the concentration of components under study was not altered during measurements.

Raman spectra were recorded on the different solutions using a Kaiser RXN spectrometer

Table 1. Composition of Mo- and CoMo-solutions used for spectroscopic studies. The pH range and the number and type of spectra that were recorded in each titration series are included.

Series	[Mo] (M)	[Co] (M)	[NO_3^-] (M)	pH	n° spectra	Analysis
1	0.10	-	0.10	2.11-8.24	26	Raman
2	0.10	0.10	0.10	2.00-5.96	19	Raman UV-Vis-NIR
3	0-0.40	0.04	0.08	5.0	8	UV-Vis-NIR

equipped with a 70 mW, 532 nm diode laser for excitation. The data-point resolution in these spectra, which were subject to baseline correction before analysis, was 2 cm^{-1}. The NO_3^- peak at 1044 cm^{-1} was used as an internal standard and spectra were scaled to this band. UV-Vis-NIR measurements (250-1100 nm) were carried out on the solutions in series 2 using a Varian Cary 50 spectrophotometer equipped with a Hellma immersion probe. UV-Vis-NIR spectra were recorded on the solutions in series 3 in the spectral range of 200-1350 nm on a Varian Cary 500 spectrophotometer with water as the reference. The data-point resolution of the UV-Vis-NIR measurements was 1 nm. All measurements were carried out under ambient conditions (298 K).

Results and discussion

Mo-solutions

The reaction equations for the formation of $H_xMo_7O_{24}^{(6-x)-}$ and $H_xMo_8O_{26}^{(4-x)-}$ polyanions from MoO_4^{2-} under acidic conditions are given in Eq. 1 and 2. The formation constants of these different complexes, as formulated in Eq. 3, have been determined by a number of different authors with the aid of potentiometric titrations [16,32,33]. Cruywagen and coworkers have subsequently used these values as the basis for their studies into the complexation of Mo(VI) with a number of different organic ligands [9,37-39]. In chapter 2B, their investigations into the formation of Mo(VI)-citrate complexes are used as a starting point [9]. Hence, for consistency, their values for the formation constants of Mo(VI)-isopolyanions are used in this section as well. The molecular formulas of the isopolyanions that can be formed and their formation constants are listed in Table 2 [16].

$$7\ MoO_4^{2-} + (8+x)\ H^+ \leftrightarrow H_xMo_7O_{24}^{(6-x)-} + 4\ H_2O \qquad \text{(Eq. 1)}$$

$$8\ MoO_4^{2-} + (12+x)\ H^+ \leftrightarrow H_xMo_8O_{26}^{(4-x)-} + 6\ H_2O \qquad \text{(Eq. 2)}$$

$$\beta_{mp} = \frac{\left[H_x Mo_m O_y\right]}{\left[MoO_4^{2-}\right]^m \cdot \left[H^+\right]^p} \qquad \text{(Eq. 3)}$$

Raman spectra recorded on 0.10 M Mo solutions in the pH range 2-8 are presented in Fig. 1. The theoretical speciation of Mo(VI)-complexes in these solutions is determined from the formation constants of isopolyanions and a concentration plot is presented in Fig. 2a. Spectra recorded on AHM-solutions of pH 6 (or higher) show bands at 896 and 842 cm^{-1} due to symmetric and anti-symmetric Mo=O stretching vibrations and a band at 318 cm^{-1} (not shown) as a result of a O=Mo=O bending vibration. These features are characteristic of MoO_4^{2-} in solution, in accordance with the speciation plot. When the pH is decreased, $Mo_7O_{24}^{6-}$ starts to be formed and a band appears at 938 cm^{-1}. A further decrease in pH to a value of 4.5 leads to a shift in the most intense Mo=O stretching band to higher wavenumber. Probably, this shift is the result of the protonation of $Mo_7O_{24}^{6-}$, which is observed in the same pH region in Fig. 2a. At a pH lower than 3, multiple Mo=O stretching vibration bands are observed (968 cm^{-1}, 952 cm^{-1}) along with a new feature at 849 cm^{-1}. In the speciation plot, the formation of $H_3Mo_7O_{24}^{3-}$, $Mo_8O_{26}^{4-}$ and $HMo_8O_{26}^{3-}$ is observed at these pH values.

Since the solutions under study contain a number of different Mo(VI)-complexes, the measured spectra are the result of contributions from these different components. With the aid of a chemometric procedure, called multivariate curve resolution (MCR), the Raman spectra can be deconvoluted into pure component spectra and the factors that describe their quantitative contributions to the measured spectra (the so-called scores). In general, this is achieved by solving Eq. 4.

Table 2. Stoichiometry [m,p], molecular formula, formation constants (β_{mp}) [9] and positions of main Mo=O stretching bands of Mo(VI) isopolyanions in solution. The stoichiometry of the complexes is defined as the number of MoO_4^{2-} (m) and H^+ (p) required for their formation (Eq. 1-3).

Complex [m,p]	Formula	Log(β_{mp}) (25°C)	Component	Raman bands (cm^{-1})
$[1,0]^{2-}$	MoO_4^{2-}	-	Mo-A-1	896, 842
$[7,8]^{6-}$	$Mo_7O_{24}^{6-}$	52.81	Mo-A-2	939, 896
$[7,9]^{5-}$	$HMo_7O_{24}^{5-}$	57.40	Mo-A-3	946, 904
$[7,10]^{4-}$	$H_2Mo_7O_{24}^{4-}$	60.97	Mo-A-4	958, 912
$[7,11]^{3-}$	$H_3Mo_7O_{24}^{3-}$	63.03	Mo-A-5	-
$[8,12]^{4-}$	$Mo_8O_{26}^{4-}$	71.19	Mo-A-5	-
$[8,13]^{3-}$	$HMo_8O_{26}^{3-}$	73.03	Mo-A-5	-

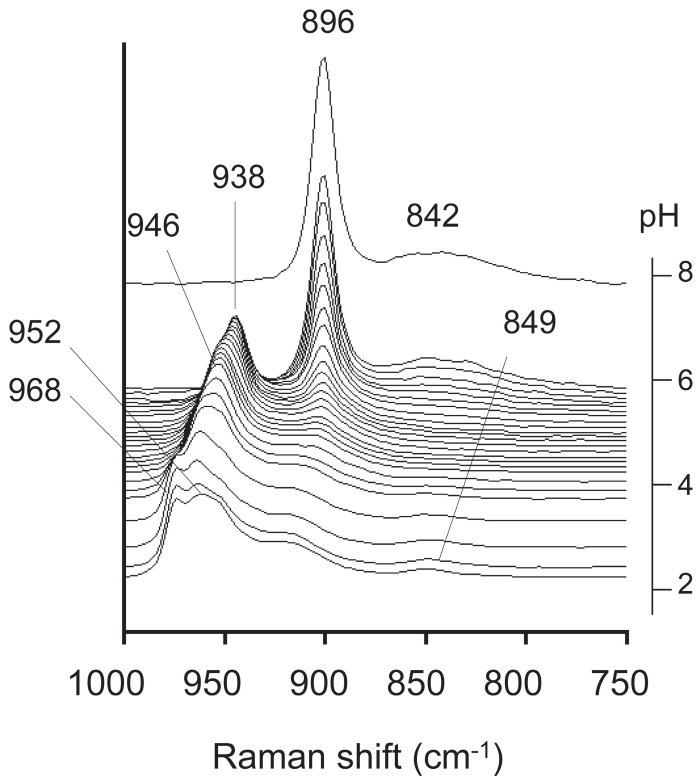

Figure 1. Selected Raman spectra recorded on the 0.10 M Mo AHM solutions in series 1 at different pH values in the pH range 2-8.

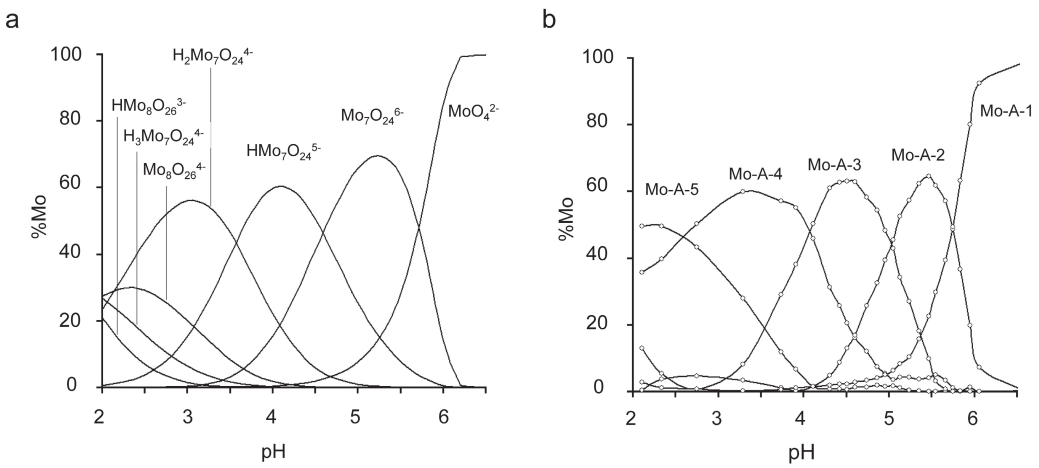

Figure 2. Theoretical speciation plot of Mo(VI)-complexes in 0.10 M Mo (AHM) solutions as a function of pH derived from formation constants (a) and a speciation plot of components Mo-A-1 to Mo-A-5 in 0.10 M Mo (AHM) solutions derived from MCR analysis of Raman spectra (b).

$$X(n_{spectra} \times n_{datapoints}) = C(n_{spectra} \times n_{comp}) \bullet S(n_{comp} \times n_{datapoints}) + E(n_{spectra} \times n_{datapoints}) \quad \text{(Eq. 4)}$$

In this equation, X represents the data matrix, in this case containing the 26 Raman spectra ($n_{spectra}$) recorded on the AHM-solutions in series 1. For the chemometric analysis, spectra have been used in the range of 750-1000 cm^1 with 2 cm^{-1} data point resolution, yielding 126 data points ($n_{datapoints}$) for each spectrum. In general, the 250-450 cm^{-1} spectral range in which the O=Mo=O bending vibrations are observed, also contains valuable information on the nature of Mo(VI)-complexes in aqueous solution [40]. However, the intensity of these bands is much lower and the signal to noise ratio in this part of the spectrum was insufficient for a reliable quantitative analysis. The matrix C contains the scores of a number of pure components ($n_{comp.}$) for all solutions on which spectra were recorded. The spectrum matrix S contains the pure component spectra. E is the residual error matrix, which consists of the difference between the measured spectra and the spectra constructed from a linear combination of the pure component spectra. Through an iteration procedure, in which the values in matrices C and S are systematically varied, the value of matrix E is minimized. In the MCR-procedure, the values in matrices C and S are forced to be positive, a prerequisite to obtain meaningful spectra. Furthermore, spectra thought to originate from the presence of one type of Mo(VI)-complex in solution can be used as input in matrix S, prior to the iteration procedure. In this way, the measured spectra are deconvoluted into the spectra and the scores of the different components that are simultaneously present in solution. The algorithms used for the MCR-analysis can be found in references [41,42]. When it is assumed that all Mo(VI)-complexes in solution are Raman active, the concentrations of the different Mo(VI)-complexes can be calculated from the scores of the different components.

Using MCR, the best fit of the spectra recorded on the 0.10 M Mo AHM-solutions was obtained with five components. After the iteration procedure, the absolute values in the error matrix were on average 1.6 % of the values in the corresponding data matrix. The lines in Fig. 2b indicate the concentration of these components as a function of pH. By comparison to the speciation plot in Fig. 2a, it can be concluded that the scores of components Mo-A-1, Mo-A-2, Mo-A-3, and Mo-A-4 represent the concentration of MoO_4^{2-}, $Mo_7O_{24}^{6-}$, $HMo_7O_{24}^{5-}$ and $H_2Mo_7O_{24}^{4-}$ anions, respectively. The presence of component Mo-A-5 at pH 2-3 indicates that this component represents the formation of $H_3Mo_7O_{24}^{3-}$, $Mo_8O_{26}^{4-}$ and $HMo_8O_{26}^{3-}$ complexes. Although these complexes are expected to give rise to different Raman spectra, with this limited data set, a more detailed deconvolution of the contributions of these different complexes was not possible. The deconvoluted Raman spectra of components Mo-A-1 to Mo-A-5 are presented as the solid

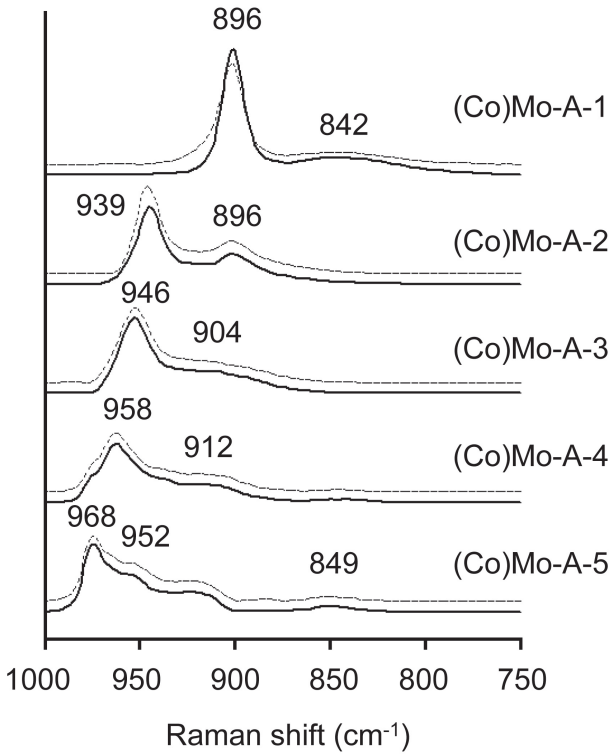

Figure 3. Pure spectra of components Mo-A-1 to Mo-A-5 obtained from MCR analysis of Raman spectra recorded on 0.10 M Mo (solid lines) and CoMo-A-1 to CoMo-A-5 obtained from MCR analysis of Raman spectra recorded on 0.10 M Mo/0.10 M Co solutions (dotted lines).

lines in Fig. 3. The assignment of the different components to actual Mo(VI)-complexes and the location of their main Raman bands are included in Table 2. The positions of the most intense Mo=O stretching vibration bands are in good agreement with values reported for different Mo(VI) isopolyanions in the literature [31,40].

CoMo-solutions

The interaction between Co(II) and Mo(VI)-anions was evaluated by Raman and UV-Vis-NIR spectroscopy on the solutions in series 2 and 3 (Table 1). UV-Vis-NIR spectra recorded on 0.04 M Co(II) solutions with varying Mo-concentrations (0-0.40 M) are presented in Fig. 4. In these solutions, the pH was kept constant at a value of 5.0. The spectrum of the solution without Mo, shows absorption bands at 511 nm (with a shoulder at 475 nm) and 1256 nm, corresponding to d-d transitions of the $[Co(H_2O)_6]^{2+}$ complex [43]. The part of the spectrum at larger wavelengths could no be used due to the strong absorption of water in this spectral range. Addition of AHM and the introduction of Mo(VI)-anions led to a considerable increase in intensity and a slight red shift in the maxima of both bands. At a Mo:Co ratio of 10, the band maxima are located at 515 and 1262 nm and the intensity of the bands has increased by a factor 2.3 (515

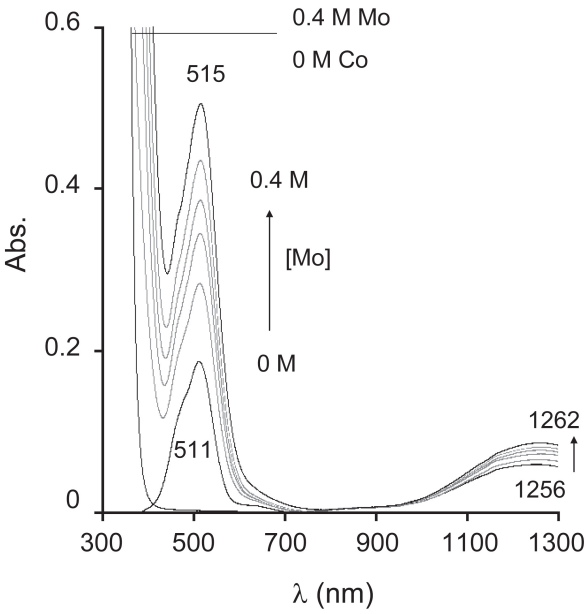

Figure 4. Selected UV-Vis-NIR spectra recorded on the 0.04 M Co solutions with different Mo-concentrations (0-0.40 M) in series 3. The pH of all solutions was 5. The spectrum of a 0.40 M Mo solution of the same pH is included for comparison.

nm) and 1.5 (1262 nm). The spectrum of a 0.40 M Mo AHM solution of pH 5.0 without Co(II) is included in the same figure. It can be observed that the presence of Co(II) results in a red shift in the O→Mo(VI) charge transfer band. From the changes in the UV-Vis-NIR spectra, it can be inferred that a chemical interaction must exist between Co(II)- and Mo(VI)-complexes in these solutions.

In analogy to the experiment described above, Raman spectroscopy was applied to 0.10 M Mo AHM-solutions of different pH in the presence of 0.10 M $Co(NO_3)_2$ (series 2). The resulting Raman spectra are presented in Fig. 5a. By comparison to Fig. 1, it can be seen that at pH ≈ 2, spectra recorded on Mo and CoMo solutions are remarkably similar. At a pH between 3 and 4.5 a shift in the most intense Mo=O stretching vibration to a final value of 941 cm^{-1} is observed. As compared to the spectra recorded on the Mo-solutions, this shift takes place at lower pH. From pH 5, the formation of MoO_4^{2-} is again observed by the appearance of a band at 896 cm^{-1}. Finally, at pH ≈ 6 the formation of a purple precipitate ($CoMoO_4$) was observed. However, all Raman spectra presented in Fig. 5a were recorded on clear solutions. Besides Raman spectra, UV-Vis-NIR spectra were recorded on these CoMo-solutions, as well, which are presented in Fig. 5b. A continuous increase in the d-d transition band of Co(II) is observed upon increasing the pH.

For the MCR-analysis of these Raman spectra, the same parameters were used as for the

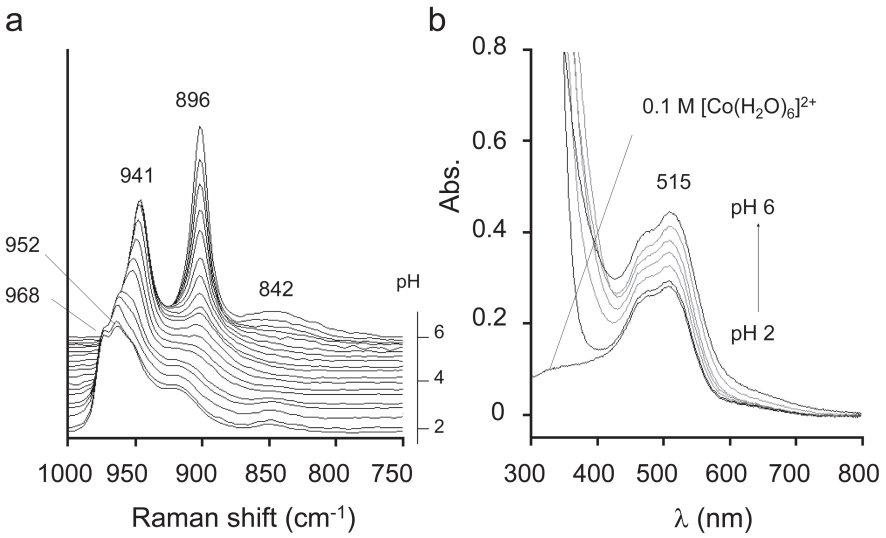

Figure 5. Selected Raman (a) and UV-Vis-NIR (b) spectra recorded on the 0.10 M Mo/0.10 M Co solutions in series 2 at different pH values in the pH range 2-6.

deconvolution of Raman spectra recorded on the cobalt-free Mo-solutions. This time, the goodness of fit, defined as the overlap between the measured spectra and the fitted spectra was 98.3 %. The thus obtained spectra of pure components CoMo-A-1 to CoMo-A-5 are presented as the dotted lines in Fig. 3. The spectra of components CoMo-A-1 to CoMo-A-5 are practically identical to the corresponding spectra (Mo-A-1 to Mo-A-5) obtained from the MCR-analysis of the Mo-solutions. It can be concluded, that the presence of Co(II) doesn't influence the structure of Mo(VI)-complexes in aqueous solution to a large extent.

The calculated concentration profiles of components CoMo-A-1 to CoMo-A-5 in the CoMo-solutions, as calculated from the MCR-analysis, are presented in Fig. 6. For comparison, the concentration profiles of components Mo-A-1 to Mo-A-5 in Mo-solutions are presented as the dotted lines in the same plot. The maxima in the concentration profiles of the different $H_xMo_7O_{24}^{(6-x)-}$ complexes have shifted to lower pH after the addition of $Co(NO_3)_2$. Apparently, the presence of Co(II) induces deprotonation of these complexes. The intensity of the d-d transition band of Co(II), which is presented as the grey line in the same figure, was determined at 550 nm, to avoid any influence of the Mo(VI)-O charge transfer band. A correlation is found between the formation of deprotonated heptamolybdates (components Mo-A-2 and Mo-A-3) and the increase of the Co(II) d-d transition band in the UV-Vis-NIR spectra. Coordination of Co(II) to the outside of the $HMo_7O_{24}^{5-}$ and $Mo_7O_{24}^{6-}$ anions can explain both features. Apparently, Co(II) is preferentially coordinated by more and more deprotonated (and thus more negatively

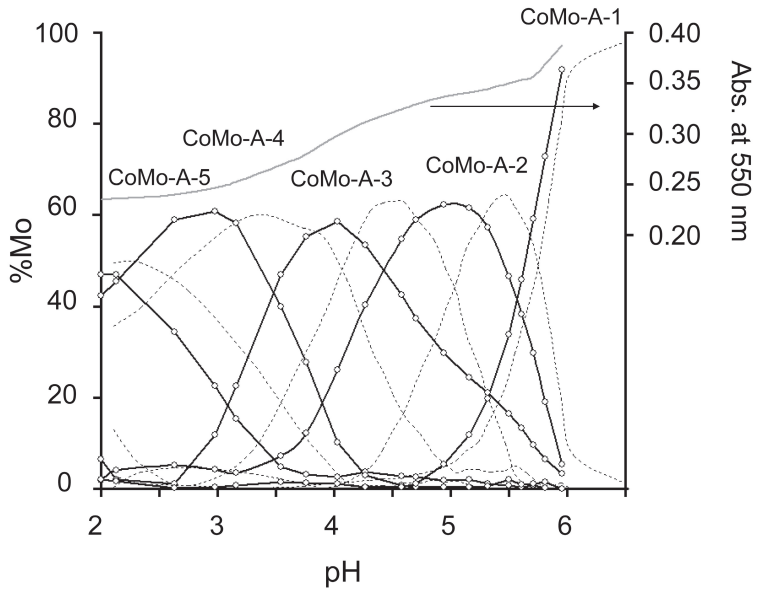

Figure 6. Speciation plots of components CoMo-A-1 to Co-Mo-5 obtained from MCR analysis of Raman spectra recorded on 0.10 M Mo/0.10 M Co solutions (solid lines) and components Mo-A-1 to Mo-A-5 derived from 0.10 M Mo solutions (dashed lines). The absorbance at 550 nm in the UV-Vis-NIR spectra recorded on 0.10 M Mo/0.10 M Co solutions is indicated by the grey line.

charged) $H_xMo_7O_{24}^{(6-x)-}$ anions. Inversely, this results in the deprotonation of heptamolybdate anions at lower pH in the presence of Co(II). Complexation leads to the exchange of one or two water ligands of the $[Co(H_2O)_6]^{2+}$ complexes by one or two terminal oxygens from the Mo(VI)-anions, resulting in an increased intensity of the d-d transition bands, as the coordination sphere of Co(II) is no longer perfectly octahedral. Nevertheless, Co(II) is still almost octahedrally surrounded by oxygen atoms explaining the small shift in the position of the d-d bands. Crystal structures of $[(Fe)_2(H_2O)_9Mo_7O_{24}]^{2-}$ and $[(Mn)_2(H_2O)_9Mo_7O_{24}]^{2-}$ cluster compounds have recently been obtained, in which the complexation of the divalent cations takes place on the outside of the heptamolybdate anions [11]. Co_2-Mo_7O_{24} complexes could be formed in the CoMo-solutions having a similar configuration. The tentative structure of these complexes, based on the structure of the Fe and Mn-heptamolybdates [11], is presented in Fig. 7. In this figure, the coordination of Co(II)-atoms to the $Mo_7O_{24}^{6-}$ complex via one oxygen (Co(II) a) or two oxygens (Co(II) b) is illustrated. Although disintegration of $Mo_7O_{24}^{6-}$ occurs at a pH > 5, the intensity of the Co(II) d-d band increases even further under these conditions. Apparently, MoO_4^{2-} is able to coordinate to Co(II) in a similar manner as heptamolybdate complexes, without the formation of a $CoMoO_4$ precipitate. The proposed complexation of Co(II) by Mo(VI)-anions seems to provide a plausible explanation for the observed spectroscopic features.

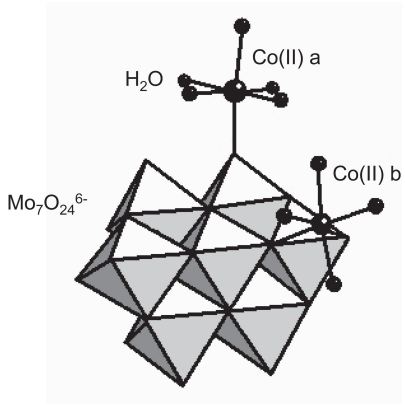

Figure 7. Tentative structure of $Co_2Mo_7O_{24}^{2-}$ complexes present in CoMo-solutions. The structure is based on the crystal structure of $[(Fe)_2(H_2O)_9Mo_7O_{24}]^{2-}$ and $[(Mn)_2(H_2O)_9Mo_7O_{24}]^{2-}$ reported by Long et al. [11].

Conclusions

Interaction between Co(II)-cations and different molybdate anions has been revealed by Raman and UV-Vis-NIR spectroscopy studies on CoMo-solutions. Most probably, complexes are formed in which Co(II) is bound to the outside of molybdate ions. However, further studies on these solutions are required to determine the exact structure of the CoMo-complexes. Potentiometric titrations could help to elucidate the stoichiometry of the complexes that are formed in solutions. The preparation of crystal structures or the analysis of solutions using EXAFS could also yield valuable information. In any case, the observed interaction can have consequences for the preparation of supported CoMo-HDS catalysts. Since Co acts as a promotor in these catalysts, a close interaction between Co and Mo in the final catalyst is of prime importance for their activity. The formation of CoMo-complexes in the impregnation solution has previously been used as an approach to maximize the promoting effect of Co [36,44,45]. The observed interaction of Co(II)- and Mo(VI)-complexes in AHM/$Co(NO_3)_2$ solutions is therefore a remarkable finding.

Chapter 2B

Spectroscopic Investigation of the Molecular Structure of Citrate, Co(II)-citrate and Mo(VI)-citrate Complexes in Aqueous Solution

Abstract

An assignment has been made of the vibrational bands in Raman and IR spectra of aqueous citrate solutions with the aid of DFT-calculations and isotopic labeling. Reference UV-Vis-NIR spectra were derived for three different Co(II)-citrate complexes. Three different types of Mo(VI)-citrate complexes complexes could be distinguished by Raman spectroscopy on Mo-citrate solutions. Reference spectra of these complexes were obtained with the aid of MCR analysis.

Introduction

Chelating agents, such as citric acid (CA), nitrilotriacetic acid (NTA) and ethylene diaminetetraacetic acid (EDTA), are added to industrial CoMo-impregnation solutions to increase the solubility of Mo(VI) in acidic solutions or to prevent the precipitation of Co-hydroxides at high pH. In this way, it is possible to prepare stable solutions with a higher concentration of metal-complexes and increase the concentration of active sites in the final catalyst. Furthermore, the presence of chelating agents is found to increase the promoting effect of Co in the final $CoMoS_2$ catalyst [22,25,27]. Throughout this thesis, the role of citric acid in the preparation process of (Co)Mo/Al_2O_3 catalysts is investigated. Citric acid was chosen as an example of organic chelates for its ability to form stable complexes with both Mo(VI) and Co(II) [7,10,12,15,17-21], its frequent appearance in recipes for industrial impregnation solutions [46-49] and its high solubility. The molecular structure of the citrate trianion (CTA) is presented in Fig. 8. The configuration of citric acid, the citrate trianion [50,51] and various metal-citrate complexes in solution [7,9,10,12,15,17-21,32,50,52-55] have been the subject of many publications, due to the relevance of these compounds in physiology and biochemistry. In this section, the results of a study into the structure of citrate, Co(II)-citrate and Mo(VI)-citrate complexes in aqueous solution are presented. Raman and IR measurements on (^{13}C labeled) Na_3citrate solutions were carried out to obtain a complete and reliable assignment of the vibrational bands of the citrate trianion in solution. In addition, DFT-calculations were carried out to determine theoretical vibrational modes of the unperturbed citrate molecule and facilitate the interpretation of the different vibrational spectra. The results are discussed in the first part of this section. Subsequently, the speciation of Co(II)- and Mo(VI)-citrate complexes in solution as a function of concentration and pH is discussed on the basis of spectroscopic studies and literature data.

Experimental

Raman and IR measurements were carried out on aqueous 0.40 M Na_3citrate solutions, prepared from citric acid (Acros, p.a.) and NaOH (Aldrich, p.a.). Solutions of Na_3citrate, in which either the terminal carbon atoms (1,5) or the carbon atoms of the CH_2 groups (2,4) consisted of ^{13}C, were prepared from 99% ^{13}C labeled citric acid (Aldrich). To examine vibrational bands of citrate in areas of the spectra where vibrational bands of H_2O are present, D_2O was used as a solvent in some cases.

DFT-calculations were performed using the TURBOMOLE quantum chemistry package [56,57].

The geometry of the citrate trianion was optimized before calculating the positions of the vibrational bands in IR and Raman spectra. The calculations were performed using a Triple Zeta Valence plus Polarization (TZVP) basis set and the B3LYP parameterization of the exchange-correlation functional. All molecules were considered to be closed- shell molecules. The energy convergence criterion was set to 10^{-6} Hartree and the SCF convergence criterion to 10^{-8}.

The compositions of the solutions used for spectroscopic studies on Co(II)-citrate and Mo(VI)-citrate solutions are listed in Table 3. Citric acid (Acros, p.a.), $Co(NO_3)_2 \cdot 6\ H_2O$ (Acros, p.a.) and $(NH_4)_6Mo_7O_{24}$ (Acros, p.a.) were used for the preparation of these solutions. Concentrated NaOH (Merck, p.a.) and HCl (Merck, p.a.) solutions were used for pH adjustment. Care was taken that the concentration of components under study was not altered during measurements in a series. For IR measurements, $CoCl_2 \cdot 6\ H_2O$ (Acros, p.a.) was used as the Co(II)-source to prevent the occurrence of bands due to NO_3^- in the IR-spectra. For Raman measurements on Mo(VI)-citrate solutions (series 10-12) NH_4NO_3 (Acros Organics, p.a.) was added to serve as an internal standard. Potentiometric titrations were carried out on different (Co(II))-citrate solutions, in which the pH of the solution was measured as a function of the amount of NaOH that was added. Raman and IR-spectra were also recorded on 0.40 M solutions of tricarballylic acid sodium salt in the presence and absence of 0.40 M Co(II) (ex $CoCl_2 \cdot 6\ H_2O$) .

Raman spectra were recorded with a data point resolution of 2 cm^{-1} using a Kaiser RXN spectrometer equipped with a 70 mW, 532 nm diode laser for excitation. Spectra were subject to baseline correction before analysis. The NO_3^- peak at 1044 cm^{-1} was used as an internal

Table 3. Composition of Co(II)-citrate and Mo(VI)-citrate solutions used for spectroscopic studies. The pH range and the number and type of spectra that were recorded in each titration series are included.

Series	[Mo] (M)	[Co] (M)	[CA] (M)	[NO_3^-] (M)	pH	nº spectra	Analysis
4	-	0.01	0.01	0.02	1.60-11.20	25	UV-Vis-NIR
5	-	0.01	0.02	0.02	2.16-11.96	29	UV-Vis-NIR
6	-	0.01	0.05	0.02	1.72-12.34	26	UV-Vis-NIR
7	-	0.2	0.2	0.4	1.56-8.23	28	UV-Vis-NIR
8	-	0.2	0.4	0.4	1.33-8.18	27	UV-Vis-NIR
9	-	0.2	1.0	0.4	1.33-8.78	30	UV-Vis-NIR
10	1.0	-	1.0	0.4	1.00-9.75	39	Raman
11	1.0	-	0.5	0.4	1.23-9.91	34	Raman
12	0.02	-	0.02	0.02	1.64-9.00	16	Raman

standard in the Raman measurements and spectra were scaled to this band. UV-Vis-NIR measurements (250-1100 nm) were carried out with 1 nm data point resolution using a Varian Cary 50 spectrophotometer equipped with a Hellma immersion probe. A Perkin-Elmer 2000 FT-IR spectrometer equipped with a DTGS detector was used for IR measurements. Spectra were recorded with a PIKE diamond ATR. All measurements were carried out under ambient conditions (298 K).

Results and discussion

Citrate solutions

In the remainder of the text, the numbering of the carbon atoms, as indicated in Fig. 8, will be used to refer to individual carbon atoms. Complexation of metal-ions can take place through the two equivalent carboxylate groups (C_1 and C_5), the central carboxylate group (C_6) and the hydroxyl group. Raman and IR spectra recorded on Na_3citrate solutions including the ^{13}C labeled compounds are presented in Fig. 9a and b, respectively. To determine the position of vibrational bands of citrate that are normally obscured by stretching (3000-3400 cm^{-1}) and bending (1550-1800 cm^{-1}) vibrations of H_2O, solutions of Na_3citrate and 1.5 ^{13}C-labeled Na_3citrate in D_2O were also prepared. The corresponding Raman and IR spectra are included in Fig. 9. DFT calculations were carried out to facilitate assignment of relevant IR and Raman bands in the citrate spectra. For this purpose, the vibrational modes and frequencies of the unperturbed citrate trianion, the ^{13}C labeled citrate analogues and the citrate ion with the deuterated hydroxyl group were calculated. It should be emphasized that these calculations were restricted to the unperturbed molecule, as it proved to be impossible to mimic the hydration sphere of the citrate trianion in a realistic manner. The results have been summarized in Table 4 together with the measured band positions in aqueous solution and the corresponding tentative assignments.

For obvious reasons, the carboxylate groups play the major role in the coordination of the citrate ions. It follows that the corresponding IR and Raman bands and, in particular, the symmetrical (ν_s COO^-) and anti-symmetrical (ν_{as} COO^-) stretching vibrations will be of the highest diagnostic value. In general, these bands are found in the range 1600-1350 cm^{-1} with the anti-symmetrical vibrations located at higher wavenumber than the symmetric ones. According to the results of DFT calculations, coupling of the ν_{as} COO^- vibrations of the individual carboxylate groups of citrate, does not occur. This implies that ν_{as} COO^- vibrations of non-equivalent carboxylate groups should give rise to separate bands in the vibrational spectra. Furthermore, DFT structure optimization revealed the formation of an internal hydrogen bond between the hydroxyl group and one of the equivalent (C_1 or C_5) carboxylates. As a consequence, all carboxylate groups are

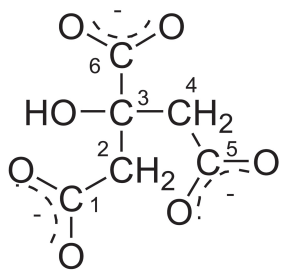

Figure 8. Molecular structure of citrate with the numbering of the carbon-atoms.

principally different resulting in three different ν_{as} COO^- frequencies. However, the formation of the internal hydrogen bond in aqueous solution is unlikely, since water molecules are available for the formation of external H-bonds. As a result, the carboxylate groups in solvated citrate molecule can be expected to be much more equivalent, giving rise to only one or two $\nu_{as}COO^-$ bands. Unfortunately, it was not possible to include the presence of water in the DFT calculations in a reliable manner to confirm this assumption. However, the measured IR and Raman spectra of the Na_3citrate solutions revealed a broad asymmetric ν_{as} COO^- band around 1575 cm^{-1} with a shoulder at the high frequency side, which clearly points to differences in vibrational frequency. Indeed, upon ^{13}C labeling of the C_1 and C_5 carboxylates, the band splits into two separate bands; one around 1590 cm^{-1} and one at 1530 cm^{-1}. Consequently, the 1590 cm^{-1} band can be assigned to ν_{as} COO^- of the central C_6 carboxylate, since it will be unaffected by the ^{13}C labeling, while the 1530 cm^{-1} band can be attributed to the C_1 and C_5 carboxylates in accordance with the expected red shift as a result of ^{13}C labeling.

DFT-calculations also predicted that coupling of the ν_s COO^- vibrations of the three carboxylate groups results in three different vibrational modes and hence, possibly, three different ν_s COO^- bands in the vibrational spectra. Of these, the mode in which the ν_s COO^- groups stretch in phase is supposed to have the highest wavenumber. Regarding the large polarizability change accompanied with this vibration, it is assigned to the intense band at 1418 cm^{-1} in the Raman spectra (Fig. 9a). ^{13}C labeling of the carboxylates results in a shift of this band to 1398 cm^{-1}. As was observed for the ν_{as} COO^- band at 1575 cm^{-1}, a band at 1422 cm^{-1} appears to be present underneath the 1418 cm^{-1} band. It should be noted that in-phase and out-of-phase CH_2 scissoring vibrations (δ CH_2) may also give rise to bands in this same region, but assignment to the ν_s COO^- vibration of the central C_3 carboxylate group is preferred because of its higher intensity. Finally, a band is present in the IR spectrum at 1391 cm^{-1}, which shifts to 1363 cm^{-1} after ^{13}C labeling of the C_1 and C_5 carboxylates. It is probably the result of an out-of-phase

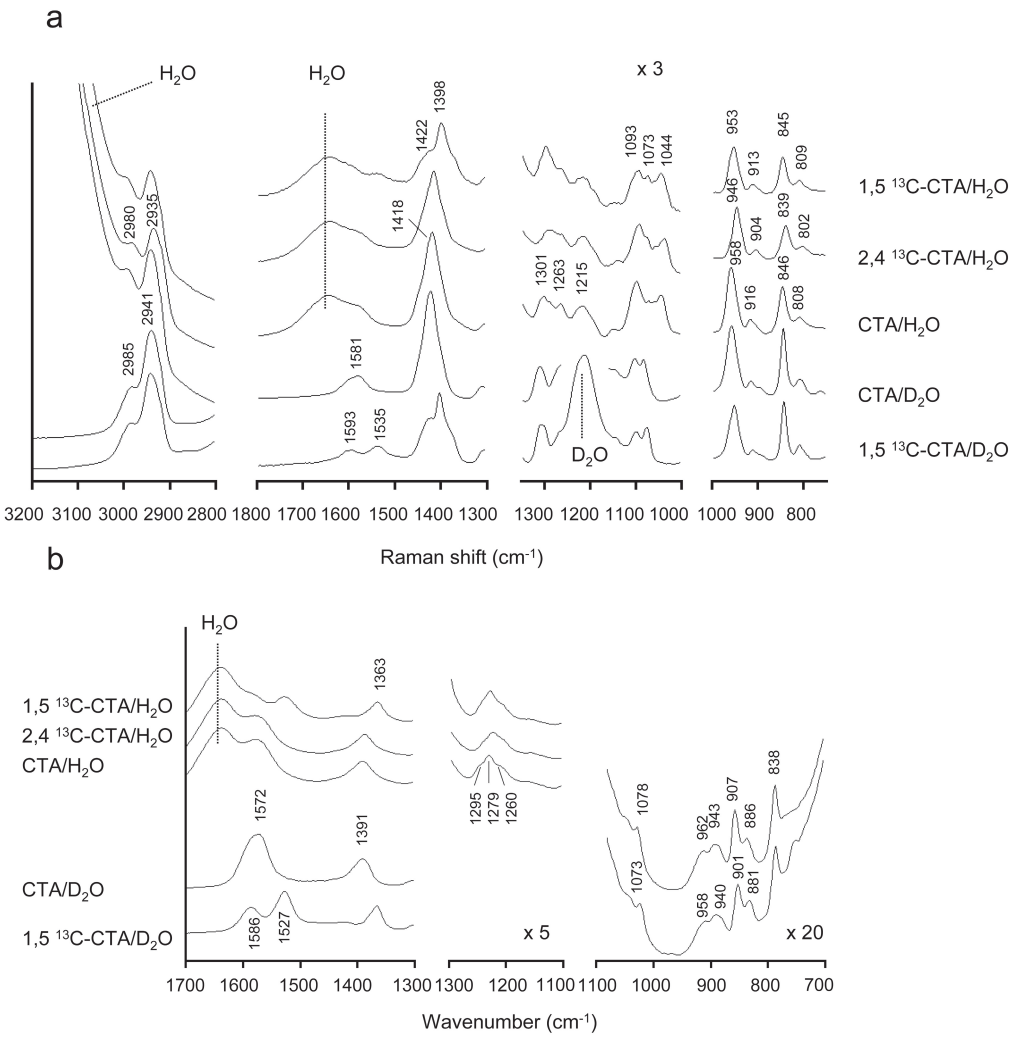

Figure 9. Raman (a) and IR (b) spectra recorded on 0.40 M Na_3citrate solutions. Spectra of solutions prepared from ^{13}C labeled citric acid and D_2O are included, as indicated.

Table 4. Calculated positions and assignments of vibrational bands of gas-phase citrate based on DFT-calculations (left) and the observed positions of bands in the Raman and IR spectra of Na_3citrate solutions (right). The positions of the different bands after isotopic labeling are included.

DFT-calculations			assignment	Raman/IR measurements		
CTA	1,5-^{13}C CTA	2,4-^{13}C CTA		CTA	1,5-^{13}C CTA	2,4-^{13}C CTA
3086	3086	3077	ν_{as} CH_2 in phase	2985/-	2985/-	2980/-
3039	3039	3029	ν_{as} CH_2 o.o. phase	-/-	-/-	-/-
2997	2996	2990	ν_{s} CH_2 in phase	2941/-	2941/-	2935/-
2953	2953	2945	ν_{s} CH_2 o.o. phase	-/-	-/-	-/-
1635	1632	1634	ν_{as} C_6OO^-	1593/1586	1593/1586	1593/1586
1621	1580	1621	ν_{as} C_1OO^-/ C_5OO^-	1581/1572	1535/1527	1581/1572
1605	1566	1604				
1451	1451	1448	δ CH_2 o.o. phase	-/-	-/-	-/-
1435	1434	1431	δ CH_2 in phase	-/-	-/-	-/-
1368	1344	1366	ν_{s} C_1OO^-/ C_5OO^- in phase	1418/-	1398/-	1415/-
1354	1355	1353	ν_{s} C_6OO^-	1422/-	1422/-	1422/-
1338	1319	1337	ν_{s} C_1OO^-/ C_5OO^- o.o. phase	-/1391	-/1363	-/1391
1300	1292	1296	ω CH_2 o.o. phase	1301/1295	1301/1295	1301/1295
1289	1285	1286	τ CH_2 o.o. phase	-/1279	-/1279	-/1279
1269	1268	1259	ω CH_2 in phase	1263/1260	1263/1260	1263/1260
1205	1202	1203	τ CH_2 in phase	1215/-	1215/-	1215/-
				1093/-	1093/-	1093/-
1120	1119	1111	ν CO	1078/1078	1073/1073	1078/1078
1013	1013	1008	δ COH	1044/-	1044/-	1044/-
916	911	903	ν C_1C_2/ν C_4C_5 i.p.	958/962	953/958	946/-
860	852	856	ν C_1C_2/ν C_4C_5 o.o.p.	916/907	913/901	904/-
820	818	811	ν C_2C_3/ν C_3C_4 i.p.	846/838	845/838	839/-

COO^- stretching vibration of these groups. However, as already mentioned, it was not possible to take the hydration sphere into account in the DFT-calculations. In our opinion, this explains the occasional poor agreement in the calculated and the measured positions of the ν COO^- bands.

After the carboxylates, the hydroxyl group is the most interesting functional group because of its coordinating potential at high pH. Obviously, the O-H stretching vibration would be ideal to study this, but the interference of H_2O and D_2O bands prevents its use in both IR and Raman. In principle, the C-O(H) stretching and C-O-H bending vibrations offer a possible alternative, particularly in IR, since these modes are attended with a relatively large change of the dipole moment. Besides, the corresponding band(s) for a tertiary alcohol are usually found between 1200 and 1050 cm^{-1}, a region that is only partly obscured by H_2O or D_2O bands. For that reason the band around 1075 cm^{-1} in the IR spectra in D_2O (Fig. 9b) is assigned to (one of) these vibrations. A band at about the same position is also present in the Raman spectra, but regarding the high Raman activity this could also be a C-C mode. In contrast, a band at 1044 cm^{-1} in the Raman spectra of the H_2O solutions is not present in D_2O. Since H-D exchange will particularly affect the C-O-H bending mode, this band is assigned to this vibration.

Next to the previously mentioned CH_2 scissoring vibrations, the other bands related to citrate CH_2 vibrations are found in two spectral regions, i.e., the C-H stretching region between 3000 and 2800 cm^{-1} and the H-C-H bending region between 1350 and 1200 cm^{-1}. Although the CH_2 groups are separated by the central (C_3) carbon-atom, DFT calculations point to a coupling of the ν CH_2 vibrations, resulting in four stretching modes (anti-symmetrical/symmetrical, in phase/out of phase). The Raman spectrum shows only two bands, located at 2985 and 2941 cm^{-1} of which the latter is assigned to the in-phase ν_s since this vibration is by far attended with the largest change in polarizability. For the same reason, assignment of the band at 2985 cm^{-1} to the in-phase anti-symmetrical ν CH_2 vibration is preferred over attributing the band to (one of) the out-of-phase vibrations. In accordance with the DFT-calculations, ^{13}C labeling of the C_2 and C_4 atoms leads to small shift in the position of both bands to lower wavenumber.

Besides the CH_2 stretching and scissoring bands, a number of H-C-H deformation bands can be expected; i.e. wagging (ω CH_2) and twisting (τ CH_2) bands in the region 1350-1150 cm^{-1}. In analogy to the CH-stretching vibrations, the latter vibrations couple to give rise to four different vibrational modes. The calculated positions of the vibrations (Table 4) match fairly well with the observed bands in the IR and Raman spectra around 1300 cm^{-1}, 1280 cm^{-1} , 1260 cm^{-1} and 1215 cm^{-1}. Besides, in accordance with the DFT-calculations, ^{13}C labeling has only

a minor frequency effect and therefore these bands are assigned accordingly to ω CH_2 (o.o. phase), τ CH_2 (o.o. phase), ω CH_2 (in-phase) and τ CH_2 (in-phase), respectively.

The remaining bands in the range 1100-700 cm^{-1} are skeletal modes, mainly C-C vibrations. The bands, around 960 cm^{-1} and 910 cm^{-1} in the IR and Raman spectrum of citrate, show a significant shift upon both C_1,C_5 and C_2,C_4 ^{13}C labeling and must therefore correspond to C_1-C_2 and C_4-C_5 stretching vibrations. Coupling of these vibrations is likely and for that reason, as indicated by the results of DFT-calculations, the high frequency (and most Raman active) band is assigned to the in-phase mode and the low frequency one to the out-of-phase vibration. The positions of the IR and Raman bands at 840 cm^{-1} and the Raman band at 808 cm^{-1} in the spectra of the unlabeled Na_3citrate solution are only affected by C_2,C_4 ^{13}C labeling. Hence, they can be assigned to C_2-C_3 and C_3-C_4 stretching vibrations. A similar coupling can be expected, the in-phase vibrational mode showing the highest wavenumber and hence the bands are assigned accordingly. Finally, the band at 1093 cm^{-1} in the Raman spectra seems unaffected by ^{13}C isotopic labeling although a minor intensity decrease is observed in D_2O solution. The former points to a vibrational mode that involves the C_3 atom. However, based on the available results, it was not possible to attribute this band to e.g. a C_3-C_6 or C_3-O stretching vibration or another skeletal mode such as a carboxylate deformation vibration.

Co-citrate solutions

The formation of Co(II)-citrate complexes in aqueous solutions has mainly been addressed from a biochemical point of view [10,12]. Formation constants for Co(II)-citrate complexes were derived by potentiometric titrations for solutions with a low concentration of citrate (0.002-0.004 M) [10]. Crystal structures of various Co(II)-citrate complexes have been determined, but speculation remains over the structures of these complexes in solution. For instance, in highly concentrated solutions (2M Co(II)) the formation of Co(II)-citrate polymers of different stoichiometry has been reported [21]. The use of formation constants derived from measurements on dilute solutions to predict the composition of more concentrated solutions, is therefore not without risk. In this paragraph, the application of UV-Vis-NIR spectroscopy to monitor the speciation of Co(II)-citrate complexes in solution was evaluated. Raman and IR spectroscopy were applied to determine the structure of different Co(II)-citrate complexes in solution.

Potentiometric titrations were used to get an idea of the stoichiometry of different Co(II)-citrate complexes in solution. In Fig. 10, titration curves are shown for citrate solutions in the absence and presence of Co(II). In the absence of Co(II), the addition of NaOH to a solution of citric

acid leads to deprotonation of the carboxylate groups. A steady increase in pH was observed until 3 equivalents of NaOH were added to solutions without Co(II). Once deprotonation of the carboxylate groups is complete, the pH rapidly increases from 6 to 12. However, when equimolar amounts of Co(II) and citrate are present, deprotonation is observed at a lower pH, which is a clear indication for complexation. Furthermore, the buffering effect of citrate is prolonged until the Na/citrate ratio is ~ 4.

UV-Vis-NIR spectra were recorded on 0.01 M and 0.20 M Co solutions with different Co:citrate ratios (1:1, 1:2 and 1:5) in the pH range 1-10 (series 4-9 in Table 3). A selection of spectra recorded on 0.01 M Co solutions is presented in Fig. 11. In both the 0.01 M and 0.20 M Co solutions, the spectrum recorded at low pH (~1) corresponds to that of $[Co(H_2O)_6]^{2+}$ with the main band at 511 nm and a shoulder at 475 nm. From pH 1-6 the intensity of this band gradually increases while its maximum remains at approximately the same position. The increase in intensity is more pronounced when the citrate concentration is higher. From pH 6-9 a shift of the main d-d band towards 532 nm is observed along with the appearance of a new band at 727 nm. At pH 9, all solutions show the same spectrum irrespective of the Co:citrate ratio. UV-Vis-NIR spectra recorded on the 0.20 M Co solutions show the same features, although changes in the spectra occur at different pH-values.

The proposed structures of Co(II)-citrate complexes, present in dilute solutions are shown in Fig. 12 [10]. At low pH, the carboxyl groups of citric acid are protonated and no interaction exists between $[Co(H_2O)_6]^{2+}$ and $citrH_4$. Deprotonation of the carboxyl groups leads to the

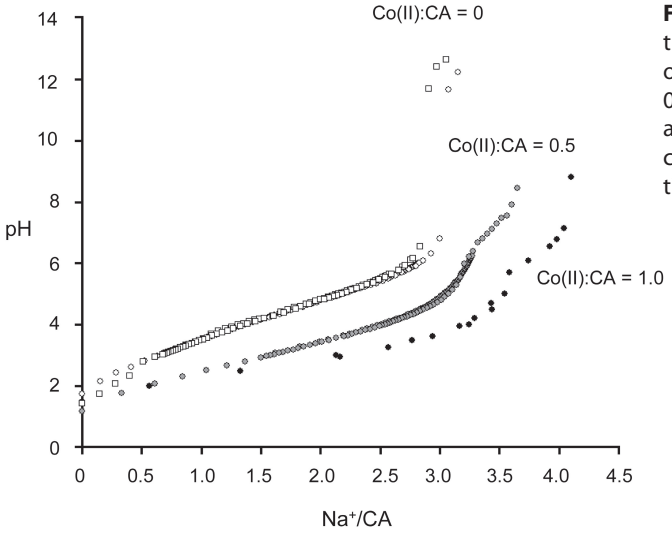

Figure 10. Titration curves showing the effect of the addition of NaOH on the pH of 0.20 M citric acid (○), 0.40 M citric acid (□), 0.40 M citric acid/0.20 M $Co(NO_3)_2$ (◉) and 0.20 M citric acid/0.20 M $Co(NO_3)_2$ (●) solutions.

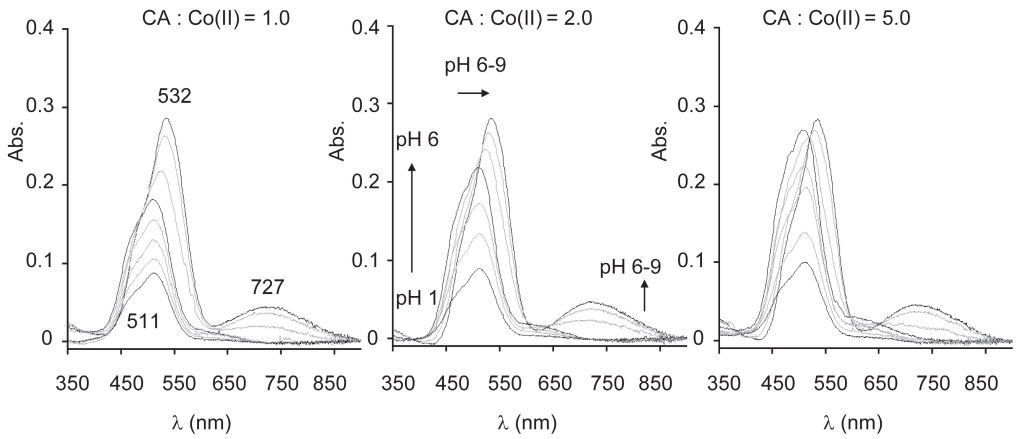

Figure 11. Selected UV-Vis-NIR spectra recorded on the 0.01 M Co solutions with different citrate concentrations in series 4-6. Spectra recorded on solutions of pH 1, 6 and 10 are shown in black.

formation of Co(II)-citrate complexes. In the titration curves in Fig. 10, this can be observed since deprotonation is facilitated by the presence of Co(II). The formation of Co(II)-citrate complexes leads to an increase in the intensity of the Co(II) d-d-band in the UV-Vis-NIR spectra. At a pH of 6, deprotonation of the carboxyl groups is complete and complexes are formed in which coordination of Co(II) is reported to occur through two carboxylate groups (one central and one terminal) and the hydroxyl group of the citrate ligand. Crystal structures of complexes with Co:citrate ratios 1:1 $[Co(citrH)(H_2O)_3]$ and 1:2 $[Co(citrH)_2]$ have been obtained from solutions of pH > 6, in which coordination takes place as described above. The formation of Co(II)-citrate complexes with different Co:citrate ratio explains why, at this pH, the intensity of the d-d transition bands in the UV-Vis-NIR spectra is a function of the citrate concentration.

At pH > 9, on the other hand, 1:1 Co(II):citrate complexes are exclusively formed, since identical UV-Vis-NIR spectra are found irrespective of the Co:citrate ratio in the solutions under study. The titration curves in Fig. 10 show that the addition of 4 equivalents of NaOH is required to increase the pH of an equimolar citric acid:$Co(NO_3)_2$ solution to a pH of 9. Upon changing the pH from 5-9, the Co(II)-citrate complexes apparently loose another proton. According to Kotsakis et al., deprotonation of the hydroxyl group is most likely to take place, resulting in the formation of complexes with $[Co(citr)(H_2O)_3]^{2-}$ stoichiometry [10]. Deprotonation of the hydroxyl group is observed in the crystal structure of a $(NH)_5[Mn(citr)_2]$ complex, in which the same type of tridentate coordination takes place [54].

The formation constants of the proposed Co(II)-citrate complexes, as taken from literature [10]

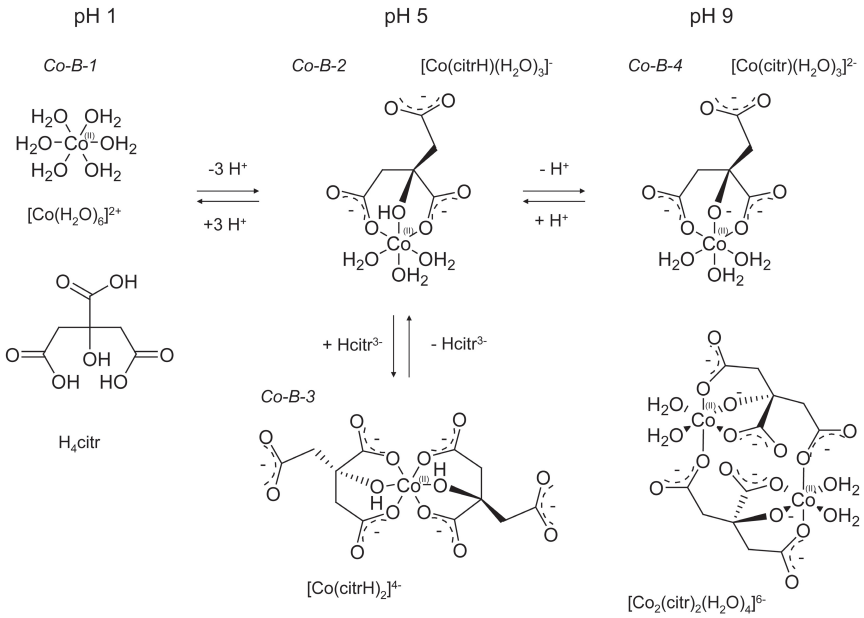

Figure 12. Molecular structure of Co(II)-citrate complexes in aqueous solution at different pH and Co: citrate ratios as proposed by Kotsakis et al. The assignment of components Co-B-1 to Co-B-4 to the presence of actual complexes is indicated as well.

are listed in Table 5. In this case, the general formula in Eq. 5 is used to describe the formation of the complexes. The formation constants are defined as in Eq. 6. With the aid of the formation constants, the theoretical concentrations of the different Co(II)-citrate complexes in the solutions in series 4-9 were calculated. The thus obtained speciation plots of Co(II)-complexes in 0.20 M and 0.01 M Co solutions with different citrate concentrations are presented in Fig. 13. It can be clearly observed that the formation of Co(II)-citrate complexes from $[Co(H_2O)_6]^{2+}$ occurs at lower pH in more concentrated solutions. Furthermore, the formation of the $[Co(citrH)_2]^{4-}$ complex is favored by low Co:citrate ratios and high concentrations.

$$c\ Co(II) + r\ citrH^{3-} + p\ H^{+} \leftrightarrow (Co(II))_c(citrH^{3-})_r(H^{+})_p \qquad \text{(Eq. 5)}$$

$$\beta_{crp} = \frac{\left[\left(Co(II)\right)_c\left(citrH^{3-}\right)_r\left(H^{+}\right)_p\right]}{\left[Co(II)\right]^c \cdot \left[citrH^{3-}\right]^r \cdot \left[H^{+}\right]^p} \qquad \text{(Eq. 6)}$$

Through analysis of the UV-Vis-NIR spectra recorded on the solutions in series 4-9, the validity of the theoretical speciation plots was examined. However, due to the broadness of the

Table 5. Stoichiometry [c,r,p], molecular formula, formation constants (β_{crp}) [10] and positions and extinction coefficients of characteristic absorption bands of Co(II)-citrate complexes in aqueous solution. The stoichiometry of the complexes is defined as the number of Co(II)-atoms (c), $citrH^{3-}$ (r) and H^+ (p) required for their formation (Eq. 5 and 6).

Complex [c,r,p]	Formula	Log(β_{crp}) (25°C)	Component	UV-Vis-NIR bands (nm)	Extinction Coefficient ($M^{-1}cm^{-1}$)
$[1,0,0]^{2+}$	$[Co(H_2O)_6]^{2+}$	-	Co-B-1	511 (475)	4.4
[1,1,1]	$[Co(citrH_2)(H_2O)_3]$	8.28	Co-B-2	513 (480, 460)	9.2
$[1,1,0]^-$	$[Co(citrH)(H_2O)_3]^-$	4.63			
$[1,2,0]^{4-}$	$[Co(citrH)_2]^{4-}$	7.01	Co-B-3	509 (480, 460)	13.4
$[1,1,-1]^{2-}$	$[Co(citr)(H_2O)_3]^{2-}$	-3.23	Co-B-4	534 (490)	14.1
				727	2.2

absorption bands and the similarity in UV-Vis-NIR spectra of different Co(II)-complexes, MCR-analysis applied on the series of UV-Vis-NIR spectra did not yield useful information. Instead, reference spectra were recorded of solutions, for which the calculations predict the presence of a single type of Co(II)-complex. Subsequently, a linear combination of these reference spectra was used to fit the UV-Vis-NIR spectra recorded on 0.01 M Co(II) solutions with different citrate concentrations (series 4-6).

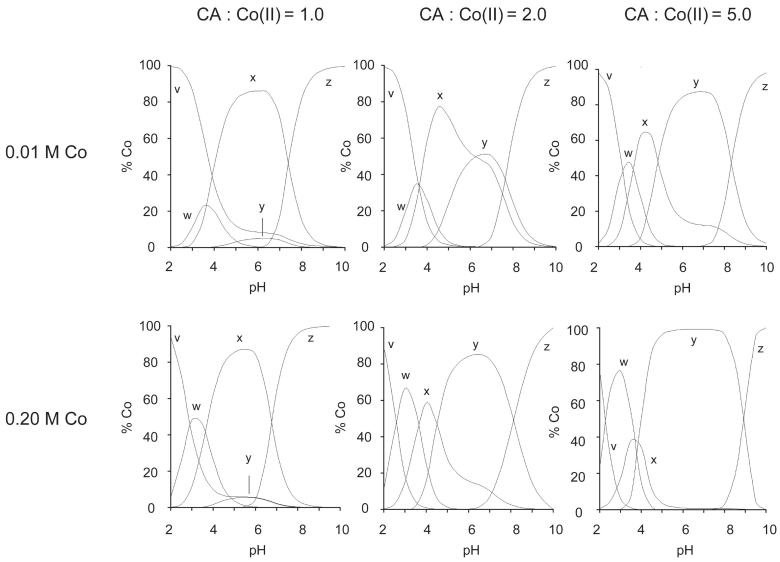

Figure 13. Speciation plots showing the theoretical concentration of $[Co(H_2O)_6]^{2+}$ (v), $[Co(citrH_2)(H_2O)_3]$ (w), $[Co(citrH)(H_2O)_3]^-$ (x), $[Co(citrH)_2]^{4-}$ (y) and $[Co(citr)(H_2O)_3]^{2-}$ (z) complexes in 0.01 M (top) and 0.20 M (bottom) Co(II)-solutions with different citrate-concentrations (series 4-9), as derived from calculations using formation constants.

The spectrum of a 0.20 M $Co(NO_3)_2$ solution was used as the reference spectrum of the $[Co(H_2O)_6]^{2+}$ complex (Co-B-1). The $[Co(citrH_2)(H_2O)_3]$ and $[Co(citrH)(H_2O)_3]^-$ complexes probably give rise to the same UV-Vis-NIR spectrum (Co-B-2), as these complexes only differ in the protonation of the uncoordinated carboxylate group and the coordination of Co(II) is identical in both complexes. The spectrum recorded on a 0.20 M Co, equimolar Co:citrate solution at pH 5 was used as the reference spectrum. The $[Co(citrH)_2]^{4-}$ complex (Co-B-3) is predicted to be the only complex present in a 0.20 M Co 1:5 Co(II)-citrate solution at pH 5 and the spectrum recorded on this solution is used to represent this complex. Finally, the spectrum of a 0.20 M Co equimolar Co:citrate solution at pH 9 was used as a reference spectrum of the $[Co(citr)(H_2O)_3]^{2-}$ complexes (Co-B-4). The different reference spectra are presented in Fig. 14 and their main characteristics are included in Table 5.

As in the MCR-analysis, an iteration procedure was used to minimize the values in the error matrix in Eq. 4. However, in this case, the values in the spectrum matrix S, containing the reference spectra Co-B-1 to Co-B-4 in the spectral range 430-900 nm, were fixed. The values for the scores of components Co-B-1 to Co-B-4 in matrix C were varied, in such a way that their sum (in other words the total concentration of Co(II)-atoms) remained constant throughout the iteration procedure. In this way, an average goodness of fit of 94 % of the UV-Vis-NIR spectra was obtained. The thus obtained concentrations of components Co-B-1 to Co-B-4 in the 0.01 M Co(II) solutions are shown in the speciation plots in Fig. 15. It can be seen that a

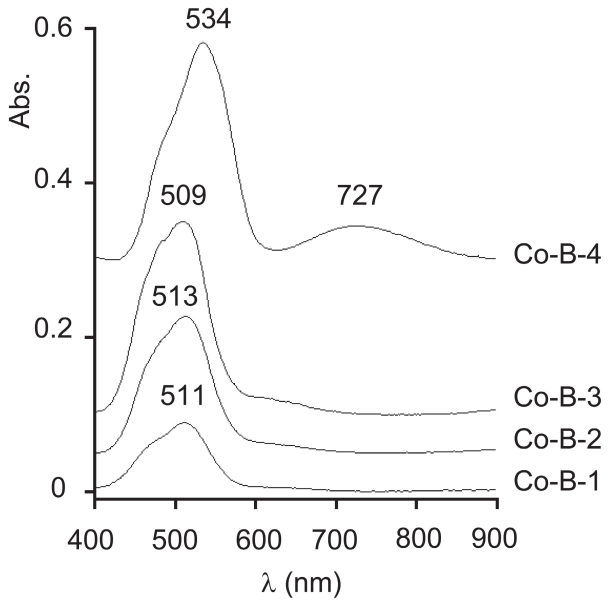

Figure 14. Reference spectra of components Co-B-1 to Co-B-4, used for the fitting of UV-Vis-NIR spectra recorded on the Co(II)-citrate solutions in series 4-9.

good correlation exists between the calculated concentrations of complexes Co-B-1 to Co-B-4 (dotted lines) and their concentration as determined from the analysis of the UV-Vis spectra. The presented spectra can therefore be considered to be reliable reference spectra of the different Co(II)-citrate complexes in aqueous solution. The fitting procedure seems to provide a reliable method to determine the speciation of Co(II)-complexes in Co(II)-citrate solutions.

The same method can now be used to obtain the speciation of complexes Co-B-1 to Co-B-4 from UV-Vis-NIR spectra recorded on 0.20 M Co solutions (series 7-9). In this way, the applicability of UV-Vis-NIR spectroscopy for the determination of the speciation of Co(II)-citrate complexes in more concentrated solutions, such as industrial impregnation solutions, can be put to the test. The speciation plot of components Co-B-1 to Co-B-4 in 0.20 M Co, 0.40 M citrate solutions obtained from fitting of the UV-Vis-NIR spectra is presented in Fig. 16. When the concentration profile of component Co-B-4 is compared to what was expected from calculations using the formation constants (Fig. 13) and what was observed in diluted solutions (Fig. 15), it can be concluded that Co-B-4 is formed at considerably lower pH in the more concentrated solutions. This experiment illustrates that care should be taken if one wants to predict the speciation of metal-ion complexes in concentrated solutions on the basis of formation constants derived from diluted solutions.

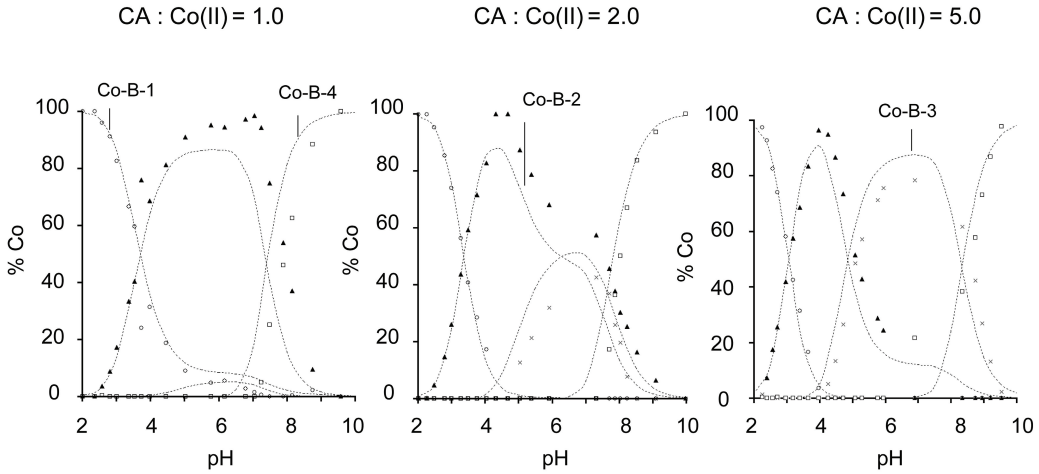

Figure 15. Speciation plot showing the concentration of components Co-B-1 to Co-B-4 in the 0.01 M Co solutions with different citrate concentrations in series 4-6, as derived from the analysis of UV-Vis-NIR spectra. The theoretical concentrations of components Co-B-1 to Co-B-4, obtained from calculations using formation constants is indicated by the dotted lines.

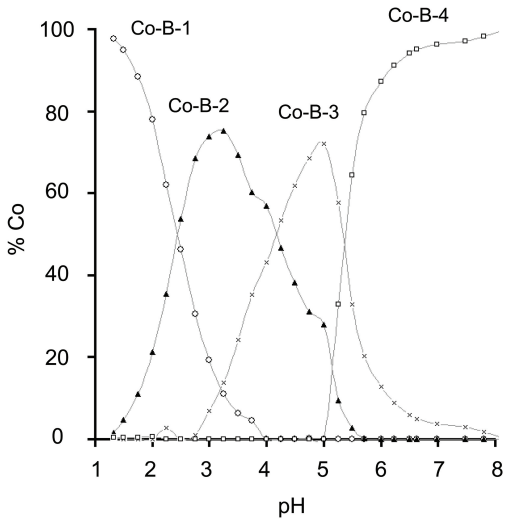

Figure 16. Speciation plot of components Co-B-1 to Co-B-4 in the 0.20 M Co(II), 0.40 M citrate solutions in series 8, as derived from the analysis of UV-Vis-NIR spectra.

To investigate the validity of the proposed structures of the Co(II)-citrate complexes presented in Fig. 12, Raman and IR spectroscopy was carried out on Co(II)-citrate solutions. In Fig. 17, spectra of 0.40 M citrate solutions of pH 5 with different Co(II) concentrations are presented. The features in these spectra are completely different than those observed in spectra obtained on the Na_3citrate solutions in the absence of Co(II) (Fig. 9). The coordination of Co(II) has clearly induced a considerable change in the configuration of the citrate molecule. The Raman and IR spectra recorded on solutions with Co:citrate ratios 1:1 (where Co-B-2 is mainly present) and 1:2 (where Co-B-3 is the dominant complex) are practically identical. Apparently, the configuration of the citrate ligand in complexes Co-B-2 and Co-B-3 is very similar. Close examination of the structures of $[Co(citrH)(H_2O)_3]^-$ (Co-B-2) and $[Co(citrH)_2]^{4-}$ (Co-B-3), shown in Fig. 12, learns that a similar coordination of citrate indeed exists in both complexes. In the spectrum of the 0.20 M Co(II)/0.40 M citrate solution no sign of peaks that can be attributed to the free CTA could be observed, confirming the stoichiometry of the $[Co(citrH)_2]^{4-}$ complex.

To evaluate the role of the hydroxyl group of citrate in the complexation of Co(II), solutions were prepared containing the sodium salt of tricarballylic acid in the presence and absence of Co(II). The Raman spectra of these solutions are presented in Fig. 18. The structures of CA and tricarballylic acid only differ in the absence of the hydroxyl group in the latter and it can be seen that, regardless of the presence of Co(II), identical spectra are obtained. It follows that, in this case, complexation only takes place through, at most, one carboxylate group and the configuration of the citrate ligand is not influenced by the complexation to Co(II). In the case of citrate, coordination of the hydroxyl group provides the opportunity for citrate to bind in a tridentate fashion. The configuration of the citrate molecule is changed, leading to a completely

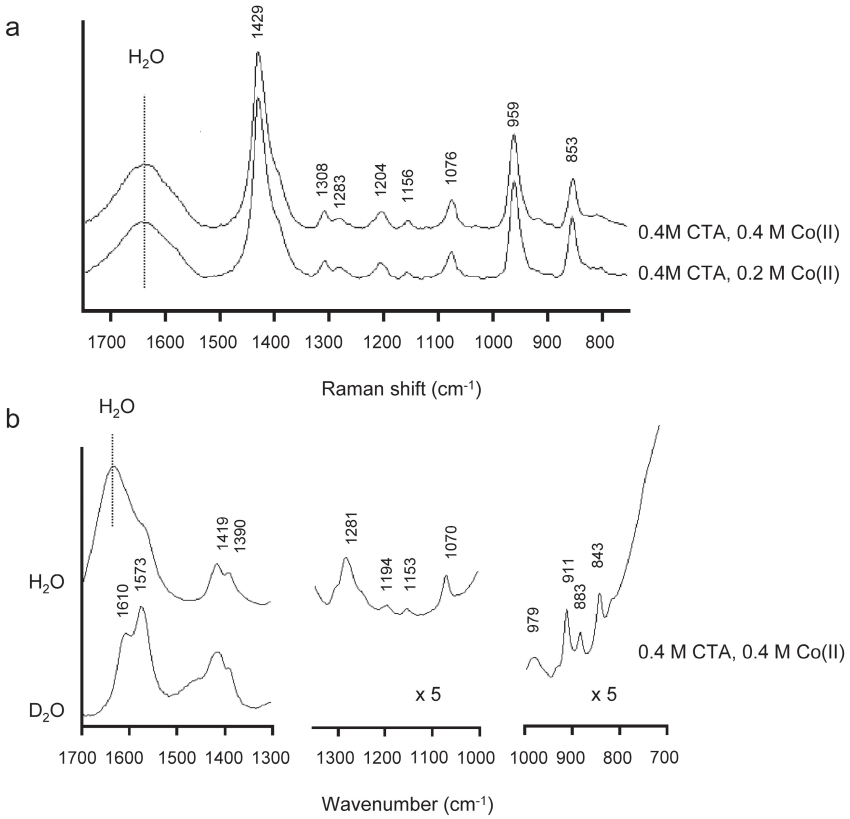

Figure 17. Raman (a) and IR (b) spectra recorded on 0.40 M citrate solutions with different Co-concentrations at pH 5. The exact composition of the solutions is indicated next to the spectra.

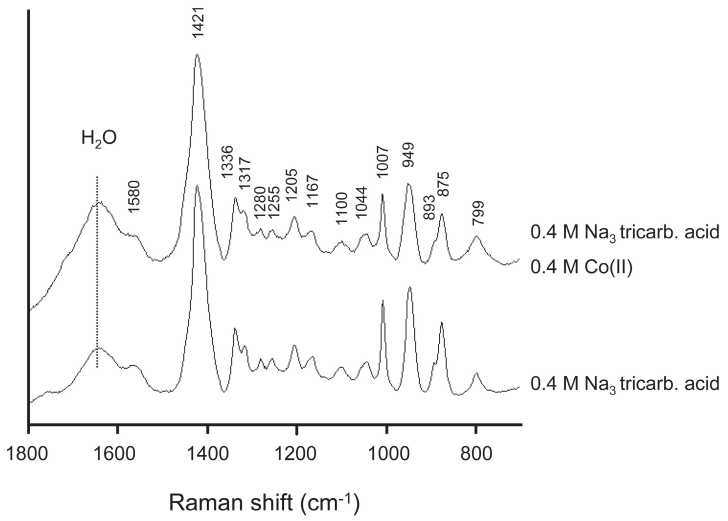

Figure 18. Raman spectra recorded on 0.40 M tri-sodium salt of tricarballylic acid in the presence (top) and absence (bottom) of 0.40 M Co(II).

different spectrum The Raman spectra recorded on the Co(II)-citrate solutions of pH 5 are very similar to the spectrum recorded on a $NiCl_3$/Na_3citrate solution, reported in literature. Citrate is also reported to bind to Ni(II) through two carboxylates and its hydroxyl group [50].

The position of the ν_{as} COO^- band in the IR spectra provides the most direct information on the binding between the carboxylates and Co(II), since coupling of the ν_{as} COO^- vibrations does not occur and bands are the result of vibrations of individual COO^- groups. In the IR spectrum of the 0.40 M citrate/0.40 M Co(II) solutions, two ν_{as} COO^- bands are observed. The band at 1573 cm^{-1} can be ascribed to the vibration of a free C_1 or C_5 carboxylate group, while the band at 1602 cm^{-1} is assigned to the remaining carboxylates bound to Co(II).

The Raman and IR spectra of 0.40 M citrate solutions of pH 9 with different Co-concentrations are presented in Fig. 19. The Raman spectrum of a 0.40 M Na_3citrate solution is included for

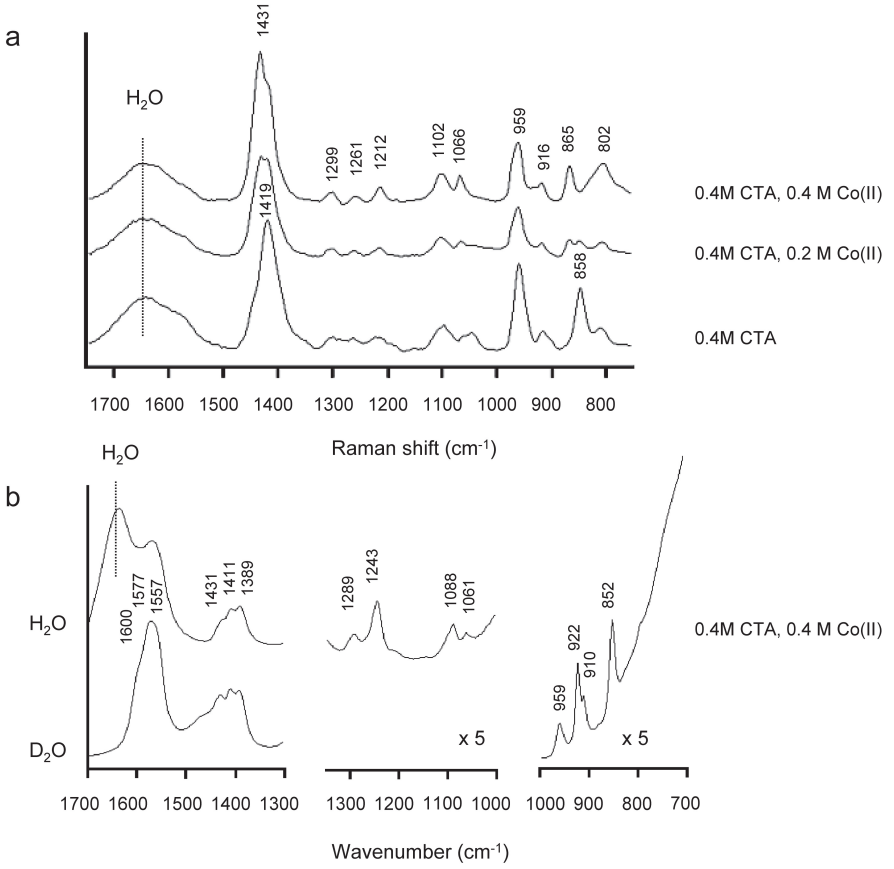

Figure 19. Raman (a) and IR (b) spectra recorded on 0.40 M citrate solutions with different Co(II)-concentrations at pH 9. The exact composition of the solutions is indicated next to the spectra.

comparison. The spectra recorded on the equimolar Co:citrate solutions are representative of component Co-B-4, since this was found to be a 1:1 Co:citrate complex. Indeed, in the spectrum recorded on the 0.20 M Co(II), 0.40 M citrate solution bands corresponding to the presence of free citrate are observed, most noticeably at around 845 cm^{-1} and 1420 cm^{-1}. The positions and number of the bands in the IR and Raman spectra are entirely different from what was observed at pH 5. Nevertheless, the proposed structures of components Co-B-2 ($[Co(citrH)(H_2O)_3]^-$) and Co-B-4 ($[Co(citr)(H_2O)_3]^-$) only differ in the protonation state of the hydroxyl group. Apparently, deprotonation of the hydroxyl group induces considerable changes in the configuration of the citrate ligand.

Three symmetrical (1389 cm^{-1}, 1411 cm^{-1} and 1431 cm^{-1}) and three anti-symmetrical (1557 cm^{-1}, 1577 cm^{-1} and 1600 cm^{-1}) ν COO^- vibration bands can be distinguished in the IR-spectra. The presence of three different ν_{as} COO^- bands indicates that all carboxylate groups differ. The $\nu_{as}COO^-$ band at 1577 cm^{-1} can be ascribed to a C_1 or C_5 carboxylate group that is not involved in complexation of Co(II), since its position is similar to that of a 'free' C_1 or C_5 carboxylate in CTA (1571 cm^{-1}). Next, the other ν_{as} COO^- bands can be ascribed to the remaining C_1 or C_5 carboxylate (1557 cm^{-1}) and the C_6 one (1600 cm^{-1}) bound to Co(II).

Besides $[Co(citr)(H_2O)_3]^{2-}$ complexes, the formation of binuclear $[Co_2(citr)_2(H_2O)_4]^{6-}$ complexes at high pH has also been considered in literature [10]. The structure of this complex, as shown in Fig. 12, consists of two $[Co(citr)(H_2O)_3]^{2-}$ complexes held together by the coordination of the free carboxylate group of one complex to the Co(II)-atom of the other complex. The formation of component Co-B-4 at lower pH in the 0.20 M Co(II) solutions could indeed point to the formation of these dimers, which would be more readily formed in more concentrated solutions. Furthermore, the large differences in the Raman an IR spectra obtained from 0.40 M citrate/0.40 M Co solutions at pH 5 and 9 could then be attributed to the different configuration of the citrate ligand in the $[Co(citrH)(H_2O)_3]^-$ and $[Co_2(citr)_2(H_2O)_4]^{6-}$ complexes. Further studies are required to determine the exact nature of the Co(II)-citrate complexes present at high pH in Co(II)-citrate solutions. EPR and ^{13}C-NMR, could be interesting techniques to distinguish between $[Co(citr)(H_2O)_3]^{2-}$ and $[Co_2(citr)_2(H_2O)_4]^{6-}$ complexes.

Mo-citrate solutions

The complex formation between citrate and Mo(VI) has been studied by several authors [7,9,15,17-20]. Crystal structures of different Mo(VI)-citrate complexes were obtained. By means of potentiometry, UV-Vis-NIR spectroscopy, differential pulse polarography and calorimetry, Cruywagen et al. proposed a model for the formation of Mo(VI)-citrate complexes in dilute

solutions (0.01-0.10 M Mo) and derived a complete set of formation constants [9]. In this model, it is assumed that in acidic environment, no less than 16 different Mo(VI)-citrate complexes can be formed with varying number of Mo-atoms (1, 2 and 4), Mo:citrate ratio (0.5, 1 and 2) and protonation state. The stoichiometry and molecular formulas of these complexes are listed in Table 6. The formation of Mo(VI)-citrate complexes may be represented by a general equation (Eq. 7). The definition of the formation constants is given in Eq. 8. Using the formation constants of the different Mo(VI)-citrate complexes, which are also included in Table 6, their speciation can be derived as a function of Mo-concentration, citrate-concentration and pH. In Fig. 20, such concentration profiles are presented for Mo-citrate solutions with 1.0 M Mo/1.0 M citrate (a) 1.0 M Mo/0.5 M citrate (b) and 0.02M Mo/0.02M citrate (c) concentrations.

Table 6. Stoichiometry [m,r,p], molecular formula, formation constants (β_{mrp}) [9] and positions of characteristic Raman bands of Mo(VI)-citrate complexes in aqueous solution. The stoichiometry of the complexes is defined as the number of MoO_4^{2-} (m), $citrH^{3-}$ (r) and H^+ (p) required for their formation (Eq. 7 and 8).

Complex [m,r,p]	Formula	Label Fig. 20	Log(β_{mrp}) (25°C)	Component	Raman bands (cm^{-1})
$[0,1,0]^{2-}$	MoO_4^{2-}	-	-	Mo-B-1	896,842 318
$[1,1,1]^{4-}$	MoO_3citr^{4-}	a	8.35	Mo-B-2	890,862 352
$[1,1,2]^{3-}$	$MoO_2(OH)citr^{3-}$	b	15.00		
$[1,1,3]^{2-}$		c	19.62		
$[1,1,4]^{-}$		d	21.12		934,902,864
$[2,2,4]^{6-}$	$Mo_2O_5citr_2^{6-}$	e	31.02	Mo-B-3	
$[2,2,5]^{5-}$		f	35.86		386,328
$[2,2,6]^{4-}$		g	40.08		
$[4,4,11]^{9-}$		h	77.45		
$[2,1,3]^{4-}$		i	21.73		
$[2,1,4]^{3-}$		j	26.90		944,904,862
$[2,1,5]^{2-}$	$Mo_2O_5(OH)(H_2O)(citrH)^{2-}$	k	31.53	Mo-B-4	
$[4,2,9]^{5-}$		l	60.76		382
$[4,2,10]^{4-}$	$Mo_4O_{11}(citrH)_2^{4-}$	m	64.69		
$[1,2,4]^{4-}$		-	25.34	-	
$[1,2,5]^{4-}$		-	29.54	-	
$[1,2,6]^{4-}$		n	33.34	-	

$$m\ MoO_4^{2-} + r\ citrH^{3-} + p\ H^+ \leftrightarrow (MoO_4^{2-})_m(citrH^{3-})_r(H^+)_p \quad \text{(Eq. 7)}$$

$$\beta_{mrp} = \frac{\left[\left(MoO_4^{2-}\right)_m\left(citrH^{3-}\right)_r\left(H^+\right)_p\right]}{\left[MoO_4^{2-}\right]^m \cdot \left[citrH^{3-}\right]^r \cdot \left[H^+\right]^p} \quad \text{(Eq. 8)}$$

From these plots, it can be observed that the formation of Mo(VI)-citrate complexes from MoO_4^{2-} and free citrate starts at pH 9. In solutions with equimolar concentrations of Mo and citrate, complexes with a Mo:citrate ratio of 2 (labeled i-m) are dominant at low pH, while 1:1 Mo-citrate complexes (labeled b-h) are mainly present at intermediate pH. In the 1.0 M Mo, 0.50 M citrate solutions, 2:1 Mo-citrate complexes are stable in a wide pH range, as illustrated in Fig. 20b. When plots 20a and 20c are compared, it is clear that higher concentrations of Mo and citrate lead to the formation of larger complexes. According to the calculations, the formation of 1:2 Mo-citrate complexes is not expected to take place to any significant extent in these solutions and their formation will not be further considered in this work.

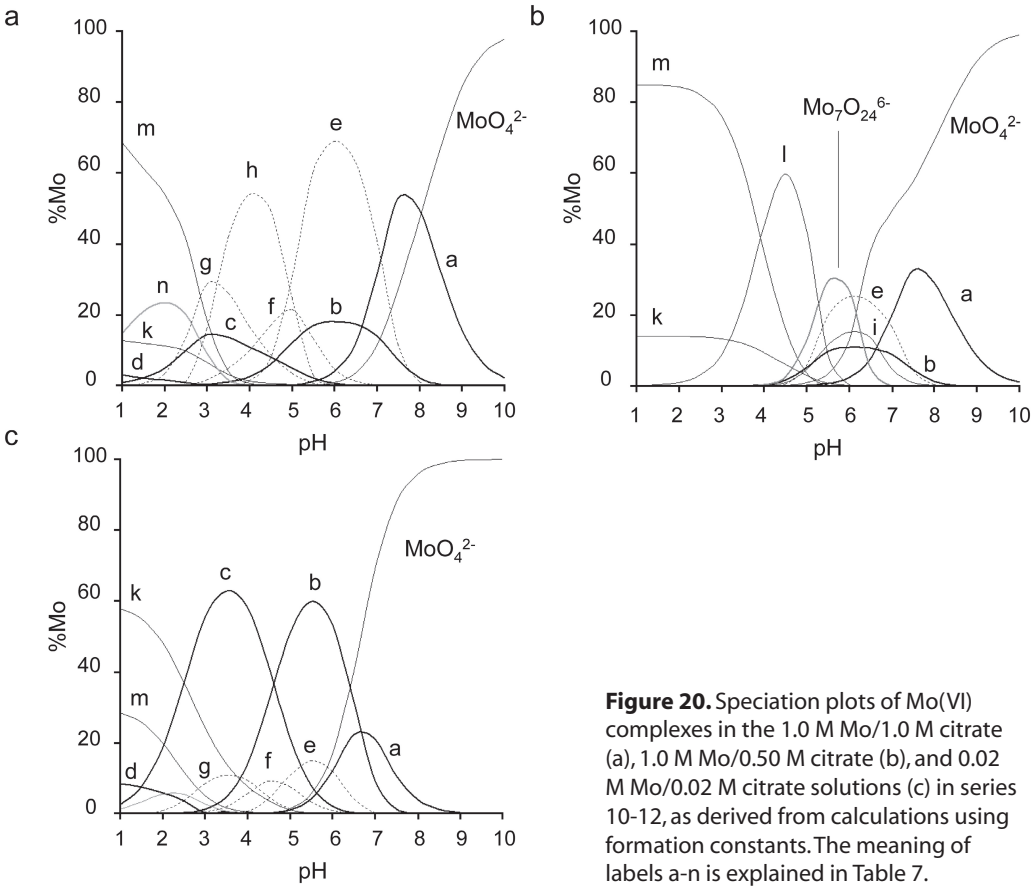

Figure 20. Speciation plots of Mo(VI) complexes in the 1.0 M Mo/1.0 M citrate (a), 1.0 M Mo/0.50 M citrate (b), and 0.02 M Mo/0.02 M citrate solutions (c) in series 10-12, as derived from calculations using formation constants. The meaning of labels a-n is explained in Table 7.

In the Raman spectra recorded on Mo(VI)-citrate solutions, bands due to Mo=O vibrations are by far the most intense. In this section, an attempt is made to discriminate between different Mo(VI)-citrate complexes in solution on the basis of the position and intensity of the main Mo=O vibration bands in Raman spectra. Furthermore, the use of the formation constants listed in Table 6 for the prediction of the composition of concentrated Mo-citrate solutions is evaluated. To this end, Raman spectra were recorded on the solutions, for which the composition is given in Table 3 (series 10-12) and the theoretical speciation is presented in Fig. 20. As an example, the spectra recorded on the equimolar 1.0 M Mo-citrate solutions (series 10) are presented in Fig. 21. The spectrum recorded on the solution of pH 1, shows bands due to Mo=O stretching vibrations at 944, 904, and 862 cm^{-1} and bands due to O=Mo=O bending vibrations at 384 and 346 cm^{-1}. Addition of NaOH leads to a shift in the most intense Mo=O stretching band to 934 cm^{-1}, which is complete at pH ~ 4. An increase in pH above 6 leads to a decrease in intensity of the 934 cm^{-1} band and the simultaneous appearance of two new bands at 894 and 348 cm^{-1}. At a pH of 9 bands are only present at 896, 842 and 318 cm^{-1}, showing that disintegration of the Mo(VI)-citrate complexes is complete and MoO_4^{2-} is the only Mo-complex in solution.

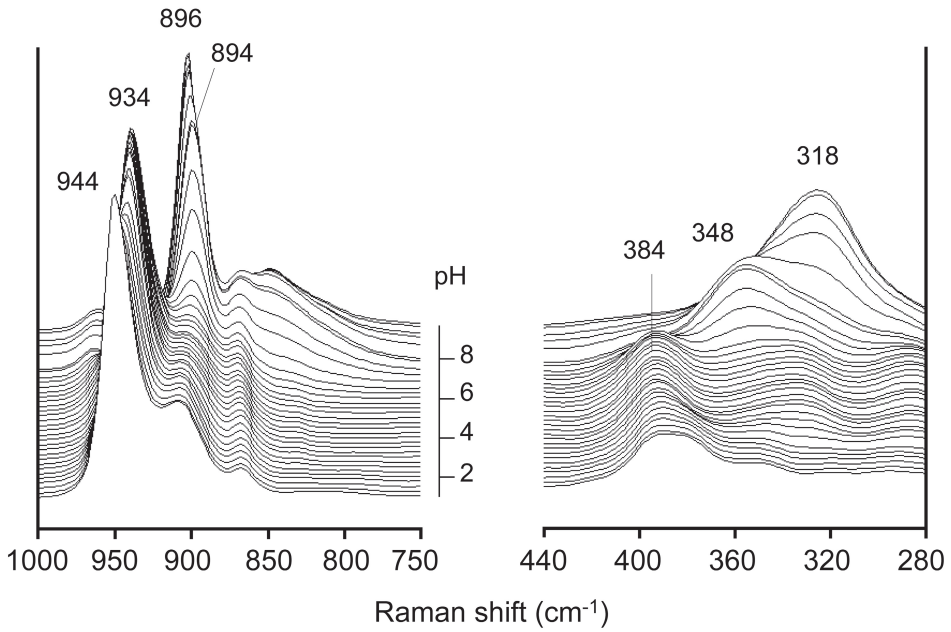

Figure 21. Selected Raman spectra recorded on the 1.0 M Mo/1.0 M citrate solutions in series 10 in the pH range 1-9.

With the aid of MCR, the spectra recorded on the Mo-citrate solutions were deconvoluted into pure component spectra and the concentrations of these components in the solutions. Spectra were used in the spectral range 1000-750 and 450-280 cm^{-1}. For 1.0 M Mo/1.0 M citrate solutions, this procedure resulted in a goodness of fit of 98.6%, when the presence of 4 pure components (Mo-B-1 to Mo-B-4) was assumed. Addition of more components didn't improve the fit. The resulting concentrations of components Mo-B-1 to Mo-B-4 in these solutions are presented in Fig. 22a. The MCR-derived spectra of components Mo-B-1 to Mo-B-4 are shown in Fig. 23. These spectra were used as input for the MCR-analysis of the Raman spectra recorded on the 1.0 M/0.5 M citrate solutions (series 11). However, as can be seen in Fig. 20b, the formation of $Mo_7O_{24}^{6-}$ is also predicted in this case. Therefore, the spectrum of a 1.0 M AHM-solution of pH 5 (known to contain almost exclusively $Mo_7O_{24}^{6-}$ complexes) was used as input for the fifth pure component (Mo-B-5). In this way, a goodness of fit of 97.9% was obtained. The resulting speciation plot of components Mo-B-1 to Mo-B-5 is presented in Fig. 22b.

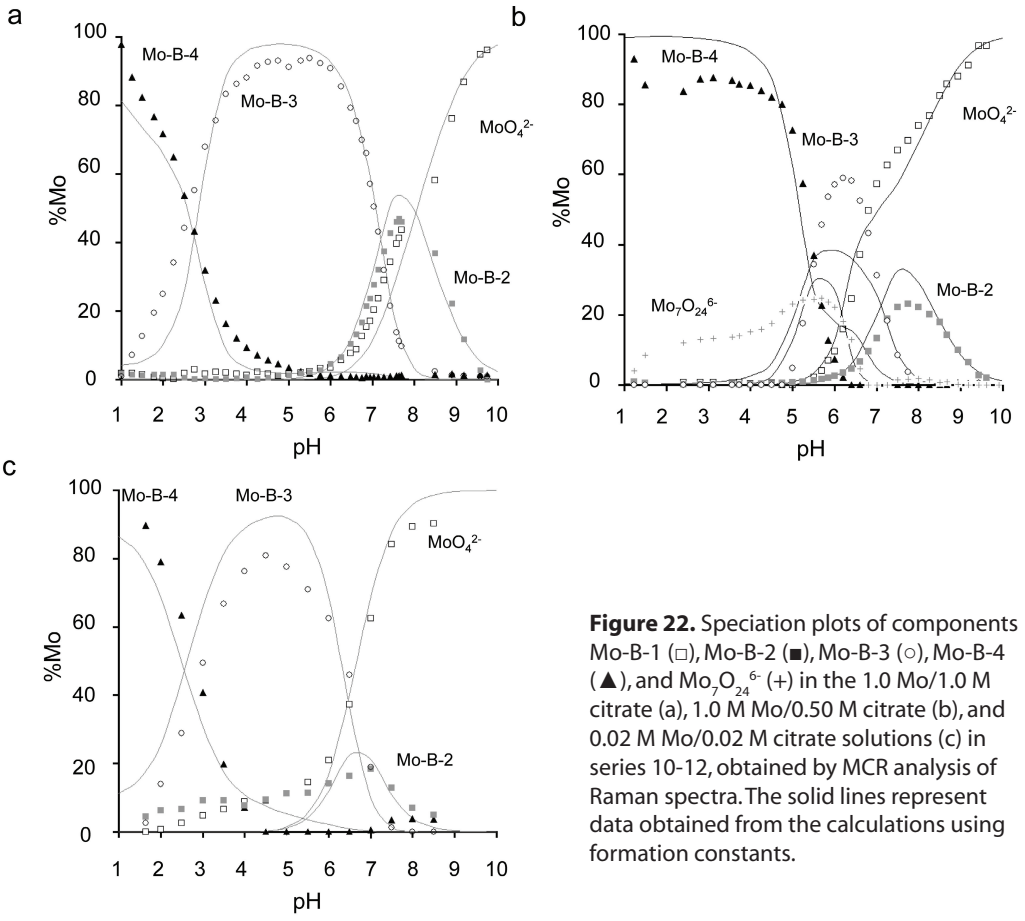

Figure 22. Speciation plots of components Mo-B-1 (□), Mo-B-2 (■), Mo-B-3 (○), Mo-B-4 (▲), and $Mo_7O_{24}^{6-}$ (+) in the 1.0 Mo/1.0 M citrate (a), 1.0 M Mo/0.50 M citrate (b), and 0.02 M Mo/0.02 M citrate solutions (c) in series 10-12, obtained by MCR analysis of Raman spectra. The solid lines represent data obtained from the calculations using formation constants.

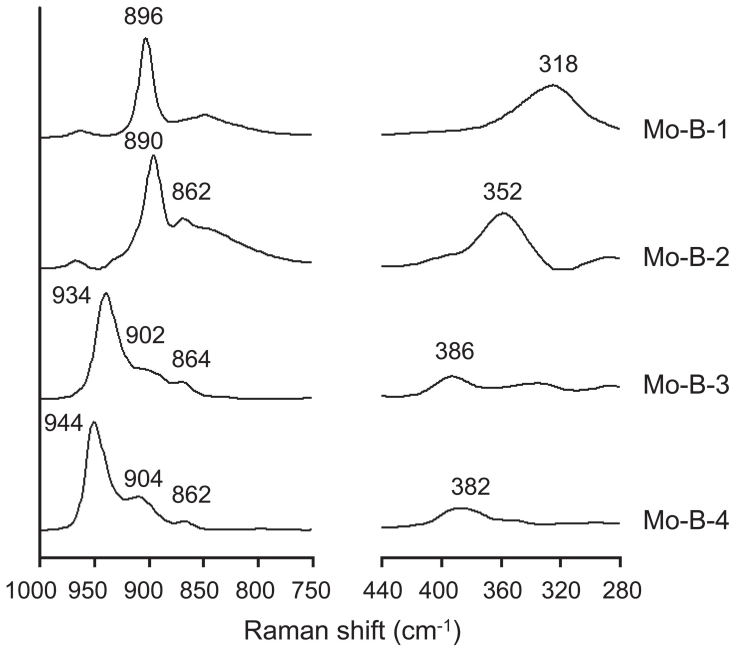

Figure 23. Pure spectra of components Mo-B-1 to Mo-B-4 obtained from MCR-analysis of Raman spectra recorded on Mo(VI)-citrate solutions in series 10-12.

Raman spectra recorded on the 0.02 M Mo/0.02 M citrate solutions (series 12) are shown in Fig. 24. Unfortunately, the signal to noise ratio of the spectra in the 450-280 cm^{-1} spectral range was not good enough to allow for an evaluation of the bands due to O=Mo=O bending vibrations and only the region between 978 and 780 cm^{-1} was used for the MCR-analysis. Using the spectra of components Mo-B-1 to Mo-B-4 as input for the iteration procedure, 95.3 % of the spectra could be fitted. The obtained concentration profiles for components Mo-B-1 to Mo-B-4 is presented in Fig. 22c. According to the concentration plots in Fig. 20, no less than 13 different Mo(VI)-citrate complexes could have been observed in these experiments. Apparently, the Raman spectra of a number of different Mo(VI)-citrate complexes differ only in detail. The large polarizability change induced by terminal Mo=O stretching vibrations makes that these vibrations give rise to the most intense bands in Raman spectra recorded on Mo(VI)-compounds. The main differences in the Raman spectra of Mo(VI)-citrate complexes are likely to be the result of differences in the strength of these bonds. Therefore, the structures of the Mo(VI)-citrate complexes must be examined to link the concentration of components Mo-B-1 to Mo-B-4 to the concentrations of actual complexes. The crystal structures of different Mo(VI)-citrate complexes reported in literature [7,17-20] were examined to get an idea of the molecular structure of these complexes in solution. Proposed structures of different Mo(VI)-citrate complexes in aqueous solution are presented in Fig. 25.

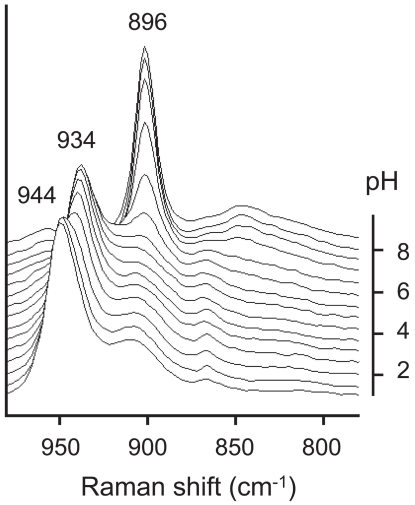

Figure 24. Selected Raman spectra recorded on the 0.02 M Mo/0.02 M citrate solutions in series 12 in the pH-range 1-9.

The Raman spectrum of component Mo-B-1 is assigned to MoO_4^{2-} (Table 2). Its presence at high pH in all solution series is in accordance with this assignment. Component Mo-B-5 corresponds to $Mo_7O_{24}^{6-}$, as discussed above. Component Mo-B-2 is only present in considerable amounts at pH 6-8 and is most apparent in 1M Mo/1M citrate solutions. The observed formation of this component corresponds to the concentration profile of $MoO_3(cit)^{4-}$ as derived from calculations (Fig. 20a). The molecular structure of this complex, as derived from X-ray crystallography, is also depicted in Fig.25 [19]. In the crystal structure of its potassium salt, the average distance of the three terminal Mo=O bonds is reported to be 1.74 Å.

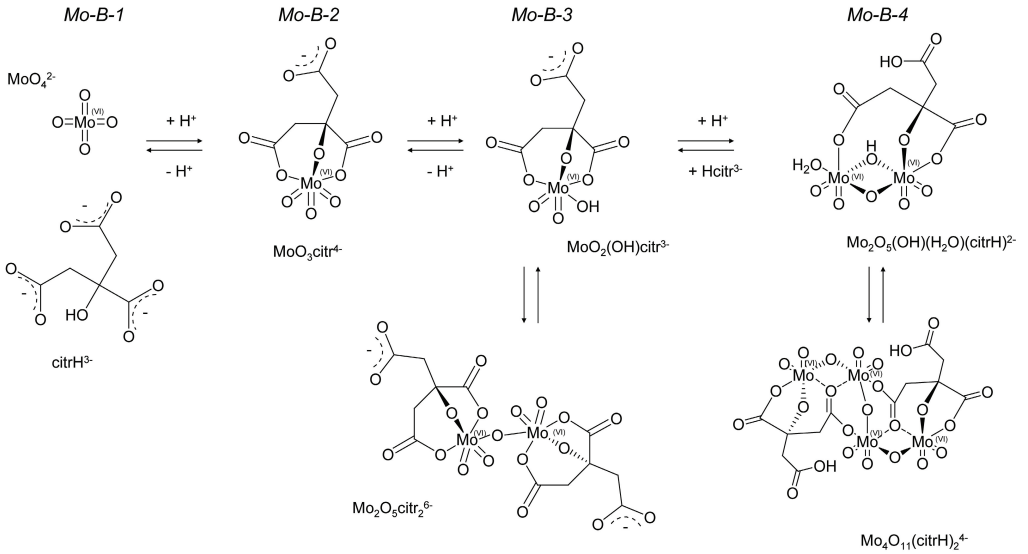

Figure 25. Proposed molecular structure of Mo(VI)-citrate complexes formed in aqueous solution. The assignment of components Mo-B-1 to Mo-B-4 to the presence of actual complexes is indicated as well.

In 1.0 M Mo/0.5 M citrate solutions, component Mo-B-3 is only present at pH 5-7.5 (Fig. 22b). On the other hand, the same component is found to be almost exclusively present in the equimolar Mo-citrate solutions in the pH region 3.5-6, regardless of the total Mo-concentration (Fig. 22a and 22c). Hence, it must be concluded that this component represents 1:1 Mo(VI)-citrate complexes with one, two or four Mo-atoms. The structures of a 1:1 Mo(VI)-citrate complex and a 2:2 Mo(VI)-citrate complex are also presented in Fig. 25. The coordination environment around Mo is very similar for both complexes. The 4:4 Mo(VI)-citrate complex is reported to be formed through dimerization of two protonated 2:2 Mo(VI)-citrate complexes, where bonding between the two units occurs through the carboxylate groups [19]. All in all, it seems likely that these different complexes (b-h in Table 6) exhibit the same Mo=O stretching bands in the Raman spectra. The crystal structure of $K_4[(MoO_2)O(Hcitr)_2]$ was determined and shows an average bond distance of the Mo=O of 1.71 Å [19], explaining the shift in the main Mo=O vibrations to a higher wavenumber as compared to the $MoO_3(cit)^{4-}$ complex (component Mo-B-2).

Component Mo-B-4 represents the dominant complexes in 1.0 M Mo/0.5 M solutions at a pH lower than 4. In Fig. 20b, it can be observed that $Mo_4O_{11}(citrH)_2^{4-}$ is predominantly formed under these conditions. The spectrum recorded on the 0.02 M Mo/0.02 M citrate solution at low pH also corresponds to the spectrum of component Mo-B-4. In these solutions, $Mo_2O_5(OH)(H_2O)(Hcitr)^{2-}$ is supposed to be present (Fig. 20c) Apparently the two complexes, as depicted in Fig. 25 give rise to virtually the same Raman spectrum. The similar coordination of citrate in both complexes seems to support this observation. Component Mo-B-4 corresponds to the presence of complexes i-m in Table 6. The average Mo=O bond distance in the crystal structure of $K_4[(Mo_4O_{11}(citrH)_2]$ was reported to be 1.70 Å [7]. The lower frequency of the Mo=O vibrations as compared to the spectrum of component Mo-B-2 and Mo-B-3 can thus be explained.

Three different families of Mo(VI)-citrate complexes can be distinguished by Raman spectroscopy. The theoretical speciation of components Mo-B-1 to Mo-B-4 in the solutions in series 10-12 can now be obtained from Fig. 20a-c, as summation of complexes b-h and i-m yields the concentration of components Mo-B-3 and Mo-B-4, respectively. A good correlation between the speciation of components Mo-B-1 to Mo-B-4 obtained from theoretical calculations (solid lines in Fig. 22) and MCR-analysis of Raman spectra can be observed.

Conclusions

With the help of DFT calculations and isotope labeling, and by using D_2O as a solvent, most of the bands in the Raman and IR spectra of the citrate ion in aqueous solution have been assigned. Especially, the bands related to the carboxylate vibrations turned out to be helpful in the structure elucidation of the Co(II)-citrate complexes. UV-Vis-NIR reference spectra for three types of Co(II)-citrate complexes were derived and subsequently used to determine the speciation of these complexes in aqueous solution. Care should be taken if one aims at deriving the speciation of Co(II)-citrate complexes in concentrated solutions from formation constants obtained from diluted solutions. Using Raman-spectroscopy, three families of Mo(VI)-citrate complexes could be distinguished in aqueous solution. MCR-analysis was used to obtain the speciation of these complexes in diluted and concentrated solutions of different Mo:citrate ratios. Reference spectra for these three types of Mo(VI)-citrate complexes were derived. The formation constants published by Cruywagen et al. [9] provided a solid basis for the estimation of the concentrations of Mo(VI)-citrate complexes in concentrated solutions.

Chapter 2C

Spectroscopic Investigation of the Molecular Structure of Phosphomolybdate Complexes in MoP and CoMoP solutions

Abstract

The formation of $P_2Mo_5O_{23}^{6-}$, $HP_2Mo_5O_{23}^{5-}$ and $H_2P_2Mo_5O_{23}^{6-}$ complexes in acidic MoP-solutions was monitored using Raman spectroscopy. Reference spectra for these complexes were obtained. In the presence of Co(II), the formation of $H_2PMo_{11}CoO_{40}^{5-}$ was observed through Raman and UV-Vis-NIR spectroscopy and reference spectra were derived for this heteropolyanion.

Introduction

To increase the stability of acidic Mo(VI)-impregnation solutions, phosphate is sometimes added for its ability to form phosphomolybdate complexes. Besides, under certain conditions, phosphate is reported to act as a second promoter in hydrotreating reactions [27,31]. The speciation of these phosphomolybdate complexes in MoP-solutions is well documented [14,31,58]. Their formation in aqueous solution was studied as a function of the pH and the Mo:P ratio. Potentiometric measurements [14], ^{31}P NMR [14,58,59], ^{95}Mo NMR [59], and Raman spectroscopy [58] were used to determine the molecular structure of the different complexes in aqueous solution. Heteropolyanions can be formed varying in molecular weight, P:Mo ratio and protonation state. In this subchapter, the formation of phosphomolybdate complexes in solution in the absence and presence of Co(II) was studied using Raman and UV-Vis-NIR spectroscopy.

Experimental

The compositions of the solutions used for spectroscopic studies are listed in Table 7. $(NH_4)_6Mo_7O_{24}$ (Acros, p.a.), $Co(NO_3)_2{\cdot}6\ H_2O$ (Acros, p.a.) and a 85% aqueous H_3PO_4 solution (Baker, p.a.) were used for the preparation of these solutions. For Raman measurements on MoP-solutions (series 13) NH_4NO_3 (Acros, p.a.) was added to serve as an internal standard. Concentrated NaOH (Merck, p.a.) and HCl (Merck, p.a.) solutions were used for pH adjustment. Care was taken that the concentration of components under study was not altered in the course of a measurement series.

Raman spectra were recorded using a Kaiser RXN spectrometer equipped with a 70 mW, 532 nm diode laser for excitation. The data point resolution was 2 cm^{-1}. Spectra were subject to baseline correction before analysis. The NO_3^- peak at 1044 cm^{-1} was used as an internal standard and spectra were scaled to this band. UV-Vis-NIR measurements (250-1100 nm) were carried

Table 7. Composition of MoP and CoMoP solutions used for spectroscopic studies. The pH range and the number and type of spectra that were recorded in each titration series are included.

Series	[Mo] (M)	[Co] (M)	[PO_4^{3-}] (M)	[NO_3^-] (M)	pH	n° spectra	Analysis
13	1.0	-	1.0	1.0	1.40-8.45	25	Raman
14	1.0	0.5	0-0.5	1.0	(1.97-4.94)	58	Raman UV-Vis-NIR

out with 1 nm data point resolution using a Varian Cary 50 spectrophotometer equipped with a Hellma immersion probe. All measurements were carried out under ambient conditions (298 K).

Results and Discussion

MoP-solutions

$H_xP_2Mo_5O_{23}^{(6-x)-}$, $H_{(3+x)}PMo_9O_{34}^{(6-x)-}$, $H_xPMo_{11}O_{39}^{(7-x)}$, and $PMo_{12}O_{40}^{3-}$ are reported to be the predominant complexes in acidic MoP-solutions [14]. Their structures are schematically depicted in Fig. 26 and their formation from phosphate ($H_2PO_4^-$ in acidic conditions) and MoO_4^{2-} is expressed in Eq. 9-12. The formation constants of the different complexes (defined as β_{msp} in Eq. 13), as reported in literature, are listed in Table 8 [14]. $H_xP_2Mo_5O_{23}^{(6-x)-}$ complexes consist of a ring of linked MoO_6 octahedra, stabilized by two phosphate groups. $PMo_{12}O_{40}^{3-}$ is a classical Keggin ion with a central phosphate group surrounded by four units, each of them consisting of three MoO_6 octahedra. $H_xPMo_{11}O_{39}^{(7-x)-}$ is proposed to have the same structure with one of the Mo-atoms missing. Two different isomers for the $H_{(3+x)}PMo_9O_{34}^{(6-x)-}$ complex could be distinguished using NMR. One complex consists of a central phosphate group, symmetrically surrounded by three units of three MoO_6 octahedra (structure B). In the other isomer the structure is less symmetrical and the phosphate group is partially exposed (structure A). From Eq. 9-12, it can be seen that in general, a high P:Mo ratio and mildly acidic conditions favor the formation of $H_xP_2Mo_5O_{23}^{(6-x)-}$ complexes, while larger complexes, such as $H_{(3+x)}PMo_9O_{34}^{(6-x)-}$ and $H_xPMo_{11}O_{39}^{(7-x)-}$ are generally formed at lower P:Mo ratio and lower pH.

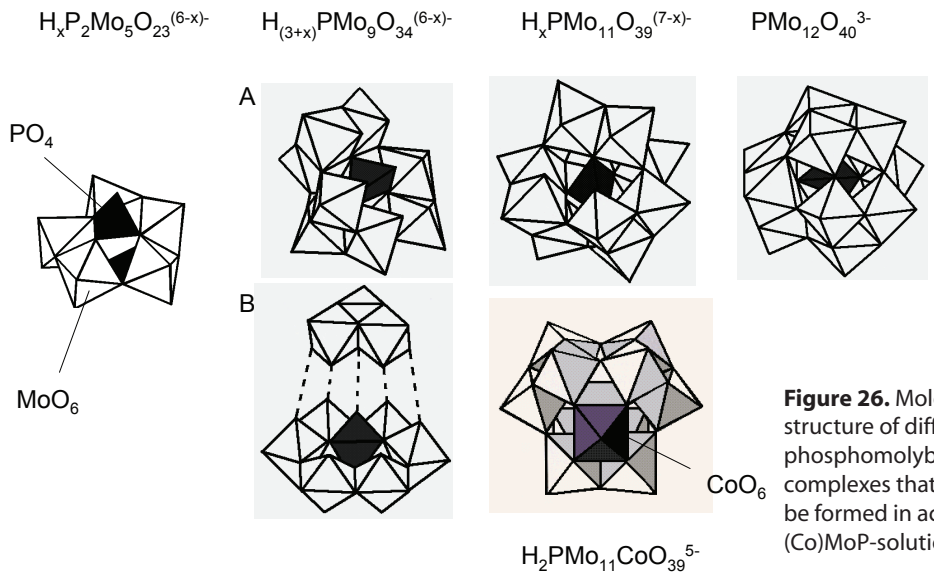

Figure 26. Molecular structure of different phosphomolybdate complexes that can be formed in acidic (Co)MoP-solutions.

$$5\ MoO_4^{2-} + 6\ H^+ + 2\ H_2PO_4^- \leftrightarrow P_2Mo_5O_{23}^{6-} + 5\ H_2O \quad \text{(Eq. 9)}$$

$$9\ MoO_4^{2-} + 13\ H^+ + H_2PO_4^- \leftrightarrow H_3PMo_9O_{34}^{6-} + 6\ H_2O \quad \text{(Eq. 10)}$$

$$11\ MoO_4^{2-} + 16\ H^+ + H_2PO_4^- \leftrightarrow PMo_{11}O_{39}^{7-} + 9\ H_2O \quad \text{(Eq. 11)}$$

$$12\ MoO_4^{2-} + 22\ H^+ + H_2PO_4^- \leftrightarrow PMo_{12}O_{40}^{3-} + 12\ H_2O \quad \text{(Eq. 12)}$$

$$\beta_{msp} = \frac{\left[\left(MoO_4^{2-}\right)_m \left(HPO_4^{2-}\right)_s \left(H^+\right)_p\right]}{\left[MoO_4^{2-}\right]^m \cdot \left[HPO_4^{2-}\right]^s \cdot \left[H^+\right]^p} \quad \text{(Eq. 13)}$$

Table 8. Stoichiometry [m,s,p], molecular formula, formation constants (β_{msp}) [14] and positions of characteristic Raman bands of phosphomolybdate complexes in aqueous solution. The stoichiometry of the complexes is defined as the number of MoO_4^{2-} (m), HPO_4^{2-} (s) and H^+ (p) required for their formation (Eq. 9-12).

Complex [m,s,p]	Formula	log(β_{msp}) (25°C)	Component	Raman bands (cm^{-1})
$[0,1,0]^{2-}$	MoO_4^{2-}	-	Mo-C-1	-
$[5,2,8]^{6-}$	$P_2Mo_5O_{23}^{6-}$	61.97	Mo-C-2	956, 926, 870 395, 370
$[5,2,9]^{5-}$	$HP_2Mo_5O_{23}^{5-}$	67.07	Mo-C-3	936, 882 395, 370
$[5,2,10]^{4-}$	$H_2P_2Mo_5O_{23}^{4-}$	70.86	Mo-C-4	944, 894 395, 370
$[9,1,14]^{6-}$	$H_3PMo_9O_{34}^{6-}$	98.21		
$[9,1,15]^{6-}$		102.04		967 [58]
$[9,1,16]^{6-}$	Structure A	104.71		
$[9,1,17]^{6-}$		106.42		
$[9,1,16]^{6-}$	$H_5PMo_9O_{34}^{4-}$	104.89		
$[9,1,17]^{6-}$	Structure B	107.17		
$[11,1,17]^{7-}$	$PMo_{11}O_{39}^{7-}$	118.68		
$[11,1,18]^{6-}$		123.10		970 [58]
$[11,1,19]^{5-}$		126.05		
$[12,1,23]^{3-}$	$PMo_{12}O_{40}^{3-}$	139.7		995 [58]
-	$H_2PMo_{11}CoO_{40}^{5-}$	-	Mo-C-5	1008, 971, 954 886, 818

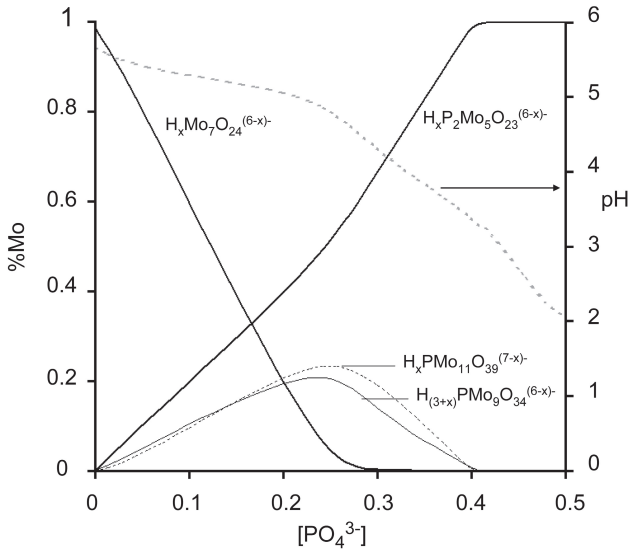

Figure 27. Theoretical speciation of Mo(VI)-complexes in a 1.0 M Mo AHM solution, as a function of the phosphate concentration, after addition of H_3PO_4. The theoretical pH of the resulting solutions is indicated by the grey dotted line.

As a starting point for our investigations, calculations were carried out using the formation constants of the different phosphomolybdate complexes taken from literature. Fig. 27 shows the predicted concentration profiles of different Mo(VI)-complexes present in solution after addition of phosphoric acid to a 1.0 M Mo AHM-solution. The pH of the resulting solution is indicated in the same figure by the dashed grey line. The AHM solution, with a pH of 5.7, contains predominantly $Mo_7O_{24}^{6-}$ complexes, as discussed in subchapter 2A. Addition of phosphoric acid to this solution leads to the formation of mostly $H_xP_2Mo_5O_{23}^{(6-x)-}$ complexes, as the pH of the solution is still rather high. As the pH decreases due to the addition of more phosphoric acid, $H_{(3+x)}PMo_9O_{34}^{(6-x)-}$ and $H_xPMo_{11}O_{39}^{(7-x)-}$ are being formed. However, as the P:Mo ratio further increases, the formation of $H_xP_2Mo_5O_{23}^{(6-x)-}$ is again favored and all Mo is contained in this type of complex. These calculations show that the formation of considerable amounts of larger phosphomolybdate complexes can only be brought about by the addition of extra acid to AHM/phosphoric acid solutions. However, a combination of low pH and low phosphate concentrations tends to lead to the precipitation of Mo(VI)-complexes and is therefore generally avoided in industrial impregnation solutions. Furthermore, precipitation makes it difficult to conduct spectroscopic studies on concentrated MoP-solutions in the absence of additional phosphate. For this reason, only the formation of $H_xP_2Mo_5O_{23}^{(6-x)-}$ complexes is further considered in this paragraph.

Raman spectra recorded on 1.0 M Mo, 1.0 M phosphate solutions with pH between 1.4 and 8.5 (series 13) are presented in Fig. 28. Using their formation constants, the theoretical speciation of the $H_xP_2Mo_5O_{23}^{(6-x)-}$ complexes of different protonation state in these solutions was calculated as a function of pH. The resulting concentration profiles are presented as the

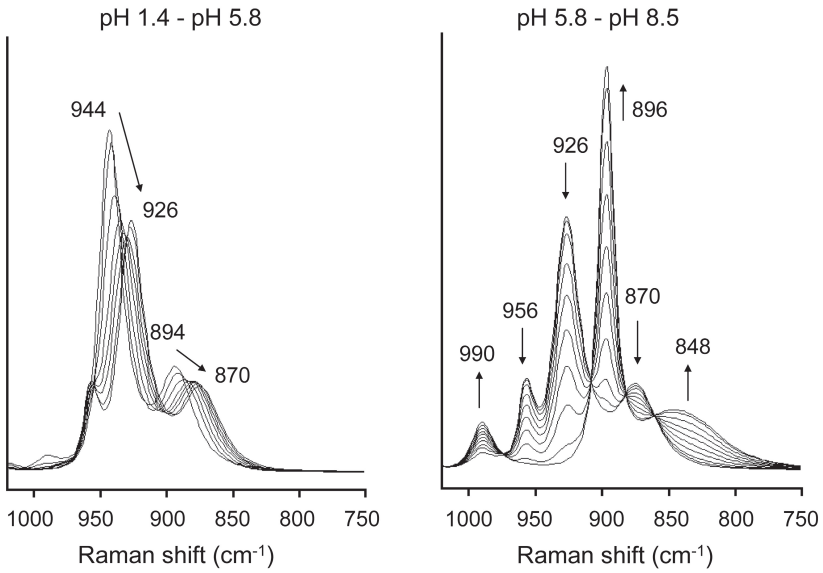

Figure 28. Selected Raman spectra recorded on the 1.0 M Mo/1.0 M PO_4^{3-} solutions in series 13 in the pH-range 1.4-8.5

grey lines in Fig. 29. At a pH of 1.4, all Mo is present in the fully protonated $H_2P_2Mo_5O_{23}^{4-}$ anion. In the corresponding Raman spectrum, the maxima of the bands due to Mo=O stretching vibrations are located at 944 and 894 cm^{-1}. An increase in pH leads to a gradual deprotonation of the complex and a decrease in the intensity and wavenumber of the Raman bands. At a pH of 5.85, a spectrum is observed with bands at 956, 926, and 870 cm^{-1}. At this pH, according to the calculations, most of the Mo is contained in the fully deprotonated $P_2Mo_5O_{23}^{6-}$ complex. In all spectra recorded on these acidic 1-1 MoP solutions O=Mo=O bending vibrations are observed at 370 and 395 cm^{-1}. Apparently, these bands are diagnostic of the presence of any $H_xP_2Mo_5O_{23}^{(6-x)-}$ complexes, regardless of their protonation state. Upon increasing the pH even more, decomposition of the phosphomolybdate complex takes place and MoO_4^{2-} is formed as the equilibrium in Eq. 9 shifts to the left. In the corresponding Raman spectra (Fig. 28), the direct disintegration of $P_2Mo_5O_{23}^{6-}$ into MoO_4^{2-} and HPO_4^{2-} is clearly indicated by the isobestic points at 910, 882, and 862 cm^{-1}. At a pH of 8.5, only MoO_4^{2-} complexes are present as the Raman spectrum only shows Mo=O bands at 896 and 848 cm^{-1} and a band originating from the presence of HPO_4^{2-} at 990 cm^{-1} [44].

To derive reference spectra of the different $H_xP_2Mo_5O_{23}^{(6-x)-}$ complexes, MCR was carried out on this series of spectra. Hereby, it was assumed that the solution of pH 1.4 merely contained $H_2P_2Mo_5O_{23}^{4-}$ complexes, while the solution of pH 8.45 only contained MoO_4^{2-}. The spectra of the solution at pH 1.4 and 8.45 were used as input for the pure component spectra of $H_2P_2Mo_5O_{23}^{4-}$

and MoO_4^{2-} respectively before the iteration process. The spectra were fitted in the 750-1150 cm^{-1} range using 4 pure component spectra. Again non-negativity constraints were imposed on these calculations in order to obtain meaningful spectra. A good fit of 99.8% of the total intensity in the Raman spectra was obtained. The derived concentrations of the different components as a function of pH are included in Fig. 29. When these values are compared to the concentration profiles derived from formation constants (grey lines), it can be seen that a qualitative correlation exists. As the spectra of these complexes were used as input in the MCR procedure, the formation of $H_2P_2Mo_5O_{23}^{4-}$ at low pH and MoO_4^{2-} at high pH can be observed rather well through the analysis of the Raman spectra. The concentration curves of $HP_2Mo_5O_{23}^{5-}$ and $P_2Mo_5O_{23}^{4-}$ obtained after MCR-analysis, match only roughly with the values predicted from formation constants. It appears difficult to separate contributions from both complexes. The large similarity in spectra may be one reason for this poor fit. Furthermore, an excess of phosphate is present in these solutions and the P=O vibration bands of H_3PO_4 and $H_2PO_4^-$, reported to be located between 840 and 960 cm^{-1}, are superimposed on the Mo=O stretching vibrations [60]. Although the intensity of these P=O bands is much lower than the Mo=O stretching vibrations, their presence may disturb the deconvolution of spectra as changes in the speciation of phosphate anions may not coincide with changes in the protonation state of the $H_xP_2Mo_5O_{23}^{(6-x)-}$ anions. The pure component spectra of the complexes are presented as traces Mo-C-2 to Mo-C-4 in Fig. 30. Positions of the main Mo=O vibrations of the different

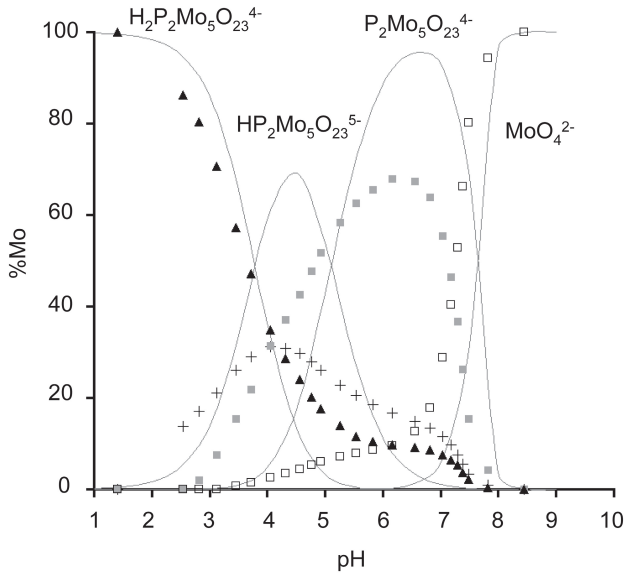

Figure 29. Speciation plot of the concentration of different Mo(VI)-complexes in the 1.0 M Mo/1.0 M PO_4^{3-} solutions in series 13, as derived from calculations using formation constants (solid lines). The concentrations of MoO_4^{2-} (□), and components Mo-C-2 (■), Mo-C-3 (+), and Mo-C-4 (▲) obtained from MCR analysis of Raman spectra are indicated as well.

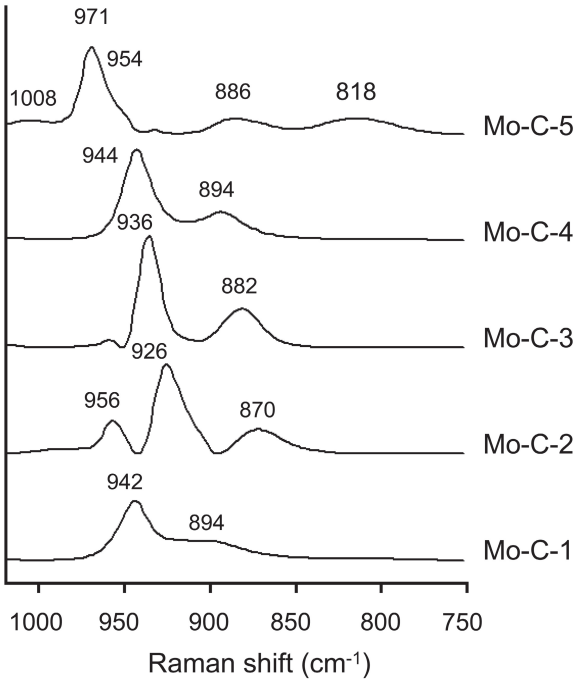

Figure 30. Pure spectra of components Mo-C-1 to Mo-C-4 obtained from MCR analysis of Raman spectra recorded on the (Co)MoP solutions in series 13 and 14.

$H_xP_2Mo_5O_{23}^{(6-x)-}$ complexes are included in Table 8.

CoMoP-solutions

The addition of Co(II) to MoP-solutions allows for the formation of even more types of heteropolyanions. Cobalt can be present as counter ion, or incorporated in the structure of the heteropolyanion. To evaluate the formation of CoMoP-complexes, an experiment was carried out, in which the phosphate concentration in a 0.5 M Co, 1.0 M Mo solution was varied between 0 and 0.5 M (series 14). Raman and UV-Vis-NIR measurements were carried out to evaluate the formation of different Mo(VI)- and Co(II)-complexes. The resulting spectra are presented in Fig. 31 and 32, respectively. The Raman spectrum of the solution without phosphate shows bands at 942 and 894 cm^{-1}, corresponding to the presence of $Mo_7O_{24}^{6-}$ complexes in this solution. The corresponding d-d band in the UV-Vis-NIR spectrum shows a maximum at 511 nm, corresponding to the presence of $[Co(H_2O)_6]^{2+}$ in solution. Addition of phosphate leads to the appearance of additional bands at 1008, 971 (with a shoulder at 954), 886 and 818 cm^{-1} in the Raman spectra. The intensities of these bands increase as the phosphate concentration is increased. Simultaneously, a steady increase of two broad bands at 455 and 588 nm is observed in the corresponding UV-Vis-NIR spectra. A maximum in the intensity of both the Raman and UV-Vis-NIR features is observed when a phosphate concentration of 0.15 M is

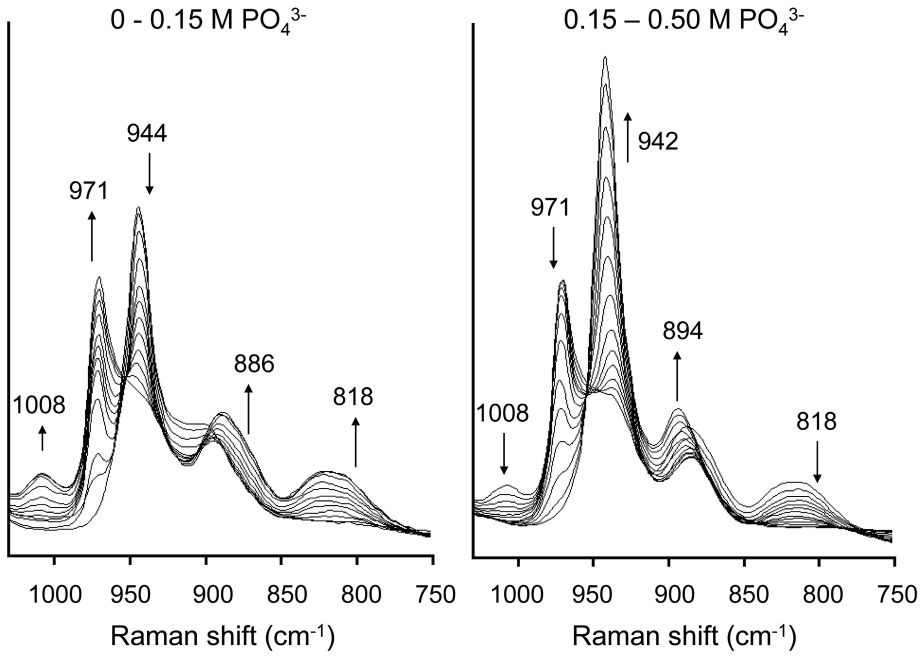

Figure 31. Selected Raman spectra recorded on the1.0 M Mo/0.5 M Co solutions in series 14 at different phosphate concentrations after the addition of phosphoric acid.

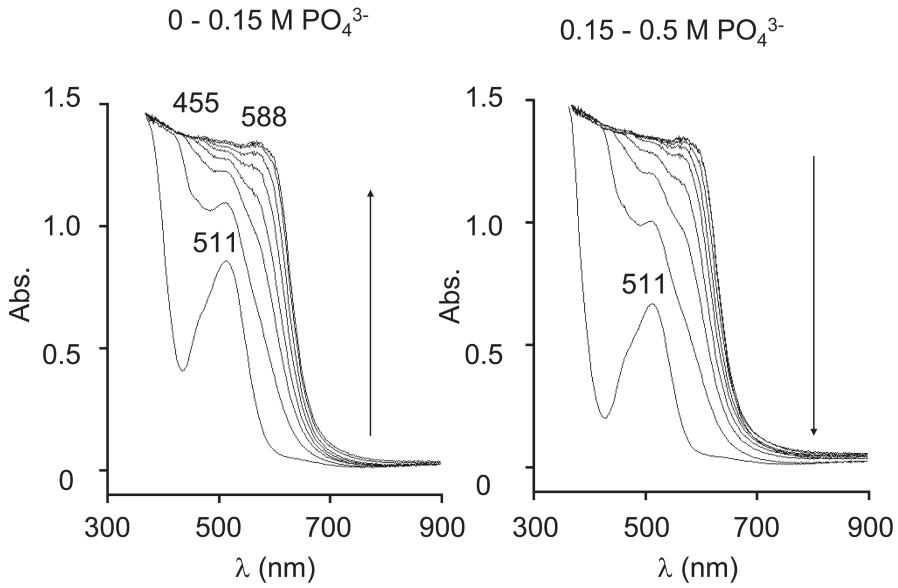

Figure 32. Selected UV-Vis-NIRspectra recorded on 1.0 M Mo/0.5 M Co solutions in series 14 at different phosphate concentrations after the addition of phosphoric acid.

reached. A further increase in the phosphate concentration leads to a decrease in the 971 cm^{-1} Raman band and the bands at 455 and 588 nm in the UV-Vis-NIR spectra. At a phosphate concentration of 0.5 M, only bands at 942, 894, 395 and 370 cm^{-1} are observed in the Raman spectrum, indicating the presence of $H_2P_2Mo_5O_{23}^{4-}$. In the corresponding UV-Vis-NIR spectrum the position of the absorption maximum at 511 nm shows that $[Co(H_2O)_6]^{2+}$ is the only Co(II)-containing complex present in the solution.

MCR analysis was carried out on the Raman spectra, in a similar procedure that was used for the MoP solution spectra. The spectrum of the CoMo solution without any phosphate was used as the first pure component (Mo-C-1). The pure component spectra of the $H_xP_2Mo_5O_{23}^{(6-x)-}$ anions, derived from the analysis of the MoP solution spectra were used as input as well (Mo-C-2 to Mo-C-4). The spectrum of the fifth component was allowed to change during the iteration process. These calculations resulted in a 91.0 % fit of the data. The addition of extra pure components didn't increase the goodness of the fit. The concentration plot of the different components in the CoMoP solutions, as a function of phosphate concentration, is presented in Fig. 33. The spectrum of the fifth component is presented as trace Mo-C-5 in Fig. 30.

Values for the intensity of the 588 nm band in the UV-Vis-NIR spectra, as a function of phosphate concentration were obtained by determination of the absorbance at 670 nm. Due

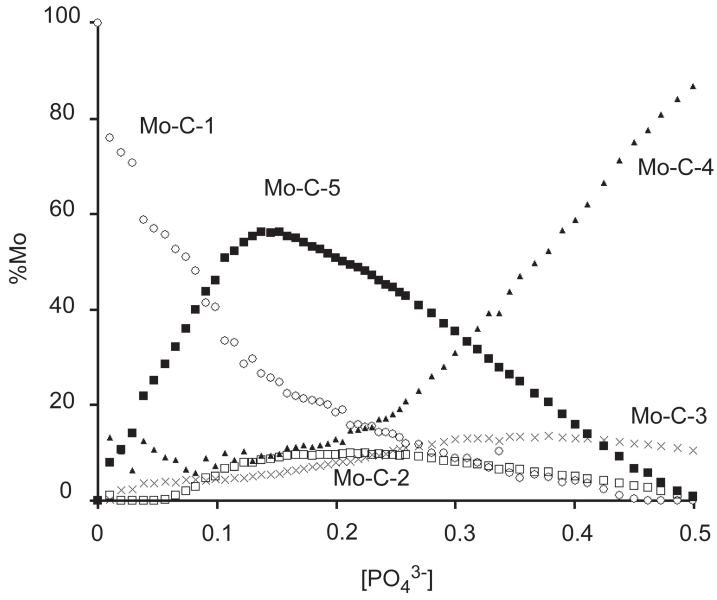

Figure 33. The concentration of components Mo-C-1 (○), Mo-C-2(□), Mo-C-3 (x), Mo-C-4 (▲) and Mo-C-5 (■) in the 1.0 M Mo/0.5 M Co solutions in series 14, as a function of phosphate concentration after the addition of H_3PO_4, as derived from MCR analysis of Raman spectra.

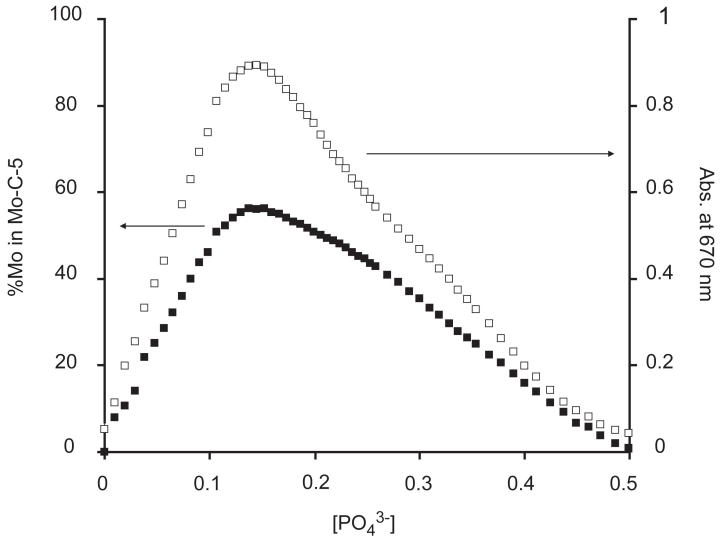

Figure 34. The concentration of component Mo-C-5 (■) in the 1.0 M Mo/0.5 M Co solutions in series 14, as a function of phosphate concentration after the addition of H_3PO_4. The absorbance at 670 nm in UV-Vis-spectra recorded on these solutions (□) is indicated as well.

to the high intensity of the band, quantitative analysis is only possible at the down-slope of the band, where Lambert-Beer's law still applies. In Fig. 34, the value for the absorbance at 670 nm is plotted as a function of the phosphate concentration together with the concentration profile of Mo-C-5 as determined by MCR of the Raman spectra. Both profiles show the same shape, which indicates that they are caused by the presence of the same complex, containing both Mo(VI) and Co(II) in solution. As the spectroscopic features are predominantly observed at a Mo:P ratio between 20 and 4, the complex probably has a high Mo:P ratio. The position of the main Raman band at 971 cm^{-1}, suggests that a $H_xPMo_{11}O_{39}^{(7-x)-}$ type complex is being formed. Co(II) can then be incorporated in the complex yielding a complete $H_2PMo_{11}CoO_{40}^{5-}$ Keggin structure, as proposed by different authors [61,62]. In this structure, depicted in Fig. 26, Co(II) is pseudo-octahedrally surrounded by oxygen atoms. The location of five of these ligands is more or less fixed by the structure of the phosphomolybdate complex. One water molecule can be coordinated to the outside of the complex to complete the six-fold coordination. The high intensity of the d-d transition bands is ascribed to the distortion of the Co(II) coordination from octahedral symmetry. Leyrie et al. reported a formation constant for the $H_2PMo_{11}CoO_{40}^{5-}$ complex, which is included in Table 8. The formation constants of isopolymolybdates, phosphomolybdate complexes and $H_2PMo_{11}CoO_{40}^{5-}$ were used to calculate the theoretical speciation of Mo-complexes of the solutions in series 14, as shown in Fig 35. A good correlation is found between the concentration of $H_2PMo_{11}CoO_{40}^{5-}$ in this speciation plot,

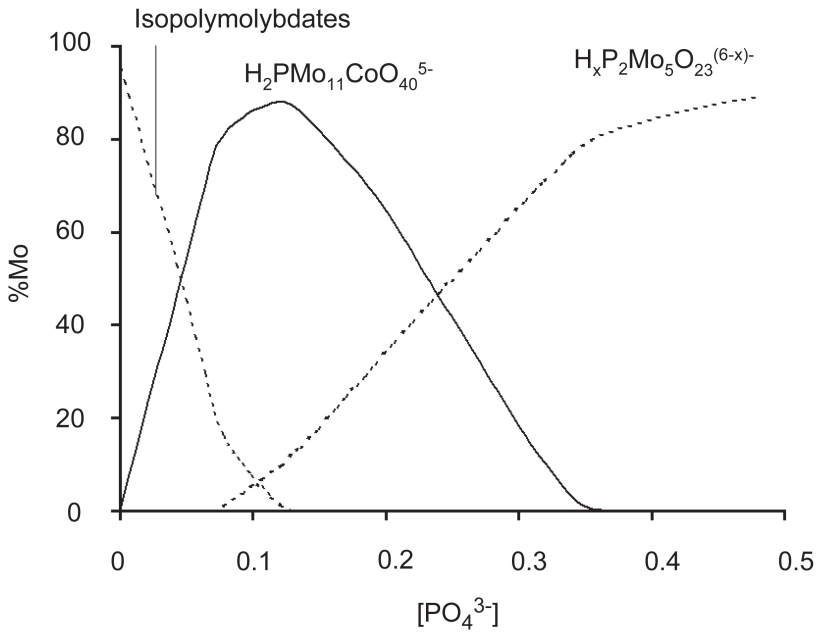

Figure 35. The theoretical concentrations of isopolymolybdates, $H_2PMo_{11}CoO_{40}^{5-}$ and $H_xP_2Mo_5O_{23}^{(6-x)-}$ in the 1.0 M Mo/0.5 M Co solutions in series 14, as derived from calculations using formation constants.

the concentration of component Mo-C-5 derived from the MCR analysis of Raman spectra (Fig. 33) and the increase in the Co(II) d-d band in the UV-Vis-NIR spectra (Fig. 34). The formation of an $H_2PMo_{11}CoO_{40}^{5-}$ Keggin ion is therefore a plausible explanation for the spectroscopic observations.

Conclusions

In AHM-H_3PO_4 solutions, only the formation of $H_xP_2Mo_5O_{23}^{(6-x)-}$ complexes needs to be considered when no additional acid is present. The protonation state of these complexes can be monitored using Raman spectroscopy. The addition of Co(II) to these solutions results in the formation of $H_2PMo_{11}CoO_{40}^{5-}$ Keggin-ions at specific pH and Mo:P ratios. The formation of this complex can be observed through characteristic features in Raman (971 cm^{-1}) and UV-Vis-NIR (588 nm) spectra. Unlike the CoMo-complexes found in AHM/$Co(NO_3)_2$ solutions, where only one or two oxygens of the $H_xMo_7O_{24}^{(6-x)-}$ complexes are involved, in this case, Co(II) is coordinated to the Mo(VI)-complex through five oxygen atoms. Due to this stronger interaction, this complex seems to be a better candidate for the preparation of supported CoMo-catalysts if one aims at retaining a close interaction between Co and Mo throughout the preparation process.

Acknowledgments

Bas Vogelaar en Peter de Peinder are kindly acknowledged for their help with the MCR-analysis. The DFT-calculations were carried out by Ingmar Swart. Measurements on Co-citrate solutions were carried out by Marieke Rijneveld-Ockers in the context of her bachelor thesis and Danny Verboekend in the context of his master thesis. Fouad Soulimani is thanked for his help with the experiments.

References

1 A. V. Neimark, L. I. Kheifez, V. B. Fenelonov, *Ind. Eng. Chem. Prod. Res. Dev.* **1981**, *20*, 439.
2 S. Y. Lee, R. Aris, *Catal. Rev. Sci. Eng.* **1985**, *27*, 207.
3 A. Lekhal, B. J. Glasser, J. G. Khinast, *Chem. Eng. Sci.* **2001**, *56*, 4473.
4 A. Lekhal, B. J. Glasser, J. G. Khinast, *Chem. Eng. Sci.* **2004**, *59*, 1063.
5 L. M. Knijff, *The Application of Active Components into Catalyst Support Bodies* PhD thesis, Utrecht University, 1993.
6 P. J. van den Brink, *The Selective Oxidation of Hydrogen Sulfide on Supported Iron-Based Catalysts* PhD thesis, Utrecht University, 1992.
7 N. W. Alcock, M. Dudek, R. Grybos, E. Hodorowicz, A. Kanas, A. Samotus, *J. Chem. Soc. Dalton Trans.* **1990**, 707.
8 J. J. Cruywagen, J. B. B. Heyns, *Inorg. Chem* **1987**, *26*, 2569.
9 J. J. Cruywagen, E. A. Rohwer, G. F. S. Wessels, *Polyhedron* **1995**, *14*, 3481.
10 N. Kotsakis, C. P. Raptopoulou, V. Tangoulis, A. Terzis, J. Giapintzakis, T. Jakusch, T. Kiss, A. Salifoglou, *Inorg. Chem.* **2003**, *42*, 22.
11 D. L. Long, P. Kogerler, L. J. Farrugia, L. Cronin, *Dalton Trans.* **2005**, 1372.
12 M. Matzapetakis, M. Dakanali, C. P. Raptopoulou, V. Tangoulis, A. Terzis, N. Moon, J. Giapintzakis, A. Salifoglou, *J. Biol. Inorg. Chem.* **2000**, *5*, 469.
13 T. Ozeki, H. Kihara, S. Hikime, *Anal. Chem.* **1987**, *59*, 945.
14 L. Pettersson, I. Andersson, L.-O. Öhman, *Inorg. Chem.* **1986**, *25*, 4726.
15 A. Samotus, A. Kanas, M. Dudek, R. Grybos, E. Hodorowicz, *Transit. Met. Chem.* **1991**, *16*, 495.
16 K. H. Tytko, G. Beathe, J. J. Cruywagen, *Inorg. Chem.* **1985**, *24*, 3132.
17 Z. H. Zhou, H. L. Wan, K. R. Tsai, *Polyhedron* **1997**, *16*, 75.
18 Z. H. Zhou, H. L. Wan, K. R. Tsai, *J. Chem. Soc. Dalton Trans.* **1999**, 4289.
19 Z. H. Zhou, H. L. Wan, K. R. Tsai, *Inorg. Chem.* **2000**, *39*, 59.
20 Z. H. Zhou, Y. F. Deng, Z. X. Cao, R. H. Zhang, Y. L. Chow, *Inorg. Chem.* **2005**, *44*, 6912.
21 Z. H. Zhou, Y. F. Deng, H. L. Wan, *Cryst. Growth Des.* **2005**, *5*, 1109.
22 R. Cattaneo, F. Rota, R. Prins, *J. Catal.* **2001**, *199*, 318.
23 R. Cattaneo, T. Shido, R. Prins, *J. Catal.* **1999**, *185*, 199.
24 R. Cattaneo, T. Weber, T. Shido, R. Prins, *J. Catal.* **2000**, *191*, 225.
25 L. Coulier, V. H. J. de Beer, J. A. R. van Veen, J. W. Niemantsverdriet, *J. Catal.* **2001**, *197*, 26.
26 A. J. van Dillen, R. Terorde, D. J. Lensveld, J. W. Geus, K. P. de Jong, *J. Catal.* **2003**, *216*, 257.
27 M. Y. Sun, D. Nicosia, R. Prins, *Catal. Today* **2003**, *86*, 173.
28 J. Y. Carriat, M. Che, M. Kermarec, M. Verdaguer, A. Michalowicz, *J. Am. Chem. Soc.* **1998**, *120*, 2059.
29 H. Kraus, R. Prins, *J. Catal.* **1997**, *170*, 20.
30 L. Medici, R. Prins, *J. Catal.* **1996**, *163*, 38.
31 R. Iwamoto, J. Grimblot, *Adv. Catal.* **2000**, *44*, 417.
32 K. Murase, H. Ando, E. Matsubara, T. Hirato, Y. Awakura, *J. Electrochem. Soc.* **2000**, *147*, 2210.
33 L. O. Ohman, *Inorg. Chem.* **1989**, *28*, 3629.

34 H. Y. Lee, K. M. Park, U. Lee, H. Ichida, *Acta Crystallogr. Sect. C. Cryst. Struct. Commun.* **1991**, *47*, 1959.
35 H. Y. An, Y. G. Li, D. R. Xiao, E. B. Wang, C. Y. Sun, *Cryst. Growth Des.* **2006**, *6*, 1107.
36 C. I. Cabello, I. L. Botto, H. J. Thomas, *Appl. Catal. A-General* **2000**, *197*, 79.
37 J. J. Cruywagen, J. B. B. Heyns, E. A. Rohwer, *J. Chem. Soc. Dalton Trans.* **1994**, 45.
38 J. J. Cruywagen, E. A. Rohwer, *J. Chem. Soc.-Dalton Trans.* **1995**, 3433.
39 J. J. Cruywagen, E. A. Rohwer, R. F. vandeWater, *Polyhedron* **1997**, *16*, 243.
40 G. Mestl, T. K. K. Srinivasan, *Catal. Rev. Sci. Eng.* **1998**, *40*, 451.
41 W. Windig, J. Guilment, *Anal. Chem.* **1991**, *63*, 1425.
42 K. Schostack, P. Parekh, S. Patel, E. R. Malinowski, *J. Res. Natl. Bur. Stand.* **1988**, *93*, 256.
43 A. B. P. Lever *(Eds.)*, *Inorganic Electronic Spectroscopy*, Elsevier, Amsterdam, 1984.
44 A. Griboval, P. Blanchard, L. Gengembre, E. Payen, M. Fournier, J. L. Dubois, J. R. Bernard, *J. Catal.* **1999**, *188*, 102.
45 C. Martin, C. Lamonier, M. Fournier, O. Mentre, V. Harle, D. Guillaume, E. Payen, *Chem. Mater.* **2005**, *17*, 4438.
46 H. D. Simpson, European Patent 0.349.223, **1989**.
47 H. D. Simpson, P. B. Borgens, US Patent 4.879.625, **1988**.
48 P. J. Shukis, J. D. Carruthers, V. J. Lostagio, WO Patent 9.531.280, **1995**.
49 J. A. Fetchin, US Patent 4.409.131, **1983**.
50 R. I. Bickley, H. G. M. Edwards, R. Gustar, S. J. Rose, *J. Mol. Struct.* **1991**, *246*, 217.
51 P. Tarakeshwar, S. Manogaran, *Spectroc. Acta Pt. A. Molec. Biomolec. Spectr.* **1994**, *50*, 2327.
52 M. Matzapetakis, C. P. Raptopoulou, A. Tsohos, V. Papaefthymiou, N. Moon, A. Salifoglou, *J. Am. Chem. Soc.* **1998**, *120*, 13266.
53 M. Matzapetakis, C. P. Raptopoulou, A. Terzis, A. Lakatos, T. Kiss, A. Salifoglou, *Inorg. Chem.* **1999**, *38*, 618.
54 M. Matzapetakis, N. Karligiano, A. Bino, M. Dakanali, C. P. Raptopoulou, V. Tangoulis, A. Terzis, J. Giapintzakis, A. Salifoglou, *Inorg. Chem.* **2000**, *39*, 4044.
55 M. Matzapetakis, M. Kourgiantakis, M. Dakanali, C. P. Raptopoulou, A. Terzis, A. Lakatos, T. Kiss, I. Banyai, L. Iordanidis, T. Mavromoustakos, A. Salifoglou, *Inorg. Chem.* **2001**, *40*, 1734.
56 P. Deglmann, K. May, F. Furche, R. Ahlrichs, *Chem. Phys. Lett.* **2004**, *384*, 103.
57 R. Ahlrichs, M. Bar, M. Haser, H. Horn, C. Kolmel, *Chem. Phys. Lett.* **1989**, *162*, 165.
58 J. A. R. van Veen, O. Sudmeijer, C. A. Emeis, H. De Wit, *J. Chem. Soc. Dalton Trans.* **1986**, 1825.
59 H. Kraus, R. Prins, *J. Catal.* **1996**, *164*, 251.
60 M. Cherif, A. Mgaidi, N. Ammar, G. Vallee, W. Furst, *J. Solut. Chem.* **2000**, *29*, 255.
61 M. Leyrie, M. Fournier, R. Massart, *C. R. Acad. Sc. Paris* **1971**, *273*, 1569.
62 L. A. Combs-Walker, C. L. Hill, *Inorg. Chem.* **1991**, *30*, 4016.

Chapter 3

Raman Micro-spectroscopy Study on the Impregnation of Al_2O_3 Support Bodies with Mo(VI)-Solutions

Abstract

Raman micro-spectroscopy has been applied to study the impregnation of γ-Al_2O_3 support bodies with different Mo(VI)-solutions. The speciation of different Mo(VI)-complexes over the support bodies was followed in time after impregnation. The addition of NH_4NO_3 to the impregnation solutions allows for a quantitative Raman analysis of the distribution of different complexes over the catalyst bodies as the NO_3^- ion could be used as an internal standard. After impregnation with an acidic ammonium heptamolybdate (AHM) solution, the strong interaction between $Mo_7O_{24}^{6-}$ and Al_2O_3 resulted in slow transport of this complex through the support and extensive formation of $Al(OH)_6Mo_6O_{18}^{3-}$ near the outer surface of the support bodies. A weaker interaction between Mo(VI)-complexes and Al_2O_3 could be achieved by using basic impregnation solutions or by the addition of complexing agents, such as citrate and phosphate, to the impregnation solution. In this way, transport was facilitated and a homogeneous distribution of Mo(VI)-complexes was obtained on a reasonable timescale. In general, time-resolved Raman micro-spectroscopy can be a valuable tool to study the physico-chemical processes during the ageing of impregnated support bodies.

Introduction

The industrial manufacture of Mo/Al_2O_3 catalysts starts with the incipient wetness impregnation of γ-Al_2O_3 extrudates with a solution containing the Mo-precursor, followed by consecutive drying, calcination and sulphidation steps. The activity of the final catalyst depends on the nature and distribution of the MoO_x phase obtained after impregnation and hence on the properties of the impregnation solution. It is therefore not surprising that over the years a vast amount of research has been dedicated to the understanding of the interaction of aqueous Mo(VI)-complexes with Al_2O_3 surfaces [1-11]. Raman spectroscopy is a powerful method to monitor the nature of the Mo(VI)-complexes in both the impregnation solution and in wet, dried and calcined catalysts and has therefore found extensive application in this field of research [1,2,4-6,12-16]. However, characterization is most often carried out on powder supports or crushed extrudates, which makes it impossible to study the specific processes that take place during the impregnation of support bodies.

It is generally accepted that after impregnation, imbibition of the water phase by the support is practically instantaneous due to the huge capillary suction created by its pore system. However, as a result of the interaction between the metal complexes in solution and the surface of the support, transport of the metal-ion precursor can be much slower [17,18]. It may take considerable time before a homogeneous distribution of the metal precursor over the support bodies is achieved and irreversible adsorption can even result in an egg-shell distribution of the active phase [17,19-21]. To allow for equilibration of the system, an aging step is therefore applied before drying in industrial catalyst preparation. In this chapter, this equilibration process after the impregnation of γ-Al_2O_3 support bodies with Mo-precursor solutions is followed using Raman micro-spectroscopy. Instead of the smaller extrudates generally used in industrial applications, Al_2O_3 pellets of 3 mm diameter are used for impregnation to extend the aging process and facilitate characterization.

By making cross-section scans, Raman spectra are recorded at different positions inside the individual catalyst bodies. This procedure can be repeated at several points in time after impregnation, which allows one to monitor the transport and formation of different Mo(VI)-complexes in the pore-system of the support as a function of time. Impregnation is carried out using Mo(VI)-solutions of different pH, enabling study of the interaction between the MoO_4^{2-} and $Mo_7O_{24}^{6-}$ anions and the Al_2O_3 support. Furthermore, the effect of citrate and phosphate as complexing agents has been investigated.

Experimental

Cylindrical γ-Al_2O_3 pellets (Engelhard) were calcined at 600°C for 6 h and stored at 120°C before impregnation. The pore volume of the support was 1.1 ml/g, while its BET surface area was 200 m^2/g. The pellets were 3 mm in both length and diameter. The point of zero charge (PZC) of the γ-Al_2O_3 was determined to be between 8.8 and 9.0 by potentiometric mass titrations [22]. Pore volume impregnation was carried out using 1.0 M Mo solutions, yielding a theoretical loading of 15-wt% MoO_3 in the final catalyst. Care was taken that the impregnation solution was homogeneously distributed over all particles by rotating the impregnation vessel continuously. After impregnation, the support bodies were kept in a closed vessel to prevent evaporation of water. At several points in time after impregnation, pellets were cleaved in the middle, perpendicular to their axis, using a razor blade. Raman spectra were recorded on the surface of the resulting cross-sections, as presented in Fig. 1. A Kaiser RXN spectrometer equipped with a 785 nm diode laser was used in combination with a Hololab 5000 Raman microscope. A 10x objective was used for beam focusing and collection of scattered radiation, resulting in a spot size on the sample of approximately 50 µm. The laser output power was 70 mW. When recording a series of measurements at the same spot on the sample, identical

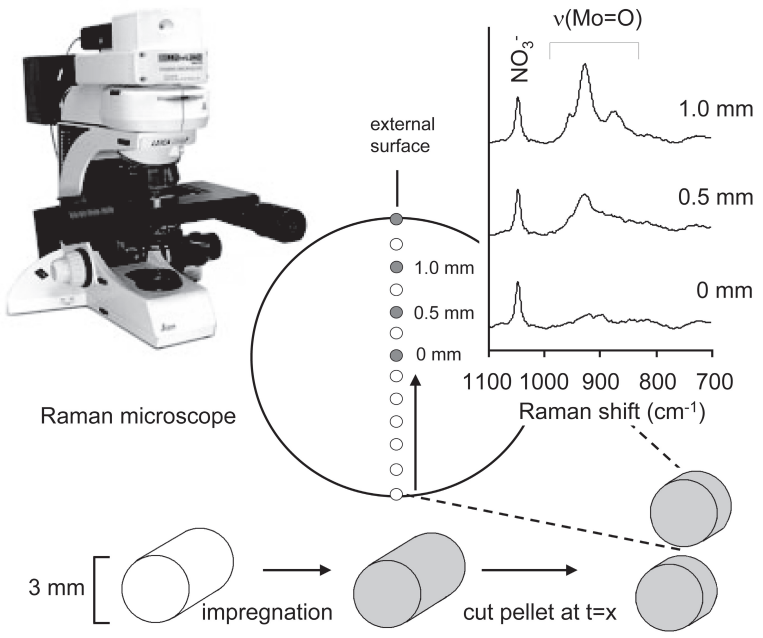

Figure 1. Lay-out of the experimental procedure used for the spatially resolved Raman measurements on bisected catalyst bodies after impregnation

spectra were found, indicating that no damage was done, by e.g. laser radiation, to the sample during measurements. For a typical measurement, 5 spectra were accumulated with a 3 s exposure time. Background correction was carried out by subtraction of a reference spectrum recorded on wet Al_2O_3.

All impregnation solutions were prepared using appropriate amounts of $(NH_4)_6Mo_7O_{24}$ (Acros, p.a.). Impregnation was carried out with AHM-solutions at a pH of 5.2 and 9.0, in the following referred to as AHM-pH5.2 and AHM-pH9.0. The pH of the latter solution was adjusted by addition of NH_4OH solution (Lamers & Pleuger, p.a.). An AHM-citrate solution with a Mo:citrate ratio of 1:1 and a pH of 0.5 was prepared using crystalline citric acid (OPG Farma, p.a.). Solutions with Mo:P ratio of 2:1 and 1:1 were prepared using 85% H_3PO_4 (Merck, p.a.). They are referred to as AHM-H_3PO_4(0.5) and AHM-H_3PO_4(1.0), respectively. The pH of the AHM-H_3PO_4(1.0) solution was adjusted to a pH of 2, the natural pH of the AHM-H_3PO_4(0.5) solution, by addition of NH_4OH solution. The chemical composition of the different solutions used is given in Table 1.

NH_4NO_3 (Acros, p.a.) was added to all solutions in a concentration of 0.66 M. In this way, the NO_3^- peak at 1044 cm^{-1} could be used as an internal standard in Raman micro-spectroscopy measurements. In order to make sure that this method is valid during measurements on Al_2O_3 bodies after impregnation, a homogeneous distribution of NO_3^- throughout the support is a prerequisite. This was verified by impregnating the Al_2O_3 pellets with a 0.66 M NH_4NO_3 solution of pH 1. Already after 10 min, a homogeneous distribution of NO_3^- was found, judging from the constant intensity of the peak at 1044 cm^{-1} after scaling to the Al_2O_3 background. From this, it can be concluded that transport of NO_3^- through the pores of the support is fast and there is no noticeable interaction between NO_3^- ions and the Al_2O_3 surface. An even distribution of NO_3^- may therefore be assumed. Hence, the NO_3^- peak at 1044 cm^{-1} could be used as an internal standard.

Table 1. Chemical composition and pH of the impregnation solutions used for the preparation of supported molybdenum oxide catalysts.

Sample code	[Mo] (M)	[phosphate] (M)	[citrate] (M)	[NO_3^-] (M)	pH
AHM-pH5.2	1.00	-	-	0.66	5.2
AHM-pH9.0	1.00	-	-	0.66	9.0
AHM-citrate	1.00	-	1.00	0.66	0.5
AHM-H_3PO_4(0.5)	1.00	0.50	-	0.66	2.0
AHM-H_3PO_4(1.0)	1.00	1.00	-	0.66	2.0

Results and Discussion

AHM solutions

Characteristic vibrations of relevant Mo(VI)-complexes, derived in chapter 2A, are listed in Table 2. According to calculations on the Mo-speciation in AHM solutions $Mo_7O_{24}^{6-}$ anions are mainly present in 1.0 M Mo solutions at pH 5.2. The Raman spectra recorded on the impregnation solutions used in this study, are presented in Fig. 2. The spectrum of the AHM-pH 5.2 solution showed peaks at 941 cm^{-1} (ν Mo=O), 896 cm^{-1} (ν Mo=O) and 358 cm^{-1} (δ O=Mo=O) in accordance with the presence of $Mo_7O_{24}^{6-}$ in solution [4]. At higher pH, formation of MoO_4^{2-} occurs according to Eq. 1. MoO_4^{2-} shows characteristic vibrational bands at 896 cm^{-1} (ν Mo=O), 836 cm^{-1} (ν Mo=O) and 320 cm^{-1} (δ O=Mo=O). The AHM-pH 9.0 impregnation solution merely contained MoO_4^{2-} anions.

$$Mo_7O_{24}^{6-} + 8\ OH^- \leftrightarrow 7\ MoO_4^{2-} + 4\ H_2O \qquad \text{(Eq. 1)}$$

Fig. 3 shows the Raman spectra recorded at three positions along the diameter of the support bodies 10 min after impregnation with an AHM-pH 9.0 solution. The values that are indicated in the figure represent the distance from the core of the pellet. In all spectra, only peaks at 896, 836 and 320 cm^{-1} were present, characteristic of MoO_4^{2-} in solution. The intensity of the (ν Mo=O) peaks compared to the NO_3^- peak serves as an indication for the concentration of Mo in the solution present in the pores of the support. After comparison to the spectra of

Table 2. Positions of characteristic Raman bands of relevant Mo(VI)-complexes in AHM, AHM-citrate and AHM-phosphate solutions, as derived in chapter 2.

Solution composition	pH	Mo(VI)-complex	ν(Mo=O) (cm^{-1})			δ(O=Mo=O) (cm^{-1})	
AHM	> 8.0	MoO_4^{2-}	896	842		318	
	5.0	$Mo_7O_{24}^{6-}$	939	896		358	
AHM:citrate 1:1	< 3.0	2:1 Mo-citrate complexes (e.g. $Mo_4(Hcitrate)_2O_{11}^{4-}$)	944	904	862	382	
	3.0-8.0	1:1 Mo-citrate complexes	934	902	864	386	328
AHM:$H_xPO_4^{(3-x)-}$ 2:1	6.0	$P_2Mo_5O_{23}^{6-}$	956	926	870	395	370
	4.0	$H_xP_2Mo_5O_{23}^{(6-x)-}$	936	882		395	370
	2.0	$H_xP_2Mo_5O_{23}^{(6-x)-}$	944	894		395	370

the impregnation solution in Fig. 2, an indication for the amount of Mo that has penetrated the support bodies can be obtained. In this case, it could be concluded that a homogeneous distribution of this anion was obtained throughout the support, as the Mo-concentration of the solution inside the pores of the support is similar to that of the impregnation solution. Raman spectra recorded at the exterior of the catalyst bodies impregnated with AHM-solutions are presented in Fig. 4. Again, after impregnation with an AHM-pH 9.0 solution, only Raman peaks corresponding to MoO_4^{2-} were observed at 896, 836 and 320 cm^{-1} (Table 2).

Impregnation with an AHM-pH 9.0 solution resulted in a homogeneous distribution of MoO_4^{2-} throughout the support bodies within 10 min. As the pH of the AHM-pH 9.0 impregnation solution is close to the PZC of alumina, the surface charge of the support is approximately zero and interaction between the Al_2O_3 surface and the MoO_4^{2-} anions solution is not significant [23]. Not hampered by adsorption, the MoO_4^{2-} anions travel with the convective flow of the water phase and fast transport of the complex through the pores of the support can take place. As there is little interaction with the support, the spectrum of MoO_4^{2-} observed in the impregnated Al_2O_3 was identical to that of the same compound in solution.

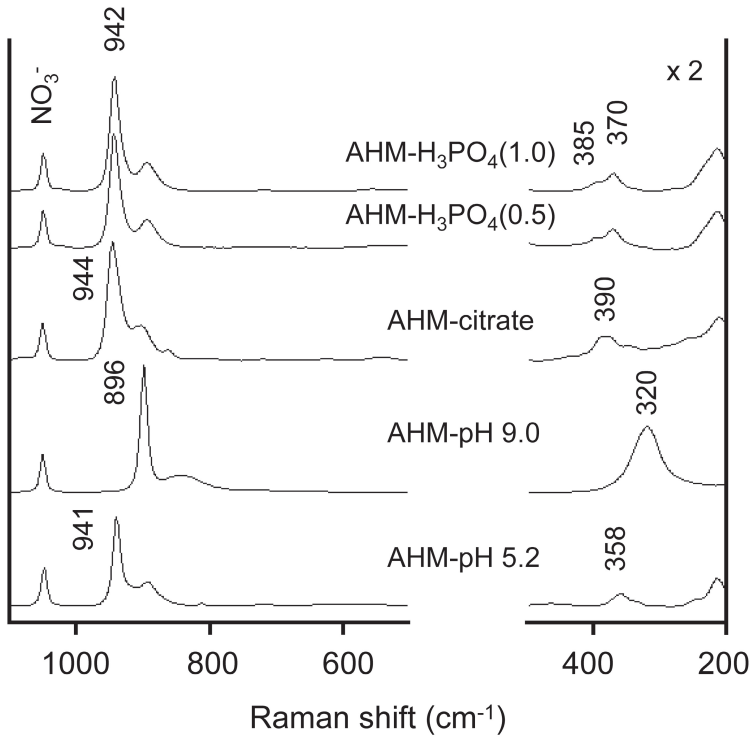

Figure 2. Raman spectra recorded on the 1.0 M Mo impregnation solutions used in this chapter.

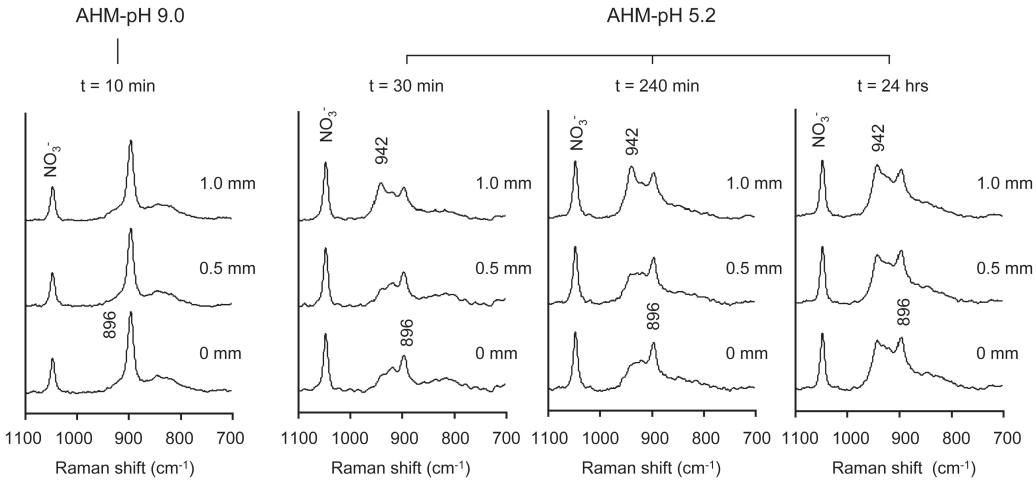

Figure 3. Raman spectra of bisected catalyst support bodies impregnated with AHM solutions of different pH. The Raman laser was focused 0, 0.5 and 1.0 mm from the centre. Spectra were recorded 10 min after impregnation with an AHM-pH 9.0 solution and 30 min, 240 min and 24 h after impregnation with an AHM-pH 5.2 solution.

Raman spectra of the interior of pellets impregnated with an AHM-pH 5.2 solution are also presented in Fig. 3. Spectra were recorded after 30 min, 240 min and 24 h. From the relative intensity of the ν(Mo=O) bands, it could be concluded that in this case, the Mo-concentration on the inside of the support bodies was much lower than in the AHM-pH 5.2 solution used for impregnation. After 30 min, Mo was predominantly present as MoO_4^{2-} near the core of the pellets, as could be concluded from the position of the ν(Mo=O) vibration band at 896 cm^{-1}. An additional feature was observed at 920 cm^{-1}. This peak was never observed in Raman spectra recorded on Mo(VI)-solutions (chapter 2A) and must therefore be attributed to a Mo(VI)-complex in interaction with the Al_2O_3 support. In literature, it is ascribed to some form of tetrahedrally coordinated Mo(VI)-anion adsorbed onto the support [4]. Near the edge of the pellets, a ν(Mo=O) vibration band was observed at 942 cm^{-1} pointing to the presence of $Mo_7O_{24}^{6-}$ (Table 2). In time, $Mo_7O_{24}^{6-}$ was also observed near the centre of the support bodies. 24 h after impregnation, the spectrum recorded near the core of the support body was similar to that recorded near the edge and MoO_4^{2-} and $Mo_7O_{24}^{6-}$ were present in the same amount throughout the pellets. After impregnation with an AHM-pH 5.2 solution, intense Raman peaks were observed at 947, 899, 570 and 356 cm^{-1} in the spectrum recorded on the outside of the pellets (Fig. 4). In literature, they are ascribed to the formation of $Al(OH)_6Mo_6O_{18}^{3-}$, an Anderson-type heteropolyanion [7,16]. The peak at 570 cm^{-1} is generally regarded to originate from a ν(Al-O) vibration [16].

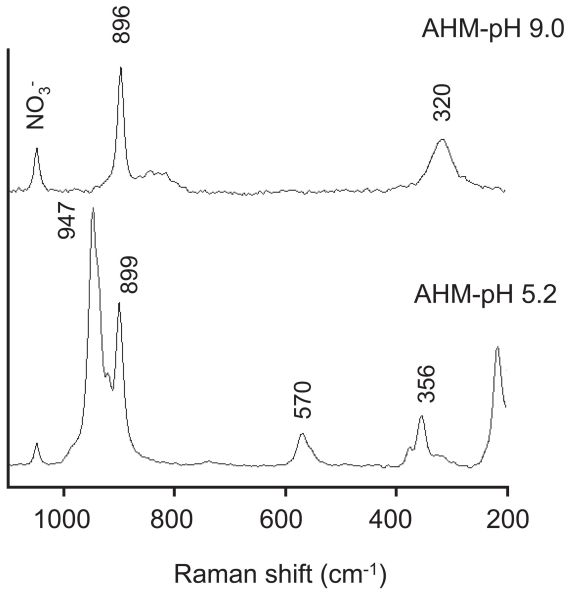

Figure 4. Raman spectra recorded of the external surface of catalyst bodies impregnated with AHM-pH 5.2 solution after 30 min and AHM-pH 9.0 solution after 45 min.

In contrast to what was observed for the AHM-pH 9.0 solution, impregnation with an AHM-pH 5.2 solution resulted in slow transport of Mo(VI)-anions through the pores of the support, as a result of adsorption of these complexes onto the Al_2O_3 surface. Interaction between the Al_2O_3 support and Mo(VI)-anions in solution can take place according to Eq. 2 [10]. This reaction is facilitated by the lower pH of this impregnation solution. As a consequence of this interaction between the anions in solution and the surface of the support, transport of the anions was slow. Water is distributed rapidly throughout the support, due to the viscous flow that results from the capillary forces. Consequently, in the first period after impregnation, the Mo-concentration is very high at the external surface of the extrudates.

$$2\,Al_sOH + MoO_4^{2-} \leftrightarrow (Al_s)_2MoO_4 + 2\,OH^- \qquad \text{(Eq. 2)}$$

In accordance with Eq. 2, the adsorption of MoO_4^{2-} is accompanied with an increase in pH inside the pores of the Al_2O_3. As a result, the equilibrium in Eq. 1 is shifted to the left and more MoO_4^{2-} is formed. Hence, as the Mo-front travels through the support, $Mo_7O_{24}^{6-}$ is converted into free and adsorbed MoO_4^{2-}. Near the centre of the pellets, only MoO_4^{2-} and $(Al_s)MoO_4$ complexes were indeed observed in the first hours after impregnation. In time, $Mo_7O_{24}^{6-}$ was found to diffuse towards the core of the pellets without disintegration. After titration of the basic hydroxyls with MoO_4^{2-}, $Mo_7O_{24}^{6-}$ can be stable inside the pores of the alumina support. The fact that the position of its ν(Mo=O) peak (941 cm^{-1}) has not changed as compared to the impregnation solution indicates that only a weak interaction exists between this complex and the support. Electrostatic adsorption of $Mo_7O_{24}^{6-}$ entities is reported to occur on coordinatively

unsaturated Al(III) sites of an Al_2O_3 surface [10].

The formation of the $Al(OH)_6Mo_6O_{18}^{3-}$ Anderson-type heteropolyanion, due to ligand-promoted dissolution of the Al_2O_3 support is often observed when impregnation with an acidic AHM solution is carried out [7]. Formation of this complex is reported to take place in an acidic environment where hydrated Al(III)-ions react with MoO_4^{2-} in solution in accordance with Eq. 3.

$$12\ Mo_7O_{24}^{6-} + 7\ Al_2O_3 + 27\ H_2O + 30\ H^+ \rightarrow 14\ Al(OH)_6Mo_6O_{18}^{3-} \qquad \text{(Eq. 3)}$$

Formation of $Al(OH)_6Mo_6O_{18}^{3-}$ was observed on the outside of the pellets, probably due to both the high local Mo-concentration and the favorable pH. As the solubility of $Al(OH)_6Mo_6O_{18}^{3-}$ is low, precipitation of this species takes place instantly. Large clusters of this compound were thus formed on the outside of the support bodies in which a considerable amount of the Mo that was present in the system was contained. For this reason, the Mo-concentration inside the pellets was found to be low, as can be seen from the relative intensity ratio of the ν(Mo=O) and NO_3^- peaks (compare Fig. 2 and 3). The formation of the $Al(OH)_6Mo_6O_{18}^{3-}$ compound could be detrimental to the activity of the final catalyst as calcination of this compound is reported to result in the formation of MoO_3 clusters [8] .

AHM-citrate solutions

In a 1.0 M Mo, 1:1 AHM-citrate solution, the $Mo_4(Hcitrate)_2O_{11}^{4-}$ complex is the most prominent complex at pH 0.5. The Raman spectrum of the AHM-citrate impregnation solution, presented in Fig.2, shows bands at 944 and 901 cm^{-1}, and a small peak at 861 cm^{-1}, which seem to be diagnostic for 2:1 Mo:citrate complex. The main δ(O=Mo=O) vibration is found at 385 cm^{-1}. At higher pH and higher concentrations of citrate, the formation of 1:1 Mo-citrate complexes is favored. Their formation can be recognized by the ν(Mo=O) bands at 933, 901 and 861 cm^{-1} and δ(O=Mo=O) band at 385 cm^{-1} [24]. A detailed discussion on the speciation of Mo(VI)-complexes in Mo:citrate solution and their characterization with the aid of Raman spectroscopy can be found in chapter 2B.

Raman spectra recorded on a bisected Al_2O_3 pellet 30 min after impregnation with the AHM-citrate solution are presented on the top left in Fig. 5. All Raman spectra of the support bodies impregnated with this solution show only the characteristic ν(Mo=O) vibrations of 2:1 Mo-citrate complexes at 944, 901 and 861 cm^{-1} (Table 2). As discussed in chapter 2B, on the basis of Raman spectra, no discrimination could be made between different 2:1 Mo:citrate

complexes. However high Mo-concentrations strongly favor the formation of larger complexes, such as $Mo_4(Hcitrate)_2O_{11}^{4-}$. Therefore, this complex was assumed to be predominantly present in the Al_2O_3 pores. The amount of $Mo_4(Hcitrate)_2O_{11}^{4-}$ at a certain position in the pellet could be estimated by taking the ratio of the area of the ν(Mo=O) (integration width: 840-970 cm^{-1}) and the area of the NO_3^- (integration width: 1038-1058 cm^{-1}) Raman bands. In this way, a distribution profile of the $Mo_4(Hcitrate)_2O_{11}^{4-}$ complex over the cross section of the catalyst bodies was obtained at different times after impregnation. In Fig. 5, the distribution of the complex over the profile of an Al_2O_3 pellet, 15, 60 and 180 min after impregnation, is illustrated in three-dimensional plots. From these plots, it is clear that a radial distribution of the Mo-complex was established at all time. In this way, the use of cross-section scans as a faster way to monitor the distribution of Mo(VI)-complexes throughout the pellets was validated. The $Mo_4(Hcitrate)_2O_{11}^{4-}$ concentration gradient over the support bodies decreased as a function of time. A reasonably homogeneous distribution of the complex was reached 180 min after impregnation. In Raman spectra recorded on the exterior surface of pellets, presented in Fig. 6, peaks corresponding to $Mo_4(citrate)_2O_{11}^{4-}$ (944, 901, 861 and 373 cm^{-1}) were observed at all time.

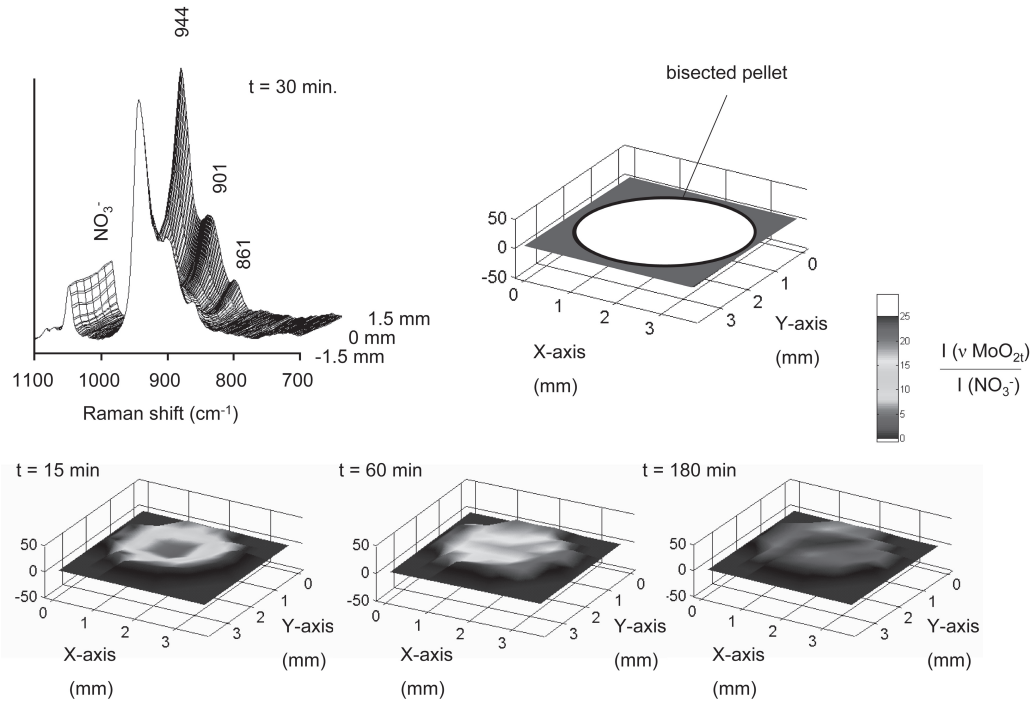

Figure 5. Raman spectra recorded on bisected catalyst bodies impregnated with a Mo-citrate solution, recorded 30 min after impregnation (left). Three-dimensional plots illustrating the spatial distribution of the $Mo_4(Hcitrate)_2O_{11}^{4-}$ complex in 3 mm Al_2O_3 pellets 15, 60 and 180 min after impregnation with an AHM-citrate solution (bottom). The intensity plots are obtained by referencing to the NO_3^- Raman band. *For a color-version of this figure, see Appendix (p. 208).*

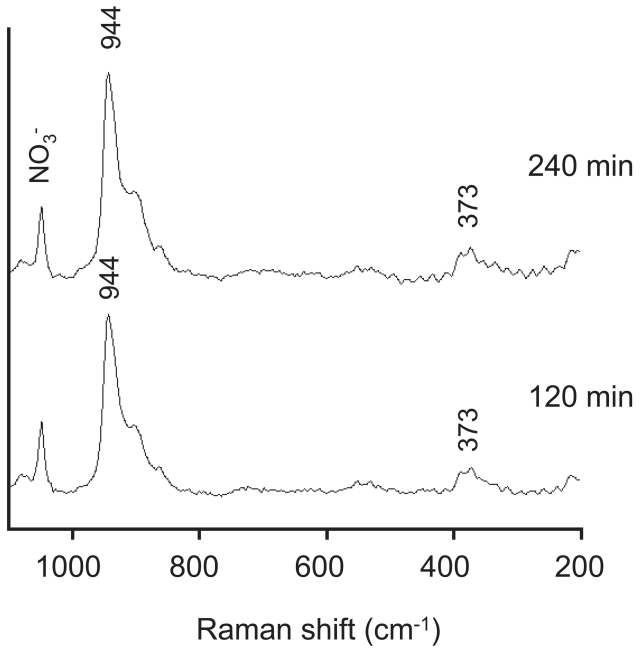

Figure 6. Raman spectra recorded of the external surface of catalyst bodies impregnated with the AHM-citrate solution after 120 and 240 min.

After impregnation with a solution of $Mo_4(Hcitrate)_2O_{11}^{4-}$, a very slow transport of this complex was observed through the pores of the support, until finally a homogeneous distribution is obtained 180 min after impregnation. Transport is slower than for the MoO_4^{2-} species in the case of AHM-pH 9.0 and AHM-pH 5.2 solutions, as there probably is a considerable electrostatic interaction between the positively charged support surface and the $Mo_4(Hcitrate)_2O_{11}^{4-}$ complex, due to the low pH of the impregnation solution [23]. Furthermore, the increased viscosity of the impregnation solution and the size of the $Mo_4(Hcitrate)_2O_{11}^{4-}$ complexes may result in slower diffusion [20]. It can be expected that protonation of the surface hydroxyl groups results in an increase of the pH of the impregnation solution inside the pores of the support. Formation of 1:1 Mo:citrate complexes might then be expected. However, these complexes were not observed at any moment after impregnation. Apparently, the pH of the impregnation solution was sufficiently low to counteract the buffering influence of the support. Furthermore, adsorption of excess citrate on the Al_2O_3-surface can lead to a decrease in the concentration of this ligand, further favoring the formation of 2:1 Mo-citrate complexes. Immediately after impregnation, the Mo-concentration was extremely high near the edges of the support bodies. Nevertheless, precipitation of Mo-compounds was avoided as the solubility of Mo(VI) is enhanced due to the complexing ability of the citrate ligands.

AHM-H_3PO_4 solutions

Calculations based on formation constants indicate that only $H_xP_2Mo_5O_{23}^{(6-x)-}$ complexes are formed in acidic solutions at Mo:P ratios of 2:1 and 1:1. The $H_xP_2Mo_5O_{23}^{(6-x)-}$ complex is stable in different protonation states over a wide pH range. Characteristic peaks in the corresponding Raman spectra can be found at 370 and 395 cm^{-1} (δ(O=Mo=O)). At pH 2.0 the ν_s(Mo=O) vibration bands of the fully protonated $H_2P_2Mo_5O_{23}^{4-}$ complex are found at 942 cm^{-1} and 893 cm^{-1}. As can be seen in Fig. 2, both impregnation solutions show identical Raman spectra, as $H_2P_2Mo_5O_{23}^{4-}$ complexes are exclusively present. These bands shift to lower frequency upon deprotonation. The $P_2Mo_5O_{23}^{6-}$ complex, present in solution at pH 6, shows bands at 956, 926 and 874 cm^{-1}. A more detailed discussion on the speciation of Mo(VI)-complexes in MoP-solutions can be found in chapter 2C.

In Fig. 7, Raman spectra recorded along the diameter of the interior of support bodies are presented 30, 90 and 360 min after impregnation with the AHM-H_3PO_4(1.0) solution. At 30 min after impregnation, ν(Mo=O) bands at 956, 928 and 878 cm^{-1} were observed near the edge of the pellets. The δ(O=Mo=O) vibration bands were observed at 370 and 395 cm^{-1} (not shown), which revealed that $H_xP_2Mo_5O_{23}^{(6-x)-}$ complexes were present. At the same time, hardly any Mo(VI)-complexes were observed near the core of the catalyst bodies. At 90 min after impregnation, δ(O=Mo=O) vibrations at 370 and 395 cm^{-1} were observed over the entire profile, indicating the presence of $H_xP_2Mo_5O_{23}^{(6-x)-}$ throughout the support bodies (Table 2). The main ν(Mo=O) band was observed at 929 cm^{-1} for all positions inside the alumina support.

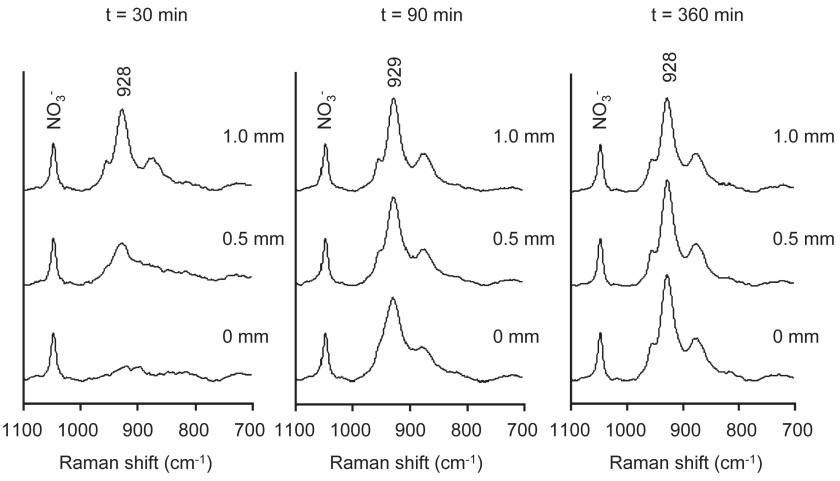

Figure 7. Raman spectra of bisected catalyst bodies impregnated with an AHM-H_3PO_4(1.0) solution. The Raman laser was focused 0, 0.5 and 1.0 mm from the center. Spectra were recorded 30, 90 and 360 min after impregnation.

Near the core, a slightly higher Raman intensity was observed at 935-940 cm^{-1}. A reasonably homogeneous distribution of Mo(VI)-complexes could be assumed from the relative intensity of the ν(Mo=O) bands. After 360 min, the feature at 935-940 cm^{-1} had disappeared and identical Raman spectra were recorded over the entire cross-section.

Fig. 8 shows the Raman spectra recorded along the diameter of the interior of the catalyst bodies 30, 90 and 360 min after impregnation with the AHM-H_3PO_4(0.5) solution. No ν(Mo=O) peaks were observed on the inner part of the pellets after 30 min. Near the edge, a broad ν(Mo=O) band was observed with a maximum at 931 cm^{-1}. After 360 min, Mo(VI)-complexes were present throughout the profile of the support bodies. However, from the intensity ratio of the ν(Mo=O) and NO_3^- bands, it was clear that the loading was considerably lower than, what could be assumed from the Mo-concentration in the impregnation solution. The maximum in the ν(Mo=O) band was found at 930 cm^{-1} at all positions, with a shoulder at 940 cm^{-1} observed near the core of the pellets. The δ(O=Mo=O) vibrations at 370 and 395 cm^{-1} (not shown) indicated that Mo was predominantly present as $H_xP_2Mo_5O_{23}^{(6-x)-}$ in all cases (Table 2).

Spectra recorded from the outside of pellets, at several points in time after impregnation with the different AHM-H_3PO_4 solutions are presented in Fig. 9. $H_xP_2Mo_5O_{23}^{(6-x)-}$ was the only species on the outside of pellets impregnated with a AHM-H_3PO_4(1.0) solution, yielding a Raman spectrum with characteristic vibrations at 955, 930, 878, 395 and 370 cm^{-1}. During the first 90 min after impregnation with a AHM-H_3PO_4(0.5) solution, $H_xP_2Mo_5O_{23}^{(6-x)-}$ was the only observed

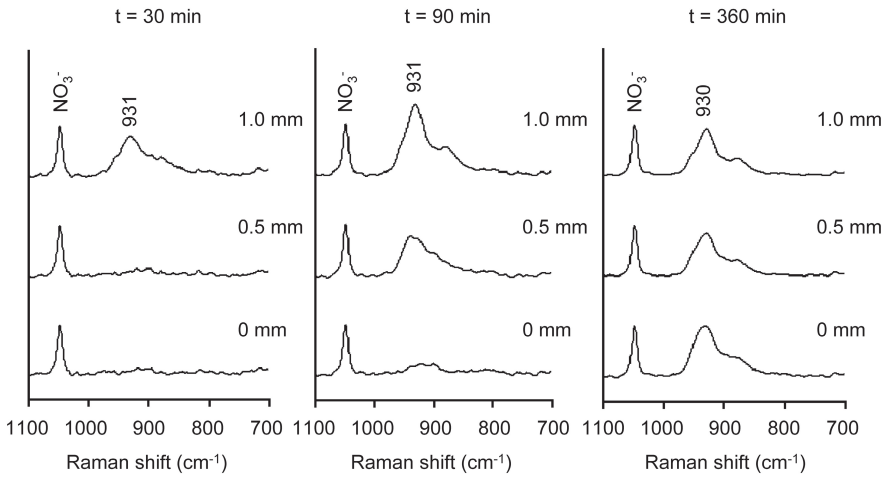

Figure 8. Raman spectra of bisected catalyst bodies impregnated with an AHM-H_3PO_4(0.5) solution. The Raman laser was focused 0, 0.5 and 1.0 mm from the center. Spectra were recorded 30, 90 and 360 min after impregnation.

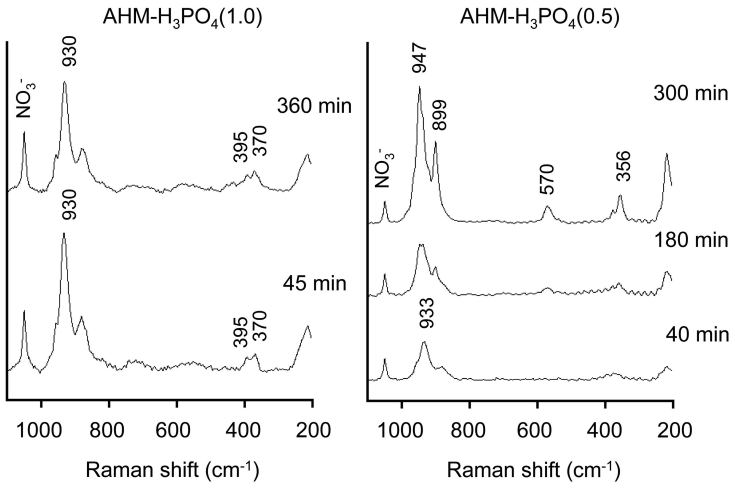

Figure 9. Raman spectra recorded of the external surface of catalyst bodies impregnated with the AHM-H_3PO_4(1.0) solution after 45 min and 360 min (left) and AHM-H_3PO_4(0.5) solution after 40 min, 180 min and 300 min (right).

Mo(VI)-complex. However, after 180 min, the formation of $Al(OH)_6Mo_6O_{18}^{3-}$ was observed and after 300 min, this compound was apparently present in large amounts on the outer surface of the support bodies.

When a molar ratio of Mo:P 1:1 or 2:1 is used in the impregnation solution, excess $H_xPO_4^{(3-x)-}$ is present as only 40% and 90% of the phosphorus is respectively contained in the $H_xP_2Mo_5O_{23}^{(6-x)-}$ complexes. Under acidic conditions, this free phosphate is known to react with the hydroxyl groups of the Al_2O_3-support to form an amorphous $AlPO_4$ layer [25,26], as indicated by Eq. 4. This reaction leads to a decrease in the free phosphate concentration and an increase in pH of the solution inside the pores of the support. As a result, the stability of the $H_xP_2Mo_5O_{23}^{(6-x)-}$ is decreased, as the equilibrium in Eq. 5 is shifted to the right. The free phosphate, which is formed upon disintegration of $H_xP_2Mo_5O_{23}^{(6-x)-}$ is again available for reaction with the support, speeding up this reaction cycle. Finally, an equilibrium state is reached in which the phosphate concentration in the impregnation solution determines the stability of the $H_xP_2Mo_5O_{23}^{(6-x)-}$ inside the pores of the support. This is in accordance with literature, in which it is stated that interaction of $H_xP_2Mo_5O_{23}^{(6-x)-}$ with the hydroxyl groups of the Al_2O_3 supports results in the disintegration of the complex, when no excess free phosphate is present [9,11]. It is also reported that physisorption of $H_xP_2Mo_5O_{23}^{(6-x)-}$ and $Mo_7O_{24}^{6-}$ can take place on the $AlPO_4$ layer that has been formed [11].

$$Al_sOH + HPO_4^{2-} + H^+ \leftrightarrow AlHPO_4^- + H_2O \qquad \text{(Eq. 4)}$$

$$7\ P_2Mo_5O_{23}^{6-} + 15\ H_2O \leftrightarrow 5\ Mo_7O_{24}^{6-} + 14\ HPO_4^{2-} + 16\ H^+ \qquad \text{(Eq. 5)}$$

Impregnation with an AHM-H_3PO_4(1.0) solution resulted in a reasonably homogeneous distribution of $H_xP_2Mo_5O_{23}^{(6-x)-}$ throughout the support after 90 min. Disintegration of the complex (Eq. 5) was prevented, since enough free phosphate was present. However, the reaction between free phosphate and the support was accompanied with an increase in the pH of the impregnation solution inside the pores of the support, as is obvious from Eq. 4. For this reason, the ν(Mo=O) vibration band was shifted to lower frequency due to deprotonation of the $H_2P_2Mo_5O_{23}^{(6-x)-}$ complex. From the position of the main ν(Mo=O) vibration band at 929 cm^{-1} it could be concluded that the pH of the solution in the pores of the Al_2O_3 was raised to a pH of ~ 5. Above the $AlPO_4$ overlayer that is formed, $H_xP_2Mo_5O_{23}^{(6-x)-}$ can be stable inside the pores of the support. Possibly, the diffusion of free phosphate was somewhat lagging behind that of the $H_xP_2Mo_5O_{23}^{(6-x)-}$ complex. The feature at 935-945 cm^{-1}, observed near the core of the pellets after 90 min, may then be explained by the formation of $Mo_7O_{24}^{6-}$, as a result of a low local free phosphate concentration.

When impregnation is carried out with a AHM-H_3PO_4(0.5) solution, diffusion of Mo(VI)-complexes was found to be slower and the amount of Mo that finally diffused to the inside of the catalyst bodies was considerably lower. Not enough free phosphate was present in the impregnation solution to prevent disintegration of $H_xP_2Mo_5O_{23}^{(6-x)-}$. $Mo_7O_{24}^{6-}$ was therefore formed. As was observed in the impregnation with an AHM-pH 5.2 solution, diffusion of $Mo_7O_{24}^{6-}$ inside the pellets is a slow process. Hence, a high concentration of Mo was again established near the edge of the pellets. Reaction of the $Mo_7O_{24}^{6-}$ species with dissolved Al(III)-ions once again resulted in the formation of considerable amounts of $Al(OH)_6Mo_6O_{18}^{3-}$ on the outside of the catalyst bodies. Phosphomolybdate complexes with lower P:Mo ratio were not observed, since the formation of these complexes requires a low pH, as discussed in chapter 2C.

Conclusions

The interaction between aqueous Mo(VI)-complexes and Al_2O_3 can have severe consequences for the impregnation of millimeter-scale Al_2O_3 support bodies. A strong interaction between the Mo-anions and the support results in a slow transport of these compounds. As a result, the concentration of Mo(VI)-complexes near the outer surface of the support bodies is dramatically increased. For this reason, measures have to be taken to prevent precipitation of Mo(VI)-complexes near the outer phase of the support bodies. A high concentration of Mo in combination with long contact times can result in the formation of $Al(OH)_6Mo_6O_{18}^{3-}$ clusters, which may be converted into MoO_3 upon calcination [8].

This unwanted process may be avoided in three ways. First of all, the interaction between the anions and the support can be diminished by choosing an impregnation solution with a pH that is close to the PZC of the support. In this case, the anions have no electrostatic interaction with the neutral Al_2O_3 surface and the formation of $(Al_s)_2MoO_4$ is prevented, resulting in a fast transport of MoO_4^{2-}. A homogeneous distribution of the anions is established within minutes after impregnation, as was illustrated in this study by the impregnation with an AHM-pH 9.0 solution. However, a weak interaction between the metal precursor and the support could be a problem during drying, as the Mo(VI)-complexes are not anchored to the support. A second approach is to use agents that are able to form stable complexes with Mo(VI), such as citrate and phosphate. The solubility of Mo is enhanced, which prevents precipitation and its reactivity is decreased. In this way, formation of $Al(OH)_6Mo_6O_{18}^{3-}$ can be avoided. Finally, reactive hydroxyl groups on the support can be titrated by an additional compound in the impregnation solution. A less reactive overlayer is thus created and diffusion of the Mo(VI)-complexes can be faster. This is the case when phosphate in AHM-H_3PO_4 solutions reacts with the Al_2O_3 to form amorphous $AlPO_4$. When a solution with sufficient free phosphate is used, a homogeneous distribution of $P_2Mo_5O_{23}^{6-}$ complexes was found within 120 min after impregnation.

Acknowledgments

Ad Mens is thanked for the N_2 physisorption measurements on the Al_2O_3 support. Brenda Rossenaar is kindly acknowledged for facilitating the preliminary Raman micro-spectroscopy measuremants at the laboratories of Akzo Nobel Chemicals Research in Arnhem.

References

1 H. Knözinger, H. Jeziorowski, *J. Phys. Chem* **1978**, *82*, 2002.
2 H. Jeziorowski, H. Knözinger, P. Grange, P. Gajardo, *J. Phys. Chem.* **1980**, *84*, 1825.
3 J. Grimblot, *Catal. Today* **1998**, *41*, 111.
4 G. Mestl, T. K. K. Srinivasan, *Catal. Rev. Sci. Eng.* **1998**, *40*, 451.
5 H. Jeziorowski, H. Knözinger, *J. Phys. Chem.* **1979**, *83*, 1166.
6 L. Wang, W. K. Hall, *J. Catal.* **1980**, *66*, 251.
7 X. Carrier, J. F. Lambert, M. Che, *J. Am. Chem. Soc.* **1997**, *119*, 10137.
8 X. Carrier, J. F. Lambert, S. Kuba, H. Knozinger, M. Che, *J. Mol. Struct.* **2003**, *656*, 231.
9 W. C. Cheng, N. P. Luthra, *J. Catal.* **1988**, *109*, 163.
10 J. A. R. van Veen, P. Hendriks, E. Romers, R. R. Andrea, *J. Phys. Chem.* **1990**, *94*, 5275.
11 J. A. R. van Veen, P. Hendriks, R. R. Andrea, E. Romers, A. E. Wilson, *J. Phys. Chem.* **1990**, *94*, 5282.
12 G. Deo, I. E. Wachs, *J. Phys. Chem.* **1991**, *95*, 5889.
13 M. A. Banares, I. E. Wachs, *J. Raman Spectros.* **2002**, *33*, 359.
14 I. E. Wachs, *Catal. Today* **1996**, *27*, 437.
15 K. Chen, S. Xie, A. T. Bell, E. Iglesia, *J. Catal.* **2001**, *198*, 232.
16 L. Le Bihan, P. Blanchard, M. Fournier, J. Grimblot, E. Payen, *J. Chem. Soc. Faraday Trans.* **1998**, *94*, 937.
17 S. Y. Lee, R. Aris, *Catal. Rev. Sci. Eng.* **1985**, *27*, 207.
18 K. P. de Jong, *Stud. Surf. Sci. Catal.* **1991**, *63*, 19.
19 A. Lekhal, B. J. Glasser, J. G. Khinast, *Chem. Eng. Sci.* **2001**, *56*, 4473.
20 A. Lekhal, B. J. Glasser, J. G. Khinast, *Chem. Eng. Sci.* **2004**, *59*, 1063.
21 A. V. Neimark, L. I. Kheifez, V. B. Fenelonov, *Ind. Eng. Chem. Prod. Res. Dev.* **1981**, *20*, 439.
22 J. Vakros, C. Kordulis, A. Lycourghiotis, *Chem. Commun.* **2002**, 1980.
23 J. Park, J. R. Regalbuto, *J. Colloid Interface Sci.* **1995**, *175*, 239.
24 K. Murase, H. Ando, E. Matsubara, T. Hirato, Y. Awakura, *J. Electrochem. Soc.* **2000**, *147*, 2210.
25 H. Kraus, R. Prins, *J. Catal.* **1996**, *164*, 251.
26 H. Kraus, R. Prins, *J. Catal.* **1997**, *170*, 20.

Chapter 4

Influence of the Preparation Method on the Hydrodesulphurization Activity of MoS_2/Al_2O_3 Catalyst Extrudates: A Raman Micro-spectroscopy Study on the Genesis of the Active Phase

Abstract

Raman micro-spectroscopy has been used to study the preparation of industrial MoS_2/Al_2O_3 extrudates. Using this technique, the influence of the impregnation solution composition on the nature and macro-distribution of Mo(VI)-complexes inside these catalyst bodies was evaluated during the individual preparation steps that comprised impregnation, drying and calcination. It was shown that a poor dispersion of the MoO_x-phase in the calcined samples could be brought about by (i) the formation of bulk $(NH_4)_3[Al(OH)_6Mo_6O_{18}]$ during impregnation or (ii) a redistribution of Mo(VI)-complexes during drying. The formation of crystalline MoO_3 and $Al_2(MoO_4)_3$ in the oxidic precursors led to a poorly dispersed MoS_2-phase in the final catalyst and a significantly lower hydrodesulphurization (HDS) activity. The spatially resolved information that can be obtained and its inherent sensitivity for the detection of crystalline phases make Raman micro-spectroscopy a powerful characterization technique to study the preparation of supported metal oxide catalysts.

Introduction

In chapter 3, it was shown how Raman micro-spectroscopy can be applied to study the impregnation of Mo(VI)-solutions onto Al_2O_3 pellets. A strong interaction between Mo(VI)-complexes and the Al_2O_3 support was found to lead to the formation of a $[Al(OH)_6Mo_6O_{18}]$ precipitate or the occurrence of Mo-concentration gradients inside the impregnated pellets. Pellets of 3 mm diameter were used in this study, which elongates the ageing process and allows one to study the processes that take place after impregnation in great detail. However, in industrial practice, extrudates of smaller size are generally used [1]. In this chapter, the technique is applied to monitor the nature and macro-distribution of the MoO_x-phase in 1.5 mm cylindrical Mo/Al_2O_3 extrudates during the preparation process. In this way, the implications of the processes described above on the nature and activity of the MoS_2 phase in the final catalyst is evaluated. At the same time, the applicability of Raman micro-spectroscopy to study the preparation of smaller size catalyst extrudates is put to the test.

A series of catalysts was prepared using $(NH_4)_6Mo_7O_{24}$ (AHM) as the Mo-precursor salt. The influence of the pH of the impregnation solution and the addition of citric acid as a complexing agent on the Mo-speciation in the extrudates after impregnation, drying and calcination was evaluated. Subsequently, the activity of the different samples in the hydrotreatment of light gas oil (LGO) feed was tested. Finally, the morphology of the MoS_2-phase in the catalysts after reaction was studied by TEM. It was investigated whether a correlation existed between the dispersion of the MoO_x phase in the calcined catalysts, the dispersion of the MoS_2 phase under reaction conditions and the hydrodesulphurization activity of the different catalyst samples.

Experimental

Pore volume impregnation was carried out on 20 g batches of cylindrical γ-Al_2O_3 extrudates with a diameter of 1.5 mm and a length of 10-15 mm. The pore volume of this support was 0.86 ml/g and its BET surface area was 245 m^2/g. A 5% excess of solution was used in all cases to ensure complete wetting of all extrudates. After impregnation, the wet samples were left to age for 1 h in a closed container before drying, which was carried out by passing hot air over the catalyst bodies. Drying was regarded to be complete, when the temperature of the catalyst bed had reached a temperature of 120°C. During ageing and drying, the extrudates were kept in constant motion by rotation of the impregnation vessel. The dried extrudates were heated to 500°C at a heating rate of 5°C/min and calcined at this temperature for 1 h in stagnant air.

Two series of Mo/Al_2O_3 catalysts were prepared using Mo(VI)-solutions with a concentration of 1.3 M and 1.8 M Mo, yielding a theoretical MoO_3 loading in the calcined catalyst of 14.5 wt% and 19.0 wt% respectively. Within each series, impregnation was carried out with three AHM (Acros, p.a.) solutions of different composition. Besides AHM solutions at their natural pH of 6, basic AHM-solutions (pH of 9) were prepared by addition of aqueous 25 wt% NH_4OH solution (Baker, p.a.). A solution containing Mo(VI)-citrate complexes was prepared by addition of citric acid (Merck, p.a.) in a Mo:citrate ratio of 1:1. The effect of ageing was studied in the case of the Mo(VI)-citrate solutions, where the ageing step was omitted in an additional experiment and drying was started immediately after impregnation. The codes for the different catalysts and procedures used for their preparation are summarized in Table 1.

For Raman micro-spectroscopy measurements Mo/Al_2O_3 extrudates were bisected and spectra were recorded on the resulting cross-section, without additional treatment. The roughness of the thus created surface makes that the total intensity of the inelastically scattered light varies when measurements are carried out at different positions on the sample. For presentation purposes, all spectra are therefore scaled to the fluorescence background. A Kaiser RXN spectrometer equipped with a 785 nm diode laser was used in combination with a Hololab 5000 Raman microscope. A 10x objective was used for beam focusing and collection of scattered radiation, resulting in a spot size on the sample of approximately 50 µm. The Raman laser power on the sample was approximately 10 mW. Care was taken that beam damage didn't occur by comparing the spectra thus obtained to spectra obtained with lower Laser power. X-ray fluorescence (XRF) and X-ray diffraction (XRD) analyses were performed on crushed extrudates after calcination. XRD measurements were carried out on a Bruker-AXS D8

Table 1. Preparation parameters of the different samples used in this study. The MoO_3 loading, obtained from XRF-analysis of calcined catalysts is included.

Sample code	[Mo] (M)	[Citrate] (M)	pH	Ageing time (h)	MoO_3-loading (wt%)
1.3AHM-pH 6	1.3	0	6	1	13.5
1.3AHM-pH 9	1.3	0	9	1	14.5
1.3AHM-citrate-l	1.3	1.3	0.5	1	14.5
1.3AHM-citate-s	1.3	1.3	0.5	-	14.6
1.8AHM-pH 6	1.8	0	6	1	18.7
1.8AHM-pH 9	1.8	0	9	1	19.1
1.8AHM-citrate-l	1.8	1.8	0.5	1	19.0
1.8AHM-citrate-s	1.8	1.8	0.5	-	19.1

Advance powder X-ray diffractometer, equipped with automatic divergence slit and a Våntec-1 detector. The radiation used is Cobalt $K\alpha_{1,2}$ (λ = 1.79026 Å, 30kV and 45 mA). To determine the distribution of Mo over the calcined extrudates, a scanning electron microscopy (SEM) study was preformed in combination with energy dispersive analysis of X-rays (EDX). Samples were embedded in Castoglas and polished on SiC paper with 2-propanol. Samples were then carbon-coated and line-scans were recorded across the cross-section of bisected extrudates with a step-size of 10 µm at a 20 kV acceleration voltage.

For the determination of the amount of crystalline material in Mo/Al_2O_3 extrudates, approximately 1 g of calcined extrudates prepared from AHM-pH 6 solutions (14 wt% and 19 wt% MoO_3) and AHM-pH 9 solutions (19 wt% MoO_3) was crushed until a < 63 µm sieve fraction could be prepared of this material. Care was taken that all material was passed through the sieve to obtain a representative sample. 0.40 g of the crushed extrudates was well mixed with 0.01 g of a < 63 µm sieve fraction of BN (Aldrich, p.a.). Likewise, physical mixtures of MoO_3 (Aldrich, p.a.), Al_2O_3 and BN were prepared in which all components were passed through a 63 µm sieve before mixing. Compositions of the different physical mixtures are listed in Tables 2 and 3. Raman spectra were recorded on the resulting physical mixtures using the same Raman set-up that was used for the measurements on bisected extrudates. For each sample at least 25 spectra were recorded at different positions in the sample with a defocused Laser beam (spot size > 300 µm).

To determine the Mo-loading at which the dispersion limit is reached and bulk MoO_3 starts to form on the surface of the particular γ-Al_2O_3 used in this study, a series of Mo/Al_2O_3 samples with different Mo-loading were prepared. To this end, impregnation was carried out on a 150-

Table 2. Composition of crushed Mo/Al_2O_3 extrudates/BN physical mixtures and the intensitiy ratio of the MoO_3 and BN peaks (I_{819}/I_{1365}) in the corresponding Raman spectra (Fig. 8). Values for the amount of crystalline MoO_3 in the different samples, as determined after correlation to calibration line A and B (Fig. 9) are presented in the bottom part.

	AHM-pH 6 14 wt% MoO_3		AHM-pH 6 19 wt% MoO_3		AHM-pH 9 19 wt% MoO_3	
wt catalyst (mg)	397.4		409.9		815.9	
wt BN (mg)	10.6		10.2		10.5	
I_{819}/I_{1365}	1.18		1.31		-	
Calibration line used	A	B	A	B	A	B
wt MoO_3 (mg)	2.7	13.0	2.9	13.9	-	
wt % crystalline MoO_3	0.7	3.3	0.7	3.4	-	

Table 3. Composition of $MoO_3/Al_2O_3/BN$ and $m_{crust}/Al_2O_3/BN$ physical mixtures and the intensities of the intensity ratio of the MoO_3 and BN peaks in the corresponding Raman spectra.

	MoO_3 (Aldrich)			m_{crust}		
Sample nr.	1	2	3	1	2	3
wt m_{crust} (mg)				24.4	10.3	11.4
wt MoO_3 (mg)	22.3	11.1	9.7	10.1	4.3	4.7
wt BN (mg)	10.3	20.3	39.1	4.3	4.9	10.3
MoO_3/BN wt ratio	2.2	0.55	0.25	2.4	0.88	0.46
I_{819}/I_{1365}	9.9	2.6	1.2	2.3	0.9	0.5

500 µm sieve fraction of crushed extrudates, using AHM and equimolar Mo:citrate solutions with a Mo-concentration of 1.2, 1.4, 1.6, 1.8 and 2.0 M. These samples were dried at 120°C and calcined at 500°C for 6 h. Raman spectra were recorded on the calcined samples.

The catalytic activity of the different extrudates was evaluated in the hydrotreatment of a light gas oil fraction. Characteristics of the feedstock can be found in Table 4. Of each catalyst, 5.9 g was loaded into a multitubular set-up in which 10 catalyst samples can be tested simultaneously. Reaction was carried out at a weight hourly space velocity (WHSV) of 1.7 $g_{feed} \cdot g_{cat}^{-1} \cdot h^{-1}$, a H_2/oil ratio of 200 $Nl(H_2)/l_{feed}$ and a total pressure of 60 bar. The sulphur content of the oil was determined after reaction at 345°C, 360°C and 375°C using XRF for samples containing more than 0.06 wt% S and UV-detection for samples containing less than 0.06 wt% S. The relative error in these measurements is below 2%. Sulphidation of the catalysts was carried out

Table 4. Properties of the light gas oil used in the hydrotreatment tests.

		Distillation	(°C)
Sulfur (wt%)	1.2		
Nitrogen (ppmwt)	102	Initial boiling point	178.4
		10 vol%	224.0
Mono aromatics (wt%)	16.5	30 vol%	261.4
Di aromatics (wt%)	11.0	50 vol%	283.8
		70 vol%	309.3
Di + aromatics (wt%)	0.8	90 vol%	347.8
Total aromatics (wt%)	28.3		
		Final boiling point	372.0

at 345°C by addition of dimethyldisulfide (DMDS) to the oil stream. After reaction the catalyst samples were unloaded and stored in oil to prevent reoxidation.

For TEM analysis on the MoS_2/Al_2O_3 extrudates, whole extrudates were rinsed with toluene to remove the oil and vacuum impregnated with the standard mixture Ultra Low Viscosity Kit, hard version (Polaron Instruments Inc.). The mixture was transferred into a polyethylene capsule (BEEM) and mixed with fresh embedding medium. The epoxy embedding medium was hardened at least 48 h under N_2 (0.2 MPa, 338 K). Sections of about 60 nm thickness were prepared using a Leica Reichert Ultracut-S ultramicrotome. Shortly after preparation, the sections were investigated with a JEOL JEM-2010F-HR TEM, with a 200 keV electron beam (Field Emission Gun, FEG). SEM analyses were performed on bisected embedded MoS_2/Al_2O_3 extrudates with a Leo Gemini 1550 SEM (Field Emission Gun), equipped with an Oxford INCA EDX system. EDX analysis was performed at 15 keV. To check for any possible reoxidation, Raman micro-spectroscopy was carried out on these samples as well.

Results and Discussion

Mo/Al_2O_3 powder catalysts

Mo/Al_2O_3 and other supported metal-oxide catalysts are often referred to as monolayer systems, for the tendency of the active phase to spread over the support at elevated temperatures [2]. In this way, an overlayer containing an amorphous MoO_x phase is formed on the support surface and the surface free energy of the system is minimized. Thermodynamics dictate that bulk MoO_3 is only formed, when the Al_2O_3 surface has been completely covered. The Raman spectra of powdered, calcined Mo/Al_2O_3 samples prepared from AHM-pH 6 and AHM-citrate solutions of different concentrations are presented in Fig. 1. In the case of the AHM-pH 6 samples, an amorphous MoO_x phase is detected in samples prepared from 1.2-1.8 M Mo solutions, corresponding to 12-19 wt% MoO_3 in the final catalyst. A broad band at ~ 980 cm^{-1} is observed in the Raman spectra recorded on these samples [3]. The sample prepared from a 2.0 M Mo AHM-pH 6 solution (21 wt% MoO_3) clearly contains bulk MoO_3 as intense bands at 995, 819, 667, 378, 337, 290 and 242 cm^{-1} are present in the spectrum [3]. Apparently saturation coverage is reached at an MoO_3-loading between 19 and 21 wt%, corresponding to a theoretical surface coverage between 4.0 and 4.4 Mo-atoms.nm^{-2}, in good agreement with values reported in literature [3,4]. Note that for the preparation of the Mo/Al_2O_3 extrudates, 1.3 M and 1.8 M Mo solutions are used resulting in an overall MoO_3 loading below the dispersion limit. In other words, the total Al_2O_3 surface present in the extrudates should be sufficient to accommodate all Mo in an amorphous MoO_x phase. In contrast to the AHM–pH 6 samples, no

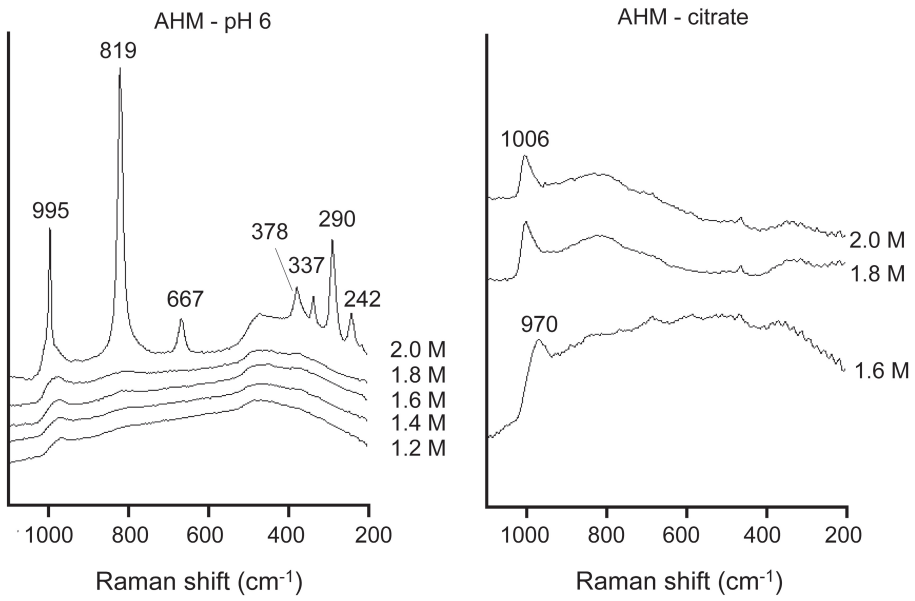

Figure 1. Raman spectra recorded on calcined Mo/Al_2O_3 powder samples prepared from AHM-pH 6 (left) and AHM-citrate (right) solutions of different concentration.

bulk MoO_3 was detected in any of the AHM-citrate samples, even when a 2.0 M Mo solution was used. The formation of an amorphous MoO_x phase was found in the sample prepared from a 1.6 M Mo solution, judging from the position of the ν(Mo=O) band maximum at 970 cm^{-1}. At higher Mo-loadings, a band at 1006 cm^{-1} was observed which is generally assigned to $Al_2(MoO_4)_3$ [5]. The low intensity and broadness of this band, however, suggest that this was not a crystalline phase.

Impregnation of Al_2O_3 extrudates

The speciation of Mo(VI)-complexes in AHM solutions at moderate pH is discussed in chapter 2A, on the basis of a Raman spectroscopy study and literature data [3,6]. At the natural pH of AHM solutions (pH of 5-6) $Mo_7O_{24}^{6-}$ is the predominant species and the corresponding Raman spectrum exhibits bands at 940, 901 and 360 cm^{-1} [3,6]. At higher pH, MoO_4^{2-} is formed, as the reaction in Eq. 1 proceeds to the right. MoO_4^{2-} is the only complex present in the AHM-pH 9 solutions used in this study. Its Raman spectrum shows characteristic peaks at 895, 840 and 320 cm^{-1} [3,6].

$$Mo_7O_{24}^{6-} + 8\ OH^- \leftrightarrow 7\ MoO_4^{2-} + 4\ H_2O \qquad \text{(Eq. 1)}$$

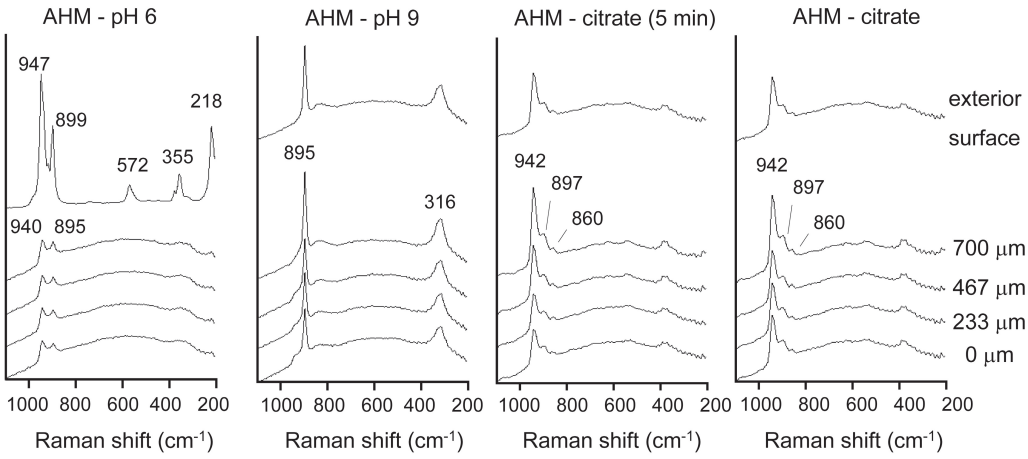

Figure 2. Raman spectra recorded on bisected extrudates, 1 h after impregnation with 1.8 M AHM-pH 6, AHM-pH 9 and AHM-citrate solutions and 5 min after impregnation with a 1.8 M AHM-citrate solution. The distance of the measurement spot from the core of the extrudates is indicated on the right.

Raman spectra recorded on the bisected extrudates, after impregnation with the different 1.8 M Mo AHM solutions, are presented in Fig. 2. After impregnation with the AHM-pH 6 solution, peaks at 895 and 940 cm^{-1} are observed for all positions inside the extrudates, which are superimposed on the fluorescence background, probably caused by impurities in the Al_2O_3 support. These peaks demonstrate the presence of both MoO_4^{2-} and $Mo_7O_{24}^{6-}$ anions inside the Al_2O_3 pores. The formation of MoO_4^{2-} shows that the pH of the solution inside the Al_2O_3 has increased as compared to the impregnation solution. This is caused by the protonation of basic hydroxyl groups on the Al_2O_3 surface. In the spectrum recorded of the outer surface, intense peaks at 947, 899, 572, 355 and 218 cm^{-1} indicate the presence of $Al(OH)_6Mo_6O_{18}^{3-}$ anions [7,8]. The observation of a white precipitate by visual inspection and the absence of a fluorescence background in the Raman spectrum indicate that an $Al(OH)_6Mo_6O_{18}^{3-}$ precipitate is covering the Al_2O_3 on the outside of the extrudates. The observation of bands at 895 and 316 cm^{-1} in spectra recorded throughout the wet extrudates shows that impregnation with the AHM-pH 9 solution leads to a homogeneous distribution of MoO_4^{2-} in the extrudates. This is in line with the phenomena observed after impregnation of Al_2O_3 pellets with AHM-solutions (chapter 3).

A whole range of different Mo(VI)-citrate complexes can be present in AHM-citric acid solutions, as discussed in chapter 2B. Stable complexes are documented in which the Mo:citrate ratio (2:1, 1:1 and 1:2), the number of Mo-atoms (1, 2 and 4) and the protonation state varies with pH and concentration [9,10]. From calculations using formation constants for Mo(VI)-citrate complexes and a Raman spectroscopy study on Mo(VI)-citrate solutions, it was determined that

$Mo_4(citrate)_2O_{11}^{4-}$ is the predominant complex present in the AHM-citrate solutions used in this study [10]. The Raman spectrum of the impregnation solution showed bands at 942, 897 and 860 cm^{-1}. Raman measurements were also carried out directly after impregnation of the Al_2O_3 extrudates with the AHM-citrate solutions. In this way the distribution of Mo(VI)-complexes before the start of the drying process was obtained for all Mo/Al_2O_3 samples described in this study. In all cases, peaks are observed exclusively at 942, 897 and 860 cm^{-1}, indicating that the $Mo_4(citrate)_2O_{11}^{4-}$ complex remains intact inside the Al_2O_3 pores after impregnation. An impression of the distribution of Mo(VI)-complexes inside the extrudates can be obtained by comparing the intensity of the ν(Mo=O) bands in spectra obtained at different positions after scaling to the Al_2O_3 background. However, since these two features are caused by completely different phenomena (Raman scattering vs. fluoresence), no quantitative distribution profiles can be derived. Since ν(Mo=O) bands of considerable intensity are observed in the spectrum recorded near the center of the extrudates, it could be concluded that the distribution of Mo(VI)-complexes, 5 min after impregnation is fairly homogeneous. In chapter 3, the transport of this complex through the Al_2O_3 pore-system was found to be slow and a homogeneous distribution of $Mo_4(citrate)_2O_{11}^{4-}$ was only found 3 h after impregnation of 3 mm Al_2O_3 pellets with a 1.0 M Mo AHM-citrate solution [11]. This was explained to be the result of an electrostatic interaction between the negatively charged Mo(VI)-complexes and the Al_2O_3 surface, which is protonated due to the low pH of the impregnation solution. In this case, however, the concentration of the impregnation solution is higher and the diameter of the extrudates is half of that of the pellets used before. Both changes favor a uniform distribution of Mo(VI)-complexes. Apparently, this results in a more or less homogeneous distribution of the Mo(VI)-citrate complexes within 5 min after impregnation despite the interaction between $Mo_4(citrate)_2O_{11}^{4-}$ and the Al_2O_3 surface.

Drying and calcination of Mo/Al_2O_3 extrudates

The formation of a layer of white powder on the external surface was observed by visual inspection of dried and calcined extrudates prepared from AHM-pH 6 solutions, regardless of the Mo-loading. In approximately 50% of all calcined AHM-pH 6 extrudates, areas of different color were also observed on the inside of these extrudates. Both phenomena are clearly illustrated in the SEM-image in Fig. 3, in which cross-sections of calcined extrudates, prepared from different 1.8 M Mo solutions are shown. A crust of white material and a ring of lighter color is observed in the AHM-pH 6 sample, while the other extrudates appear much more homogeneous. The corresponding EDX-linescans are also included in this figure. It can be seen that at the external surface and at the divergent spots on the inside of the AHM-pH 6 extrudate, the Mo-loading is much higher than in the rest of the sample. Raman spectra were recorded

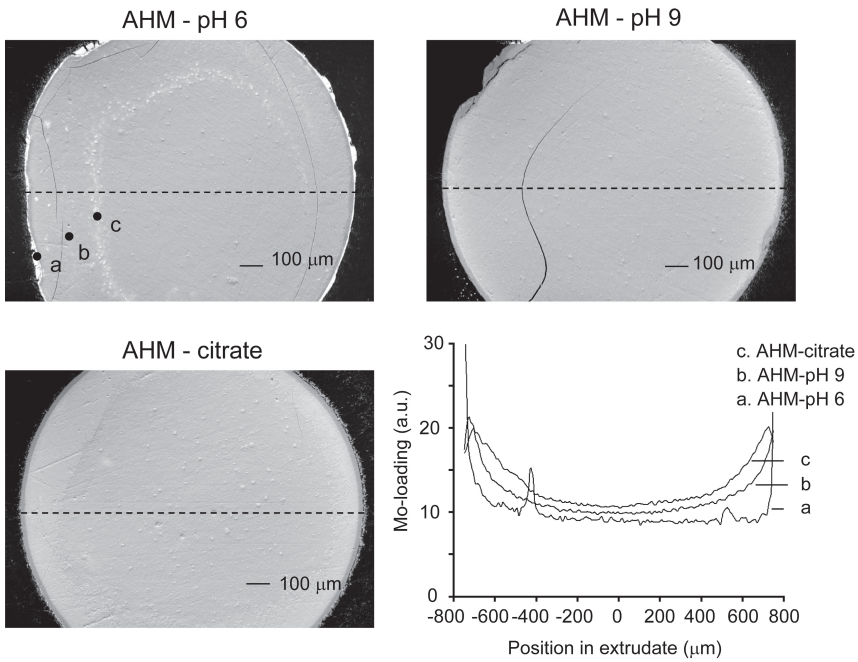

Figure 3. SEM-images of bisected 19 wt% Mo/Al_2O_3 extrudates, prepared from AHM-pH 6, AHM-pH 9 and AHM-citrate solutions after calcination. The corresponding Mo-concentration profiles, derived from EDX measurements are also shown.

on similar positions in both dried and calcined catalyst bodies (labeled as a, b and c in the SEM image) which are presented in Fig. 4. The crust on the outside of the dried catalyst bodies (a) was found to consist of $(NH_4)_3[Al(OH)_6Mo_6O_{18}]$, as indicated by the intense bands at 947, 899, 563 and 355 cm^{-1} [7,12]. This material was also present in areas with high Mo-concentration on the inside of the extrudates (c), while $Mo_7O_{24}^{6-}$ complexes are mainly present in the bulk of the sample (b), as indicated by the position of the main ν(Mo=O) band at 940 cm^{-1} [3].

The $(NH_4)_3[Al(OH)_6Mo_6O_{18}]$ phase that was formed during impregnation is clearly retained after drying. Its formation is due to the so-called ligand-promoted dissolution of the Al_2O_3 support [8]. It is the result of the complexation of Al(III)-ions by oxomolybdate complexes under acidic conditions, as described in Eq. 2.

$$12\ Mo_7O_{24}^{6-} + 7\ Al_2O_3 + 27\ H_2O + 30\ H^+ \rightarrow 14\ Al(OH)_6Mo_6O_{18}^{3-} \qquad \text{(Eq. 2)}$$

The high Mo-concentration present near the exterior surface of the extrudates after impregnation, allows for a chain reaction to occur. Al(III) ions are generated by dissolution of the support at low pH and consumed in the formation of $Al(OH)_6Mo_6O_{18}^{3-}$. The low solubility of this compound leads to the precipitation of $(NH_4)_3[Al(OH)_6Mo_6O_{18}]$. The Al(III)-concentration in

solution is thus kept low, more and more Al_2O_3 is dissolved if sufficient acid is available and a layer of $(NH_4)_3[Al(OH)_6Mo_6O_{18}]$ is formed [8]. Inside the pores of the Al_2O_3, towards the inside of the extrudates, the pH of the solution increases due to the buffering action of the support and MoO_4^{2-} is being formed instead of $Al(OH)_6Mo_6O_{18}^{3-}$ complexes. Apparently, in certain domains inside the extrudates, circumstances after impregnation are similar to those found at the exterior of the extrudates and the formation of the $Al(OH)_6Mo_6O_{18}^{3-}$ phase is observed. These domains could consist of cracks in the extrudates or areas of low density Al_2O_3 that are created during the extrusion process. At these positions, the amount of $Mo_7O_{24}^{6-}$ anions per unit Al_2O_3 surface area is high and the buffering effect of the support is not sufficient to prevent the formation of bulk $(NH_4)_3[Al(OH)_6Mo_6O_{18}]$.

$Mo_7O_{24}^{6-}$ was observed to be the stable complex in the bulk of the dried extrudates. In general, the nature of Mo(VI)-complexes present in dried Mo/Al_2O_3 catalysts under ambient conditions is reported to be a function of the Mo-loading and the nature of the support [13]. On the hydrated Al_2O_3 surface, the same Mo(VI)-complexes can be formed as in solution. Just like the pH determines the speciation of Mo(VI)-complexes in a solution, the point of zero charge

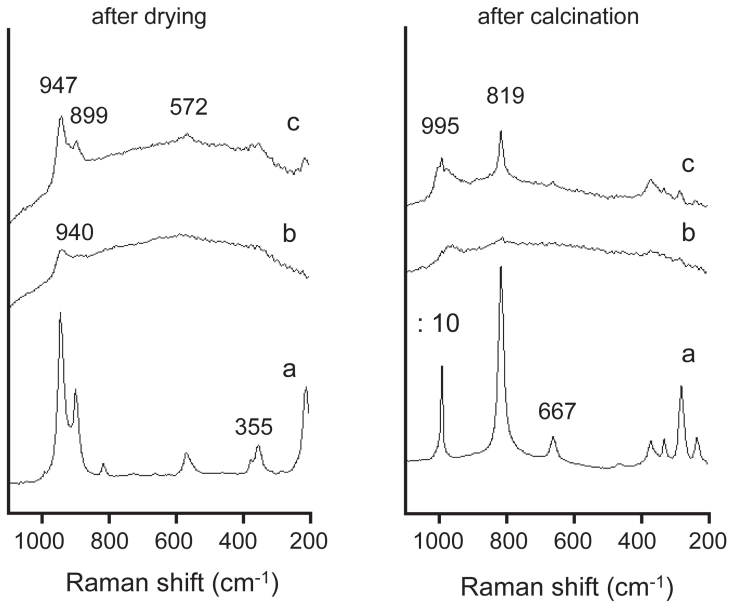

Figure 4. Raman spectra recorded at different positions on bisected 19 wt% MoO_3/Al_2O_3 extrudates prepared from an AHM-pH 6 solution after drying (left) and calcination (right). Spectra are recorded on (a) external surface (b) internal bulk of the extrudates (c) inhomogeneities in the extrudates. Measurement positions are similar to the points labeled as a-c indicated in the SEM-image in Fig. 3.

(PZC) of the hydrated surface layer determines which Mo(VI)-complexes are present. The value of the PZC of the total surface is a result of the individual PZC-values of bulk Al_2O_3 (~ 9) and the AHM (~ 6) that is deposited on the surface [14]. Hence the PZC of a Mo/Al_2O_3 system decreases with increasing Mo-loading. Consequently, at the high Mo-loadings used in this study, the PZC of the system will be close to 6 and $Mo_7O_{24}^{6-}$ entities are predominantly present in the bulk of the dried material. Furthermore drying results in a concentration of Mo(VI)-complexes on the surface, which also favors the formation of $Mo_7O_{24}^{6-}$.

As can be seen in Table 1, XRF measurements showed that the total MoO_3-loading in the calcined catalysts was largely unaffected by the preparation method. After calcination, sharp peaks at 995, 819, 667, 378, 337, 290 and 242 cm^{-1} are observed in the Raman spectra recorded on calcined AHM-pH 6 samples for positions that showed the presence of $(NH_4)_3[Al(OH)_6Mo_6O_{18}]$ after drying. Upon calcination, the $(NH_4)_3[Al(OH)_6Mo_6O_{18}]$ agglomerates are converted into bulk MoO_3 in accordance with literature [12]. The formation of bulk MoO_3 is also observed in the XRD pattern recorded on crushed 19 wt% MoO_3 AHM-pH 6 extrudates, which is shown in Fig. 5. In this pattern all main diffraction lines of orthorhombic MoO_3 (2θ = 14.9° (6.99 Å), 27.2° (3.80 Å), 30.0° (3.45 Å), 31.8° (3.27 Å), 39.4° (2.65 Å), 58.0° (1.85 Å), and 62.2° (1.73 Å)) are observed besides the broad peaks originating from the γ-Al_2O_3 support [15]. In other areas, an amorphous MoO_x phase is detected and a broad ν(Mo=O) band is observed in the Raman spectra. As was discussed before, at elevated temperature, bulk MoO_3 can be expected to spread over the Al_2O_3 support to form an amorphous MoO_x overlayer. Although the total Al_2O_3

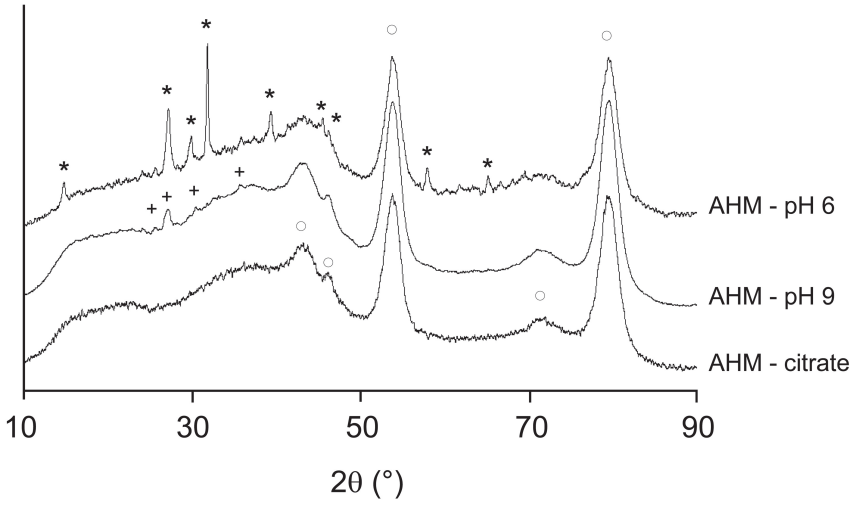

Figure 5. XRD patterns recorded on crushed 19 wt% MoO_3/Al_2O_3 extrudates after calcination, prepared from different AHM solutions. Reflections corresponding to the presence of crystalline γ-Al_2O_3 (o) (ICDD 48-0367), MoO_3 (*) (ICDD 5-508) and $Al_2(MoO_4)_3$ (+) (ICDD 23-764) are indicated.

surface area in the extrudates is sufficient to accommodate all Mo present in the system in an amorphous overlayer, the creation of areas with a high Mo-concentration has lead to the formation of bulk MoO_3. Apparently, in mm-scale catalyst bodies, transport distances are too large for a complete spreading of the MoO_3 over the support during calcination for 1 h, a calcination period typical for the industrial preparation of (Ni/Co)Mo/Al_2O_3 catalysts.

Upon visual inspection, the calcined extrudates, prepared from AHM-pH 9 solutions appear rather homogeneous. This can also be seen in the SEM-image in Fig. 3. Nevertheless, an egg-shell distribution of Mo is observed in the corresponding EDX-linescan. The Raman spectra recorded on these dried extrudates, presented in Fig. 6 (left), indicate that $Mo_7O_{24}^{6-}$ complexes are present throughout the extrudates, judging from the maximum in the spectra at 940 cm^{-1} for all positions inside the sample. Drying of the extrudates leads to evaporation of excess ammonia from the solution and a decrease in the pH of the solution inside the pores of the Al_2O_3. As a consequence, after drying, the composition on the interior of the extrudates is similar to the AHM-pH 6 sample, and $Mo_7O_{24}^{6-}$ is formed, as was already discussed above. The egg-shell distribution of Mo that was observed in the EDX-linescan can also be inferred from the Raman measurements, as the intensity of the ν(Mo=O) bands increases towards the outside of the extrudates, after scaling to the Al_2O_3 fluorescence background. After calcination,

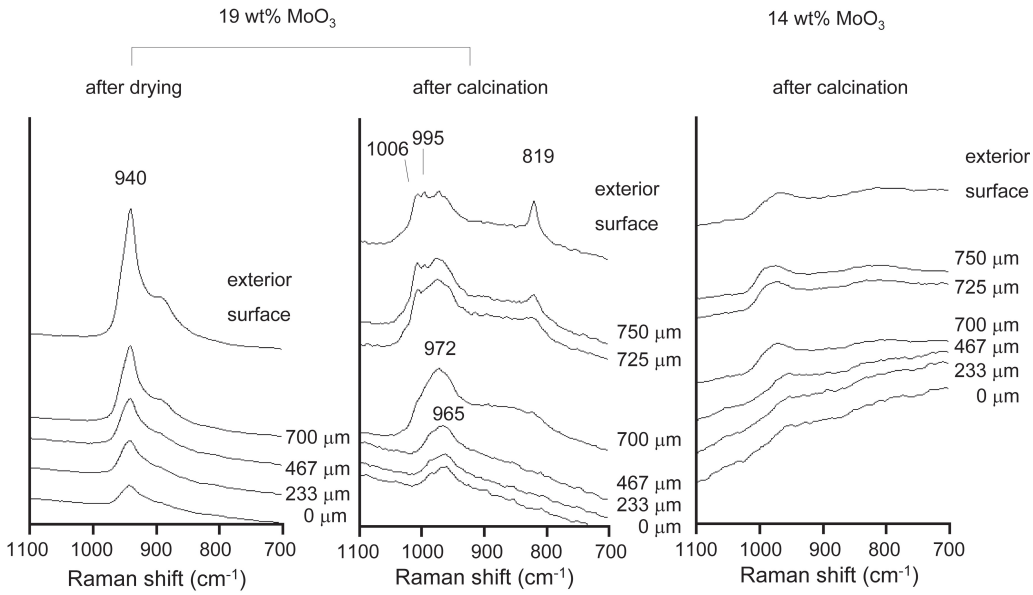

Figure 6. Raman spectra recorded on bisected extrudates after drying (left) and calcination (right) of extrudates impregnated with 1.8 M and 1.3 M AHM-pH 9 solutions. The distance of the measurement spot from the core of the extrudates is indicated to the right of the spectra.

an amorphous MoO_x phase is present throughout the 14 wt% MoO_3 extrudates prepared from the AHM-pH 9 solution (Fig. 6, right). A broad band is observed at 960-980 cm^{-1} for all positions. The same phase is present near the core of the extrudates with the 19 wt% MoO_3 loading. However, in this sample crystalline phases are detected near the outer surface of the extrudates (Fig. 6, middle). A sharp peak at 1006 cm^{-1} reveals the presence of bulk $Al_2(MoO_4)_3$ in the outer 50 µm of the sample and bulk MoO_3 (995 and 819 cm^{-1}) is found to be present at the exterior surface. The presence of crystalline $Al_2(MoO_4)_3$ is also detected in an XRD pattern recorded on the corresponding crushed extrudates (Fig. 5), as small peaks are present at 2θ values of 25.8° (4.01 Å), 27.3° (3.78 Å), 30.4° (3.41 Å) and 35.8° (2.91 Å).

After impregnation with the AHM-pH 9 solution, the interaction between MoO_4^{2-} anions and the Al_2O_3 surface can be expected to be relatively weak. As the pH of the impregnation solution is similar to the PZC of the support material, the Al_2O_3 surface will be neutrally charged and the Coulomb interaction with the MoO_4^{2-} anions is negligible. It is well-known that the drying procedure can drastically influence the distribution of metal ion-complexes in supported catalyst bodies, especially when a poor interaction exists between the metal ion precursor complexes and the support oxide after impregnation [16,17]. In the AHM-pH 9 extrudates, an egg-shell distribution of Mo(VI)-complexes was indeed found after drying. This particular distribution is often observed when catalyst bodies are dried at low drying rates. In this case, evaporation of water takes place at the periphery of the extrudates and liquid is drawn from the center of the bodies towards the external surface. This transport can proceed via connected liquid elements, but also through a film of liquid covering the walls of emptied pores. Dissolved metal ion precursor complexes travel with this flow of the liquid and when precipitation takes place, the liquid phase is primarily located in the outer layer of the catalyst bodies. When drying is complete, an egg-shell distribution of the metal ion-salts remains [18]. A regime of slow drying can be expected to be operative when (relatively) large batches of impregnated support bodies are dried, as is the case in this study.

In the case of the 19 wt% MoO_3 samples, due to the egg-shell distribution, the Mo-loading near the external surface of the extrudates exceeds the value required for the dispersion limit coverage. Hence, the formation of crystalline Mo-phases is observed after calcination. At low loadings (14 wt% MoO_3), an egg-shell distribution of Mo is expected to be present as well. However, in this case, the macro-distribution of Mo is less crucial, since a slight egg-shell distribution doesn't necessarily lead to MoO_3 loadings exceeding the dispersion limit coverage near the outside of the extrudates. An amorphous MoO_x phase is formed throughout the extrudates.

The Raman spectra recorded on the 19 wt% MoO_3 AHM-citrate samples after drying and calcination are presented in Fig. 7. For the dried sample, the peak positions of the main ν(Mo=O) bands are similar to those in the spectra recorded on the wet material. The $Mo_4(citrate)_2O_{11}^{4-}$ complex is preserved on the Al_2O_3 surface after drying. A slight Mo-concentration gradient is present, judging from the increase in intensity of the ν(Mo=O) bands, relative to the Al_2O_3 fluorescence background towards the outside of the extrudates. The Mo-profile obtained from the EDX-linescan (Fig. 3) supports this observation. The gradient is less pronounced as compared to samples prepared from the AHM-pH 9 solution, since the interaction between the $Mo_4(citrate)_2O_{11}^{4-}$ complexes and the Al_2O_3 surface after impregnation is stronger. There was no difference in the spectra of the AHM-citrate-l and AHM-citrate-s samples, as both samples already exhibited a similar distribution of $Mo_4(citrate)_2O_{11}^{4-}$ before the drying process. After calcination, merely amorphous MoO_x-phases are present in the catalysts, regardless of the MoO_3-loading. Relatively broad bands are observed in the Raman spectra and only reflections due to the γ-Al_2O_3 support are present in the XRD-pattern recorded on the crushed extrudates (Fig. 5) [15]. The position of the Raman band shifts to higher frequency as the Mo-loading increases towards the outside of the pellet. Near the external surface in the 19 wt% MoO_3 sample, the maximum of the band is found at 1006 cm^{-1}. The position of this band corresponds to the formation of an $Al_2(MoO_4)_3$ phase [5], while the broadness of the band suggests the presence of an amorphous phase. Due to the egg-shell distribution, the local Mo-concentration

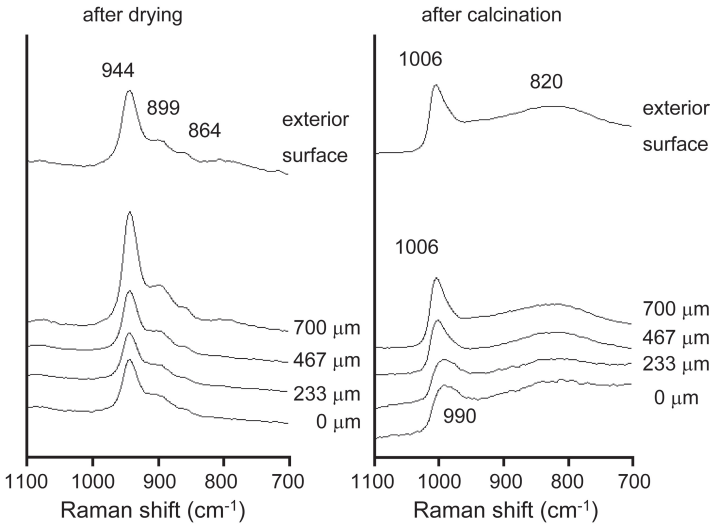

Figure 7. Raman spectra recorded on bisected 19 wt% MoO_3/Al_2O_3 extrudates prepared from an AHM-citrate solution after drying (left) and calcination (right). The distance of the measurement spot from the core of the extrudates is indicated to the right of the spectra.

near the external surface will exceed the value corresponding to the dispersion limit coverage derived from the measurements on AHM impregnated powdered Al_2O_3. Nevertheless, as in the case of the powdered samples prepared from AHM-citrate solutions, no crystalline phases are observed. Apparently, more Mo can be accommodated in an amorphous $Al_2(MoO_4)_3$ phase on the Al_2O_3 surface, when the preparation is started from AHM-citrate solutions.

Determination of the amount of crystalline MoO_3 in Mo/Al_2O_3 extrudates

An attempt was made to quantitatively determine the amount of crystalline MoO_3 that is formed on the external surface of Mo/Al_2O_3 extrudates, prepared from AHM-pH 6 solutions. Quantification was carried out by Raman spectroscopy of crushed extrudates and MoO_3/Al_2O_3 physical mixtures to which BN was added as an internal standard. The accumulated spectra of the crushed extrudates/BN physical mixtures are presented in Fig. 8. The composition of these physical mixtures is given in Table 2.

The intensities of the most intense MoO_3 band at 819 cm^{-1} and the 1365 cm^{-1} BN band were determined by integration of the peaks after baseline correction. The thus obtained intensity ratios (I_{819}/I_{1365}) are also listed in Table 2. For comparison, physical mixtures of commercial MoO_3, Al_2O_3 and BN were prepared in which the Al_2O_3/BN weight ratio was approximately 50 and the MoO_3/BN weight ratio was varied between 0.25 and 2. Raman spectra were recorded on these physical mixtures as well. The composition of these mixtures and the ratio of the

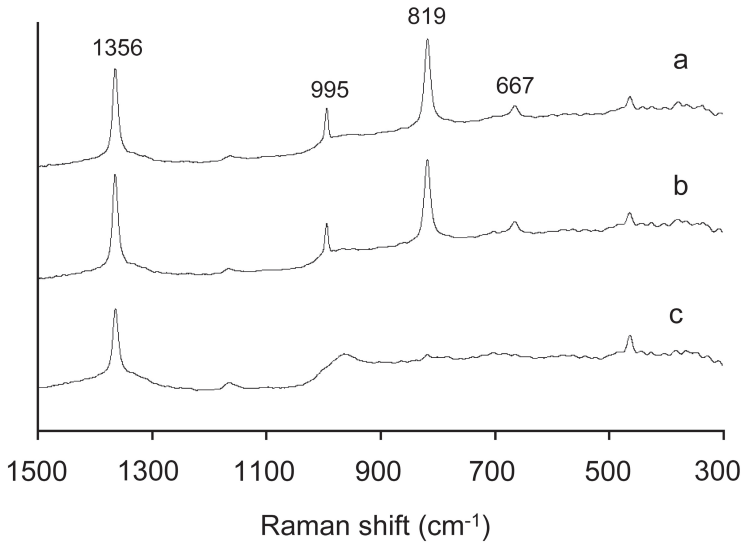

Figure 8. Raman spectra recorded on physical mixtures of crushed Mo/Al_2O_3 extrudates and BN. Spectra are presented of mixtures prepared from (a) 19 wt% MoO_3 AHM-pH 6, (b) 14 wt% MoO_3 AHM-pH 6, and (c) 19 wt% MoO_3 AHM-pH 9 samples.

integrated peak intensities (I_{819}/I_{1365}) in the corresponding Raman spectra can be found in Table 3. A calibration line was constructed by plotting the intensity ratio of the 819 and 1365 cm^{-1} peaks against the MoO_3/BN weight ratio. This plot is depicted as line A in Fig. 9. A linear correlation is observed, validating the procedure used for Raman measurements on physical mixtures and the method used for data analysis. The dotted horizontal lines in Fig. 9 represent the I_{819}/I_{1365} intensity ratio in the spectra recorded on physical mixtures prepared from crushed extrudates, prepared from 1.3 M AHM-pH 6 and 1.8 M AHM-pH 6 solutions. Using line A, the amount of crystalline MoO_3 in these extrudates is determined to be 0.69 wt% for the 14 wt% MoO_3 extrudates and 0.71 wt% for the 19 wt% MoO_3 extrudates.

Part of the MoO_3-containing crust that is formed on the 19 wt% MoO_3 catalyst extrudates prepared from AHM-pH 6 solutions was removed by shaking these extrudates in a glass container. Apart from the obvious abrasion, the general structure of the extrudates remained intact during this procedure. Hence, the thus obtained material originated from the external surface of the extrudates and will further be referred to as m_{crust}. The total amount of MoO_3 in m_{crust} was determined by dissolving the material, in an NaOH-solution. Under these conditions all Mo-containing material is dissolved and MoO_4^{2-} is formed in solution. The concentration of MoO_4^{2-} anions was determined by Raman spectroscopy on the resulting solution. The m_{crust} material was found to contain 41 wt% MoO_3.

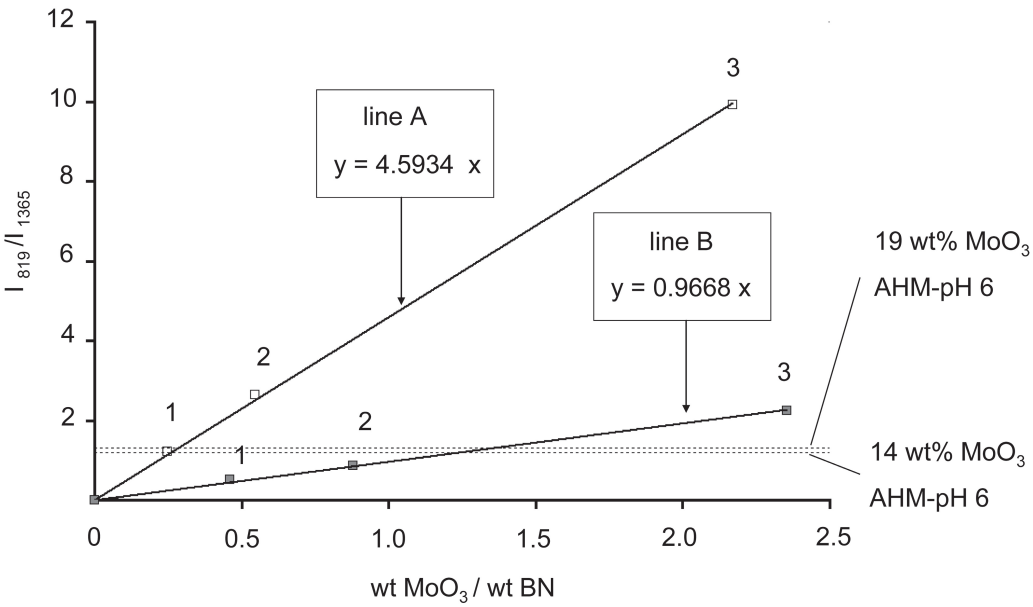

Figure 9. Plot showing the correlation between MoO_3/BN weight ratio in MoO_3/Al_2O_3/BN (line A) and m_{crust}/Al_2O_3/BN (line B) physical mixtures and the intensity of the bands at 819 and 1365 cm^{-1} in the corresponding Raman spectra.

Physical mixtures were prepared using m_{crust} instead of the commercial MoO_3. The compositions of these mixtures are also listed in Table 3. Taking into account the MoO_3-content in m_{crust}, a second calibration line was constructed by plotting the I_{819}/I_{1365} ratio of the Raman spectra recorded on the $m_{crust}/Al_2O_3/BN$ mixtures against the MoO_3/BN weight ratios in these mixtures. This calibration line is depicted as line B in Fig. 9. In the construction of line B, it is assumed that all MoO_3 in m_{crust} is present in the form of crystalline MoO_3, the remaining 59 wt% of the m_{crust} material consisting of Al_2O_3. During calcination, the $(NH_4)_3[Al(OH)_6Mo_6O_{18}]$ crust present after drying is probably converted into MoO_3 and Al_2O_3. The crust can therefore contain some Al_2O_3 originating from the $(NH_4)_3[Al(OH)_6Mo_6O_{18}]$ precipitate. However, regarding the low Al:Mo ratio in this compound, the Al_2O_3 formed in this way can only account for 2.4 % of the total weight of m_{crust}. Apparently, during the abrasion procedure also a part of the body of the extrudates is removed. This consists of high surface area Al_2O_3 with both amorphous and crystalline MoO_3. It can be assumed that the surface of this high surface area Al_2O_3 is completely covered with amorphous MoO_x phases. Using the value for MoO_x monolayer coverage, derived before (20 wt% MoO_3) it can be estimated that the maximum amount of amorphous MoO_3 in the m_{crust} material accounts for 14 % of the total weight of $m_{crust.}$ This implies that a maximum of 34% of all MoO_3 in the m_{crust} material could be amorphous. Hence, although the presence of (an unknown percentage of) amorphous MoO_3 in m_{crust} introduces a large error, it can not account for the huge difference in slope between line A and B. It can be inferred that the commercial MoO_3 displayed a larger Raman cross-section than the MoO_3 formed on the outside of the Mo/Al_2O_3. Changes in the Raman cross-section could be the result differences in crystal size of the MoO_3 phase. The crystalline MoO_3 in m_{crust} is likely to have a similar cross section as the crystalline MoO_3 formed in the Mo/Al_2O_3 extrudates. Line B is therefore used for the determination of the crystalline MoO_3 content in Mo/Al_2O_3 samples.

As presented in the bottom part of Table 2, the amount of crystalline MoO_3 in Mo/Al_2O_3 extrudates prepared from AHM-pH 6 solutions is determined to be 3.3 wt% for the 14 wt% MoO_3 sample and 3.4 wt% for the 19 wt% MoO_3 sample, after correlation to line B in Fig. 9. A considerable error (+/- 1 wt% MoO_3) exists in these values, since, as discussed above, the amount of crystalline MoO_3 in m_{crust} could not be exactly determined. Furthermore, the MoO_3 crystals formed on the inside of the Mo/Al_2O_3 extrudates could well have a different crystal size, and hence a different Raman cross-section than those formed on the external surface of the extrudates. This would mean that the crystalline MoO_3 phase in m_{crust}, which originates primarily from the external surface of the extrudates, is not entirely representative of all MoO_3 crystals that are formed in the Mo/Al_2O_3 extrudates.

An attempt was made to quantify the amount of crystalline MoO_3 in the 19 wt% MoO_3 AHM-pH 9 sample, as well. To this end, a physical mixture of 0.82 g of these crushed extrudates and 0.01 g BN was prepared (Table 2). The corresponding Raman spectrum (c) is included in Figure 8. Although $Al_2(MoO_4)_3$ and MoO_3 phases were observed in the Raman spectra recorded at certain positions in these extrudates, no crystalline phases are observed when a spectrum is recorded on crushed extrudates. Using this procedure, a quantitative determination of any crystalline material is therefore impossible for this sample. All bulk phases in this sample are formed on the interior of the Al_2O_3 extrudates, inside the Al_2O_3 pores. This confinement probably leads to the growth of small crystals and the Raman cross-section of this material is probably small.

Characterization of MoS_2/Al_2O_3 extrudates

Raman spectra recorded on the embedded MoS_2/Al_2O_3 extrudates after reaction merely showed bands at 226, 384 and 406 cm^{-1}, corresponding to the presence of MoS_2 for all positions in all samples under investigation [19]. The absence of any ν(Mo=O) bands in the 900-1000 cm^{-1} region indicates that sulphidation was complete and re-oxidation of the sample had not occurred to any significant extent during handling of the sulphidic catalysts. The Mo-distributions obtained from SEM-EDX measurements on the MoS_2/Al_2O_3 extrudates were similar to the profiles recorded on the corresponding oxidic samples. In other words, sulphidation and reaction conditions had no noticeable influence on the macroscopic distribution of Mo in the extrudates.

TEM images recorded on different MoS_2/Al_2O_3 extrudate-slices obtained from 19 wt% MoO_3/Al_2O_3 samples after reaction are shown in Fig. 10. The most striking differences between the three samples were found near the outside of the extrudates, as can be seen by comparing images a, b and c. For the AHM-pH 6 sample, a ~2 μm thick layer of dense material is observed on the external surface of the catalyst extrudates. From the high magnification micrograph recorded on this layer (image d), it is clear that these particles contain MoS_2, as slabs are clearly observed. In the AHM-pH 9 sample, areas of higher density of typically 200 nm are observed in a ring of 50 μm thickness on the outside of the extrudates. These areas are indicated by the arrows in image b. Images at higher magnification (image e) show that they consist of agglomerates of MoS_2 slabs. For the AHM-citrate sample, none of these features were observed and the sample appeared homogeneous at low magnification. Well-distributed MoS_2 slabs were observed at higher magnification, as is illustrated in image f. Only a few double slabs and no multi-stacked slabs were found, which indicates that the MoS_2 phase is in close contact with the support. Near the core of the extrudates, all samples showed a well-dispersed MoS_2-

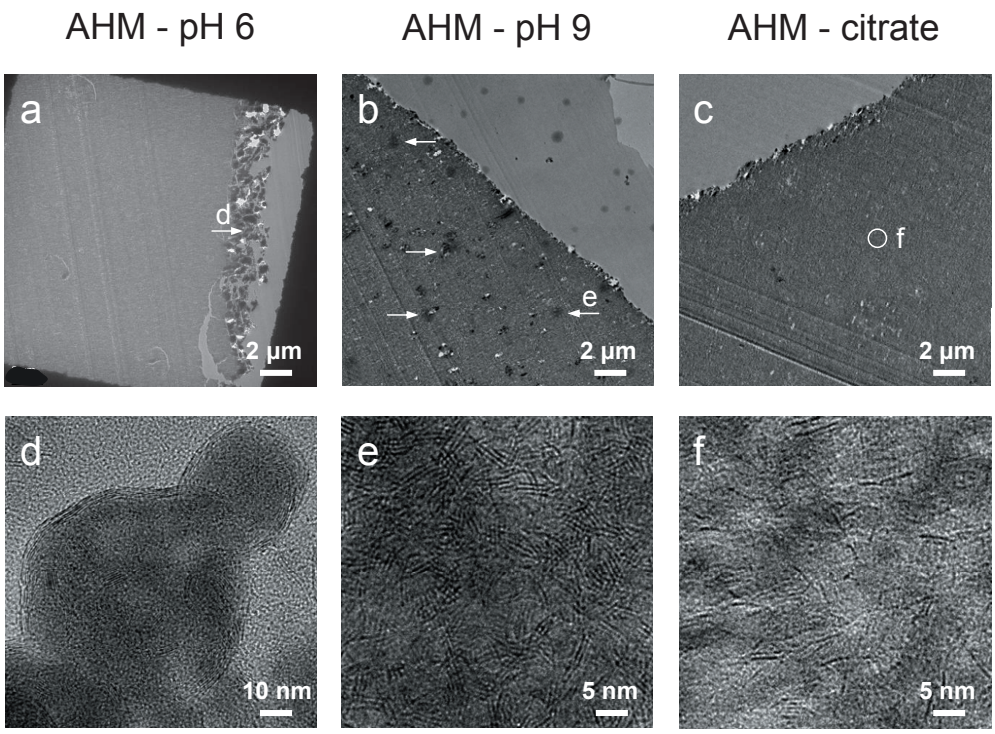

Figure 10. TEM images recorded on embedded MoS_2/Al_2O_3 extrudate slices, prepared from different 19 wt% MoO_3 samples. Low-magnification images (a-c) were recorded near the external surface of the extrudates. The positions where the high-magnification images (d-f) were recorded are indicated in images a-c.

phase, although the density was found to be lower due to the lower Mo-concentration at these positions.

Activity of MoS_2/Al_2O_3 extrudates in LGO hydrotreatment

The hydrodesulphurization activities of the different MoS_2/Al_2O_3 extrudate samples were obtained from the conversion of sulphur-containing compounds. Values for the HDS weight activities (k_{WHSV}) for the different catalysts at different reaction temperatures are presented in the Arrhenius-plot in Fig. 11. The relative HDS-activities of the different samples at 360°C, derived from the lines, are presented in Fig. 12. The HDS-conversion is between 0.7 for the least active catalyst at 345°C and 0.975 for the most active catalyst at 375°C. Reaction rate coefficients (k_{WHSV}) were determined from the weight hourly space velocity (WHSV) and the total concentration of S-containing compounds in the feed before (C_{feed}) and after reaction ($C_{product}$) assuming a first order reaction, using equation (3). Based on the relative error in the determination of the sulphur-content (< 2%), the relative error in the reaction rate constants is found to be less than 1%. The LGO-feed contained a large number of different S-containing

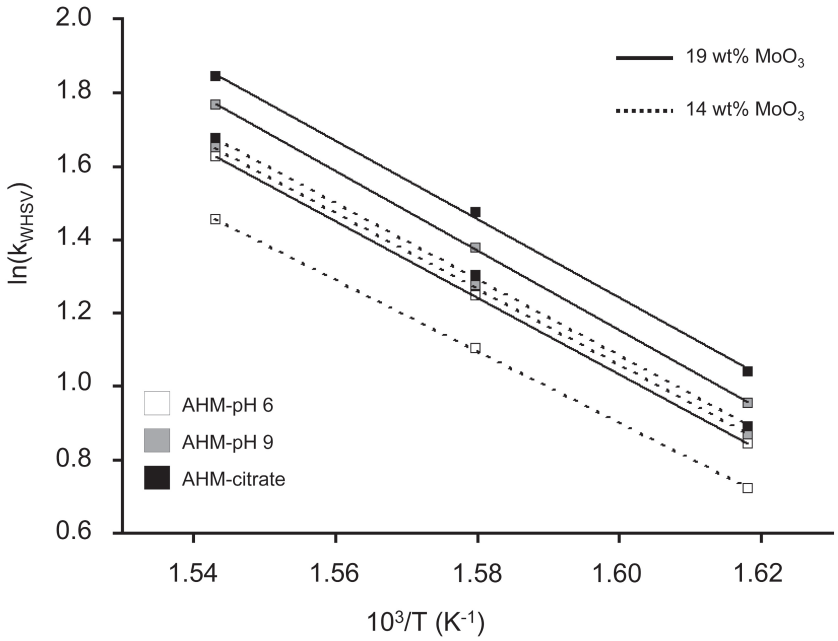

Figure 11. Arrhenius plot (ln k_{WHSV}/T^{-1}) of the HDS reaction constants for the different catalysts.

compounds ranging from reactive thiophene derivates to substituted dibenzothiophenes, that are notoriously difficult to decompose [20]. Hence, the constitution of the library of S-containing compounds and their average reactivity can change with conversion. However, the total S-concentration is inevitably used for the determination of the HDS-activity. Theoretically, this results in a decreasing apparent rate constant with increasing conversion and a decrease in the observed reaction order from 2 to 1 [21]. Indeed in literature, an HDS reaction order between 1 and 2 is found when hydrotreatment is carried out on industrial feeds using (Ni/Co)Mo/Al_2O_3 catalysts [22-24]. For these specific catalysts, feed and conversion range used in this study, a reaction order of 1 was found to give the best correlation between ln(k_{WHSV}) and T^{-1}. A similar slope is found in the Arrhenius plots for the different catalysts. Apparently, the activity differences of the catalysts is merely dictated by the number of active sites. The average activation energy derived from the slopes of the lines in the Arrhenius plot was 87 kJ·mol^{-1}.

$$k_{WHSV} = WHSV \cdot ln((c_{feed})/(c_{feed}-c_{product})) \quad \text{(Eq. 3)}$$

Samples prepared from AHM-citrate solutions show the highest activity in all cases. The absence of any crystalline oxidic material after calcination and the presence of a well-dispersed

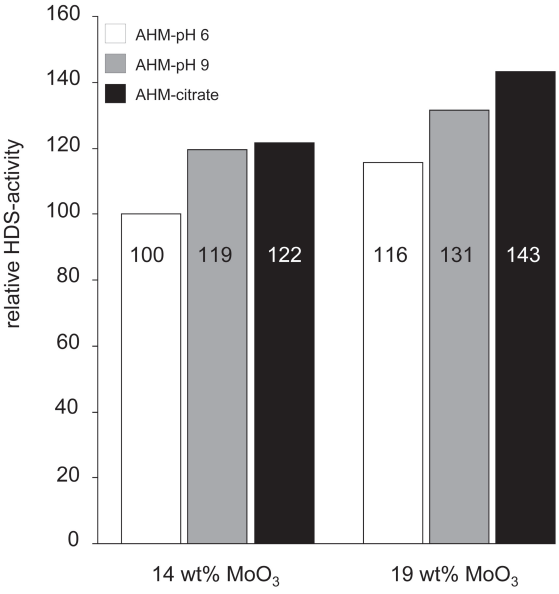

Figure 12. Bar diagram showing the normalized HDS activities of the different catalysts, derived from the reaction rate constants (k_{WHSV}) at 360°C.

MoS_2 phase throughout the extrudates explain the superior performance of these catalysts. However, the activity is not completely proportional to the MoO_3 loading. Apparently, the higher MoO_3 loading causes a slightly lower dispersion of the MoS_2 phase. The low activity of the AHM-pH 6 samples can be explained by the formation of considerable amounts of bulk MoO_3 in specific areas of the extrudates, as was observed by Raman micro-spectroscopy and XRD measurements. From TEM images, it is clear that upon sulphidation, this bulk MoO_3 is transformed into large MoS_2 clusters, which can be expected to be mainly inactive in catalysis. The amount of crystalline MoO_3 that is formed in the AHM-pH 6 samples (3 wt% ±1), can be estimated to be 21% for the 14 wt% MoO_3 sample and 15% for the 19 wt% MoO_3 sample. The AHM-pH 6 samples are 19% less active than the AHM-citrate samples of the same Mo-loading. Therefore, we conclude that a semi-quantitative correlation exists between the percentage of dispersed MoO_3 and the HDS-activity of the resulting MoS_2-phase.

At the low Mo-loading, the catalyst prepared from an AHM-pH 9, shows an HDS activity comparable to the AHM-citrate sample. No crystalline phases were observed in the oxidic precursor for this sample. At the high Mo-loading, however, the activity of the AHM-pH 9 sample is noticeably (9 %) lower than that of the AHM-citrate catalyst. In this case, the formation of bulk MoO_3 and $Al_2(MoO_4)_3$ was observed in the outer shell of the oxidic extrudates and MoS_2 clusters were visible in the TEM images recorded on the sulphidic material. Apparently, the poor dispersion of the MoS_2 phase renders these clusters inactive in the HDS-reaction.

Raman micro-spectroscopy in the preparation of supported catalyst bodies

In chapter 3 and in this chapter, it is shown that the speciation of Mo(VI)-complexes in Mo/Al_2O_3 extrudates can be monitored using Raman micro-spectroscopy at all stages of the catalyst genesis. Especially in impregnated and dried samples, the sharp peaks due to the presence of individual hydrated Mo(VI)-complexes provide detailed information on the nature of the Mo-phase on the Al_2O_3 surface. The physico-chemical processes that take place during the impregnation and drying step can thus be monitored in great detail. Transport rates of different Mo(VI)-complexes through the Al_2O_3 pore system and their reaction with the Al_2O_3 surface can be envisaged. After calcination, the amorphous nature of the supported MoO_x phase makes that broad bands are generally present in the corresponding Raman spectra. On the contrary, the presence of bulk material is detected with great ease, as the formation of these phases yields intense and sharp peaks. This inherent sensitivity is clearly illustrated by the Raman spectra recorded on calcined 19 wt% MoO_3 AHM-pH 9 extrudates (Fig. 6) as compared to the XRD-pattern recorded on the same sample (Fig. 5). Especially when the respective accumulation times for the Raman (2 min) and XRD (14 h) measurements are taken into account, the difference in sensitivity between both techniques is striking. The method is found to be largely insensitive in the characterization of the active phase in MoS_2/Al_2O_3 catalysts. Although TEM images showed different morphology of the MoS_2-phase in different catalyst samples, identical Raman spectra were obtained. However, Raman micro-spectroscopy has recently been applied for the determination of coke profiles in spent MoS_2/Al_2O_3 catalysts [25].

A number of studies, reported in the open literature, have been dedicated to the preparation of Mo/Al_2O_3 catalyst bodies [26-33]. Usually, in fundamental studies into the interaction between Mo-anions and an Al_2O_3 support during catalyst preparation, characterization has been carried out on powder supports, or on crushed extrudates [4,7,8,12,34-37]. In this way, discrimination between processes occurring on the outer surface or in the pore system of particles is impossible. Adsorption and reaction of Mo(VI)-complexes with the support are almost instantaneous, when impregnation is carried out on a powder support. During impregnation of support bodies, long diffusion path lengths act as a slow motion on the system and the time and place dependency of different molybdenum oxide species yields additional information on their origin and formation. Furthermore, the spatially resolved information obtained from the use of Raman micro-spectroscopy sheds light on detrimental processes taking place during catalyst preparation. In this specific study, the formation of bulk MoO_3 in calcined Mo/Al_2O_3 extrudates prepared from AHM-pH 6 solutions could be linked directly to the formation

of bulk $(NH_4)_3[Al(OH)_6Mo_6O_{18}]$ during impregnation. From the observation of bulk phases exclusively near the exterior of extrudates prepared from the highly concentrated basic AHM-solution, it was concluded that their formation was the result of an egg-shell distribution of Mo over the extrudates. Since the formation of crystalline material is generally to be avoided in supported catalysts Raman micro-spectroscopy could be an interesting technique for the development of a quality control expert system for industrial catalyst preparation processes.

Conclusions

Several physico-chemical processes operative at different stages of the preparation process can result in a poor dispersion of the Mo-oxide phase in oxidic Mo/Al_2O_3 extrudates. The formation of a layer of $(NH_4)_3[Al(OH)_6Mo_6O_{18}]$ on the outer surface of the extrudates during impregnation with acidic AHM-solutions was found to take place due to ligand-promoted dissolution of the support oxide. This led to the formation of bulk MoO_3 after calcination. When impregnation was carried out with basic AHM-solutions, a redistribution of Mo(VI)-complexes during drying led to an egg-shell distribution of Mo(VI)-complexes inside the extrudates. As a result, at high Mo-loadings, the Mo-concentration on the outside of the extrudates exceeded the dispersion limit of the support and MoO_3 and $Al_2(MoO_4)_3$ crystals are formed during calcination. Both phenomena are restricted to the preparation of catalyst bodies and would have been overlooked in catalyst preparation studies on powdered samples. The formation of crystalline oxidic phases after calcination led to a poorly dispersed MoS_2-phase in the active catalysts. A semi-quantitative correlation was found between the hydrotreating activity and the dispersion of the Mo-phase. Samples prepared from AHM-citrate solutions showed a good Mo-dispersion throughout the preparation process and an increased HDS-activity relative to the samples prepared from the AHM-solutions without citrate.

Acknowledgments

Catalyst preparation and testing were carried out at the laboratories of Albemarle Catalysts in Amsterdam. Thanks to all people involved. Marcel Jansen is kindly acknowledged for his help during catalyst preparation, coordination of characterization and testing and valuable discussions. Dimitri Agterveld and Brenda Rossenaar (Akzo Nobel Chemicals Research) are acknowledged for the analysis of the MoS_2/Al_2O_3 samples. Marjan Versluis-Helder is thanked for the XRD-measurements.

References

1 J. Hagen *(Eds.)*, *Industrial Catalysis: A Practical Approach*, Wiley-VCH, Weinheim, 1999.
2 H. Knözinger, E. Taglauer, *Supported Catalysts. Spreading and Wetting* in *Preparation of Solid Catalysts* (G. Ertl, H. Knözinger, J. Weitkamp, *Eds.)*, Wiley-VCH, Weinheim, 1999.
3 G. Mestl, T. K. K. Srinivasan, *Catal. Rev. Sci. Eng.* **1998**, *40*, 451.
4 I. E. Wachs, *Catal. Today* **1996**, *27*, 437.
5 H. J. Tian, I. E. Wachs, L. E. Briand, *J. Phys. Chem. B* **2005**, *109*, 23491.
6 T. Ozeki, H. Kihara, S. Ikeda, *Anal. Chem.* **1988**, *60*, 2055.
7 L. Le Bihan, P. Blanchard, M. Fournier, J. Grimblot, E. Payen, *J. Chem. Soc. Faraday Trans.* **1998**, *94*, 937.
8 X. Carrier, J. F. Lambert, M. Che, *J. Am. Chem. Soc.* **1997**, *119*, 10137.
9 Z. H. Zhou, H. L. Wan, K. R. Tsai, *Inorg. Chem.* **2000**, *39*, 59.
10 J. J. Cruywagen, E. A. Rohwer, G. F. S. Wessels, *Polyhedron* **1995**, *14*, 3481.
11 J. A. Bergwerff, T. Visser, R. G. Leliveld, B. A. Rossenaar, K. P. de Jong, B. M. Weckhuysen, *J. Am. Chem. Soc.* **2004**, *126*, 14548.
12 X. Carrier, J. F. Lambert, S. Kuba, H. Knozinger, M. Che, *J. Mol. Struct.* **2003**, *656*, 231.
13 G. Deo, I. E. Wachs, *J. Phys. Chem.* **1991**, *95*, 5889.
14 H. C. Hu, I. E. Wachs, S. R. Bare, *J. Phys. Chem.* **1995**, *99*, 10897.
15 S. Braun, L. G. Appel, V. L. Camorim, M. Schmal, *J. Phys. Chem. B.* **2000**, *104*, 6584.
16 S. Y. Lee, R. Aris, *Catal. Rev. Sci. Eng.* **1985**, *27*, 207.
17 A. V. Neimark, L. I. Kheifez, V. B. Fenelonov, *Ind. Eng. Chem. Prod. Res. Dev.* **1981**, *20*, 439.
18 L. M. Knijff, *The Application of Active Components into Catalyst Support Bodies,* PhD thesis, Utrecht University, 1993.
19 A. Muller, T. Weber, *Appl. Catal.* **1991**, *77*, 243.
20 R. Prins, A. Egorova, A. Rothlisberger, Y. Zhao, N. Sivasankar, P. Kukula, *Catal. Today* **2006**, *111*, 84.
21 K. P. de Jong, *Ind. Eng. Chem. Res.* **1994**, *33*, 3141.
22 S. K. Bej, A. K. Dalai, J. Adjaye, *Pet. Sci. Technol.* **2002**, *20*, 867.
23 D. Ferdous, A. K. Dalai, J. Adjaye, *Ind. Eng. Chem. Res.* **2006**, *45*, 544.
24 R. A. Diazreal, R. S. Mann, I. S. Sambi, *Ind. Eng. Chem. Res.* **1993**, *32*, 1354.
25 B. M. Vogelaar, *Deactivation of Hydroprocessing Catalysts; New Insights in Catalyst Structure, Activity and Stability, PhD thesis*, Delft University of Technology, 2005.
26 M. A. Goula, C. Kordulis, A. Lycourghiotis, *J. Catal.* **1992**, *133*, 486.
27 M. A. Goula, C. Kordulis, A. Lycourghiotis, J. L. G. Fierro, *J. Catal.* **1992**, *137*, 285.
28 L. Kaluza, M. Zdrazil, *Catal. Lett.* **2002**, *78*, 313.
29 Y. Okamoto, Y. Arima, K. Nakai, S. Umeno, N. Katada, H. Yoshida, T. Tanaka, M. Yamada, Y. Akai, K. Segawa, A. Nishijima, H. Matsumoto, M. Niwa, T. Uchijima, *Appl. Catal. A-General* **1998**, *170*, 315.
30 Y. Okamoto, Y. Arima, M. Hagio, K. Nakai, S. Umeno, Y. Akai, K. Uchikawa, K. Inamura, T. Ushikubo, N. Katada, S. Hasegawa, H. Yoshida, T. Tanaka, T. Isoda, I. Mochida, K. Segawa, A. Nishijima, M. Yamada, H. Matsumoto, M. Niwa, T. Uchijima, *Appl. Catal. A-General* **1998**, *170*, 329.
31 Y. Okamoto, S. Umeno, Y. Arima, K. Nakai, T. Takahashi, K. Uchikawa, K. Inamura, Y. Akai, O. Chiyoda, N. Katada, T. Shishido, H. Hattori, S. Hasegawa, H. Yoshida, K. Segawa, N. Koizumi, M. Yamada, A. Nishijima, T. Kabe, A. Ishihara, T. Isoda, I. Mochida, H. Matsumoto, M. Niwa, T. Uchijima, *Appl. Catal. A-General* **1998**, *170*, 343.
32 Y. Okamoto, S. Umeno, Y. Shiraki, Y. Arima, K. Nakai, O. Chiyoda, H. Yoshida, K. Uchikawa, K. Inamura, Y. Akai, S. Hasegawa, T. Shishido, H. Hattori, N. Katada, K. Segawa, N. Koizumi, M. Yamada, I. Mochida, A. Ishihara, T. Kabe, A. Nishijima, H. Matsumoto, M. Niwa, T. Uchijima, *Appl. Catal. A-General* **1998**, *170*, 359.
33 R. Srinivasan, H. C. Liu, S. W. Weller, *J. Catal.* **1979**, *57*, 87.
34 C. B. Wang, Y. P. Cai, I. E. Wachs, *Langmuir* **1999**, *15*, 1223.
35 W. C. Cheng, N. P. Luthra, *J. Catal.* **1988**, *109*, 163.
36 J. A. R. van Veen, P. Hendriks, E. Romers, R. R. Andrea, *J. Phys. Chem.* **1990**, *94*, 5275.
37 J. A. R. van Veen, P. Hendriks, R. R. Andrea, E. Romers, A. E. Wilson, *J. Phys. Chem.* **1990**, *94*, 5282.

Chapter 5

Combined Raman and UV-Vis-NIR Micro-spectroscopy Study on the Preparation of $CoMo/Al_2O_3$ Catalyst Bodies: Controlling the Formation of $H_2PMo_{11}CoO_{40}^{5-}$ inside Al_2O_3 Pellets after Impregnation

Abstract

The physicochemical processes that occur during the preparation of $CoMo\text{-}Al_2O_3$ hydrodesulphurization catalyst bodies have been investigated. To this end, the distribution of Mo(VI)- and Co(II)-complexes, after impregnation of $\gamma\text{-}Al_2O_3$ pellets with different CoMo(P)-solutions, was monitored using Raman and UV-Vis-NIR micro-spectroscopy. From the speciation of the different complexes over the catalyst bodies, insight was obtained into the interaction of the different components in the impregnation solution with the Al_2O_3 surface. It was shown that, after impregnation with a solution containing $H_2PMo_{11}CoO_{40}^{5-}$, the reaction of phosphate with the Al_2O_3 leads to the disintegration of this complex. The consecutive independent transport of Co(II)-complexes (fast) and Mo(VI)-complexes (slow) through the pores of the Al_2O_3 was envisaged. By the addition of extra phosphate and citrate to the impregnation solution, the formation of the desired heteropolyanion could be achieved inside the pellets. Ultimately, the $H_2PMo_{11}CoO_{40}^{5-}$ distribution could be applied by varying the aging time, that was applied after impregnation. The power of a combination of Raman and UV-Vis-NIR micro-spectroscopy in order to monitor the preparation of $CoMo/Al_2O_3$ catalyst bodies is illustrated.

Introduction

In the previous chapters, the application of Raman micro-spectroscopy in the preparation of Mo/Al_2O_3 catalyst bodies was discussed. The activity of these catalysts in hydrodesulphurization was found to be a function of the dispersion of the Mo-phase. In Co-promoted hydrotreatment catalysts, the nature of the Co(II)-complexes in the oxidic precursor is another important parameter that determines the activity of the final catalyst. In sulfided $CoMo/Al_2O_3$ catalysts Co atoms are reported to be located at the edges of the MoS_2 slabs and are thought to constitute the active sites in these promoted catalysts [1-3]. To enable the promoting function of Co, it is of crucial importance that Co and Mo are in close contact after sulphidation. Therefore, a homogeneous distribution of Mo and Co over the catalyst bodies is a prerequisite for maximal activity. Furthermore, the nature of the Mo(VI)- and Co(II)-complexes in the oxidic precursor strongly influences the activity of the final catalyst. It is known, for instance, that the formation of crystalline Co-phases, such as $CoAl_2O_4$ and $CoMoO_{4,}$ prevents the promoting effect of Co in the final catalyst. The addition of complexing agents on the other hand is reported to retard the sulphidation of Co, leading to a more active CoMoS phase in the final catalyst [4-6]. UV-Vis-NIR spectroscopy can be applied for the characterization of Co(II)-complexes through the position and intensity of their d-d transition bands. The application of this technique in a spatially resolved mode allows one to monitor the nature and distribution of Co(II)-complexes inside $CoMo/Al_2O_3$ catalyst bodies throughout their preparation.

The use of heteropolyanions containing both Mo and Co, such as $H_2PMo_{11}CoO_{40}^{5-}$ or $Co(OH)_6Mo_6O_{18}^{3-}$ as precursors for HDS-catalysts, has been studied in recent years [7-11]. These compounds were applied to minimize the formation of $Al(OH)_6Mo_6O_{18}^{3-}$ and $CoAl_2O_4$ during catalyst preparation and maximize the promoting effect of Co. Increased activity was indeed reported for the catalysts prepared using this approach [11,12]. However, the stability of these compounds during the preparation was found to be a problem, especially for the $H_2PMo_{11}CoO_{40}^{5-}$ complex. More in general, phosphate containing Keggin-type complexes are reported to decompose upon adsorption onto the Al_2O_3 surface [8,13]. In chapter 2C, the formation of $H_2PMo_{11}CoO_{40}^{5-}$ in CoMoP-solutions was studied using Raman and UV-Vis-NIR spectroscopy. The characteristic Raman and UV-Vis-NIR spectra of this complex in solution make it a suitable candidate to illustrate the power of combined spectroscopic techniques in catalyst preparation studies. In this chapter, it is illustrated how the disintegration and formation of the Keggin-type H2PMo11CoO405- heteropolyanion inside the pores of Al_2O_3 pellets can be monitored using a combination of Raman and UV-Vis-NIR micro-spectroscopy. Subsequently, the insights that were obtained in this way, were used to control the distribution of this complex after impregnation.

Experimental

Pore volume impregnation was carried out on cylindrical γ-Al_2O_3 pellets (Engelhard). These were calcined at 600°C for 6 h and stored at 120°C before impregnation. The pore volume of this support material was 1.1 ml/g, and its surface area 200 m^2/g. The pellets were 3 mm in both length and diameter. All impregnation solutions contained 1.0 M Mo and 0.5 M Co, yielding a theoretical loading of 15-wt% MoO_3 and a 4.0-wt% CoO in the final catalyst. During impregnation, care was taken that the solution was distributed homogeneously over all Al_2O_3 bodies and the pellets were kept in a closed vessel after impregnation to prevent evaporation of water. At several points in time after impregnation a pellet was collected from the impregnation vessel and a cross-section was made perpendicular to the axis of the cylinder, using a razorblade.

Raman spectra were recorded on these bisected pellets using a Kaiser RXN spectrometer equipped with a 785 nm diode laser in combination with a Hololab 5000 Raman microscope. A 10x objective was used for beam focusing and collection of scattered radiation, resulting in a spot size on the sample of approximately 50 µm. The laser power on the sample was 70 mW. For a typical measurement, 5 spectra were accumulated with a 3 s exposure time. Background correction was carried out by subtraction of a reference spectrum recorded on wet Al_2O_3 and the spectra were scaled to the NO_3^- peak at 1044 cm^{-1}, which was used as an internal standard.

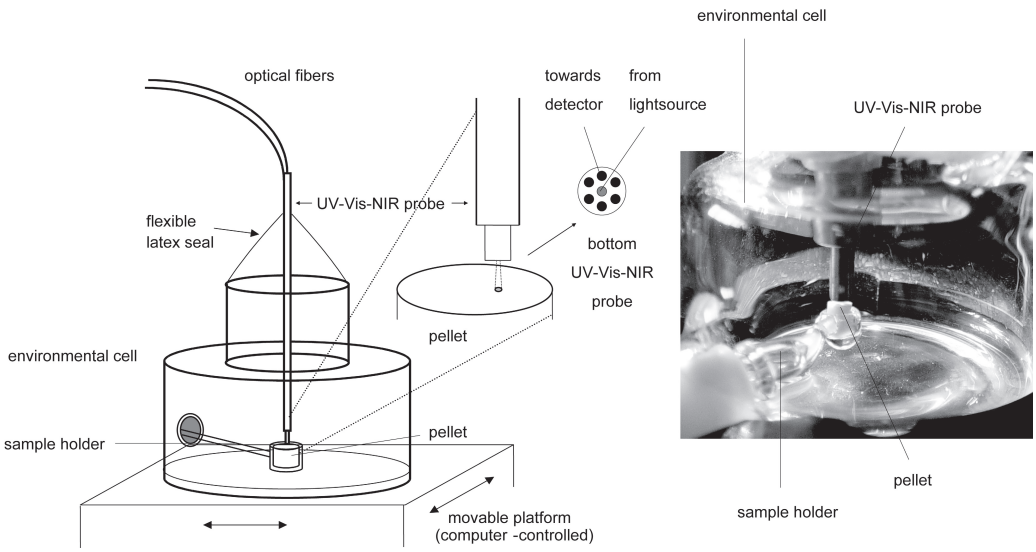

Figure 1. Schematic representation of the UV-Vis-NIR microspectroscopy set-up used for measurements on bisected catalyst pellets.

UV-Vis-NIR spectra were recorded in much the same way using a specially designed set-up for spatially resolved UV-Vis-NIR measurements [14]. A schematic representation of the experimental set-up is given in Fig. 1. Light from a Mikropack DH-2000-BAL UV-Vis-NIR light source is guided onto the sample by a single optical fiber (Ocean Optics). Light reflected from the sample is guided by six optical fibers to an Avantes Avaspec 2048 pixel CCD camera for detection. The measurement spot that is thus created on the sample is a function of the diameter of the optical fiber used for illumination. In this case, an optical fiber of 100 µm diameter was applied, resulting in a measurement spot of approximately the same size. The bisected pellets are placed in a sample holder, which can be inserted into a glass measuring cell, as shown in Fig. 1. Scans were made along the axis of bisected pellets by moving the measuring cell underneath the UV-Vis-NIR probe with the use of a remote-controlled x-y-z-stage. During UV-Vis-NIR measurements, a small amount of water was applied to the measuring cell to ensure a relative humidity of 100% and prevent dehydration of the sample. The procedure used for Raman and UV-Vis-NIR micro-spectroscopy measurements on bisected pellets is illustrated in Fig. 2.

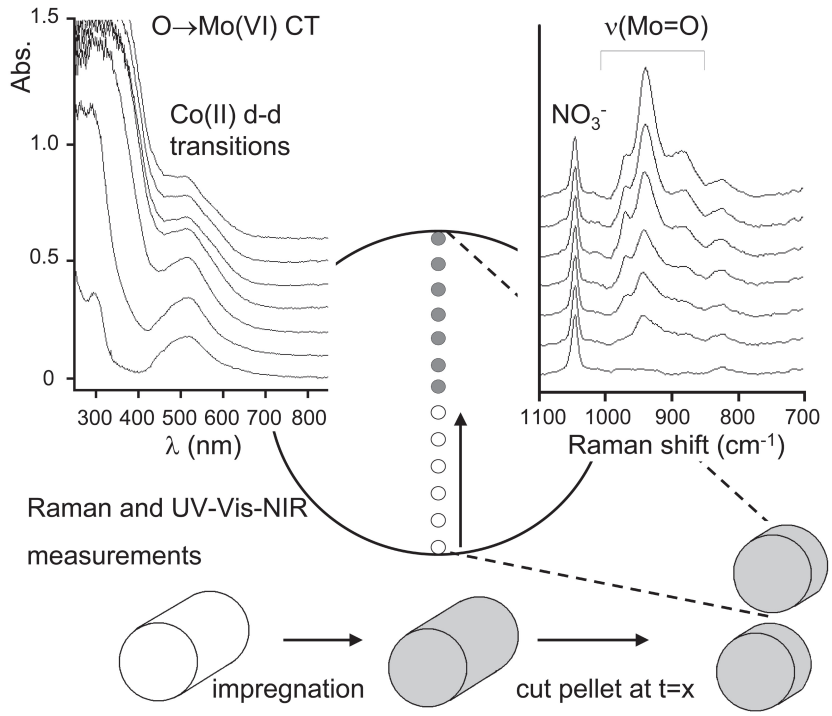

Figure 2. Lay out of spatially resolved Raman and UV-Vis-NIR measurements on bisected catalyst bodies.

For impregnation, a solution which predominantly contained $H_2PMo_{11}CoO_{40}^{5-}$ was prepared. To this end, the appropriate amount of $CoCO_3$ (Acros, p.a.) was added to a boiling suspension of MoO_3 in 0.3 M HNO_3. After stirring for 120 min, the resulting red solution was allowed to cool down to room-temperature and 85 wt% H_3PO_4 solution was added to obtain a phosphate concentration of 0.10 M. This solution will be referred to as CoMoP(0.1). Solutions containing 1.0 M Mo, 0.50 M Co and 0.20 M citric acid with different PO_4^{3-}-concentrations were prepared by dissolving $(NH_4)_6Mo_7O_{24}$ (Acros, p.a.) (AHM), $Co(NO_3)_2{\cdot}6\,H_2O$, crystalline citric acid (OPG Pharma, p.a.) and an 85 wt% H_3PO_4 solution (Merck, p.a.). Solutions were prepared with phosphate concentrations of 0.30 M, 0.50 M and 0.70 M, which will, in the following, be referred to as CoMoCAP(0.3), CoMoCAP(0.5) and CoMoCAP(0.7) respectively. Impregnation was carried out with these solutions as well. The chemical composition and final pH of the different solutions used for impregnation are presented in Table 1.

Table 1. Chemical composition and pH of the impregnation solutions used in this study.

Sample code	[Mo] (M)	[Co] (M)	[P] (M)	[Citrate] (M)	pH
CoMoP(0.1)	1.00	0.50	0.10	-	2.4
CoMoCAP(0.3)	1.00	0.50	0.30	0.20	1.2
CoMoCAP(0.5)	1.00	0.50	0.50	0.20	1.1
CoMoCAP(0.7)	1.00	0.50	0.70	0.20	1.0

Results and Discussion

Formation of $H_2PMo_{11}CoO_{40}^{5-}$ in solution

An extensive study on the speciation of metal-complexes in CoMoP-solutions can be found in chapter 2C. The main findings of this work are summarized in this paragraph. It was shown that the formation of the $H_2PMo_{11}CoO_{40}^{5-}$ heteropolyanion takes place at specific phosphate concentrations and pH. The equation for the formation of the complex from isopolymolybdates and $[Co(H_2O)_6]^{2+}$ in acidic environment is given in Eq. 1. The formation of $H_yP_2Mo_5O_{23}^{(6-y)-}$, as expressed in Eq. 2, is favored at high P:Mo ratios. The pH of the solution is another important factor determining the speciation of metal-complexes in these solutions. Larger phosphomolybdate complexes, such as $H_2PMo_{11}CoO_{40}^{5-}$ are generally formed at lower pH.

$$11\ H_xMo_7O_{24}^{(6-x)-} + 7\ H_yPO_4^{(3-x)-} + 7\ [Co(H_2O)_6]^{2+} \leftrightarrow 7\ H_2PMo_{11}CoO_{40}^{5-} + 54\ H_2O \quad \text{(Eq. 1)}$$

$$5\ H_2PMo_{11}CoO_{40}^{5-} + 17\ H_xPO_4^{(3-x)-} + 17\ H_2O \leftrightarrow 11\ H_yP_2Mo_5O_{23}^{(6-y)-} + 5\ [Co(H_2O)_6]^{2+} \quad \text{(Eq. 2)}$$

Using multivariate curve resolution (MCR), a reference Raman spectrum for $H_2PMo_{11}CoO_{40}^{5-}$ in solution was derived. The most intense bands are located at 971, 886 and 816 cm^{-1}. The locations of the main ν(Mo=O) vibration bands of this complex and other relevant Mo(VI)-complexes, are presented in Table 2. The incorporation of Co(II) into the heteropolyanion brings about distinct changes in the UV-Vis-NIR spectrum as well. The formation of the heteropolyanion is accompanied by the presence of two broad bands at 455 and 580 nm in the UV-Vis-NIR spectrum. The coordination of Co(II) in this complex is probably pseudo-octahedral, as the orientation of Co(II) towards 5 of the coordinating O-atoms is fixed by the structure of the Keggin-ion. However, the distance of the water molecule completing the 6-fold coordination towards the outside of the complex is free. This distortion from perfect octahedral coordination may be an explanation for the relatively high extinction coefficient observed for the band at 588 nm. The formation of a large Mo-O cluster results in a red-shift in the onset of the O→Mo(VI) charge transfer band [15]. This band overlaps with the Co(II) d-d- transition bands at 455 and 588 nm, resulting in the dark-brown color of solutions containing $H_2PMo_{11}CoO_{40}^{5-}$.

Table 2. Positions of ν(Mo=O) Raman bands of relevant Mo(VI)-complexes in aqueous solution, as derived from the MCR-analysis of Raman spectra presented in chapter 2.

	Position of ν(Mo=O) vibration bands (cm^{-1})				
$Mo_7O_{24}^{6-}$	939 (s)	896 (m)			
$Mo_4O_{11}(citrH)_2^{4-}$	944 (s)	904 (m)	862 (w)		
$P_2Mo_5O_{23}^{6-}$	956 (w)	926 (s)	870 (m)		
$HP_2Mo_5O_{23}^{5-}$	936 (s)	882 (m)			
$H_2P_2Mo_5O_{23}^{4-}$	944 (s)	894 (m)			
$H_2PMo_{11}CoO_{40}^{5-}$	1008 (w)	971 (s)	954 (sh)	886 (m)	818 (m)

Disintegration of $H_2PMo_{11}CoO_{40}^{5-}$ inside Al_2O_3 pellets

The Raman spectra of the impregnation solutions used in this study are presented in Fig. 3. The spectrum recorded on the CoMoP(0.1) solution showed bands at 971, 851 and 816 cm^{-1}. After comparison to the reference spectrum of $H_2PMo_{11}CoO_{40}^{5-}$ (Table 2, and Fig. 30 in chapter 2C) it can be concluded that practically all Mo in this solution is present in this heteropolyanion. The shoulder at 950 cm^{-1} shows that additional Mo(VI)-complexes are present in low concentrations. A UV-Vis-NIR spectrum of the CoMoP(0.1) solution is presented in Fig. 4. Strong absorption is observed in the 350-600 nm region. For more careful analysis of the absorption bands, a spectrum was therefore recorded on this solution after dilution (5 times). Now, it can be observed that bands are located at 455 and 580 nm, which confirms the formation of $H_2PMo_{11}CoO_{40}^{5-}$. Regarding the Co-concentration of 0.50 M, not all Co can be contained in the heteropolyanion and additional $[Co(H_2O)_6]^{2+}$ is present in the solution. This leads to the additional presence of a band at 515 nm in the UV-Vis-NIR spectrum.

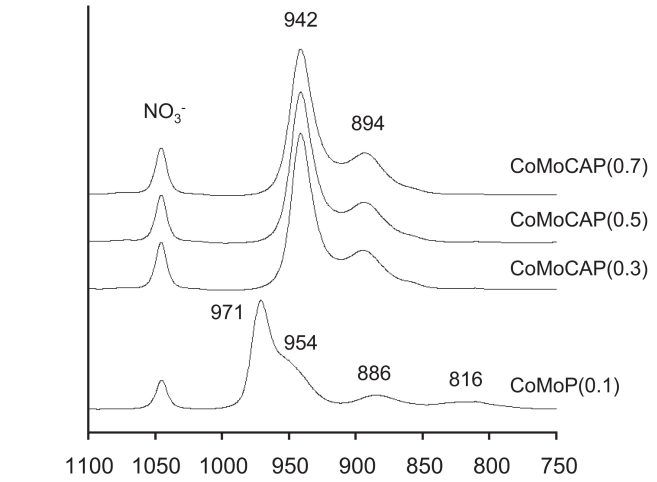

Figure 3. Raman spectra of the CoMoP(0.1) and CoMoCAP(x) impregnation solutions used in this study.

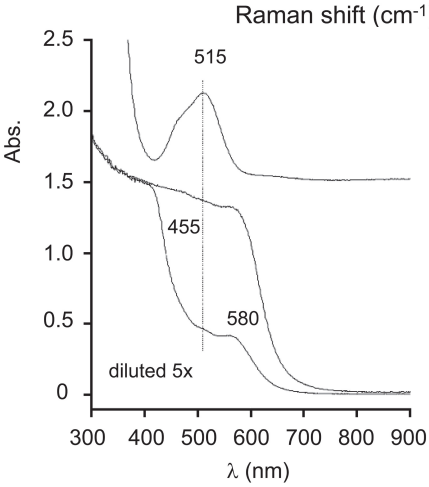

Figure 4. UV-Vis-NIR spectra of the CoMoP(0.1) (before and after 5 times dilution) and CoMoCAP(0.3) impregnation solutions used in this study.

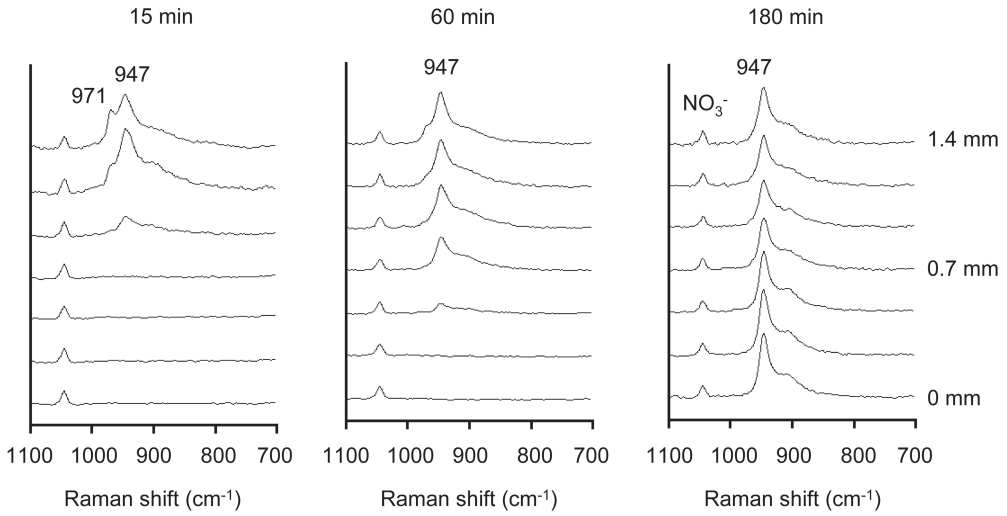

Figure 5. Raman spectra recorded at different positions inside the Al_2O_3 support bodies, 15 min, 60 min and 180 min after impregnation with the CoMoP(0.1) solution. The distance from the core of the pellets is indicated on the right, where 0 mm indicates the center of the pellet and 1.4 mm a position near the exterior surface.

In Fig. 5, Raman spectra of the cross-section of ã-Al_2O_3 pellets are presented, recorded 15 min, 60 min and 180 min after impregnation with the CoMoP(0.1) solution. The measurements were performed at different positions along the axis of the bisected pellets. The presence of $H_2PMo_{11}CoO_{40}^{5-}$ inside the Al_2O_3 pores, identifiable by the characteristic Raman peak at 971 cm^{-1}, is observed 15 min after impregnation, only in the outer shell of the pellets (i.e. 1.4 mm from the core of the pellet). More towards the center of the Al_2O_3 bodies, Mo is present as a $H_xMo_7O_{24}^{(6-x)-}$ complex as can be concluded from the position of the main ν(Mo=O) band at 947 cm^{-1}. Near the core, the absence of any Mo=O vibration peaks indicates, that no Mo(VI)-complexes are present. After 60 min, practically all Mo is present as $H_xMo_7O_{24}^{(6-x)-}$. However, a clear Mo-concentration gradient is still present over the pellets, as there is an increase in the relative intensity of the bands resulting from the ν(Mo=O) vibrations in the spectra recorded towards the outside of the pellets. Eventually, after 180 min, a homogeneous distribution of $H_xMo_7O_{24}^{(6-x)-}$ is observed throughout the support bodies; the relative intensity of the 947 cm^{-1} peak, as compared to that of the NO_3^- internal standard, is identical for all positions inside the Al_2O_3 bodies.

These observations are in agreement with the UV-Vis-NIR measurements carried out at the same points in time and at the same positions inside the pellets, as presented in Fig. 6. In the spectra recorded near the edge of the bisected pellet, 15 min after impregnation, a clear shoulder is observed at 580 nm and the onset of the O→Mo(VI) charge transfer band is shifted

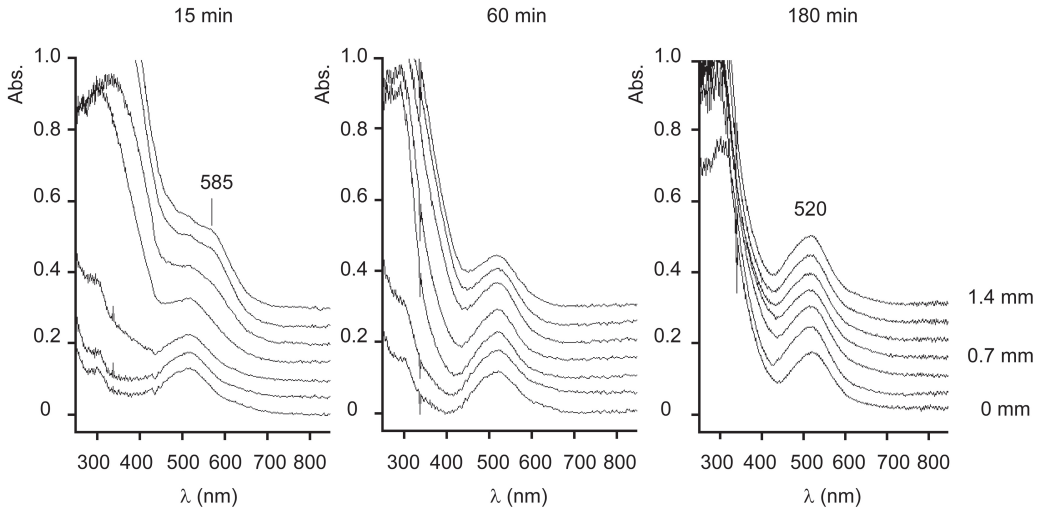

Figure 6. UV-Vis-NIR spectra recorded at different positions inside the Al_2O_3 support bodies, 15 min, 60 min and 180 min after impregnation with the CoMoP(0.1) solution. The distance from the core of the pellets is indicated on the right.

into the visible region. This confirms the presence of $H_2PMo_{11}CoO_{40}^{5-}$ in the outer shell of the support bodies at this point in time. Towards the core of the pellets however, all Co seems to be present as $[Co(H_2O)_6]^{2+}$ and the O→Mo(VI) charge transfer band is absent, validating the Mo-concentration gradient observed in the Raman measurements. Eventually, after 180 min, Mo(VI)-complexes are present throughout the support bodies, as a O→Mo(VI) charge transfer band is observed for all positions along the cross-section. A homogeneous distribution of $[Co(H_2O)_6]^{2+}$-type complexes is already obtained after 60 min, as the intensity of the Co(II) d-d transition band, with its maximum at 520 nm is the same for all positions along the cross-section.

Upon impregnation of porous support bodies with an aqueous solution, an instantaneous distribution of the liquid phase occurs, as a result of the capillary forces that are due to the pore-system of the support. However, a strong interaction between the compounds dissolved in the impregnation solution and the support can result in a slower transport of these components [16-18]. After impregnation with a solution containing Co, Mo, phosphate and nitrate, a different interaction of these components with the Al_2O_3 surface was observed. The interaction between the weakly coordinating NO_3^- and the support was negligible. This anion was transported with the flow of the solution through the Al_2O_3 pores and within 5 min after impregnation, NO_3^- was detected in the Raman measurements for all positions inside the pellet. For this reason, a homogeneous distribution of this ion can be assumed at all time and this ion

can be used as an internal standard in the Raman measurements [18]. After impregnation with the acidic solutions used in this study, the Al_2O_3 surface is positively charged, due to the protonation of the basic hydroxyl-groups. Hence, Coulomb interaction between the surface and the positively charged Co(II)-complexes is limited, and a fast transport of $[Co(H_2O)_6]^{2+}$ resulted in a homogeneous distribution of this complex throughout the support bodies, within several minutes. On the contrary, electrostatic interaction between the negatively charged Mo(VI)-complexes and the protonated Al_2O_3 hydroxyl groups can be expected. Furthermore, adsorption of Mo(VI)-complexes onto the Al_2O_3 surface may take place after their reaction with surface OH-groups. Both phenomena resulted in a much slower transport of Mo. As was already observed in chapter 3, it may take up to 180 min before a homogeneous distribution of Mo is obtained in this type of pellets.

Phosphate is known to react with Al_2O_3 in acidic environment to form an $AlPO_4$ phase (Eq. 3) [19,20]. In this way, phosphate is withdrawn from the solution inside the Al_2O_3 pores. Hence, a decreasing phosphate concentration can be expected towards the center of the pellet. The disintegration of $H_2PMo_{11}CoO_{40}^{5-}$ during impregnation of a 1.0 M solution of this complex can thus be explained. As the impregnation solution penetrated the pellets, reaction of phosphate with the Al_2O_3 resulted in a lower phosphate concentration in the solution inside the pores of the support. The equilibrium in Eq. 1 is shifted to the left and $H_xMo_7O_{24}^{(6-x)-}$ and $[Co(H_2O)_6]^{2+}$ were formed, which followed their way towards the core of the pellets, each at their own rate. The disintegration of $H_2PMo_{11}CoO_{40}^{5-}$ after impregnation onto Al_2O_3 is in line with previous studies, in which the instability of this type of complexes on an Al_2O_3 support was reported [8,13]. The processes described above are summarized in Fig. 7, in which the distribution of the different

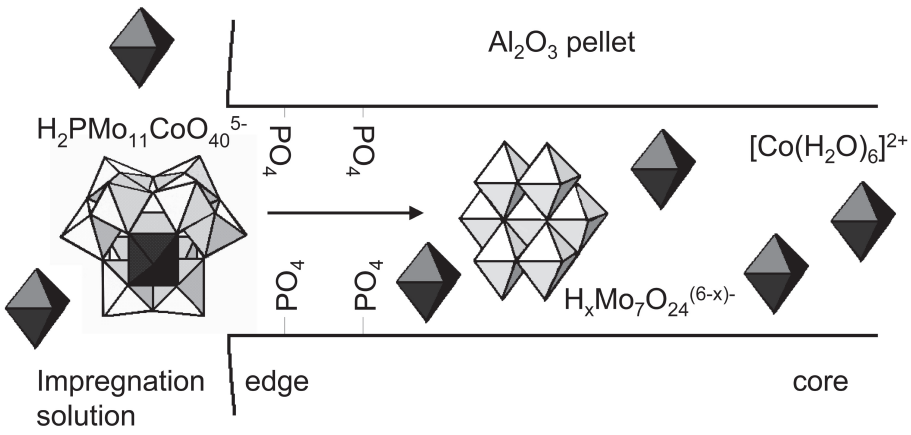

Figure 7. A schematic presentation of the distribution of Mo- and Co-complexes over an Al_2O_3 pellet, 60 min after impregnation with the CoMoP(0.1) solution, initially containing $H_2PMo_{11}CoO_{40}^{5-}$.

complexes inside the Al_2O_3 pellets at 60 min after impregnation with the $H_2PMo_{11}CoO_{40}^{5-}$ solution is presented in a schematic manner.

$$Al_sOH + HPO_4^{2-} + H^+ \leftrightarrow AlHPO_4^- + H_2O \quad \text{(Eq. 3)}$$

Formation of $H_2PMo_{11}CoO_{40}^{5-}$ inside Al_2O_3 pellets

From calculations, using the formation constants of the different Mo(VI)-complexes it could be concluded that in solutions CoMoCAP(0.3), CoMoCAP(0.5) and CoMoCAP(0.7), all citrate (and consequently 40% of all Mo) is bound in a $Mo_4(Hcitrate)_2O_{11}^{4-}$ complex [21,22]. The remaining 0.6 M of Mo is contained in $H_xP_2Mo_5O_{23}^{(6-x)}$. The Raman spectra of the different CoMoCAP(x) solutions, as presented in Fig. 3, are indeed identical and component analysis shows that they can be reconstructed by the sum of the spectra of $Mo_4(Hcitrate)_2O_{11}^{4-}$ and $H_2P_2Mo_5O_{23}^{4-}$ in solution. The colors of these solutions were also identical. The UV-Vis-NIR spectrum of the CoMoCAP(0.3) solution is presented in Fig. 4. At the low pH of these solutions, complexation of Co(II) by citrate doesn't take place and all Co was present in $[Co(H_2O)_6]^{2+}$, resulting in a band at 515 nm in the UV-Vis-NIR spectrum. Absorption due to O→Mo(VI) charge transfer bands was restricted to the UV-region of the spectrum, indicating the presence of reasonably small Mo(VI)-clusters and lack of interaction between Co and Mo. Hence, the only difference in the composition of these solutions was the amount of free phosphate present.

In Fig. 8, Raman spectra for different positions inside Al_2O_3 are presented, 15 min, 240 min and 24 h after impregnation with the CoMoCAP(0.3) solution. After 15 min, a clear Mo-gradient was present over the Al_2O_3 pellets, as the intensity of the ν(Mo=O) bands was found to decrease towards the center of the pellet. At this point in time, the presence of a shoulder at 971 cm^{-1} hints at the formation of $H_2PMo_{11}CoO_{40}^{5-}$ in a ring at 0.70-1.17 mm from the center of the extrudates. No Mo(VI)-complexes were present near the core of the pellets at this point in time and it takes several hours before a homogeneous Mo-distribution was obtained. After 240 min $H_2PMo_{11}CoO_{40}^{5-}$ was observed for all positions inside the Al_2O_3 pellet. Judging from the constant intensity of the peak at 971 cm^{-1} the distribution of this complex throughout the pellets was rather homogeneous. Besides the heteropolyanion, $H_xP_2Mo_5O_{23}^{(6-x)-}$ seemed to be formed at the outside of the pellet, while the much sharper peak at 944 cm^{-1} observed near the core of the pellet was probably due to the formation of $Mo_4(Hcitrate)_2O_{11}^{4-}$. When aging times longer than 8 h were applied, the intensity of the peak at 971 cm^{-1} decreased again and the formation of $Al(OH)_6Mo_6O_{18}^{3-}$ was observed, judging from the emergence of peaks at 947, 901, 570 and 356 cm^{-1} [23]. After 24 h, formation of this complex was observed at random positions inside the pellets after 24 h, and the intensity of the characteristic Raman bands differed

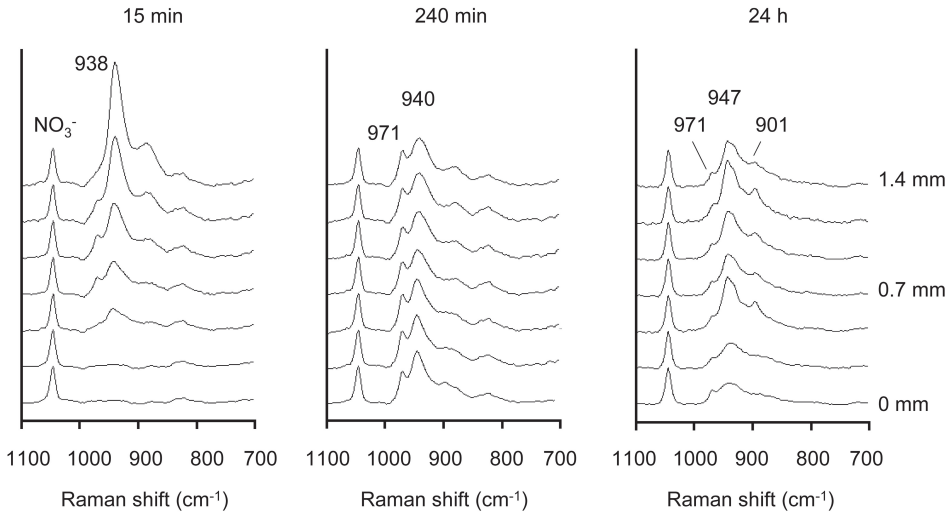

Figure 8. Raman spectra recorded at different positions inside the Al_2O_3 support bodies, 15 min, 240 min and 24 h after impregnation with the CoMoCAP(0.3) solution. The distance from the core of the pellets is indicated on the right.

strongly throughout the sample. This points to the formation of $Al(OH)_6Mo_6O_{18}^{3-}$ crystals inside the Al_2O_3 pellets (most noticeably at 0.47 mm and 1.17 mm from the center). At positions, where no $Al(OH)_6Mo_6O_{18}^{3-}$ was observed, broad features at 930-950 cm^{-1} indicate the formation of either $H_xP_2Mo_5O_{23}^{(6-x)-}$ or $H_xMo_7O_{24}^{(6-x)-}$. Only small quantities of $H_2PMo_{11}CoO_{40}^{5-}$ remained, at this point in time.

The corresponding UV-Vis-NIR spectra are presented in Fig. 9. After 15 min, the Co(II) d-d transition was observed at all positions, while the O→Mo(VI) charge transfer band was only observed near the edge of the pellets. The presence of $H_2PMo_{11}CoO_{40}^{5-}$ at this point in time was only observed for positions 0.93-1.17 mm from the center of the pellet. The spectra recorded after 240 min were practically identical for all positions. The formation of $H_2PMo_{11}CoO_{40}^{5-}$ was observed throughout the support bodies, indicated by the red-shift of both the onset of the O→Mo(VI) charge transfer band and the band due to the Co(II) d-d transition at 580 nm. Eventually, the disintegration of the heteropolyanion was again observed and $[Co(H_2O)_6]^{2+}$ is the only Co(II)-complex present throughout the pellet after 24 h.

The formation of $H_2PMo_{11}CoO_{40}^{5-}$ inside the pellets in the first hours after impregnation with the CoMoCAP(0.3) solution can be explained using the concepts that were explained in the previous paragraph. The phosphate concentration inside the Al_2O_3 pores decreased due to a reaction with the support (Eq. 3). Furthermore, the strong interaction between the phosphate

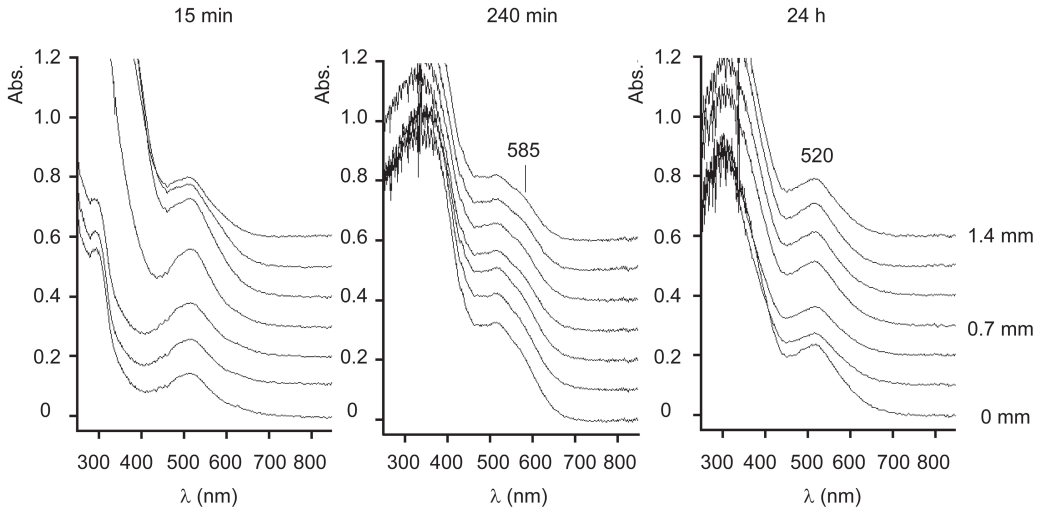

Figure 9. UV-Vis-NIR spectra recorded at different positions inside the Al_2O_3 support bodies, 15 min, 240 min and 24 h after impregnation with the CoMoCAP(0.3) solution. The distance from the core of the pellets is indicated on the right.

and the support induced an extremely slow transport of phosphate towards the center of the pellets. The occurrence of these concentration gradients resulted in a different speciation of Mo(VI)-and Co(II)-complexes for different positions inside the support bodies, as changes in the local concentration influence the equilibria in Eq. 1 and 2. Apparently, 4 h after impregnation these processes resulted in a P:Mo ratio that allows for the formation of the heteropolyanion at all positions inside the pellets. Near the outer surface the phosphate concentration was higher than near the core and, as a result, the remaining Mo near the outside of the pellets was contained in $H_xP_2Mo_5O_{23}^{(6-x)-}$, while more towards the interior $Mo_4(Hcitrate)_2O_{11}^{4-}$ was formed.

The formation of $Al(OH)_6Mo_6O_{18}^{3-}$ was reported for the impregnation of Al_2O_3 with acidic AHM-solutions, when long aging times are applied [24,25]. This Anderson-type heteropolyanion is formed by ligand-promoted dissolution of the Al_2O_3 support in a reaction represented in Eq. 4. Due to its low solubility, precipitation of this complex takes place. Al(III) ions are constantly generated by dissolution of the Al_2O_3 support, as impregnation was carried out with an acidic solution. This results in a chain-reaction in which, in time, increasing amounts of $Al(OH)_6Mo_6O_{18}^{3-}$, and eventually crystals are being formed [25]. This unwanted process may be prevented by the addition of complexing agents to the impregnation solution, as was shown in chapters 3 and 4 of this PhD-thesis [18]. In this case, the formation of this complex at 24 h after impregnation became possible, as the concentration of complexing agents, after reaction of the phosphate with the Al_2O_3, was insufficient to accommodate all Mo present. $Al(OH)_6Mo_6O_{18}^{3-}$ started

to form and the concentration of Mo in the solution inside the pores decreased due to the precipitation of this complex. The resulting increase in the P:Mo ratio probably caused the formation of $H_xP_2Mo_5O_{23}^{(6-x)-}$ at the expense of $H_2PMo_{11}CoO_{40}^{5-}$, acccording to Eq. 2.

$$12\ Mo_7O_{24}^{6-} + 7\ Al_2O_3 + 27\ H_2O + 30\ H^+ \rightarrow 14\ Al(OH)_6Mo_6O_{18}^{3-} \quad \text{(Eq. 4)}$$

When impregnation was carried out with a 1.0 M Mo, 0.50 M Co, 0.30 M P solution without citrate, the formation of $H_2PMo_{11}CoO_{40}^{5-}$ was not observed. This beneficial effect of citrate is not yet fully understood. It is known, that citrate forms stable complexes with Mo(VI) at low pH [18]. In this way, the presence of citrate prevents the adsorption of Mo onto the Al_2O_3 surface after impregnation. Consequently, a high concentration of Mo inside the pores is maintained, enough Mo is present for the formation of the heteropolyanion and the P:Mo ratio is kept sufficiently low. Furthermore, the presence of citrate prevents the formation of $Al(OH)_6Mo_6O_{18}^{3-}$ and the resulting disintegration of $H_2PMo_{11}CoO_{40}^{5-}$ as described in the previous paragraph [18]. Finally, impregnation of Al_2O_3 pellets with an acidic solution will result in an increase in the pH of the solution, due to the buffering effect of the support. The addition of citrate could counteract this effect, making sure that the pH of the solution inside the Al_2O_3 pores remains sufficiently low for the formation of $H_2PMo_{11}CoO_{40}^{5-}$. However, the validity of these assumptions is difficult to prove with the current techniques, as citrate itself could not be observed inside the support bodies using Raman or UV-Vis-NIR micro-spectroscopy. In Fig. 10, a simplified representation is given for the speciation of the different complexes, 60 min after impregnation with the CoMoCAP(0.3) solution used in this study.

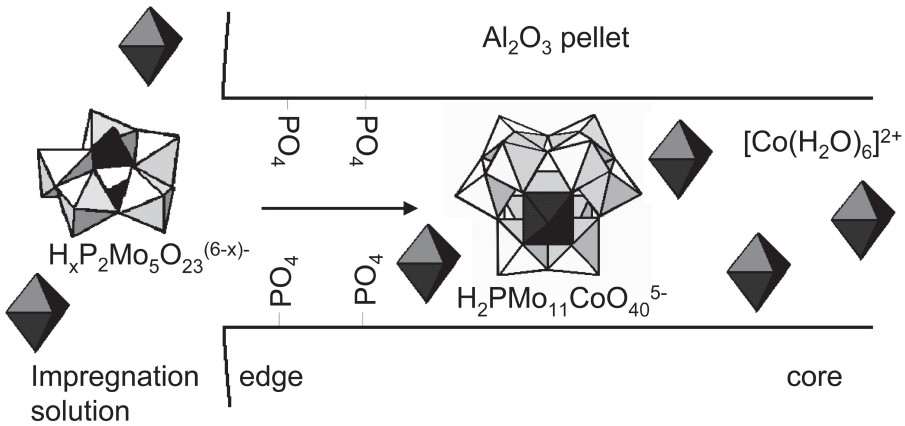

Figure 10. A schematic presentation of the distribution of Mo- and Co-complexes over an Al_2O_3 pellet, 60 min after impregnation with the CoMoCAP(0.3) solution.

Monitoring the distribution of $H_2PMo_{11}CoO_{40}^{5-}$ inside Al_2O_3 pellets

By using the NO_3^- peak as an internal standard, the local concentration of $H_2PMo_{11}CoO_{40}^{5-}$ inside of the Al_2O_3 pores was determined for the different positions inside the pellets. In principle, this could be done by deconvolution of the Raman spectra, similar to the procedures followed in chapter 2. However, the presence of adsorbed Mo(VI)-complexes, $H_xMo_7O_{24}^{(6-x)-}$, $Mo_4(Hcitrate)_2O_{11}^{4-}$ and $H_xP_2Mo_5O_{23}^{(6-x)-}$ in different protonation states all give rise to ν(Mo=O) vibration bands at a slightly different wavenumber between 930 and 950 cm^{-1}. Furthermore, the quality of the data obtained by measurements on the impregnated Al_2O_3 pellets was of inferior quality as compared to measurements on solutions. Therefore, a different approach was taken to obtain semi-quantitative distribution profiles of the heteropolyanion across the pellets. The pure component spectrum of $H_2PMo_{11}CoO_{40}^{5-}$ in solution, as derived from MCR-analysis of Raman spectra recorded on CoMoP solutions in chapter 2C, was used in a fit of the spectra recorded on the bisected pellets. This simple approach could be used as $H_2PMo_{11}CoO_{40}^{5-}$ is the only complex to give rise to a considerable intensity at 971 cm^{-1} in the Raman spectra. A typical example of a spectrum acquired on the surface of a bisected CoMo-Al_2O_3 pellet after background correction is presented in Fig. 11. The fit of the $H_2PMo_{11}CoO_{40}^{5-}$ reference spectrum and the resulting difference spectrum are given in the same figure. By calculating the contribution of the $H_2PMo_{11}CoO_{40}^{5-}$ reference spectrum to the measured spectra, the concentration of the complex was obtained for different positions inside the pellets. Distribution profiles of $H_2PMo_{11}CoO_{40}^{5-}$ inside the Al_2O_3 pellets, at 4 h and 24 h after impregnation with solutions

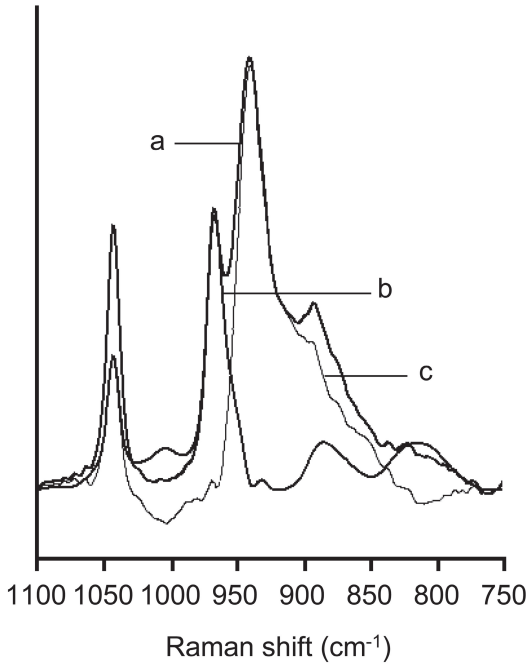

Figure 11. Illustration of the fitting procedure used to determine the concentration of $H_2PMo_{11}CoO_{40}^{5-}$ at different positions inside CoMo/Al_2O_3 pellets. A typical spectrum recorded on the bisected pellets (a), the reference spectrum of $H_2PMo_{11}CoO_{40}^{5-}$ fitted underneath the spectrum (b) and the resulting difference spectrum (c) are shown.

CoMoCAP(0.3), CoMoCAP(0.5) and CoMoCAP(0.7) are presented in Fig. 12. From these profiles it is obvious that the formation of $H_2PMo_{11}CoO_{40}^{5-}$ is observed at different positions in the pellets when the different CoMoCAP solutions were used for impregnation. For instance, 4 h after impregnation with a CoMoCAP(0.3) solution, a reasonably homogeneous distribution of the desired complex was achieved, as was discussed in the previous section. For all positions, the concentration of Mo contained in the heteropolyanion was approximately 0.45 M. At the same point in time after impregnation with a CoMoCAP(0.7) solution, however, $H_2PMo_{11}CoO_{40}^{5-}$ formation has only taken place near the core of the pellets. In the remaining part of the sample Mo was present as $H_xP_2Mo_5O_{23}^{(6-x)-}$. This is due to the phosphate concentration gradient, which was still present at this point in time. The P:Mo ratio near the core of the pellets was sufficiently low to allow for the formation of $H_2PMo_{11}CoO_{40}^{5-}$, while the high P:Mo ratio near the exterior of the bodies resulted in the formation of $H_xP_2Mo_5O_{23}^{(6-x)-}$. A slight concentration gradient was observed after impregnation with the CoMoCAP(0.5) solution and this can be regarded as an intermediate case.

No gradient was observed in the $H_2PMo_{11}CoO_{40}^{5-}$ distribution for any of the samples 24 h after impregnation. Apparently at this point in time, a phosphate gradient was no longer present over the pellets and equilibration of the system was complete. A considerable amount of $H_2PMo_{11}CoO_{40}^{5-}$ was present in the CoMoCAP(0.5) sample. In the pellets impregnated with the CoMoCAP(0.3) solution the formation of $Al(OH)_6Mo_6O_{18}^{3-}$ has taken place, as was discussed before. $H_xP_2Mo_5O_{23}^{(6-x)-}$ was predominantly present in the sample impregnated with the

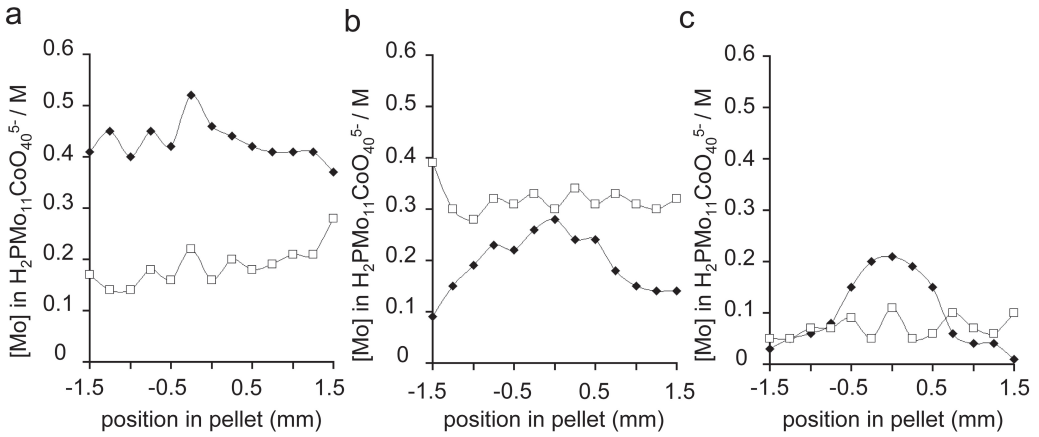

Figure 12. Distribution-profiles of $H_2PMo_{11}CoO_{40}^{5-}$ inside the pores of the Al_2O_3 pellets 4 h (♦) and 24 h (□) after impregnation with CoMoCAP(0.3) (a) CoMoCAP(0.5) (b) and CoMoCAP(0.7) (c) solutions.

CoMoCAP(0.7) solution as the P:Mo ratio was too high for all positions when a homogeneous distribution of phosphate was obtained. In brief, the observed $H_2PMo_{11}CoO_{40}^{5-}$ distribution profiles can be explained by the occurrence of phosphate concentration gradients after impregnation with an acidic CoMoCAP-solution. By controlling this phosphate gradient, the distribution of the heteropolyanion could be tuned. It is anticipated that a similar approach could be used for the deposition of other phosphate containing Keggin-ions onto Al_2O_3 bodies.

UV-Vis-NIR micro-spectroscopy in the preparation of supported catalyst bodies

As a large variety of metal-ion complexes show d-d or charge transfer transitions, the presented UV-Vis-NIR-micro-spectroscopy method is generally applicable to study their speciation inside the pores of oxidic support bodies after impregnation. It has for instance been demonstrated that the technique can be applied to quantitatively monitor the distribution of chromate anions inside Al_2O_3 pellets through the intensity of the O→Cr(VI) CT-band. Furthermore, the occurrence of pH-gradients inside catalyst bodies after impregnation with Ni-ethylenediamine solutions was illustrated. As the speciation of Ni- ethylenediamine complexes is a function of pH, and the position of the Ni(II) d-d bands shifts to lower energy when coordinating H_2O is exchanged for ethylenediamine, this system can be used as an internal pH probe to evaluate the buffering effect of the support on the impregnation solution inside the pores [14].

It is clear that drying and calcination of these systems may have a severe influence on the nature and distribution of the metal complexes inside support bodies, as well. UV-Vis-NIR micro-spectroscopy can also be applied on dried and calcined samples. In a study analogous to the work presented in this chapter, the distribution of $H_2PMo_{11}CoO_{40}^{5-}$ inside dried CoMo/Al_2O_3 pellets was evaluated as a function of the phosphate concentration in the impregnation solution, the ageing time that was applied and the drying procedure that was used [26]. The technique was also applied to monitor the nature and distribution of Co(II)-complexes inside Co/Al_2O_3 pellets throughout their preparation (impregnation, drying, calcination). By varying the composition of the impregnation solution and the drying procedure, the distribution of Co could be varied between extreme egg-shell and homogeneous. The formation of $CoAl_2O_4$ after calcination could be prevented by the addition of citrate to the impregnation solution. The activity of these catalysts in the Fisher-Tropsch synthesis was tested and maximum activity was found for catalysts with an egg-shell distribution of Co in which Co_3O_4 particles were formed instead of $CoAl_2O_4$ [27].

For the identification of $H_2PMo_{11}CoO_{40}^{5-}$, a combination of Raman and UV-Vis-NIR spectroscopy is essential, as in this way the coordination of both Co and Mo can be revealed. In studies, reported in the open literature, on the preparation of supported catalyst bodies, not much attention has been paid to the effect of concentration-profiles that occur after the impregnation of support bodies. Generally, if one strives to prepare a catalyst with a certain transition-metal complex present on the support, impregnation is simply carried out with a solution containing this specific complex. Why this approach is not always successful was illustrated by the disintegration of the $H_2PMo_{11}CoO_{40}^{5-}$ complex after impregnation with a $H_2PMo_{11}CoO_{40}^{5-}$ solution.

In this work, it was also shown that one can take advantage of the concentration profiles that are established after impregnation to form the desired complex inside the pores of the support at specific positions inside catalyst bodies. In this way, systems with different catalytic functions within a single catalyst body could be created with relatively simple means. In the field of hydrotreating catalysis in particular, extrudates with spatially controlled hydrodesulphurization and hydrodemetallization functions could be envisaged.

Conclusions

The power of combining Raman and UV-Vis-NIR micro-spectroscopy to obtain insight into the physicochemical processes that occur during the preparation of supported catalysts was illustrated by monitoring the disintegration and formation of $H_2PMo_{11}CoO_{40}^{5-}$ inside Al_2O_3 bodies. The distribution of Mo(VI)- and Co(II)-complexes inside the pores of Al_2O_3 pellets was studied after impregnation with CoMoP-solutions of different constitution, using the aforementioned techniques. It was shown that after impregnation with a $H_2PMo_{11}CoO_{40}^{5-}$ solution disintegration of this complex takes place due to a reaction of phosphate with the Al_2O_3 surface. As a result of this reaction, $H_xMo_7O_{24}^{(6-x)-}$ and $[Co(H_2O)_6]^{2+}$ were formed. Due to the limited interaction of Co(II)-complexes with the Al_2O_3 surface, transport of $[Co(H_2O)_6]^{2+}$ was fast and a homogeneous distribution of this complex was achieved almost instantaneously. Transport of negatively charged Mo(VI)-complexes was slow after impregnation with an acidic solution and aging times of several hours were required to obtain full equilibration of the system.

In an alternative approach, the formation of $H_2PMo_{11}CoO_{40}^{5-}$ inside the Al_2O_3 pellets was achieved by the addition of citrate and extra phosphate to the impregnation solution. The reaction of free phosphate with the support resulted in a lower phosphate concentration inside

the pores, creating the right conditions for $H_2PMo_{11}CoO_{40}^{5-}$ to be formed. The strong interaction between phosphate and Al_2O_3 led to strong concentration gradients of this component over the support bodies in the first hours after impregnation. These gradients were used to prepare catalyst bodies with different $H_2PMo_{11}CoO_{40}^{5-}$ distributions. This study clearly illustrates how the possibility to monitor the distribution of metal-complexes in support bodies throughout the preparation process can be of great value for the preparation of industrial supported catalysts in a controlled manner.

Acknowledgments

Leon van de Water and Xander Nijhuis are acknowledged for the development of the UV-Vis-NIR micro-spectroscopy set-up and valuable discussions. Ad Mens is thanked for N_2-physisorption measurements.

References

1 J. V. Lauritsen, S. Helveg, E. Laegsgaard, I. Stensgaard, B. S. Clausen, H. Topsoe, E. Besenbacher, *J. Catal.* **2001**, *197*, 1.
2 R. Prins, V. H. J. de Beer, G. A. Somorjai, *Catal. Rev.-Sci. Eng.* **1989**, *31*, 1.
3 J. Grimblot, *Catal. Today* **1998**, *41*, 111.
4 R. Cattaneo, F. Rota, R. Prins, *J. Catal.* **2001**, *199*, 318.
5 L. Medici, R. Prins, *J. Catal.* **1996**, *163*, 38.
6 L. Coulier, V. H. J. de Beer, J. A. R. van Veen, J. W. Niemantsverdriet, *J. Catal.* **2001**, *197*, 26.
7 A. Griboval, P. Blanchard, E. Payen, M. Fournier, J. L. Dubois, *Catal. Today* **1998**, *45*, 277.
8 A. Griboval, P. Blanchard, L. Gengembre, E. Payen, M. Fournier, J. L. Dubois, J. R. Bernard, *J. Catal.* **1999**, *188*, 102.
9 C. I. Cabello, I. L. Botto, H. J. Thomas, *Appl. Catal. A-General* **2000**, *197*, 79.
10 C. Martin, C. Lamonier, M. Fournier, O. Mentre, V. Harle, D. Guillaume, E. Payen, *Inorg. Chem.* **2004**, *43*, 4636.
11 C. Martin, C. Lamonier, M. Fournier, O. Mentre, V. Harle, D. Guillaume, E. Payen, *Chem. Mater.* **2005**, *17*, 4438.
12 C. I. Cabello, M. Munoz, E. Payen, H. J. Thomas, *Catal. Lett.* **2004**, *92*, 69.
13 K. Y. Lee, M. Misono, *Heterpoly Compounds* in *Preparation of Solid Catalysts* (G. Ertl, H. Knozinger, J. Weitkamp, *Eds.)*, Wiley-VCH, Weinheim, 1999.
14 L. G. A. van de Water, J. A. Bergwerff, T. A. Nijhuis, K. P. de Jong, B. M. Weckhuysen, *J. Am. Chem. Soc.* **2005**, *127*, 5024.
15 R. S. Weber, *J. Catal.* **1995**, *151*, 470.
16 S. Y. Lee, R. Aris, *Catal. Rev. Sci. Eng.* **1985**, *27*, 207.
17 A. V. Neimark, L. I. Kheifez, V. B. Fenelonov, *Ind. Eng. Chem. Prod. Res. Dev.* **1981**, *20*, 439.
18 J. A. Bergwerff, T. Visser, R. G. Leliveld, B. A. Rossenaar, K. P. de Jong, B. M. Weckhuysen, *J. Am. Chem. Soc.* **2004**, *126*, 14548.
19 J. A. R. van Veen, P. Hendriks, E. Romers, R. R. Andrea, *J. Phys. Chem.* **1990**, *94*, 5275.
20 J. A. R. van Veen, P. Hendriks, R. R. Andrea, E. Romers, A. E. Wilson, *J. Phys. Chem.* **1990**, *94*, 5282.
21 L. Pettersson, I. Andersson, L.-O. Öhman, *Inorg. Chem.* **1986**, *25*, 4726.

22 J. J. Cruywagen, E. A. Rohwer, G. F. S. Wessels, *Polyhedron* **1995**, *14*, 3481.
23 L. Le Bihan, P. Blanchard, M. Fournier, J. Grimblot, E. Payen, *J. Chem. Soc. Faraday Trans.* **1998**, *94*, 937.
24 X. Carrier, J. F. Lambert, S. Kuba, H. Knozinger, M. Che, *J. Mol. Struct.* **2003**, *656*, 231.
25 X. Carrier, J. F. Lambert, M. Che, *J. Am. Chem. Soc.* **1997**, *119*, 10137.
26 L. G. A. van de Water, J. A. Bergwerff, B. R. G. Leliveld, B. M. Weckhuysen, K. P. de Jong, *J. Phys. Chem B.* **2005**, *109*, 14513.
27 L. G. A. van de Water, L. G. Bezemer, J. A. Bergwerff, M. Versluijs-Helder, B. M. Weckhuysen, K. P. De Jong, *J. Catal.* **2006**, *242*, 287.

Chapter 6

Magnetic Resonance Imaging as a Non-Invasive Technique to Monitor the Preparation of Supported Catalyst Bodies

Abstract

Three different magnetic resonance imaging methods are presented to monitor the distribution of different components inside a single extrudate as a function of time after impregnation. The distribution of phosphate and (^{13}C labeled) citrate could be derived directly from ^{13}C and ^{31}P images. The detrimental influence of paramagnetic cations on the ^{1}H NMR signal was used to derive quantitative distribution plots of $[Co(H_2O)_6]^{2+}$ complexes after impregnation of Al_2O_3 extrudates with a $Co(NO_3)_2$ solution. The presence of diamagnetic components inside the Al_2O_3 pores resulted in an increase of the T_1 relaxation time of water protons. With the aid of inversion-recovery pulse sequences, the distribution of citrate inside the extrudates could be determined in an indirect manner. The applicability of magnetic resonance imaging techniques in catalyst preparation studies is discussed.

Introduction

In the previous chapters, Raman and UV-Vis-NIR micro-spectroscopy have proven to be valuable techniques for studies into the preparation of supported catalyst bodies. By measurements on bisected pellets information could be derived on the nature and distribution of metal-complexes inside these systems at the different stages of the preparation process [1,2]. However, especially in the analysis of wet extrudates after impregnation, the need to bisect the extrudates before analysis raises the question whether the processes under study are not influenced by the measurement procedure. During Raman and UV-Vis-NIR measurements on bisected extrudates, precautions have to be taken to prevent drying of the sample by absorption of the (laser) light used. Furthermore, although Raman and UV-Vis-NIR spectroscopy are inherently quantitative techniques, the determination of metal-distribution profiles proved to be far from straightforward. Finally, the distribution of complexing agents could only be derived indirectly from Raman and UV-Vis-NIR micro-spectroscopy measurements. Although citrate and phosphate show absorption in the UV-region, bands due to the presence of these compounds could not be distinguished in UV-Vis-NIR spectra recorded on CoMo/Al_2O_3 catalyst bodies, due to the dominating presence of the O→Mo(VI) CT band in this part of the spectrum. The concentration of citrate and phosphate is usually not sufficient for the observation of Raman bands due to C=O and P=O stretch vibrations on top of the Al_2O_3 fluorescence background.

In view of the above-mentioned limitations of the Raman and UV-Vis-NIR micro-spectroscopy methods magnetic resonance imaging (MRI) offers great potential as a complementary technique in studying the preparation of catalyst extrudates. The possibility to "see through" objects and the low frequency of the radiation that is used, make that the objects under study are not affected by the measurement procedure. The vast use of the technique in biological and medical applications is testimony of its non-invasive character. MRI has previously been used to study the flow dynamics in catalytic reactors [3] and monitor the state of catalyst material as a function of the location inside a reactor [4,5]. It has further been applied to study the drying of catalyst bodies [6,7] and to determine the distribution of Cu and Pt complexes catalyst extrudates after drying [8]. In this chapter the possibilities of the technique to study the transport of metal-ion complexes and complexing agents inside extrudates, after pore volume impregnation are evaluated. The non-invasive character of the technique means that a single catalyst extrudate can be monitored throughout the ageing process.

Since the application of MRI in the field of catalysis research is far from widespread [9,10],

it seems appropriate to give a brief, and in many respects simplified, introduction to the technique. More information on the principles of MRI and its applications can be found in references [11,12]. Hereafter, three different experimental procedures are explained that allow one to image the transport of metal-complexes and complexing agents inside extrudates. Imaging of nuclei with unpaired nuclear spin can yield direct information on the distribution of compounds containing NMR-sensitive nuclei. This approach was applied to obtain 2-dimensional images of the distribution of phosphate (through the ^{31}P signal) and citrate (^{13}C) inside wet extrudates after impregnation. The distribution of components could also be derived in an indirect manner from their influence on the ^{1}H NMR signal of water. Using the destructive influence of paramagnetic cations on the ^{1}H NMR signal, it proved possible to obtain quantitative distribution plots of Co(II) as a function of time after impregnation with $Co(NO_3)_2$ solutions. The effect of diamagnetic components on spin-lattice relaxation (T_1) processes was used to monitor the distribution of citrate inside extrudates.

Theory

In MRI, the principles of NMR-spectroscopy are used to obtain images from materials or a living being. When elemental particles with unpaired nuclear spins are exposed to an external magnetic field, their magnetic moments will have the tendency to be aligned with this field. Thus, two energy states are created, one state representing the nucleus with its magnetic field moment along with the external field and a higher energy state representing the nucleus with its magnetic field moment opposed to the external field. The energy difference between the spin states can be overcome by the absorption of radio frequency (RF) photons of a specific energy. The frequency of the radiation that is absorbed is called the Larmor frequency (ν_0) and its value is linearly proportional to the strength of the magnetic field (B) experienced by the nucleus, as expressed in Eq. 1. The gyromagnetic ratio (γ) is a property of a specific isotope.

$$\nu_0 = \gamma \cdot B \qquad \text{(Eq. 1)}$$

The basics of a pulsed NMR-experiment are visualized in Fig. 1. In such an experiment, the magnetization of nuclei in a constant magnetic field (B_0) is manipulated by the application of radio-frequency pulses. In general, the external magnetic field is defined to be oriented in the direction of the Z axis. Hence, at thermal equilibrium the net magnetization vector (M_0) of an ensemble of nuclei is oriented in the direction of the positive Z axis. The application of a 90° RF-pulse rotates the net magnetization vector of the spins about the X axis onto the Y axis. Detection of the signal is carried out by measuring the magnetization vector of the nuclei

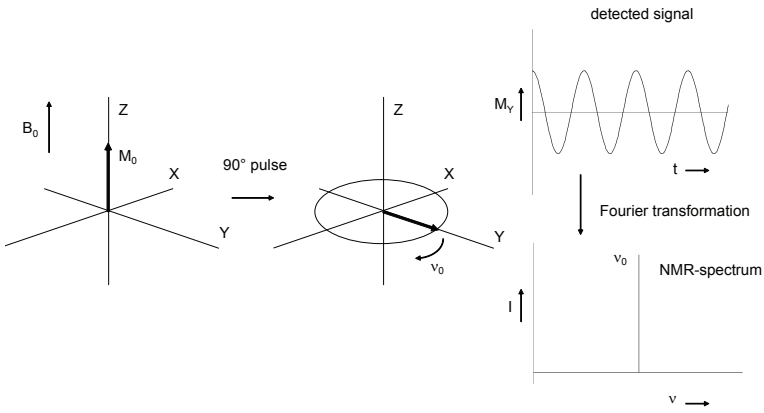

Figure 1. Basics of a pulsed NMR experiment. The orientation of the net magnetization vector (M_0) of NMR-sensitive nuclei, the resulting NMR-signal in the time domain and its conversion into a frequency-domain spectrum via Fourier transformation are schematically depicted.

along the Y axis (M_Y). When located in the XY plane, the magnetization vector will start to rotate around the Z axis at the Larmor frequency (ν_0). Hence, an oscillating signal is detected along the Y axis. This signal can be transformed into a frequency domain spectrum using Fourier transformation.

Electron clouds surrounding the nucleus will affect the magnetic field experienced by the nucleus. Hence, the actual magnetic field at the nucleus is usually smaller than the magnetic field that is applied. The extent of this shielding effect depends on the electronic environment of the nucleus. As a result, nuclei of the same isotope in different molecular environments will give rise to a signal at a slightly different frequency. In NMR spectroscopy, the value of this chemical shift (δ) is used to obtain information on the molecular structure of the sample.

The situation depicted in Fig. 1 is rather simplified. In reality, the intensity of the detected signal is not constant, but decreases with time after application of a 90° pulse as the system returns to its thermal equilibrium where the net magnetization vector is oriented along the positive Z axis. The signal is therefore called the free-induction decay (FID) signal. Different relaxation processes influence the manner in which the FID-signal decreases with time. Spin-spin (T_2) relaxation processes originate from the fact that, all nuclei in the sample experience a slightly different magnetic field. This is due to inhomogeneities in the applied magnetic field (inhomogeneous) and interaction with other molecules (homogeneous). Hence, after the application of the 90° RF-pulse, the magnetization vectors of the individual nuclei will revolve around the Z axis at a different frequency. In Fig. 2, this is illustrated for three nuclei (1, 2 and 3) that experience a slightly different magnetic field and hence rotate at a different frequency

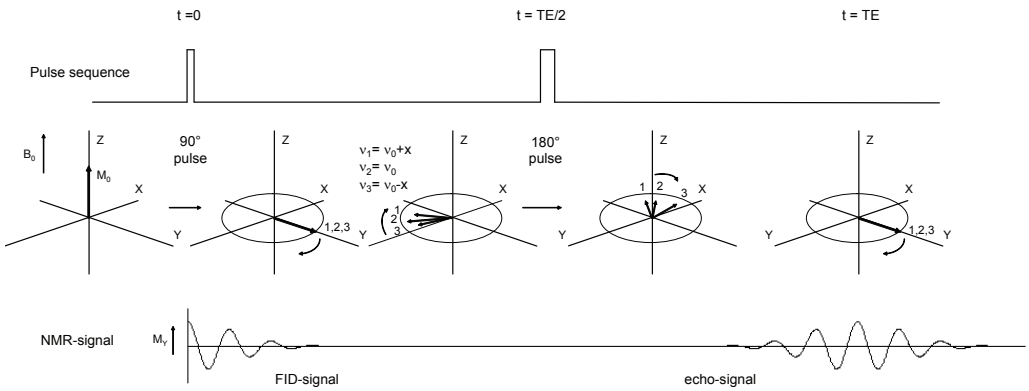

Figure 2. Basic principles of a spin-echo pulse sequence. The influence of the different RF-pulses (top) on the orientation of the magnetization vector of nuclei 1,2 and 3, each experiencing a slightly different magnetic field (middle) and the detected signal (bottom) is illustrated.

(ν_0, ν_0+x, ν_0-x). As a result, the magnetization in the XY plane starts to dephase, as shown in the images. The total magnetization vector in the XY plane (M_{XY}) decreases and the signal that is detected decreases as a function of time (t), as expressed in Eq 2. In this equation, T_2 defines the time after the application of the 90° pulse for which the transverse magnetization in the XY plane is reduced by a factor of e.

$$M_{XY} = M_0 e^{\frac{-t}{T_2}} \qquad \text{(Eq. 2)}$$

A so-called spin-echo pulse sequence can be used to measure a signal at some point in time after application of the 90° pulse. The pulses that are applied in this sequence and their effect on the magnetization vector of different nuclei (1, 2 and 3) are presented in Fig. 2. In a spin-echo pulse sequence, an additional 180° pulse is applied, at some point in time (TE/2) after the application of the 90° pulse. As a result, the magnetization vectors of the individual nuclei are rotated about the Y axis. After application of the 180° pulse, the vectors will continue to rotate around the Z axis at their respective Larmor frequencies. Note that vectors that rotate at a higher frequency (ν_0+x) are now running behind the vectors that revolve at a smaller frequency (ν_0-x). When the magnetic field experienced by individual nuclei is constant with time, the magnetic field vectors of all nuclei are again oriented along the positive Y axis at time TE (echo time). Hence, around this point in time, an echo signal can be detected. However, interactions with molecules make that the magnetic field experienced by the nuclei changes constantly and refocusing of the signal is not complete. The intensity of the signal detected at TE yields information on the homogeneous component of spin-spin relaxation of the nuclei under study.

Spin-lattice (T_1) relaxation processes cause the net magnetization vector of the nuclei to return to their equilibrium position along the positive Z axis after manipulation by an RF-pulse. The rate at which this process takes place is governed by the T_1 relaxation time. As visualized in Fig. 3, after application of a 180° RF-pulse, the magnetization vector is positioned along the negative Z axis. The net magnetization along the Z axis (M_Z) as a function of time after application of the 180° pulse (t) can be calculated through Eq. 3. Its value is plotted in the graph in Fig. 3 for three nuclei (a, b, c) with different T_1. A so-called inversion-recovery pulse sequence can be used to selectively suppress the signal of nuclei with a specific T_1. In this procedure, a 180° pulse is applied first. At a certain point in time after this pulse, often referred to as the variable delay (VD), a 90° pulse is applied to rotate the magnetization vector into the XY plane for signal detection. When, for a specific nucleus (b in Fig. 3) $T_1 = VD/\ln 2$, the magnetization vector along

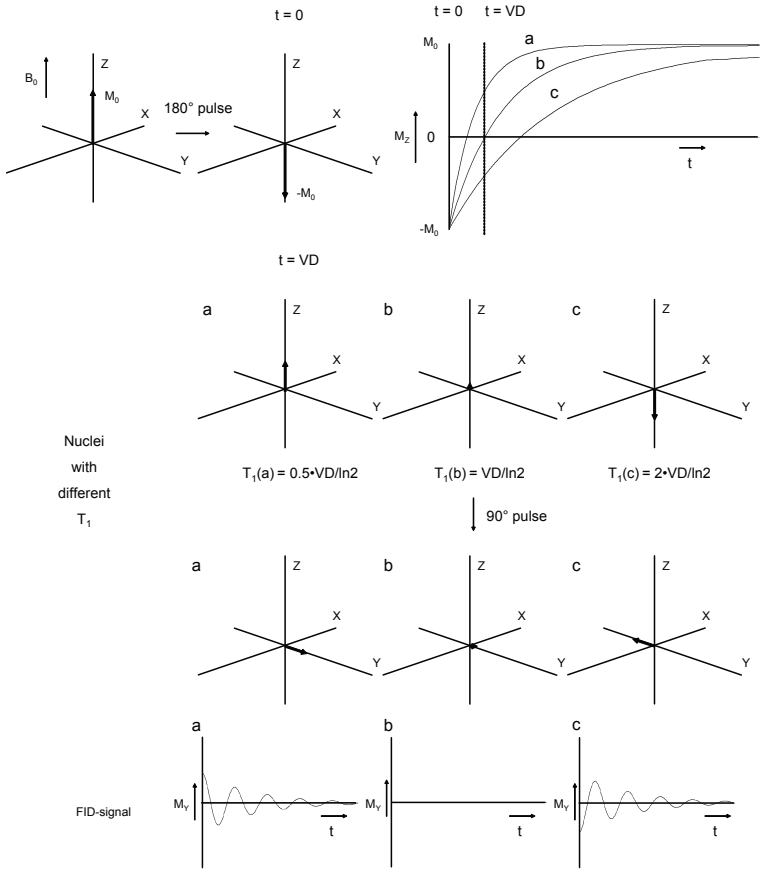

Figure 3. Lay out of an inversion-recovery experiment. The influence of the different RF-pulses on the orientation of the magnetization vector of nuclei a, b and c with different T_1 and the detected signal is illustrated. The net magnetization in the Z direction, as a function of time after application of the 180° pulse is presented as well (bottom left).

the Z axis is zero when the first 90° pulse is applied in the spin-echo pulse sequence, and no signal is observed. For nuclei (a and c) with a different T_1, a signal is observed, since M_z was not zero when the 90° pulse was applied.

$$M_Z = M_0\left(1 - 2e^{-\frac{t}{T_1}}\right) \qquad \text{(Eq. 3)}$$

In MRI, magnetic field gradients are used to obtain information on the spatial distribution of nuclei in a specific sample. Spatial resolution can be obtained in three different ways. First of all, a magnetic field gradient (G_Z) can be in place when the first 90° pulse is applied. Nuclei present at different positions along the Z axis now experience a different magnetic field strength. When the radio-frequency pulse of a specific frequency is applied, only the magnetization of nuclei present in a specific XY slice in the sample will be affected and the signal that is detected only originates from this section of the sample. In practice, slice selection was used to record an image from the cross-section of an extrudate. As schematically depicted in Fig. 4, the extrudate is positioned parallel to the Z axis. The image that is obtained represents a slice near the center of the extrudate. The thickness of the selected slice can be altered by changing the magnetic field gradient. The total number of nuclei that is observed, and hence the intensity of the total signal is inversely proportional to the slice thickness. In experiments in which the signal was detected of nuclei with small gyromagnetic ratio and low concentration, no gradient was employed in the Z direction and nuclei in the entire volume inside the RF-

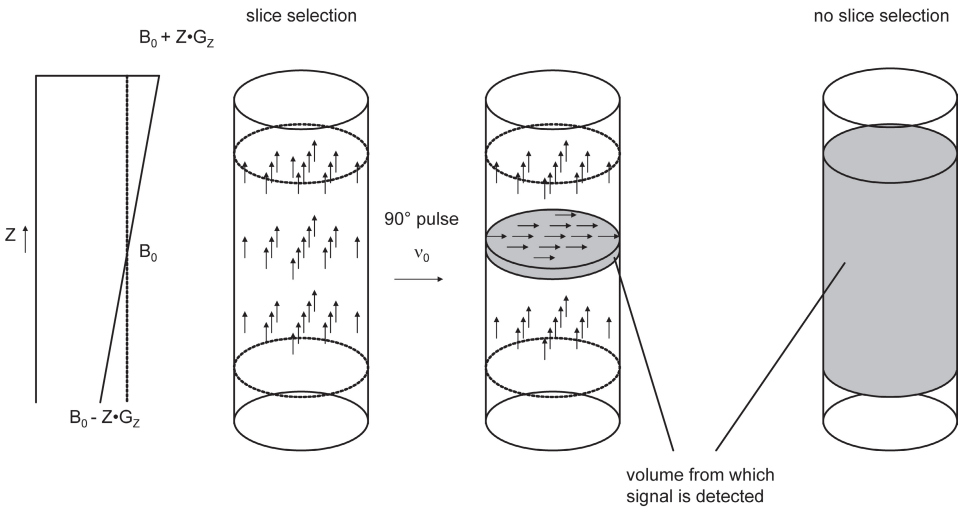

Figure 4. Lay out of an MRI experiment on catalyst extrudates with (left) and without (right) the application of slice selection. The presence of a magnetic field gradient enables one to selectively excite nuclei in a certain XY plane in the sample.

coil were excited to maximize the total signal. However, since the length of the extrudate was larger than the RF-coil, the tips of the extrudates were not observed. The section of the extrudate from which the signal was detected, when slice-selection is omitted, is indicated in Fig. 4. After impregnation, transport of components takes place from all external surfaces towards the core of the extrudate. However, only in the tips of the extrudate, transport from the small surface at the base of the cylindrical extrudate has an influence on the radial distribution profile of components inside the extrudate. In the volume from which the image is detected, transport merely takes place in the direction perpendicular to the extrudate axis, from the lateral surfaces towards the extrudate core. Hence, the recorded image can still be assumed to be representative of the cross-section of a cylindrical extrudate of infinite length.

To obtain spatial resolution along the X axis, a magnetic field gradient was applied along this direction during the detection of the signal. This procedure is called frequency-encoding and its principles are graphically depicted in Fig. 5. At each point along the X axis, nuclei now experience a different external magnetic field. Hence, after application of the 90° pulse, the magnetization vectors of these nuclei start to revolve around the Z axis at a different frequency (Eq. 1). Consequently, the signal that originates from these different nuclei oscillates at a different frequency as well. Fourier transformation of the free induction decay (or spin-echo) signal yields a spectrum in which a signal at a specific frequency represents the presence of a nucleus with a specific X coordinate.

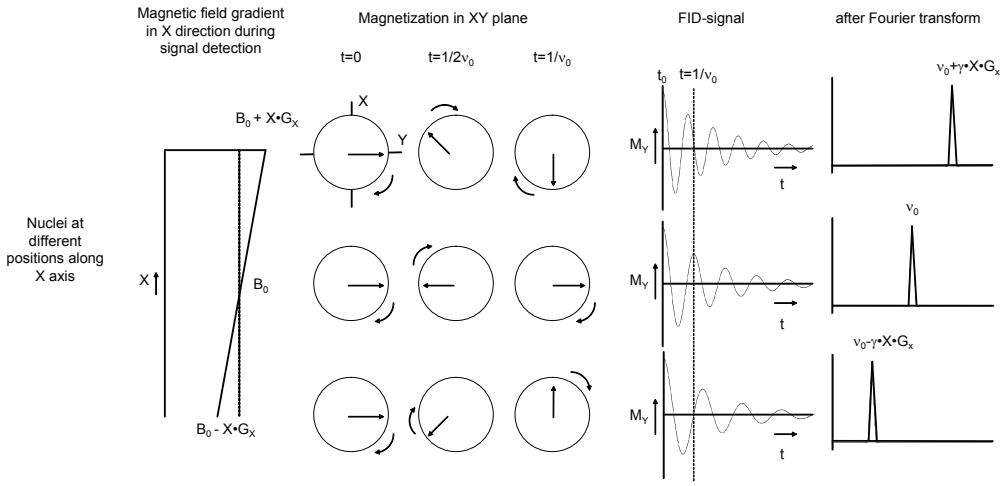

Figure 5. Basic principle of the frequency encoding method used in MRI experiments. The presence of a magnetic field gradient in the X-direction during signal detection yields a signal of different frequency for nuclei positioned at different locations along the X-axis.

Phase-encoding gradients were used to obtain spatial resolution in the Y direction. The basics of this method are illustrated in Fig. 6. A magnetic field gradient was applied along the Y axis for a certain period of time after application of the 90° pulse at t=0. During this period, the magnetization vectors of nuclei located at different positions along the Y axis rotate in the XY plane at a different frequency, as discussed above. When the magnetic field gradient is removed (for example at $t=1/\nu_0$ in Fig. 6), the magnetization vectors of the different nuclei continue to rotate, but now at identical frequencies. In contrast to the frequency encoding procedure, signal detection takes place in the absence of a magnetic field gradient. Hence, the frequency at which the magnetization vectors rotate, and thus the frequency of the oscillating signal originating from the individual nuclei is identical. However, a different phase-shift in this oscillating signal is observed for nuclei at different positions along the Y axis. If one is able to determine this phase-shift, one can determine the location of the different nuclei. In phase encoding, the magnetic field gradient is changed in a number of small steps, where after the signal is detected.

When frequency encoding and phase encoding are applied simultaneously, information on the distribution of nuclei in the XY plane can be obtained. 2-Dimensional Fourier transformation of the complete data set delivers the distribution of nuclei in the XY plane, which forms the

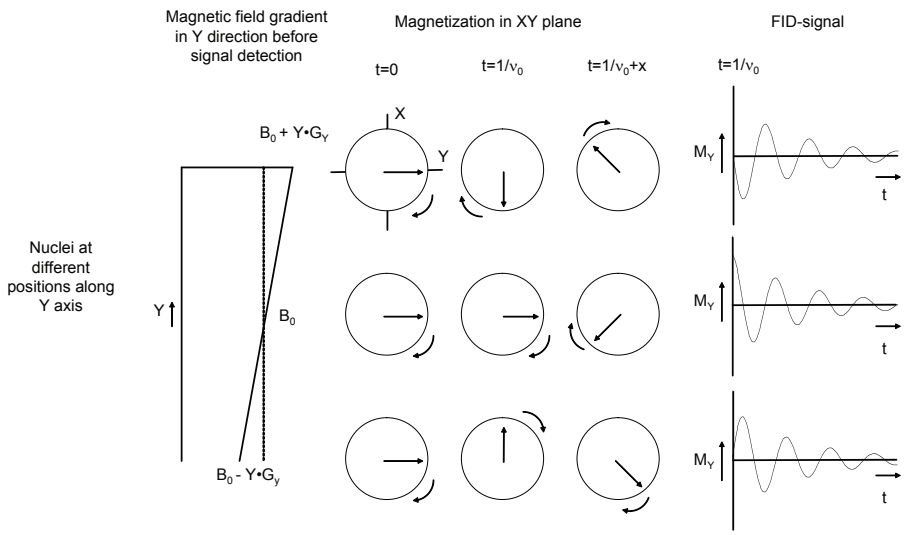

Figure 6. Basic principles of the phase encoding method used in MRI experiments. The presence of a magnetic field gradient in the Y direction before signal detection yields a signal with a different phase for nuclei positioned at different locations along the Y axis.

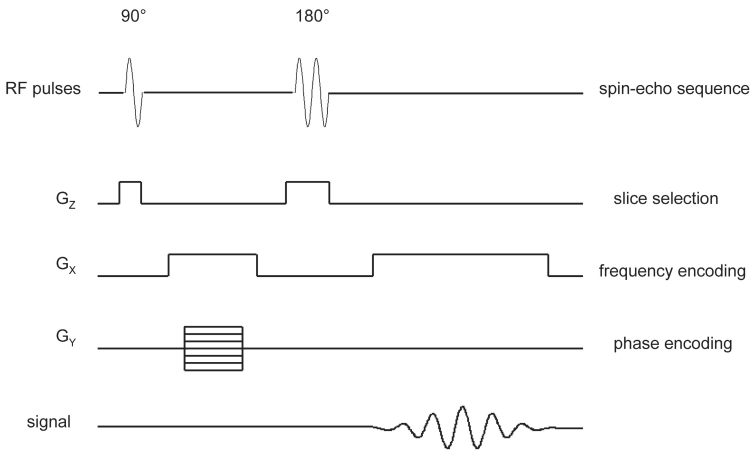

Figure 7. Schematic timing diagram of the MRI measurements used for studies on the preparation of catalyst extrudates.

2-dimensional image. The different RF-pulses and the magnetic gradients that are applied during a typical MRI experiment on catalyst extrudates are summarized in Fig. 7. In this so-called timing diagram, the signal that is detected is also shown. The time between subsequent experiments is called the repetition time.

Experimental

The same type of γ-Al_2O_3 extrudates was used for all impregnation experiments. The diameter of these extrudates was 3.85 mm and the average length 12 mm. The BET surface area of the support was 149 m^2/g and its pore volume was 0.39 ml/g. The average pore diameter was 8 nm, as determined by N_2 physisorption. XRF-analysis showed that S (0.45 wt% SO_3), Si (0.23wt% SiO_2), Ca (0.05wt% CaO) and Fe (0.04 wt% Fe_2O_3), were present as the main impurities. The PZC of this material was 7.8, as determined by potentiometric mass titrations [13]. Only for the ^{31}P MRI measurements, extrudates of the same type of Al_2O_3, but with 3.2 mm diameter were used.

For a typical experiment, the impregnation solution was applied to a single extrudate. Care was taken that sufficient solution was applied to completely fill the pores of the extrudate. Impregnation was carried out from one side first to prevent the formation of air bubbles inside the extrudates. After impregnation, any excess solution was removed. Dehydration of the wet extrudates was prevented by ensuring 100% humidity in the NMR-tube and in the containers used for storing the samples. Impregnation solutions were prepared from 85% aqueous H_3PO_4 solution (Merck, p.a.), 99% 1,5 ^{13}C-labeled citric acid (Sigma Aldrich), $Co(NO_3)_2 \cdot 6\,H_2O$ (Acros, p.a.) and citric acid (Acros, p.a.) in the concentrations mentioned in the main text. NaOH (Merck,

p.a.) was used to increase the pH of the solutions to the desired value.

All MRI experiments were performed at the International Tomography Center SB RAS in Novosibirsk (Russia) on a Bruker Avance DRX 300 MHz wide bore spectrometer with imaging accessories at 300.13 MHz (^{1}H), 121.49 MHz (^{31}P) or 75.47 MHz (^{13}C). Two-dimensional images were recorded using a two-pulse spin-echo sequence. In the ^{1}H MRI measurements, slice selection was used to record the signal from 2 mm thick slice of the extrudates. Frequency encoding was applied in the X direction yielding a spatial resolution of 139 µm for ^{1}H MRI measurements. The application of phase encoding gradients in the Y direction resulted in a spatial resolution of 231 µm in this direction in the ^{1}H images.

Results and Discussion

To determine the distribution of components inside catalyst bodies through MRI measurements, three different strategies can be applied, i.e. direct imaging of NMR-sensitive nuclei (i), indirect imaging of paramagnetic components (ii) and indirect imaging of diamagnetic components (iii). In this section, the applicability of these experimental procedures to study the preparation of supported catalyst bodies is evaluated on the basis of a number of case studies.

Direct imaging of NMR-sensitive nuclei

As a proof of principle, the distribution of ^{1}H ($I = ½, \gamma = 267.5 \cdot 10^{6}$ rad·T^{-1}·s^{-1}) and ^{31}P ($I = ½, \gamma = 108.4 \cdot 10^{6}$ rad·T^{-1}·s^{-1}) nuclei was monitored after immersion of a dry extrudate in a 0.76 M H_3PO_4 solution in a NMR-tube with 4.2 mm internal diameter. In Fig. 8, ^{1}H and ^{31}P images detected just after immersion are presented. In the ^{1}H image, a bright ring is observed, representing the signal of the solution outside the extrudate. The cross-section of the extrudate itself is observed as an area of lower intensity. The ^{1}H MRI image demonstrates that capillary action leads to an almost instantaneous permeation of water into the extrudate. An identical ^{1}H NMR signal is detected for all positions inside the extrudate within 250 s after immersion. The ^{31}P

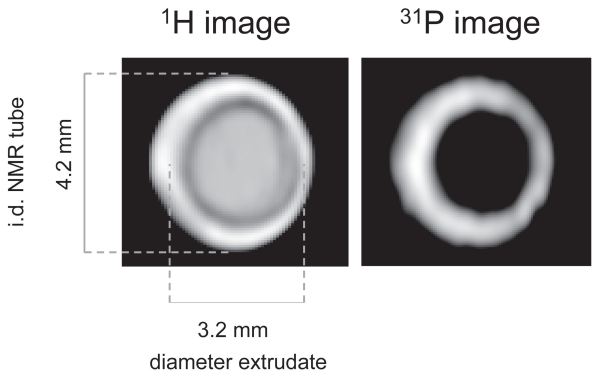

Figure 8: ^{1}H and ^{31}P images detected 250 s after immersion of a dry Al_2O_3 extrudate in a 0.76 M H_3PO_4 solution.

image shows that phosphate, on the other hand, is only present in the solution outside the extrudate and in the outer ring of the extrudate. Phosphate is not transported with the flow of water into the pore system due to its reaction with the Al_2O_3 surface.

In a subsequent experiment, an Al_2O_3 extrudate saturated with water, was placed in an NMR tube filled with the H_3PO_4 solution. Fig. 9 shows the resulting series of images detected using the ^{31}P NMR signal. In this case, no signal was detected from the solution outside the extrudate. As compared to phosphate ions in solution, spin lattice relaxation processes of ^{31}P nuclei occur much faster when the phosphate is contained in the Al_2O_3 pores. By choosing a relatively fast repetition time, the net magnetization vector of the ^{31}P nuclei of phosphate in solution was not allowed to return to its equilibrium orientation between measurements, and the signal of these nuclei was suppressed. At the same time the sensitivity for the volume inside the extrudate was optimized as a fast repetition time decreases the time required for the detection of a single image. The images clearly illustrate the dynamics of phosphate transport inside the same extrudate, illustrating the non-invasive character of the technique. A single extrudate can be used to monitor the processes that take place during impregnation and ageing. After immersion of the extrudate filled with water into the H_3PO_4 solution, the phosphate concentration gradient will bring about diffusion of phosphate towards the inside of the extrudate. A uniform distribution of phosphate is only achieved 14 h after impregnation due to adsorption of phosphate on the support surface.

Although the experiments described above provided information on the interaction of phosphate with the Al_2O_3 support, the procedure that was used to introduce phosphate into the extrudate was distinctly different from the pore volume impregnation method generally

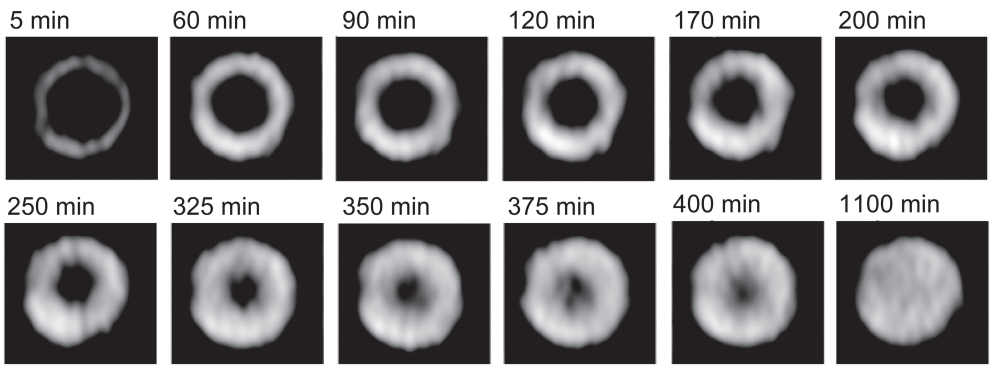

Figure 9. Selected ^{31}P images recorded at several points in time after immersion of a water-filled Al_2O_3 extrudate into a 0.76 M H_3PO_4 solution. The spatial resolution in these images is 172 μm × 371 μm.

used in an industrial context. After immersion of the wet extrudate into the H_3PO_4 solution, phosphate penetrates the pore volume of the extrudate through diffusion. This diffusion is slow due to the adsorption of phosphate onto the Al_2O_3 surface. The extrudate continues to draw phosphate from the H_3PO_4 solution until the concentration gradient is completely flattened. The amount of phosphate that is ultimately present in the extrudate depends on the adsorption capacity of the Al_2O_3.

In the case of pore volume impregnation, no excess solution is applied to the support. Two distinct steps can now be distinguished in the transport of components through the pore-system of the support. First of all, components in the impregnation solution travel with the convective flow of the water into the pore system of the dry support. Adsorption of a certain component on the Al_2O_3 surface makes that its transport is hampered. The thus established concentration gradient is subsequently reduced during ageing through desorption of the compound from the surface, followed by diffusion. In contrast to the impregnation with excess solution, the total amount of a specific component present in a single extrudate is merely determined by its concentration in the impregnation solution and doesn't change with time. To evaluate the value of MRI to study pore volume impregnation, dry extrudates were impregnated with a 3.0 M PO_4^{3-} solution of pH 1 and 8. The 1-dimensional plots of the NMR signal as a function of the position inside the extrudate are presented in Fig. 10. Although the total phosphate concentration was identical in both cases, the signal obtained from the

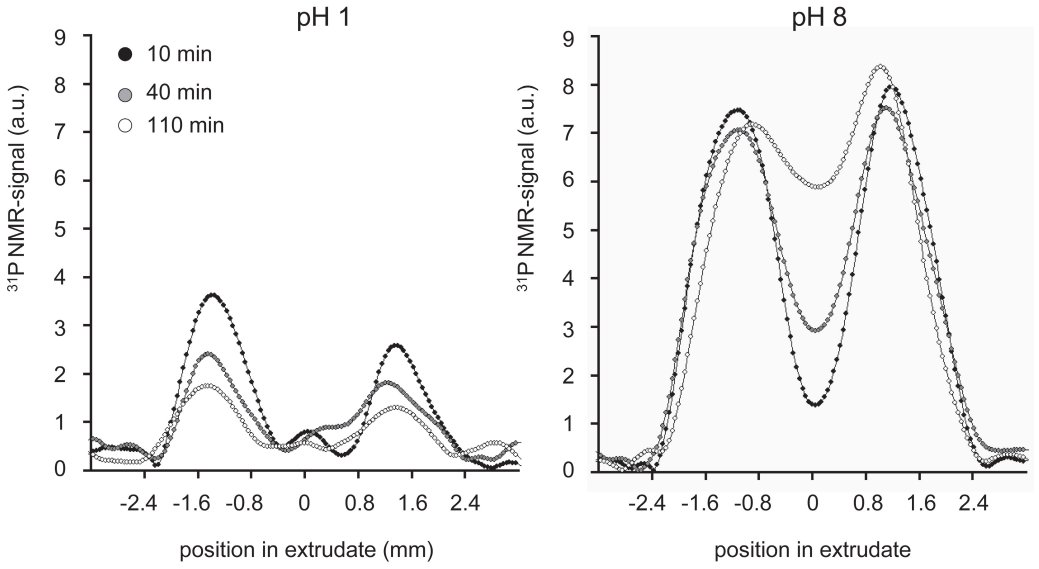

Figure 10. 1-Dimensional profiles of the ^{31}P signal as a function of the position in the extrudate at different points in time after impregnation of an Al_2O_3 extrudate with a 3.0 M H_xPO_4 solution of pH 1 and 8.

extrudate impregnated with the solution of pH 8 was much stronger. Apparently, a large fraction of the ^{31}P nuclei was not observed, when impregnation was carried out with the acidic solution. Adsorption of phosphate and the formation of a surface $AlPO_4$ phase results in a loss in mobility of the ^{31}P nuclei. As a result, the T_2 relaxation time of the ^{31}P nuclei is decreased and the ^{31}P NMR signal is suppressed [14,15]. Impregnation with the pH 8 solution resulted in a reasonably fast transport of phosphate. Equilibration of the concentration gradient that was observed just after impregnation took place within 2 h. During this period, the total signal that was obtained remained more or less constant. The number of ^{31}P nuclei that was observed didn't change, since only a weak interaction existed between phosphate and the support. Probably, no phosphate was irreversibly removed from the solution inside the pores.

Similar phenomena were observed when pore volume impregnation was carried out with a 0.40 M solution of citric acid (1,5 ^{13}C-labeled, 99 atom% ^{13}C) of pH 1 and 9. The ^{13}C ($I = ½, \gamma = 67.26 \cdot 10^6$ rad$\cdot T^{-1} \cdot s^{-1}$) images of these samples, recorded just after impregnation are presented in Fig. 11. When impregnation was carried out with an alkaline solution, the contours of the extrudate could be observed. Due to the small gyromagnetic ratio (four times smaller than ^1H) and the resulting low sensitivity of ^{13}C nuclei, considerable time (45 min) was required for the detection of a single ^{13}C image. Furthermore the smaller gyromagnetic ratio also results in a loss in spatial resolution. When the same magnetic field gradients are used, the difference in Larmor frequency of two ^{13}C nuclei with different coordinates is smaller, as compared to protons positioned at the same locations. As a result the presence of two protons at different positions is more easily resolved. In general, the spatial resolution in an MRI experiment is inversely proportional to the gyromagnetic ratio of the nuclei. After impregnation with the acidic solution, no signal was detected. At low pH, the interaction of the citrate with the surface was stronger and, as a result, the NMR signal was suppressed, as explained before for the ^{31}P MRI measurements. The mechanism of adsorption of citrate on Al_2O_3 surfaces is discussed in more detail later in this chapter.

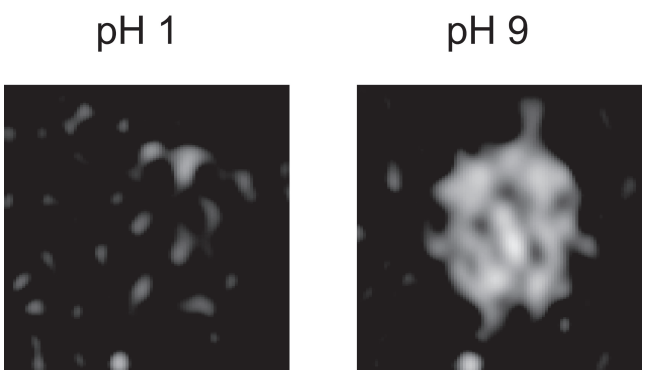

Figure 11. ^{13}C images of an Al_2O_3 extrudate directly after impregnation with a 0.40 M ^{13}C labeled citrate solution of pH 1 and 9.

Indirect imaging of paramagnetic components

As a result of the large gyromagnetic ratio of protons and the high concentration of these nuclei inside the impregnated extrudates, ^{1}H MRI can be carried out with great sensitivity on these systems. Subsequently, one can make use of the effect of different components in the impregnation solution on the ^{1}H NMR signal, to derive information on their distribution inside the catalyst bodies. Unpaired electrons create their own magnetic field. The presence of paramagnetic compounds in a sample, leads to a decrease in the T_2 relaxation time of NMR-sensitive nuclei. When a spin-echo pulse sequence is used, the signal is detected at some point in time after application of the 90° pulse and the signal from nuclei with small T_2 is suppressed.

To determine the effect of Co(II) ions on the ^{1}H NMR signal, extrudates were impregnated with $Co(NO_3)_2$ solutions of different concentrations (0-1.0 M Co). After equilibration for 15 h, ^{1}H images were recorded on these extrudates. In Fig. 12, 1-dimensional plots of the ^{1}H-NMR signal as a function of the location along the axes of the extrudates are presented. As can be observed, the average intensity of the NMR-signal decreased with increasing Co(II) concentration in the impregnation solution. Irregularities in the extrudates make that the signal shows variations in intensity as a function of the position inside the sample. These inhomogeneities may consist

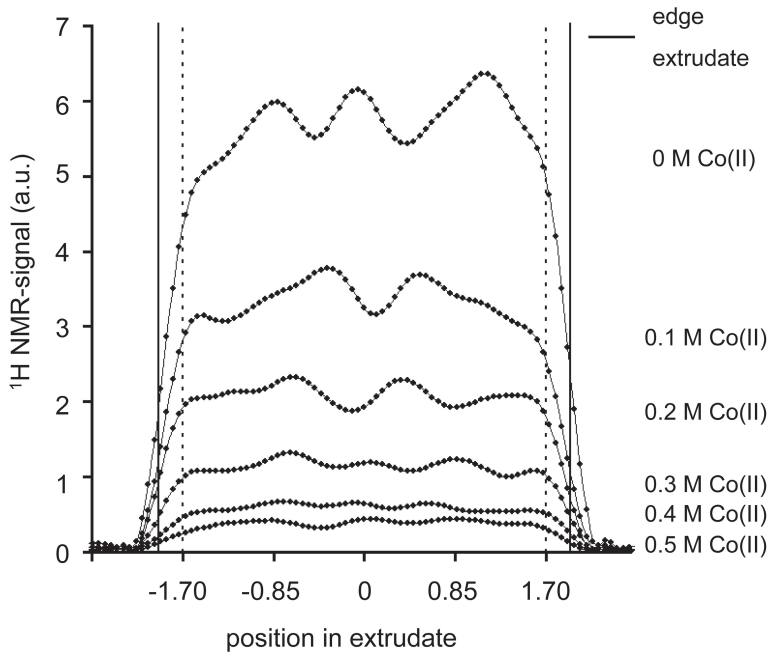

Figure 12. 1-Dimensional profiles of the ^{1}H signal as a function of the position in the extrudate after impregnation of an Al_2O_3 extrudate with water and $Co(NO_3)_2$ solutions with different Co-concentrations.

of domains with a different pore-structure. The presence of smaller pores leads to an increased interaction of water with the pore walls and suppression of the signal. Voids in the extrudate may result in a higher signal as the density of protons is higher at these positions.

From the spatial resolution of the measurements (231 µm, represented by 4 data-points in the 1-D plot) and the actual size of the extrudates (3.85 mm), the positions of the extrudate edges in the 1-D profiles could be determined. The edges are indicated by the solid lines in Fig. 12. The ^{1}H NMR signal was found to decrease towards the external surface of the extrudates. This may be due to a larger T_1 relaxation time of the water protons in the pores on the periphery of the catalyst bodies. As a result of the relatively fast repetition time used in these experiments (1 s), the signal from protons with larger T_1 was suppressed. Another explanation may be that the extrudates were not in an exact vertical position during measurements and the signal from the edges of the sample might be slightly faded. The signal recorded from a 0.25 mm thick surface layer, as indicated by the dotted lines in Fig. 12, was further omitted in the 1-D profiles, since no reliable information could be obtained from these areas.

From the 1-D plots in Fig. 12, the average ^{1}H NMR-signal was determined as a function of the Co(II) concentration in the impregnation solution. From these values, a calibration line was constructed, which is presented in Fig. 13. The empirical relation between the Co(II)-concentration and the ^{1}H NMR-signal (I_{NMR}) could be described in the concentration range of 0-0.5 M Co(II) by a third-order polynomial, as expressed in Eq. 4. From the calibration curve, it can be deduced that the sensitivity of the technique to determine the concentration of Co(II) inside the Al_2O_3 pores is highest in the concentration range of 0-0.3 M. When higher Co(II)-concentrations were applied, the NMR-signal became too low.

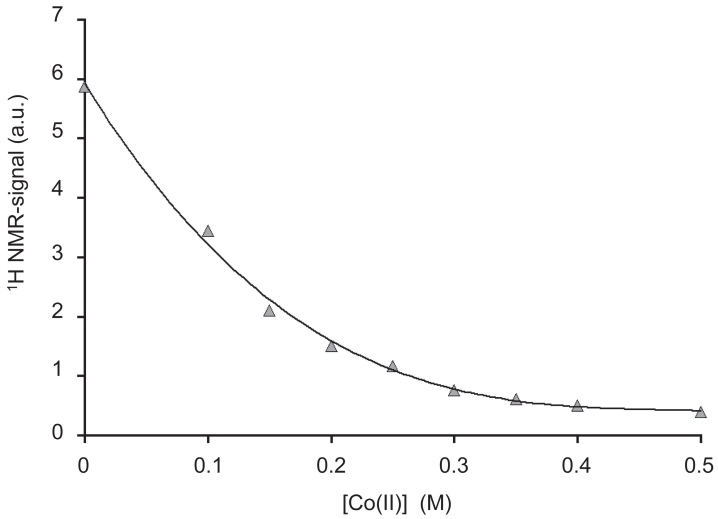

Figure 13. Plot showing the influence of the concentration of Co(II) ions in impregnation solutions on the intensity of the average ^{1}H NMR signal of protons inside extrudates impregnated with $Co(NO_3)_2$ solutions.

$$I_{NMR} = -47.6 \cdot [Co(II)]^3 + 68.7 \cdot [Co(II)]^2 - 33.5 \cdot [Co(II)] + 5.9 \quad \text{(Eq. 4)}$$

The calibration curve in Fig. 13 was used to derive quantitative information on the transport of Co(II) after impregnation of an Al_2O_3 extrudate with a $Co(NO_3)_2$ solution. Impregnation was carried out with a 0.2 M Co(II) solution for maximum sensitivity, which corresponds to a theoretical CoO loading of 0.5 wt% in calcined catalysts. ^{1}H images were obtained at several points in time after impregnation, which are presented in Fig. 14. The corresponding 1-D intensity profiles were converted into quantitative Co(II) distribution plots, using Eq. 4. The resulting profiles are presented in the same figure. It can be seen that transport of Co(II) after pore volume impregnation indeed takes place in two distinct steps. First of all, $[Co(H_2O)_6]^{2+}$ complexes are transported into the extrudate as they travel with the convective flow of the water solvent. Adsorption of Co(II) on the support surface takes place as coordinating water ligands are exchanged for support oxygens [16,17]. A Co(II) concentration profile results just after impregnation. Since impregnation was carried out without excess solution, the total amount of Co(II) inside the extrudate remained constant as a function of time after

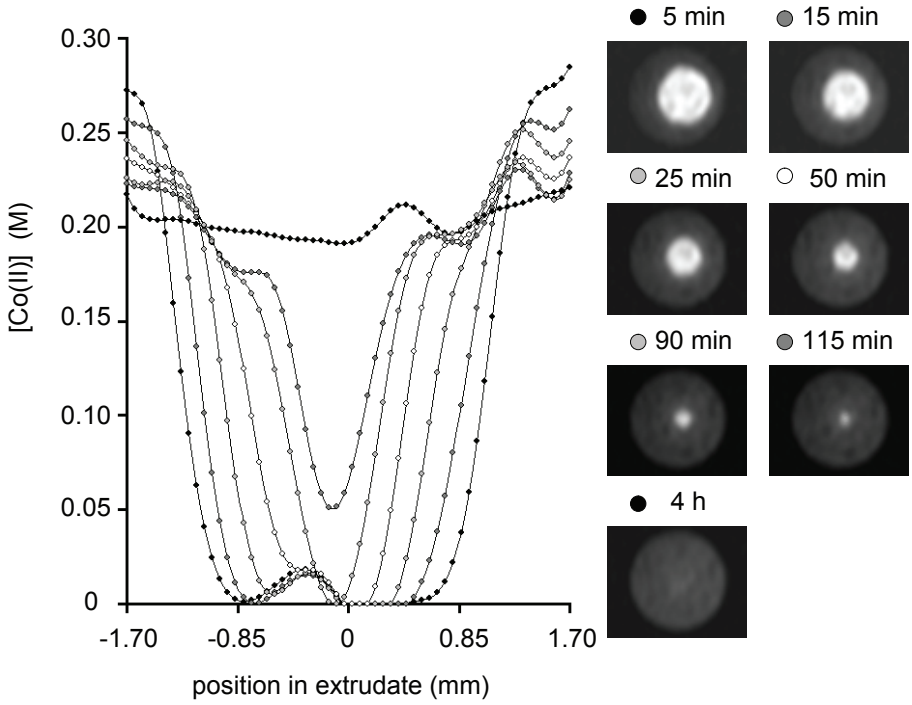

Figure 14. ^{1}H images of an Al_2O_3 extrudate recorded at several points in time after impregnation with a 0.2 M $Co(NO_3)_2$ solution (right). The resulting quantitative Co(II) distribution plots are presented on the left. *For a color-version of this figure, see Appendix (p. 208).*

impregnation. Initially, the Co(II)-concentration near the outer surface of the extrudate was therefore higher than 0.2 M. The concentration gradient over the extrudate resulted in diffusion of Co(II)-complexes towards the center. The Co(II)-front travels into the catalyst body and eventually a homogeneous distribution of Co and an average Co(II)-concentration of 0.2 M was observed 4 h after impregnation. In the experiments described in chapter 5, a homogeneous distribution of Co was observed instantaneously after impregnation. However, in these experiments different Al_2O_3 bodies were used and a higher Co(II)-concentration was applied.

Indirect imaging of diamagnetic components

As mentioned before, the interaction of water with the support leads to a decrease in the T_1 and T_2 relaxation times of the water protons. This is partly due to the presence of paramagnetic impurities in the support material. XRF-analysis indicated the presence of iron (250 µg/g), but also nickel (88 µg/g) and manganese (74 µg/g) were found to be present in small concentrations inside the Al_2O_3 extrudates. Furthermore, the mobility of water molecule is decreased by their interaction with the support. An accumulation of diamagnetic compounds near the support surface may lead to a decrease in the interaction between water and the support and an increase in the NMR-relaxation times of the protons inside the Al_2O_3 pores. As explained in the theory-section, the signal of nuclei with a specific T_1 can be selectively suppressed by using an inversion recovery pulse sequence. By systematically varying the variable delay (VD), the distribution of diamagnetic components can thus be determined. Previously, a similar procedure was used to determine the distribution of H_2PtCl_6 complexes inside dried Al_2O_3 extrudates [8].

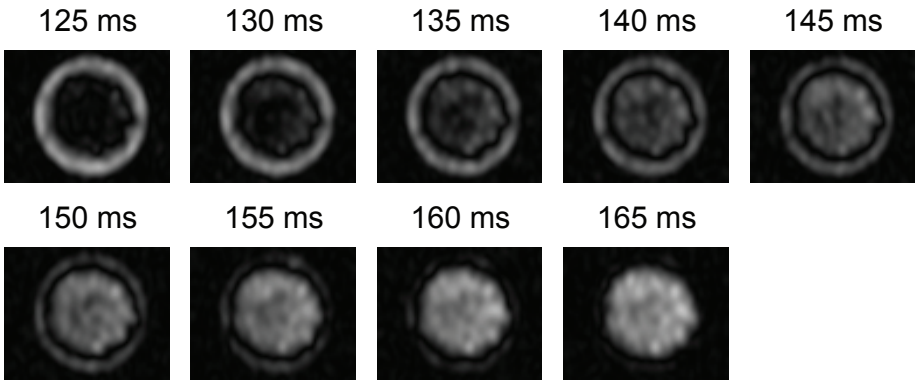

Figure 15. ^1H images of an Al_2O_3 extrudate 15 h after impregnation with a 0.4 M citrate solution of pH 5. A different delay time between the 180° and 90° pulses (VD, indicated above the images) was used in the inversion recovery pulse sequence to detect the different images.

In this case, the approach was applied to monitor the distribution of citrate inside Al_2O_3 extrudates after impregnation. ^1H images of an extrudate, 15 h after impregnation with a 0.40 M citric acid solution of pH 5 were recorded with different values for the VD period between the 180° and 90° pulses in the inversion recovery sequence. The resulting images are presented in Fig. 15 and the corresponding 1D-profiles are shown in Fig. 16 a. When a VD of 125 ms was applied, only the signal from protons in the outer ring of the extrudate could be observed. The signal from the center of the extrudate was suppressed. Apparently the protons near the core had a T_1 relaxation time of approximately 180 (125/ln2) ms. When the VD period is systematically increased, a ring is observed were the signal is suppressed, which slowly expanded towards the outside of the extrudate with increasing VD. Finally, at a VD of 165 ms, only the signal from an outer ring of ~200 µm was completely suppressed.

These results can be explained by assuming an egg-shell distribution of citrate inside the Al_2O_3 extrudates. Near the outer surface, the citrate concentration was highest and the T_1 relaxation time of the protons was increased to 225 (165/ln2) ms. The expanding ring in the ^1H images corresponds to the minima in the 1-dimensional ^1H NMR-signal profiles. By determining the VD, for which the signal is minimal for all positions in the sample, the T_1 relaxation time of protons at different locations inside the sample could be determined. From the resulting plot (Fig. 16 b), one can obtain an impression of the egg-shell distribution of citrate inside the

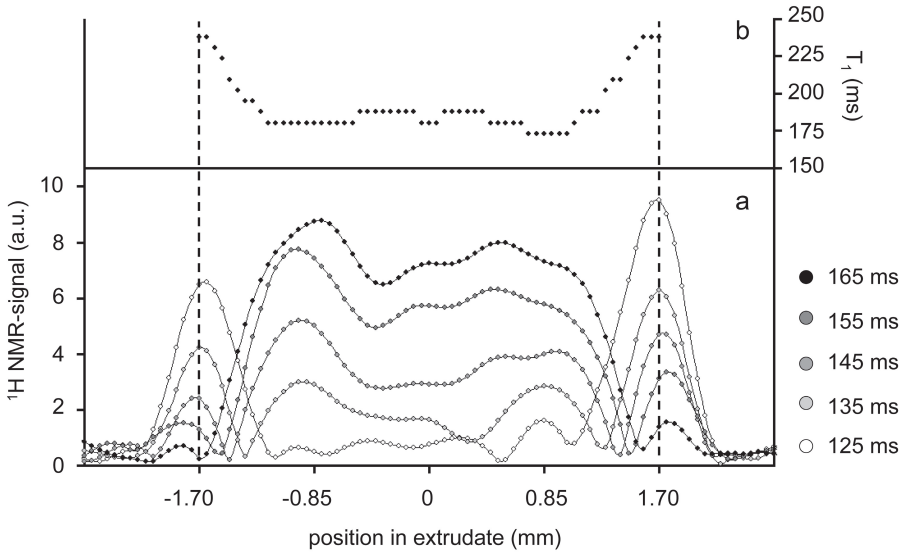

Figure 16. 1-Dimensional profiles of the ^1H signal as a function of the position in the extrudate after impregnation of an Al_2O_3 extrudate with a 0.40 M citrate solution of pH 5. Profiles were obtained with different values for VD, as indicated on the right (a). A plot showing the T_1 of water protons at different positions inside the extrudate is included as well (b).

extrudate. The T_1 relaxation time is expected to increase with increasing citrate concentration. From the shape of the plot in Fig. 16 b, it can be assumed that at positions within 1 mm from the core of the pellet no citrate is present. Nevertheless, the T_1 of protons at these positions (180 ms) is higher than the T_1 of protons in an Al_2O_3 extrudate filled with water (151 ms). A calibration procedure, in which the quantitative effect of the citrate-concentration on T_1 is determined, would be required to obtain the exact citrate distribution profiles. Besides the citrate concentration, the pH of the solution may also be an important factor.

The effect of pH on the interaction between citrate and the support was evaluated using this indirect imaging procedure. Inversion-recovery measurements were carried out with different VD, within 1 h after impregnation with 0.40 M citrate solutions of pH 1, 5 and 9. The resulting images and the VD-values that were used are presented in Fig. 17. At pH 9, the signal from the entire extrudate could be suppressed when a VD of 145 ms was used. Apparently, the T_1 of water protons is approximately 209 ms for all positions in the extrudate. An increase in T_1, as compared to an Al_2O_3 extrudate filled with water (T_1 = 151 ms), was observed, due to the presence of the ligand. As a result of a limited interaction between citrate and the support, the distribution of this compound was homogeneous just after impregnation. This observation is in line with the results of the ^{13}C MRI experiments described before, in which a ^{13}C signal was detected for all positions inside an Al_2O_3 extrudate after impregnation with a 0.40 M 1.5 ^{13}C citrate solution of pH 9 (Fig. 11).

After impregnation with a 0.40 M citrate solution of pH 5, only the outer ring of the extrudate of ~400 µm thickness was observed at a VD of 125 ms. When a VD of 165 ms was applied, the signal from positions near the outer surface could be suppressed. Both images are almost completely complementary, which points to a sharp egg-shell distribution of citrate in this extrudate. After impregnation with the solution of pH 1, the signal from positions near the

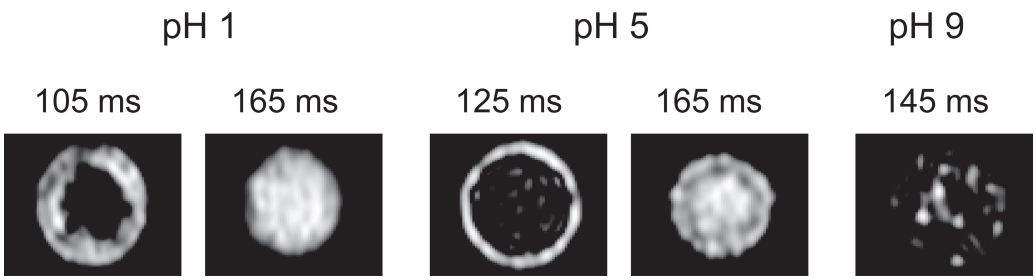

Figure 17. ^1H images of an Al_2O_3 extrudate just after impregnation with a 0.40 M citrate solution of pH 1, 5 and 9. As indicated, different VD values were used in the inversion-recovery pulse sequence to detect the different images.

core of the extrudate could be suppressed by the application of a VD period of 105 ms. The signal from the outer ring, where citrate was present, could again be suppressed with a VD of 165 ms. The egg-shell distribution of citrate in this case is probably less sharp than after impregnation with the solution of pH 5.

These observations are in good agreement with adsorption experiments of citrate on α-Al_2O_3, as reported by Hidber et al. [18]. They determined the uptake of citrate after exposure of α-Al_2O_3 to citrate solutions of different pH. Adsorption was found to be much stronger at low pH, with a maximum in the citrate uptake at pH 3. In the adsorption of citrate to the surface, it was found that hydroxyl groups were exchanged for citrate oxygen groups, as shown in Eq. (5). Coordination of citrate to the thus created Al(III) surface site through two carboxylate groups and the hydroxyl group leads to a strong adsorption of this anion. Deprotonation of at least two carboxylate groups is thus a prerequisite for this type of adsorption. Furthermore, the reaction is facilitated when protonated hydroxyls are present, since H_2O is a better leaving group than OH^-. This explains why transport of citrate was found to be slowest after impregnation with the pH 5 solution. After impregnation with the pH 1 solution, mainly protonated citrate was present, while after impregnation with the basic solution, the hydroxyl groups on the Al_2O_3 surface were less reactive.

$$Hcitr^{3-} + Al_sOH \leftrightarrow Al_s\text{-}Hcitr^{2-} + OH^- \qquad \text{(Eq. 5)}$$

Magnetic resonance imaging in the preparation of supported catalyst bodies

Surely, the strength of MRI as a technique to study the preparation of supported catalyst extrudates lies in its non-invasive character. The dynamics of the impregnation of support bodies can be imaged in great detail. However, as the frequency of the NMR-signal is used to obtain spatial resolution, chemical information on the nature of components is lost. Therefore, the combination of this technique with Raman and UV-Vis-NIR micro-spectroscopy is extremely powerful. The direct imaging of NMR-sensitive nuclei, such as ^{13}C, ^{31}P and ^{195}Pt ($I = ½, \gamma = 57.68 \cdot 10^6$ rad$\cdot$T$^{-1}\cdot$s^{-1}) allows one to determine the distribution of organic acids, phosphate and Pt-complexes as a function of time after impregnation [19]. Unfortunately, the adsorption of these components on the support surface leads to suppression of the signal, which makes it difficult to interpret results. In general, the fact that nuclei that interact with the support surface are not observed, is an important drawback of MRI in this type of research. The loss of spatial resolution, due to the relatively small gyromagnetic ratio of particularly ^{13}C and ^{195}Pt

nuclei is another inherent limitation.

The possibility to obtain quantitative distribution profiles of paramagnetic cations after impregnation, yields a lot of opportunities for the quantitative modeling of the impregnation process. Ni, Cu and Fe are among the most commonly used metals to serve as the active phase in supported catalysts. Their preparation generally starts from an aqueous solution containing paramagnetic Ni(II) (d^8), Cu(II) (d^9) and Fe(III) (d^5) complexes. The influence of these cations on the ^{1}H signal of water protons can be used to monitor their distribution after impregnation. Experiments with $Ni(NO_3)_2$ and $Cu(NO_3)_2$ solutions already showed that this approach is indeed generally applicable to determine the concentration of paramagnetic cations inside catalyst bodies [20]. Naturally, the sensitivity of the technique needs to be evaluated in each case where the number of unpaired electrons, the lability of the $[M(H_2O)_6]^{2+}$ complexes and their interaction with the support are likely to be important parameters.

Besides complexing agents, such as phosphate and organic acids, the distribution of (industrially relevant) diamagnetic metal-complexes of Mo(VI) (d^0), Cr(VI) (d^0), V(VI) (d^0) and low-spin octahedral Pt(IV) (d^6) complexes can be imaged using the inversion-recovery method. As industrial impregnation solutions generally contain a large number of different components, each with their own influence on the ^{1}H NMR-signal, the application of indirect MRI techniques in an industrial context seems rather complicated.

Conclusions

Three different MRI techniques were introduced in this chapter that allow one to envisage the transport of different components inside catalyst bodies after impregnation in a non-invasive manner. Direct imaging of NMR-sensitive nuclei was applied to monitor the distribution phosphate and (^{13}C labeled) citrate inside the extrudates. The effect of paramagnetic cations on the ^{1}H NMR signal of water was employed to monitor the transport of $[Co(H_2O)_6]^{2+}$ as a function of time after impregnation with a $Co(NO_3)_2$ solution. After a calibration procedure, it proved possible to derive quantitative distribution profiles of the Co(II)-cations. With the aid of inversion-recovery pulse sequences, an impression of the distribution of citrate could be obtained, through the influence of this complexing agent on the relaxation time of water protons inside the Al_2O_3.

Acknowledgments

Dr. Anna Lysova and prof. dr. Igor Koptyug of the International Tomography Center SB RAS in Novosibirsk (Russia) are kindly acknowledged for facilitating the MRI measurements and their help in interpretation of the results. Thanks to Leticia Espinosa Alonso for her help during the experiments and valuable discussions. Ad van der Eerden is thanked for XRF measurements and Ad Mens for N_2-physisorption.

References

1 J. A. Bergwerff, T. Visser, R. G. Leliveld, B. A. Rossenaar, K. P. de Jong, B. M. Weckhuysen, *J. Am. Chem. Soc.* **2004**, *126*, 14548.
2 L. G. A. van de Water, J. A. Bergwerff, T. A. Nijhuis, K. P. de Jong, B. M. Weckhuysen, *J. Am. Chem. Soc.* **2005**, *127*, 5024.
3 E. Harel, J. Granwehr, J. A. Seeley, A. Pines, *Nature Mater.* **2006**, *5*, 321.
4 E. H. L. Yuen, A. J. Sederman, F. Sani, P. Alexander, L. F. Gladden, *Chem. Eng. Sci.* **2003**, *58*, 613.
5 A. J. Sederman, M. D. Mantle, C. P. Dunckley, Z. Y. Huang, L. F. Gladden, *Catal. Lett.* **2005**, *103*, 1.
6 I. V. Koptyug, L. Y. Khitrina, V. N. Parmon, R. Z. Sagdeev, *Magn. Reson. Imaging* **2001**, *19*, 531.
7 I. V. Koptyug, V. B. Fenelonov, L. Y. Khitrina, R. Z. Sagdeev, V. N. Parmon, *J. Phys. Chem. B* **1998**, *102*, 3090.
8 L. Y. Khitrina, I. V. Koptyug, N. A. Pakhomov, R. Z. Sagdeev, V. N. Parmon, *J. Phys. Chem. B* **2000**, *104*, 1966.
9 L. F. Gladden, *Top. Catal.* **1999**, *8*, 87.
10 L. F. Gladden, M. D. Mantle, A. J. Sederman, *Adv. Catal.* **2006**, *50*, 1.
11 J. P. Hornak, *The Basics of MRI, a Hypertext Book on Magnetic Resonance Imaging* (www.cis.rit.edu/htbooks/mri) 1997.
12 P. T. Callagham, *Principles of Nuclear Magnetic Resonance Microscopy*, Clarendon Press, Oxford, 1995.
13 J. Park, J. R. Regalbuto, *J. Colloid Interface Sci.* **1995**, *175*, 239.
14 H. Kraus, R. Prins, *J. Catal.* **1997**, *170*, 20.
15 J. A. R. van Veen, P. Hendriks, R. R. Andrea, E. Romers, A. E. Wilson, *J. Phys. Chem.* **1990**, *94*, 5282.
16 T. Ataloglou, K. Bourikas, J. Vakros, C. Kordulis, A. Lycourghiotis, *J. Phys. Chem. B* **2005**, *109*, 4599.
17 J. Vakros, K. Bourikas, S. Perlepes, C. Kordulis, A. Lycourghiotis, *Langmuir* **2004**, *20*, 10542.
18 P. C. Hidber, T. J. Graule, L. J. Gauckler, *J. Am. Ceram. Soc.* **1996**, *79*, 1857.
19 A. A. Lysova, I. V. Koptyug, R. Z. Sagdeev, V. N. Parmon, J. A. Bergwerff, B. M. Weckhuysen, *J. Am. Chem. Soc.* **2005**, *127*, 11916.
20 L. Espinosa Alonso, A. A. Lysova, J. A. Bergwerff, I. V. Koptyug, B. M. Weckhuysen, *unpublished results*.

Chapter 7

Influence of Citrate on the Distribution of Co(II)-Complexes inside Co/Al_2O_3 Catalyst Extrudates after Impregnation: a Combined MRI and UV-Vis-NIR Micro-spectroscopy Study

Abstract

The distribution of paramagnetic Co(II)-complexes inside Al_2O_3-based catalyst extrudates was determined, after impregnation with Co(II)-citrate solutions of different pH and citrate concentrations, through their influence on the NMR signal in ^1H MRI measurements. UV-Vis-NIR microspectroscopy measurements were carried out simultaneously to obtain information on the nature of the Co(II) complexes. In this way, it could be confirmed that the actual distribution of Co inside the extrudates could be derived from the MRI images. By this combination of techniques, information was obtained on both the strength and the mode of interaction between $[Co(H_2O)_6]^{2+}$ and different Co(II)-citrate complexes with the Al_2O_3 support. Complexation of Co(II) by citrate was found to lead to a stronger interaction of Co with the support and the formation of an egg-shell distribution of Co after impregnation. By the addition of free citrate and by changing the pH of the impregnation solution, it was possible to obtain the rather uncommon egg-yolk and egg-white distributions of Co inside the extrudates after impregnation. In other words, by carefully altering the chemical composition and pH of the impregnation solution, the macro-distribution of Co(II)-complexes inside the extrudates could be fine-tuned.

Introduction

Citric acid is a popular ingredient in impregnation solutions used for the preparation of supported metal(oxide) catalysts. Apart from its use in the synthesis of CoMo and NiMo HDS-catalysts [1-4], its application has been reported in the open literature for the preparation of supported Co [5,6], Fe [7,8], Ni [9,10], Au [11,12], Sn [13] and Zn [14] catalysts. The addition of this chelating agent to impregnation solutions is claimed to serve a number of functions. First of all, the viscosity of citrate containing solutions inside the pores of the support was found to increase drastically at high concentrations, preventing the redistribution of the metal-precursor during the drying step. Crystallization of the metal-precursor was reported to be prevented by the formation of a gel-like phase [15]. Furthermore, the use of citrate allows for the preparation of highly concentrated metal-salt solutions without the necessity to use a nitrate salt, thus preventing the formation of NO_x during calcination in air. In general, it is found that the inclusion of citric acid in the recipe results in the formation of a well-dispersed metal-oxide phase on the support after calcination. The actual mechanism behind the beneficial effect of citric acid remains, however, mostly unclear. Its role in the preparation of Co/Al_2O_3 catalyst bodies during the impregnation is the subject of this chapter.

In the previous chapter, it was shown, that MRI can be a useful technique to monitor the transport of paramagnetic cations after impregnation of porous support bodies in a non-invasive manner. The destructive effect of paramagnetic $[Co(H_2O)_6]^{2+}$ complexes on the ^1H NMR signal of water protons was used to obtain quantitative Co(II)-distribution profiles after impregnation of Al_2O_3 extrudates with a $Co(NO_3)_2$ solution. It can be expected that different types of Co(II)-complexes have a different influence on the ^1H NMR-signal. Hence, the applicability of the indirect MRI method when impregnation is carried out with solutions containing complexing agents needs to be further evaluated.

In the experiments described in this chapter, the interaction of different Co(II)-citrate complexes with the Al_2O_3 support was studied. Using an indirect MRI technique, the distribution of Co(II) was monitored as a function of time after the impregnation of Al_2O_3 extrudates with Co-citrate solutions of different pH and citrate concentration. At the same time, UV-Vis-NIR micro-spectroscopy was used to determine the nature of the Co(II)-complexes in the extrudates and validate the observations made by MRI. By a combination of both techniques, an attempt is made to obtain a molecular picture of the different processes that occur inside an Al_2O_3 extrudate after impregnation with Co(II)-citrate solutions. It was shown that the macro-distribution of Co(II)-complexes, which is obtained after impregnation, could be varied from

egg-shell, via egg-white, to egg-yolk by simple means.

Experimental

Pore volume impregnation of cylindrical γ-Al_2O_3 extrudates with 3.85 mm diameter was carried out with 0.2 M Co-solutions. The BET surface area of the support was 149 m^2/g and its pore volume was 0.39 ml/g. XRF-analysis showed that S (0.45 wt% SO_3), Si (0.23wt% SiO_2), Ca (0.05wt% CaO) and Fe (0.04 wt% Fe_2O_3), were present as the main impurities. The PZC of this material was 7.8, as determined by potentiometric mass titrations [16]. In the impregnation solutions, which were prepared from $Co(NO_3)_2 \cdot 6\ H_2O$ (Acros, p.a.), citric acid (Acros, p.a.) and NaOH (Merck, p.a.), the citrate concentration and the pH were varied. The name of the different solutions used in this study, as well as their pH and composition are listed in Table 1.

^1H MRI images were recorded on the impregnated extrudates during the ageing process. Dehydration of the wet extrudates was prevented by the inclusion of a wet tissue in the NMR-tube. The MRI measurements were performed at the International Tomography Center SB RAS in Novosibirsk (Russia) on a Bruker Avance DRX 300 MHz wide bore spectrometer with imaging accessories at 300.13 MHz (^1H)). For the detection of the signal a two-pulse spin-echo sequence was used. Slice selection was used to record the signal from an 2 mm thick slice of

Table 1. Composition and pH of Co-citrate impregnation solutions used in this study. The speciation of Co(II)-complexes in these solutions (as determined by UV-Vis-NIR spectroscopy) and the concentration of free citrate is included as well.

	composition			speciation	
	[Co(II)] (M)	[citrate] (M)	pH	Co(II) complexes	$H_x$citrate$^{(4-x)-}$
1-1-Cocitrate-pH1	0.20	0.20	1.5	0.20 M $[Co(H_2O)_6]^{2+}$	0.20 M $citrH_4$
1-2-Cocitrate-pH1	0.20	0.40	1.2	0.20 M $[Co(H_2O)_6]^{2+}$	0.40 M $citrH_4$
1-5-Cocitrate-pH1	0.20	1.00	1.0	0.20 M $[Co(H_2O)_6]^{2+}$	1.00 M $citrH_4$
1-1-Cocitrate-pH5	0.20	0.20	5.0	0.20 M $[Co(citrH)(H_2O)_3]^-$	-
1-2-Cocitrate-pH5	0.20	0.40	5.0	0.14 M $[Co(citrH)_2]^{4-}$ 0.06 M $[Co(citrH)(H_2O)_3]^-$	0.06 M $citrH^{3-}$
1-5-Cocitrate-pH5	0.20	1.00	5.0	0.20 M $[Co(citrH)_2]^{4-}$	0.60 M $citrH^{3-}$
1-1-Cocitrate-pH9	0.20	0.20	10.0	0.20 M $[Co(citr)(H_2O)_3]^{2-}$	-
1-1.5-Cocitrate-pH9	0.20	0.30	9.5	0.20 M $[Co(citr)(H_2O)_3]^{2-}$	0.10 M $citrH^{3-}$
1-2-Cocitrate-pH9	0.20	0.40	9.0	0.20 M $[Co(citr)(H_2O)_3]^{2-}$	0.20 M $citrH^{3-}$

the extrudates. Frequency encoding was applied in the X direction yielding a spatial resolution of 139 µm. The application of phase encoding gradients in the Y direction resulted in a spatial resolution of 231 µm in this direction. The time required for the acquisition of a single image was 4-5 min.

For the UV-Vis-NIR micro-spectroscopy measurements, different Al_2O_3 extrudates of the same batch were impregnated with the solutions listed in Table 1. The extrudates were bisected at different points in time after impregnation and UV-Vis-NIR spectra were recorded on the bisected extrudates using the UV-Vis-NIR micro-spectroscopy set-up described in chapter 5 [17]. Pore volume impregnation was carried out on crushed Al_2O_3 extrudates as well using the same impregnation solutions. UV-Vis-NIR spectra were recorded on these samples in diffuse reflectance using a Cary 500 spectrophotometer, equipped with an integrating sphere with the use of a white Halon standard as a reference. The pH of the wet powders was determined with the aid of a spear tip electrode [16].

To help interpret the results, a simplified model was used to derive an estimation of the macro-distribution of different compounds inside the extrudates. In this model, the impregnation of a slab-shaped support body was mimicked by calculations. The distribution of components in the impregnation solution with different adsorption equilibrium constants (K_{ads}) and concentrations ($c_{imp.}$) was estimated after impregnation for different positions inside the virtual support body. The slab was divided into different sections, each having the same (pore) volume and containing the same number of adsorption sites (n_{ads}). The transport of different components through the support was simulated by assuming a stepwise penetration of the impregnation solution into the slab. In the first step, the Al_2O_3 surface in the first section is contacted with the impregnation solution. The adsorption of the different components on the Al_2O_3 surface in this section is determined assuming Langmuir adsorption and a constant concentration of components (equal to $c_{imp.}$). Subsequently, the non-adsorbed fraction of the different components is allowed to travel to the second section, while the first section is again exposed to the impregnation solution. The total concentration of a certain component in the first section is now equal to the amount adsorbed in the first step plus the concentration in the impregnation solution. The adsorption of the components in the different sections is again determined for the new situation in which the total concentration of the components has changed. Typically, the distribution of the components after 7 adsorption and transport steps was determined. By varying the values for K_{ads} and $c_{imp.}$ for the different components, the distribution of Co(II)-complexes and citrate inside extrudates could be simulated to mimic the situation in the extrudates under study.

Results and Discussion

Co(II)citrate complexes in aqueous solution

A study into the formation of Co(II)-citrate complexes in aqueous solution is reported in chapter 2B. In the following paragraph, the main findings of this characterization study are summarized. With the aid of UV-Vis, Raman and IR spectroscopy, four different types of Co(II)-complexes could be distinguished. The proposed structures of these complexes are shown in Fig. 1 [18]. Under the acidic conditions prevailing in solutions prepared from citric acid and $Co(NO_3)_2$ as the only ingredients, protonation of the citrate carboxylate groups is nearly complete, no complexation takes place between Co(II) and citrate and $[Co(H_2O)_6]^{2+}$ complexes are mainly present. At a pH of approximately 5-6, the carboxylate groups of citrate are completely deprotonated and Co(II)-citrate complexes can be formed with a Co:citrate ratio of 1:1 ($[Co(citrH)(H_2O)_3]^-$) and 1:2 ($[Co(citrH)_2]^{4-}$), depending on the amount of citrate available. The formation of these complexes from $[Co(H_2O)_6]^{2+}$ and citric acid is given in Eq. 1 and Eq. 2. Coordination of Co(II) probably takes place through two carboxylate groups and the hydroxyl group, as shown in Fig. 1. The formation of 1:1 Co(II)-citrate complexes was observed in Co(II)-citrate solutions of pH higher than 8, regardless of the amount of citrate available for complexation. The structure of the complex could not be univocally determined but, for the interpretation of the results of this study, it is assumed that $[Co(citr)(H_2O)_3]^{2-}$ complexes are formed in which coordination takes

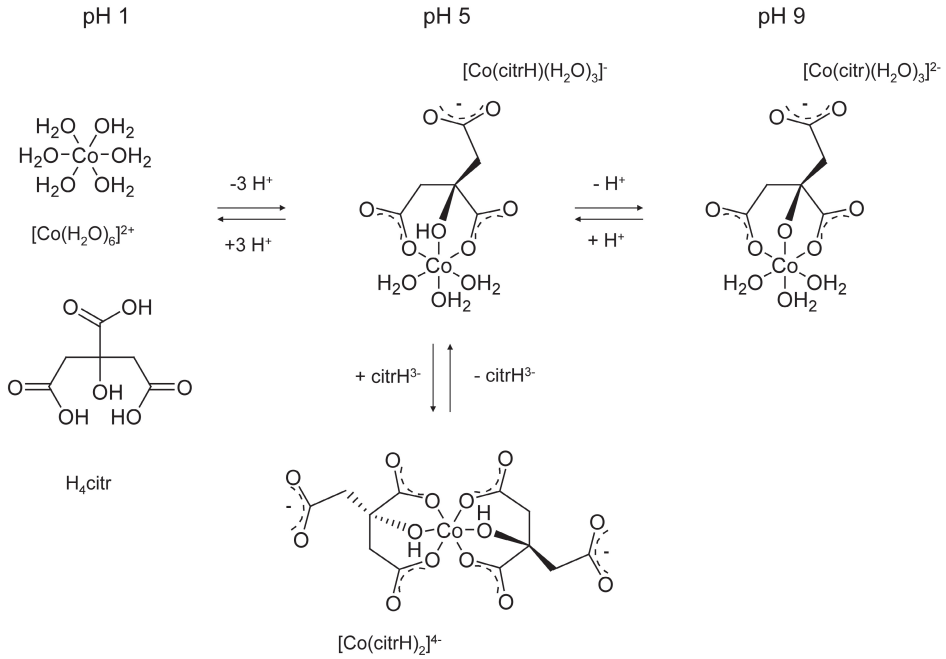

Figure 1. Molecular structure of different Co(II)-citrate complexes present in aqueous solution

place through two carboxylate groups and the deprotonated hydroxyl group. The formation of this complex from $[Co(citrH)(H_2O)_3]^-$ is expressed in Eq. 3. For the different Co(II)-complexes that can be present in aqueous solution, the positions of their characteristic UV-Vis-NIR absorption bands are listed in Table 2.

$$[Co(H_2O)_6]^{2+} + H_4citr \leftrightarrow [Co(citrH)(H_2O)_3]^- + 3\ H_2O + 3\ H^+ \quad \text{(Eq. 1)}$$

$$[Co(H_2O)_6]^{2+} + 2\ H_4citr \leftrightarrow [Co(citrH)_2]^{4-} + 6\ H_2O + 6\ H^+ \quad \text{(Eq. 2)}$$

$$[Co(citrH)(H_2O)_3]^- \leftrightarrow [Co(citr)(H_2O)_3]^{2-} + H^+ \quad \text{(Eq. 3)}$$

Reference spectra of the different Co(II)-complexes were used to fit UV-Vis-NIR spectra recorded on 0.20 M Co-solutions of different pH and citrate concentration. In this way, the speciation of these complexes in 1:1, 1:2 and 1:5 Co(II)-citrate solutions was determined as a function of pH. The resulting speciation plots are shown in Fig. 2. From these plots, the nature and concentration of the different components in the impregnation solutions used in this study could be derived. Cocitrate-pH1 solutions were found to contain $[Co(H_2O)_6]^{2+}$ and a varying amount of $citrH_4$. Using UV-Vis-NIR spectroscopy it proved to be impossible to distinguish between $[Co(citrH_2)(H_2O)_3]$ and $[Co(citrH)(H_2O)_3]^-$ complexes, since the only difference between these complexes is the protonation state of the free carboxylate group. Since deprotonation of the carboxylates is complete at this pH, the 1-1-Cocitrate-pH5 solution, almost exclusively contained $[Co(citrH)(H_2O)_3]^-$. Approximately 70% of all Co in the 1-2-Cocitrate-pH5 solution is present as $[Co(citrH)_2]^{4-}$ complexes, while it was assumed that the 1-5-Cocitrate-pH5 solution

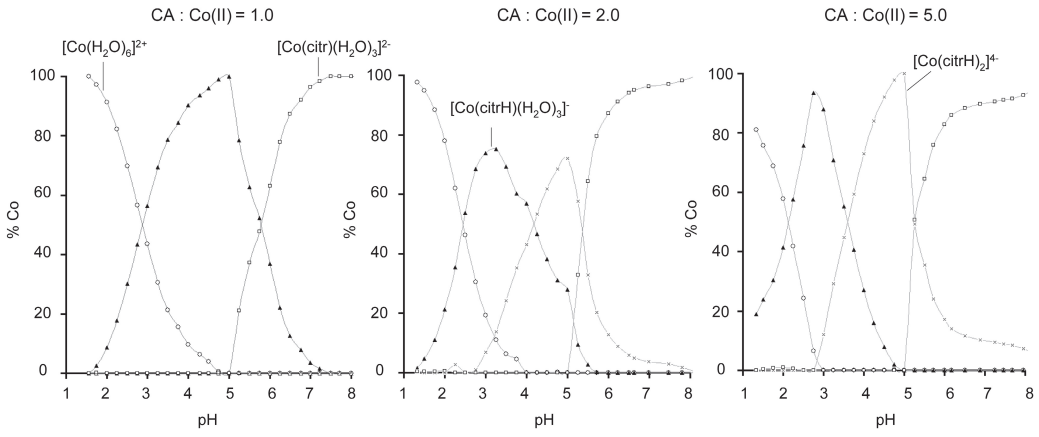

Figure 2. Speciation of $[Co(H_2O)_6]^{2+}$ (○), $[Co(citrH_n)(H_2O)_3]^{(2-n)-}$ (n=1,2) (▲), $[Co(citrH)_2]^{4-}$ (×) and $[Co(citr)(H_2O)_3]^{2-}$ (□) complexes in 0.20 M Co solutions with different citrate concentrations.

Table 2. Positions and extinction coefficients of the most intense UV-Vis-NIR absorption bands for relevant Co(II)-complexes in aqueous solution.

Formula	UV-Vis-NIR bands (nm)	Extinction coefficient ($M^{-1}cm^{-1}$)
$[Co(H_2O)_6]^{2+}$	511	4.4
$[Co(citrH_2)(H_2O)_3]$ $[Co(citrH)(H_2O)_3]^-$	513	9.2
$[Co(citrH)_2]^{4-}$	509	13.4
$[Co(citr)(H_2O)_3]^{2-}$	534	14.1
	727	2.2

Table 3. pH of the impregnation solution, before and after impregnation of crushed Al_2O_3 extrudates.

Impregnation solution	pH before	pH after
1-1-Cocitrate-pH1	1.5	3.3
1-2-Cocitrate-pH1	1.2	2.5
1-1-Cocitrate-pH5	5.0	7.1
1-2-Cocitrate-pH5	5.0	7.0
1-1-Cocitrate-pH9	10.0	8.0
1-2-Cocitrate-pH9	9.5	8.8

merely contained this complex and free citrate. In the Cocitrate-pH9 solutions, $[Co(citr)(H_2O)_3]^{2-}$ complexes were exclusively present. Besides this complex, the 1-1.5-Cocitrate-pH9 and 1-2-Cocitrate-pH9 contained varying amounts of free citrate. The estimated concentrations of free citrate and Co(II)-complexes in the impregnation solutions are included in Table 1.

Impregnation with Co-citrate-pH 1 solutions

In order to determine the effect of the support on the pH of the solution inside the Al_2O_3 pores, pH-measurements were carried out on crushed Al_2O_3-extrudates after impregnation with different solutions. The thus obtained pH values are listed in Table 3. When impregnation was carried out with Cocitrate-pH1 solutions, protonation of the Al_2O_3 surface led to an increase in pH to a value of 2.5-3.3. The UV-Vis-NIR spectra recorded on crushed extrudates after impregnation with 1-2-Co-citrate solutions of different pH are shown in Fig. 3. In this figure, the spectrum of Al_2O_3 powder impregnated with a 0.2 M $Co(NO_3)_2$ solution is included for comparison. In this spectrum, the maximum of the Co(II) d-d band is located at 525 nm. The observed red-shift as compared to the spectrum of $[Co(H_2O)_6]^{2+}$ in solution (maximum at 511

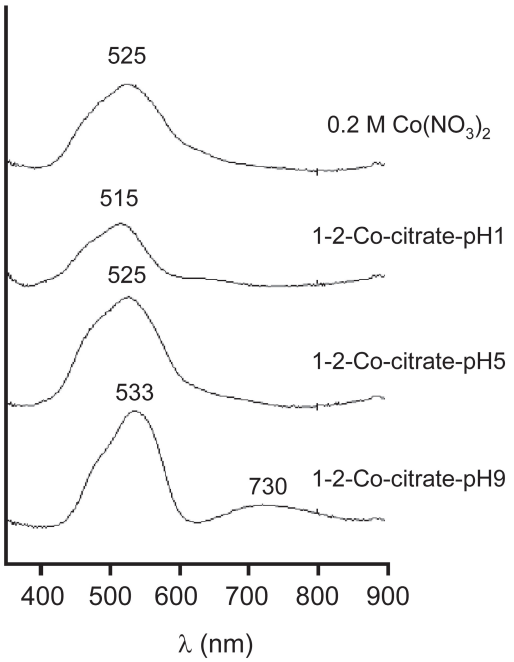

Figure 3. UV-Vis-NIR spectra of crushed Al_2O_3 extrudates after impregnation with (from top to bottom) 0.2 M $Co(NO_3)_2$, 1-2-Cocitrate-pH1, 1-2-Cocitrate-pH5 and 1-2-Cocitrate-pH9 solutions.

nm) can be explained by the exchange of water ligands for support hydroxyl groups and the formation of inner-sphere complexes between Co(II) and the Al_2O_3 surface [19]. The spectrum recorded on the Al_2O_3 impregnated with the 1-2-Co-citrate-pH1 solution shows a d-d band with lower intensity and a maximum at 515 nm. This spectrum resembles that of $[Co(H_2O)_6]^{2+}$ in solution, which points to a limited chemical interaction between these complexes and the support after impregnation. In aqueous solutions, an increase in pH to a value of 2.5-3.3 was found to lead to deprotonation of citric acid and the formation of Co(II)-citrate complexes (Fig. 2). Complexation by citrate leads to an increase in the extinction coefficient of the Co(II) d-d transition band (Table 2). Judging from the low intensity of the adsorption band in the spectrum recorded on the Al_2O_3 impregnated with the 1-2-Cocitrate-pH1 solution, it seems that, despite the increase in pH, hardly any Co(II)-citrate complexes were formed inside the Al_2O_3 matrix.

^{1}H images recorded on extrudates at several points in time after impregnation with Co-citrate-pH1 solutions of different citrate concentrations are presented in Fig. 4. In these images, the light areas represent areas in the extrudates with a high ^{1}H-NMR signal and hence a low concentration of $[Co(H_2O)_6]^{2+}$. The corresponding 1-dimensional profiles of the ^{1}H NMR signal as a function of the position inside the extrudates are depicted in Fig. 5. In these profiles, the Y axis shows the ^{1}H NMR signal in reversed order, to mimic the distribution of Co(II)-complexes.

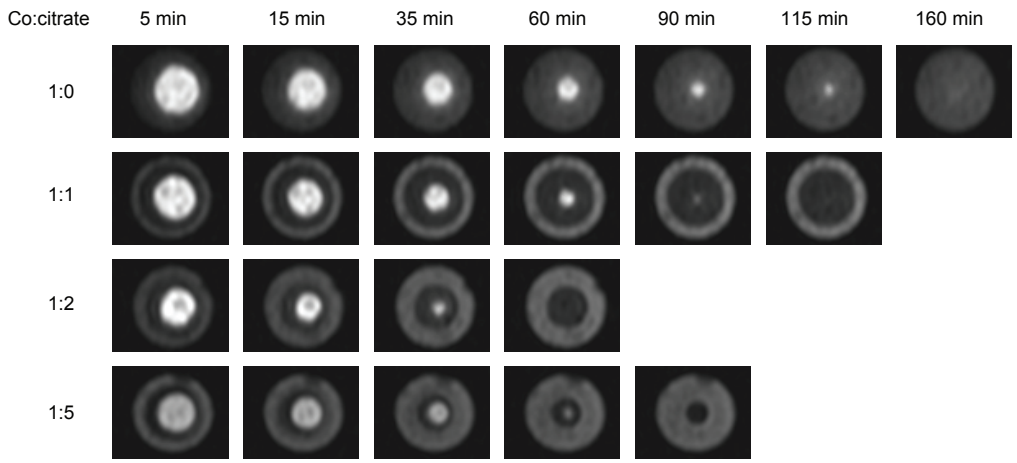

Figure 4. ^{1}H MRI images recorded on Al_2O_3 extrudates after impregnation with (from top to bottom) 0.2 M $Co(NO_3)_2$, 1-1-Cocitrate-pH1, 1-2-Cocitrate-pH1 and 1-5-Cocitrate-pH1 solutions. *For a color-version of this figure, see p. 184.*

In these figures, images and profiles of an Al_2O_3 extrudate after impregnation with a $Co(NO_3)_2$ solution are included for comparison. Transport of Co(II) from the edges towards the center of the extrudates was clearly observed as a shrinking core of high ^{1}H NMR signal. The addition of citric acid had two effects. First of all, as compared to the $Co(NO_3)_2$ solution the presence of $[Co(H_2O)_6]^{2+}$ at the center of the extrudate was observed at a shorter time after impregnation. Apparently, the addition of citric acid led to an increase in the transport rate of Co(II) inside the Al_2O_3 extrudates. Secondly, the formation of a ring with lower NMR-intensity was observed near the protruding Co(II)-front. This is most clearly observed in the 1-dimensional profiles obtained from the extrudate impregnated with the 1-5-Co-citrate-pH1 solution. 2 h after impregnation with all Cocitrate-pH1 solutions, images were obtained in which the ^{1}H NMR signal is higher near the external surface of the extrudates, which would imply an egg-yolk distribution of Co(II)-complexes inside the extrudates.

To verify that this type of distribution was actually established, extrudates were bisected 2 h after impregnation with the different Cocitrate-pH1 solutions for visual inspection. In all cases, Co(II)-complexes were obviously present throughout the extrudates, since the entire cross-section had a pink color. Besides, an outer ring of a lighter color was indeed observed. The inner diameter of this ring decreased with increasing citrate concentration in the impregnation solution, in line with the observations in the ^{1}H MRI measurements. A photograph of a bisected extrudate, 2 h after impregnation with the 1-5-Co-citrate-pH1 solution is presented in Fig. 6 alongside the corresponding ^{1}H MRI image.

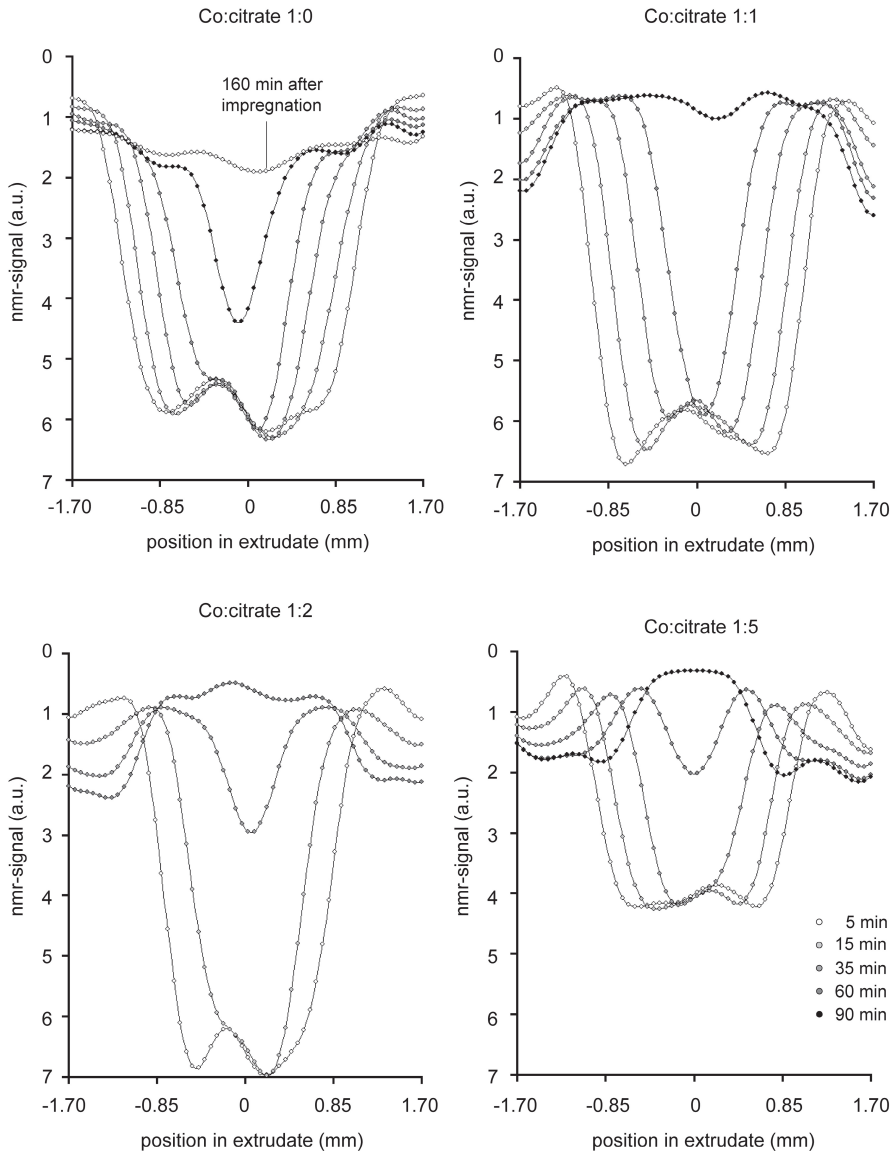

Figure 5. 1-Dimensional profiles of the ^{1}H NMR-signal as a function of position inside Al_2O_3 extrudates after impregnation with 0.2 M $Co(NO_3)_2$, 1-1-Cocitrate-pH1, 1-2-Cocitrate-pH1 and 1-5-Cocitrate-pH1 solutions.

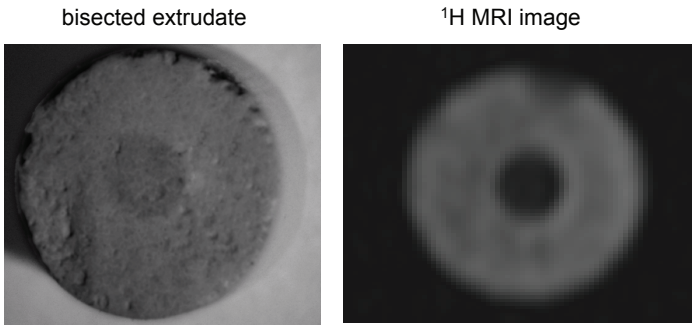

Figure 6. Photograph of an extrudate, bisected 2h after impregnation with a 1-5-Cocitrate-pH1 solution and the corresponding ^{1}H MRI image.

To explain the faster transport of $[Co(H_2O)_6]^{2+}$ and the formation of an egg yolk distribution of Co(II)-complexes, the interaction between citrate and $[Co(H_2O)_6]^{2+}$, the two components in the impregnation solutions, with the protonated Al_2O_3 surface must be evaluated. At low pH, citrate is known to react strongly with Al_2O_3 surfaces [20]. Adsorption of citrate probably takes place on Al(III)-surface sites, after the release of the hydroxyl group from the Al_2O_3 surface. Since H_2O is a better leaving group than OH^-, adsorption predominantly takes place on protonated hydroxyls. The reaction of citrate with Al_2O_3 surface hydroxyls is described in Eq. 4. Exchange of one or more water ligands of the $[Co(H_2O)_6]^{2+}$ complex for support oxygens can lead to the chemical adsorption of Co(II) onto the Al_2O_3 surface [19]. This reaction is given in Eq. 5.

$$citrH^{3-} + Al_sOH_2^{+} \xleftrightarrow{K_{ads}(citrH^{3-})} Al_s - Hcitr^{2-} + H_2O \qquad \text{(Eq. 4)}$$

$$[Co(H_2O)_6]^{2+} + xAl_sOH \xleftrightarrow{K_{ads}([Co(H_2O)_6]^{2+})} (Al_sO)_xCo(H_2O)_{(6-x)} + x\,H^{+} \qquad \text{(Eq. 5)}$$

The observed faster transport of Co(II) upon addition of citric acid may partially result from a weaker interaction between $[Co(H_2O)_6]^{2+}$ and the Al_2O_3 surface. The low pH of the impregnation solution makes that the equilibrium in Eq. 5 is shifted to the left and the formation of inner-sphere Co-surface complexes is suppressed. This is in line with the UV-Vis-NIR measurements, which also pointed to a limited interaction between $[Co(H_2O)_6]^{2+}$ complexes and the Al_2O_3 surface after impregnation with the 1-2-Cocitrate-pH1 solution (Fig. 3). The formation of a ring of high Co-concentration and the establishment of an egg-yolk distribution can be explained by competitive adsorption between $[Co(H_2O)_6]^{2+}$ and citrate. Since at low pH, $K_{ads}(citrH^{3-})$ is larger than $K_{ads}([Co(H_2O)_6]^{2+})$, adsorbed citrate was probably located in a ring near the external surface of the extrudate just after impregnation. For the same type of Al_2O_3 extrudates, impregnation

with a 0.40 M citric acid solution was indeed found to lead to an egg-shell distribution of this compound, as described in chapter 6. Adsorption of both citrate and $[Co(H_2O)_6]^{2+}$ takes place on hydroxyl groups resulting in competitive adsorption of the two components. Towards the center of the extrudate, the citrate concentration decreases, more surface sites are available for the adsorption of $[Co(H_2O)_6]^{2+}$, and the surface density of Co-surface complexes can be higher. A similar mechanism was previously proposed to explain egg-yolk Pt-distributions in the preparation of Pt/Al_2O_3 pellets [21]. The processes taking place inside an Al_2O_3 extrudate, after impregnation with Cocitrate-pH1 solutions are schematically depicted in Fig. 7a. A simplified model, explained in the experimental section, was used to derive an estimation of the distribution of citrate and $[Co(H_2O)_6]^{2+}$ inside Al_2O_3 extrudates after impregnation. The situation approximately 35 min after impregnation with the different Cocitrate-pH1 solutions is depicted in Fig. 7b.

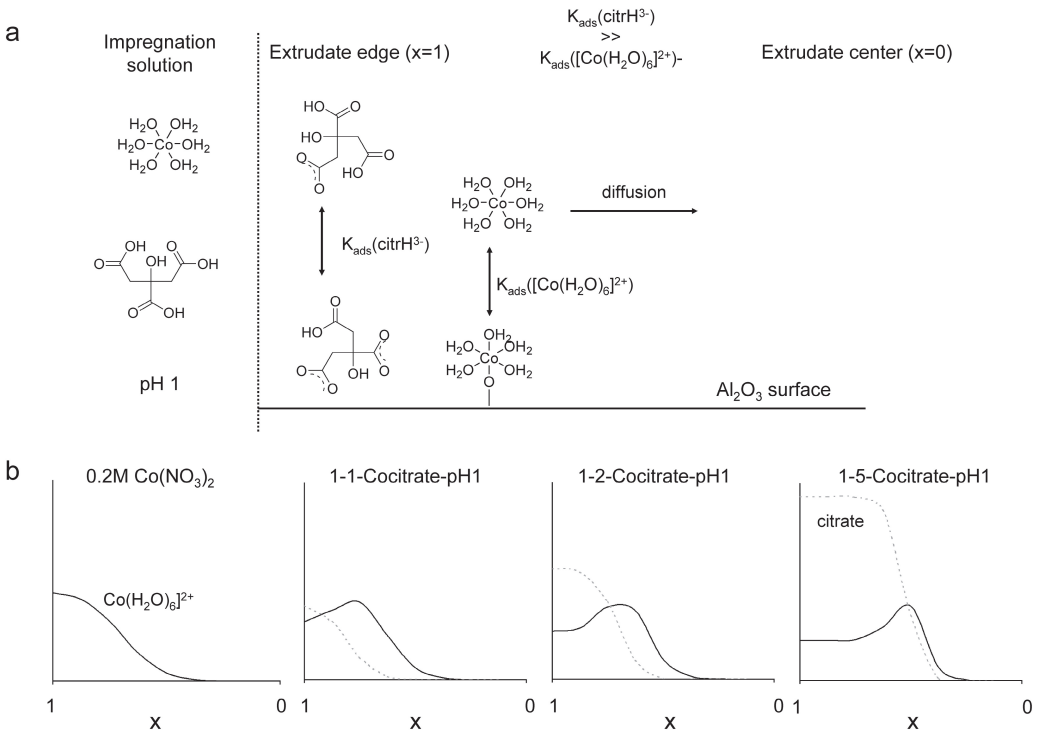

Figure 7. Schematic representation of the processes taking place inside an Al_2O_3 extrudate after impregnation with Cocitrate-pH1 solutions (a) and the estimated distribution of $[Co(H_2O)_6]^{2+}$ (solid lines) and citrate (dotted lines) inside Al_2O_3 extrudates 35 min after impregnation with different Cocitrate-pH1 solutions.

Impregnation with Co-citrate-pH 5 solutions

Impregnation of crushed extrudates with Co-citrate-pH5 solutions was found to lead to an increase in pH of the impregnation solution inside the pores to 7.0. The UV-Vis-NIR spectrum recorded on the Al_2O_3 powder, impregnated with a 1-2-Co-citrate-pH5 solution shows a d-d band with a maximum at 525 nm (Fig. 3). Despite the pH increase, the formation of $[Co(citr)(H_2O)_3]^{2-}$ complexes, the stable complex at pH 7.0 in aqueous solutions, was not observed inside the Al_2O_3 pores, since no absorption band was observed at 730 nm in the UV-Vis-NIR spectrum.

In Fig. 8, ^1H images are shown obtained from extrudates after impregnation with the Co-citrate-pH5 solutions of different Co:citrate ratios. The 1-dimensional ^1H NMR signal profiles derived from these images are presented in Fig. 9. Since the 1-1-Cocitrate-pH5 solution merely contains $[Co(citrH)(H_2O)_3]^-$ complexes, the measurements on extrudates impregnated with this solution can be used to determine the interaction between this complex and the Al_2O_3 surface. Impregnation with a 1-1-Co-citrate-pH5 solution resulted in the formation of a sharp ring of low ^1H NMR-intensity near the external surface of the extrudates, immediately after impregnation. Only a slight broadening of this ring was observed after ageing for 15 h. Fig. 10 shows a photograph recorded on an extrudate that was bisected at this point in time after impregnation. It can be seen that the observed ^1H NMR-profile indeed corresponds to a sharp egg-shell distribution of Co(II)-complexes. UV-Vis-NIR spectra recorded on this bisected extrudate are included in the same figure. An absorption band due to Co(II) d-d transitions is

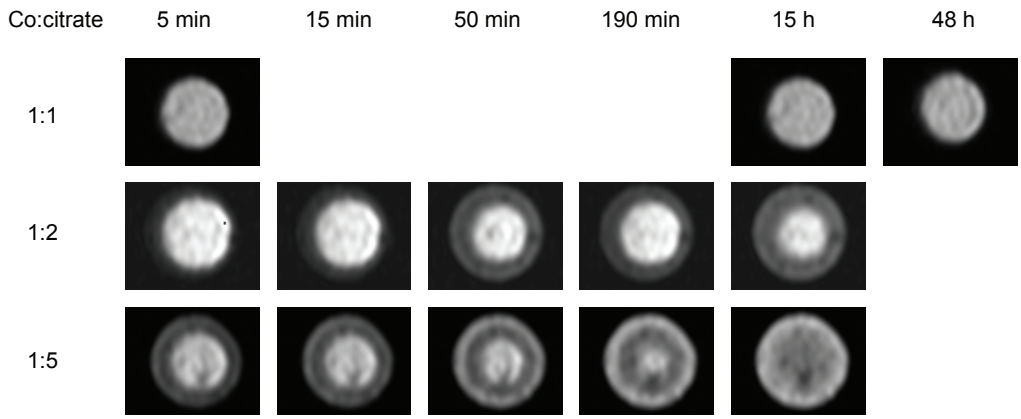

Figure 8. ^1H MRI images recorded on Al_2O_3 extrudates after impregnation with (from top to bottom) 1-1-Cocitrate-pH5, 1-2-Cocitrate-pH5 and 1-5-Cocitrate-pH5 solutions. *For a color-version of this figure, see p. 184.*

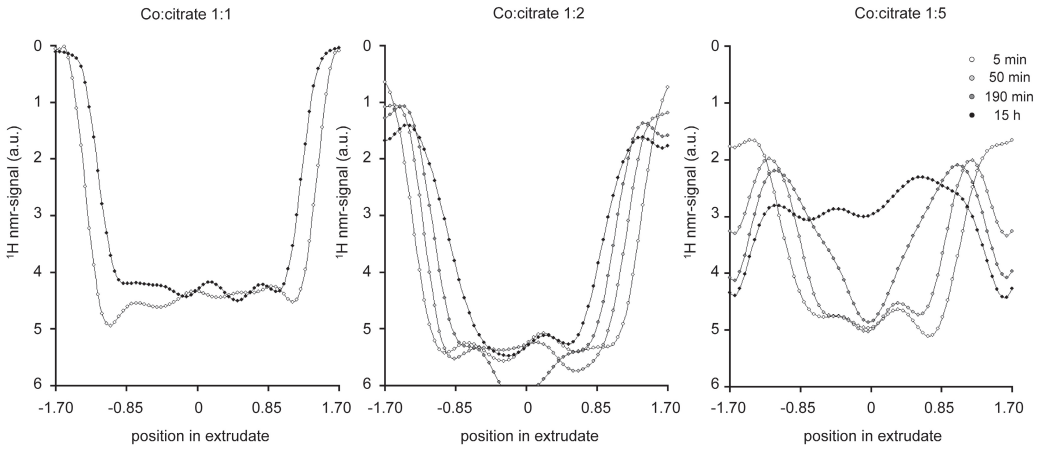

Figure 9. 1-Dimensional profiles of the ^{1}H NMR-signal as a function of position inside Al_2O_3 extrudates after impregnation with (from left to right) 1-1-Cocitrate-pH5, 1-2-Cocitrate-pH5 and 1-5-Cocitrate-pH5 solutions.

only observed in the spectrum recorded near the external surface of the extrudate. Even at 48 h after impregnation, the MRI-image reveals an egg-shell distribution of Co(II) inside the extrudate.

From the slow transport of the $[Co(citrH)(H_2O)_3]^-$ complex, it can be seen that a strong interaction exists between this component and the support surface. Adsorption of $[Co(citrH)(H_2O)_3]^-$ complexes onto the Al_2O_3 surface may take place in different ways. First of all, impregnation with the slightly acidic solution may lead to protonation of the hydroxyl groups and the creation of a positively charged surface. The increase in pH that was observed upon impregnation of the Al_2O_3 powder is probably a result of this surface protonation. An electrostatic interaction could exist between the surface and the negatively charged $[Co(citrH)(H_2O)_3]^-$ complexes. However, considering its small negative charge, the observed interaction between $[Co(citrH)(H_2O)_3]^-$-complexes and the support seems too strong to be explained by purely electrostatic interactions. Exchange of water ligands for support hydroxyl groups can lead to the formation of inner-sphere surface complexes, as expressed in Eq. 6. From this equation, it is clear that the adsorption of $[Co(citrH)(H_2O)_3]^-$ to the Al_2O_3 surface leads to liberation of protons. Nevertheless, the protonation of surface hydroxyls makes that a net pH-increase is observed after impregnation with the 1-1-Co-citrate-pH5 solution. The UV-Vis-NIR spectrum recorded near the external surface of the extrudate impregnated with the 1-1-Cocitrate-pH5 solution, presented in Fig. 10, shows an absorption band with its maximum at 525 nm. The spectrum of $[Co(citrH)(H_2O)_3]^-$ complexes in aqueous solution shows a band at

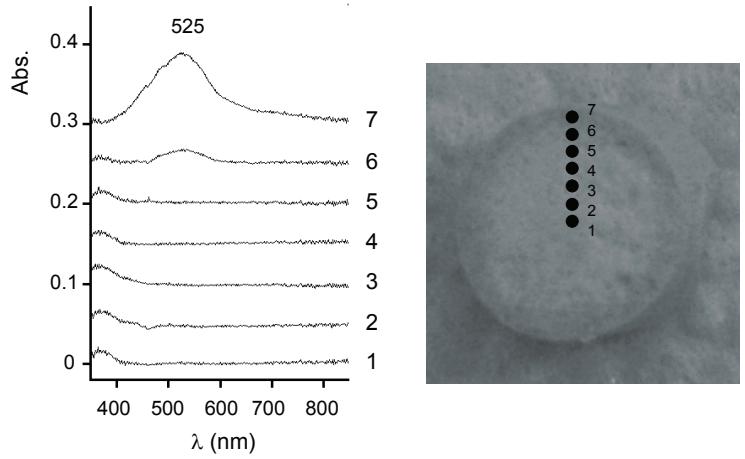

Figure 10. UV-Vis-NIR spectra recorded on an Al_2O_3 extrudate bisected 15 h after impregnation with a 1-1-Cocitrate-pH5 solution. The locations of the measurement spots are indicated in the photograph.

513 nm. This shift is a further argument for the existence of a chemical interaction between $[Co(citrH)(H_2O)_3]^-$ and the support. Apparently, the coordination of Co(II) by citrate makes that the remaining water ligands are more easily exchanged for hydroxyl groups.

$$[Co(citrH)(H_2O)_3]^- + x\ Al_sOH \xleftrightarrow{K_{ads}([Co(citrH)(H_2O)_3]^-)} (Al_s O)_x Co(citrH)(H_2O)_{(3-x)} + x\ H^+ \qquad \text{(Eq. 6)}$$

When the citrate concentration in the impregnation solution is increased, the transport of Co(II) proceeds at a higher rate. Furthermore, the formation of a ring of higher ^1H NMR-intensity near the external surface of the extrudate is observed. This phenomenon is most pronounced in the 1-dimensional ^1H NMR-signal profile obtained at 50 min after impregnation with the 1-5-Co-citrate-pH5 solution, presented in Fig. 9.

In the 1-2-Co-citrate-pH5 and 1-5-Co-citrate-pH5 solutions, most of the Co(II) is contained in $[Co(citrH)_2]^{4-}$ complexes. The UV-Vis-NIR spectrum of this complex in aqueous solution shows a band with a maximum at 509 nm (Table 2). The absorption band in the UV-Vis-NIR spectrum of the crushed extrudates impregnated with the 1-2-Co-citrate-pH5 (Fig. 3) is located at 525 nm. Apparently, after impregnation, disintegration of the $[Co(citrH)_2]^{4-}$ complex takes place inside the Al_2O_3 pores. The adsorption of citrate to the Al_2O_3 surface, described in Eq. 4, probably leads to a lower citrate concentration inside the Al_2O_3 pores and the formation of $[Co(citrH)(H_2O)_3]^-$ complexes at the expense of $[Co(citrH)_2]^{4-}$. In the following discussion, it is assumed that $[Co(citrH)(H_2O)_3]^-$ and free citrate are the only components inside the Al_2O_3 pores

after impregnation with the 1-2-Co-citrate-pH5 and 1-5-Co-citrate-pH5 solutions, despite the presence of $[Co(citrH)_2]^{4-}$ in the impregnation solution.

In chapter 6 (Figs. 15-17), a strong interaction between citrate and the Al_2O_3 surface was observed when impregnation was carried out with Na_3citrate-solutions of pH 5. As was discussed for the Cocitrate-pH1 solutions, competitive adsorption between citrate (stronger) and $[Co(citrH)(H_2O)_3]^-$ (slightly weaker) may explain the faster transport of the Co(II)-complexes, when impregnation is carried out with 1-2-Co-citrate-pH5 and 1-5-Co-citrate-pH5 solutions. However, as compared to the $[Co(H_2O)_6]^{2+}$ complexes in the Co-citrate-pH1 solutions, in this case, a stronger interaction exists between the $[Co(citrH)(H_2O)_3]^-$ complexes and the Al_2O_3 surface. During the diffusion of $[Co(citrH)(H_2O)_3]^-$ towards the center of the extrudate,

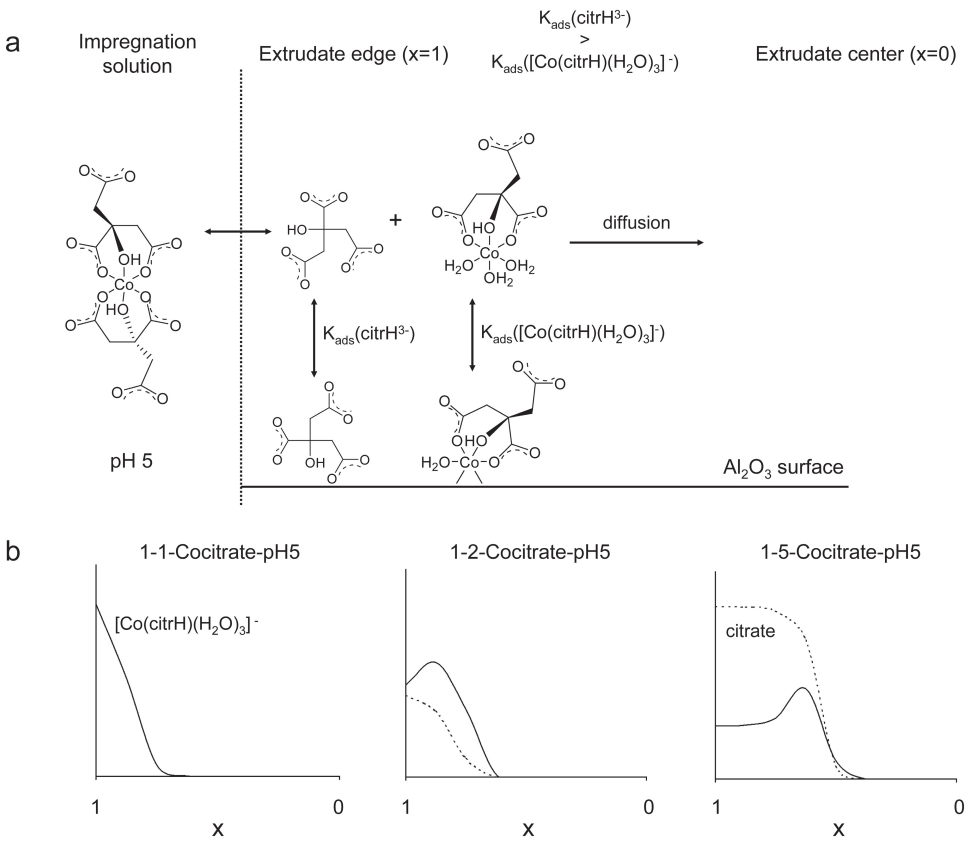

Figure 11. Schematic representation of the processes taking place inside an Al_2O_3 extrudate after impregnation with a 1-2-Cocitrate-pH5 solution (a) and the estimated distribution of $[Co(citrH)(H_2O)_3]^-$ (solid lines) and citrate (dotted lines) inside Al_2O_3 extrudates 190 min after impregnation with different Cocitrate-pH5 solutions.

adsorption of this complex takes place as soon as adsorption sites are available. As a result, during the ageing process, the formation of a sharp ring of low ^1H NMR-intensity is observed at the position of the advancing Co(II)-front. When this extrudate was allowed to age for 15 h, an egg-yolk distribution of $[Co(citrH)(H_2O)_3]^-$ complexes results. At this point in time, an egg-shell distribution of citrate is still present, but $[Co(citrH)(H_2O)_3]^-$ complexes have distributed themselves evenly over the remaining adsorption sites. The processes described above are summarized in Fig. 11a. The estimated distribution of $[Co(citrH)(H_2O)_3]^-$ and citrate inside Al_2O_3 extrudates, 190 min after impregnation with different Cocitrate-pH5 solutions is indicated in Fig. 11b.

Impregnation with Co-citrate-pH 9 solutions

A slight decrease in pH to a value of 8.0-8.8 was observed after impregnation with the Cocitrate-pH9 solutions. Since the pH of these solutions is close to the PZC of the support, impregnation has little effect on the pH of the solution inside the pores. The UV-Vis-NIR spectrum of the $[Co(citr)(H_2O)_3]^{2-}$ complexes present in all Cocitrate–pH9 solutions shows two distinct bands at 534 and 727 nm (Table 2). These bands are also observed in the spectrum recorded on the Al_2O_3 powder impregnated with the 1-2-Cocitrate-pH9 solution, as shown in Fig. 3. Apparently, the structure of the Co(II)-citrate complex remained largely intact after impregnation. The ^1H MRI images and the corresponding 1-dimensional profiles of the ^1H NMR signal as a function of position inside the extrudates, recorded at different points in time after impregnation, are presented in Fig. 12 and 13, respectively.

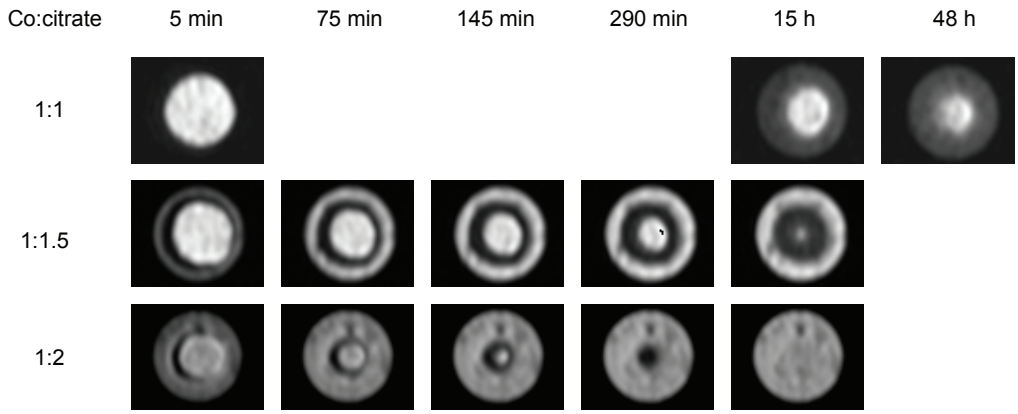

Figure 12. ^1H MRI images recorded on Al_2O_3 extrudates at different points in time after impregnation with (from top to bottom) 1-1-Cocitrate-pH9, 1-1.5-Cocitrate-pH9 and 1-2-Cocitrate-pH9 solutions.
For a color-version of this figure, see p. 185.

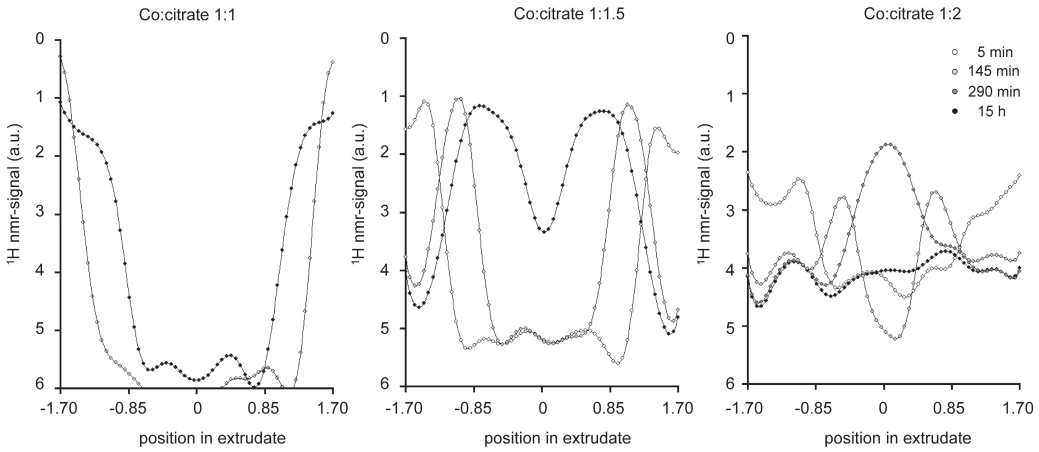

Figure 13. 1-Dimensional profiles of the ^{1}H NMR-signal as a function of position inside Al_2O_3 extrudates at different points in time after impregnation with (from left to right) 1-1-Cocitrate-pH9, 1-1.5-Cocitrate-pH9 and 1-2-Cocitrate-pH9 solutions.

The distribution of Co(II) after impregnation with the 1-1-Cocitrate-pH9 solution provides information on the interaction of the $[Co(citr)(H_2O)_3]^{2-}$ complex with the Al_2O_3 surface. A slow transport of Co(II)-complexes was observed in this case. Even at 48 h after impregnation, no constant ^{1}H NMR signal was observed for all positions inside the extrudate and from the intensity of the signal near the core of the extrudate, it is clear that no paramagnetic complexes are present at this position. The presence of an egg-shell distribution of Co(II)-complexes is confirmed by the photograph of a bisected extrudate, taken 120 min after impregnation with a 1-1-Cocitrate-pH9 solution shown on the top left of Fig. 14. UV-Vis-NIR microspectroscopy measurements (not shown) indicated that only $[Co(citr)(H_2O)_3]^{2-}$ complexes were present near the external surface of this extrudate. Since the pH of the impregnation solutions was close to the PZC of the support, the Al_2O_3 surface was probably neutrally charged after impregnation with the Cocitrate-pH9 solutions. Hence, the observed strong interaction between $[Co(citr)(H_2O)_3]^{2-}$ complexes and the Al_2O_3 surface can only be explained by a ligand-exchange mechanism, as expressed in Eq. 7. These complexes appear to be less strongly adsorbed than the $[Co(Hcitr)(H_2O)_3]^{-}$ complexes after impregnation with the 1-1-Cocitrate-pH5 solution. In comparison to the impregnation of Al_2O_3 extrudates with the 1-1-Cocitrate-pH5 solution, transport of Co(II)-complexes proceeded at a higher rate at pH 9.

$$[Co(citr)(H_2O)_3]^{2-} + x\ Al_sOH \xleftrightarrow{K_{ads}([Co(citr)(H_2O)_3]^{2-})} (Al_sO)_x Co(citr)(H_2O)_{(3-x)} + x\ H^+ \qquad \text{(Eq.7)}$$

Again, an increase in the citrate concentration of the impregnation solution leads to a faster transport of Co(II)-complexes. The size of the area with a high ^1H NMR-signal near the core of the extrudates (where no Co(II) complexes are present) decreases at a faster rate when impregnation is carried out with 1-1.5-Cocitrate-pH9 and 1-2-Cocitrate-pH9 solutions. This trend is also illustrated in Fig. 14, where photographs recorded on bisected extrudates 120 min after impregnation are shown, together with the corresponding ^1H MRI images. The domains where no Co(II)-complexes were present are labeled with the letter *a* in these images. A ring with low ^1H NMR intensity is observed at the edges of the extrudate impregnated with the 1-1-Cocitrate-pH9 solution and at positions near the advancing Co(II)-front, when impregnation is carried out with the 1-1.5-Cocitrate-pH9 and 1-2-Cocitrate-pH9 solutions. These areas are indicated by the letter *b*. In the corresponding photographs, a ring with a darker color is indeed observed at these positions. Towards the edges of the extrudates, a ring with a lighter color is observed, which is labeled with the letter *c*. In the corresponding MRI-images a higher signal is found for these positions. 15 h after impregnation with a 1-2-Cocitrate-pH9 solution, a constant signal is found throughout the extrudate. The intensity of the ^1H-NMR signal is only slightly lower than what was observed for an extrudate filled with water. Apparently, the Co(II) cations present in areas labeled as *c* are effectively shielded from the water protons and their destructive effect on the ^1H NMR signal is minimized.

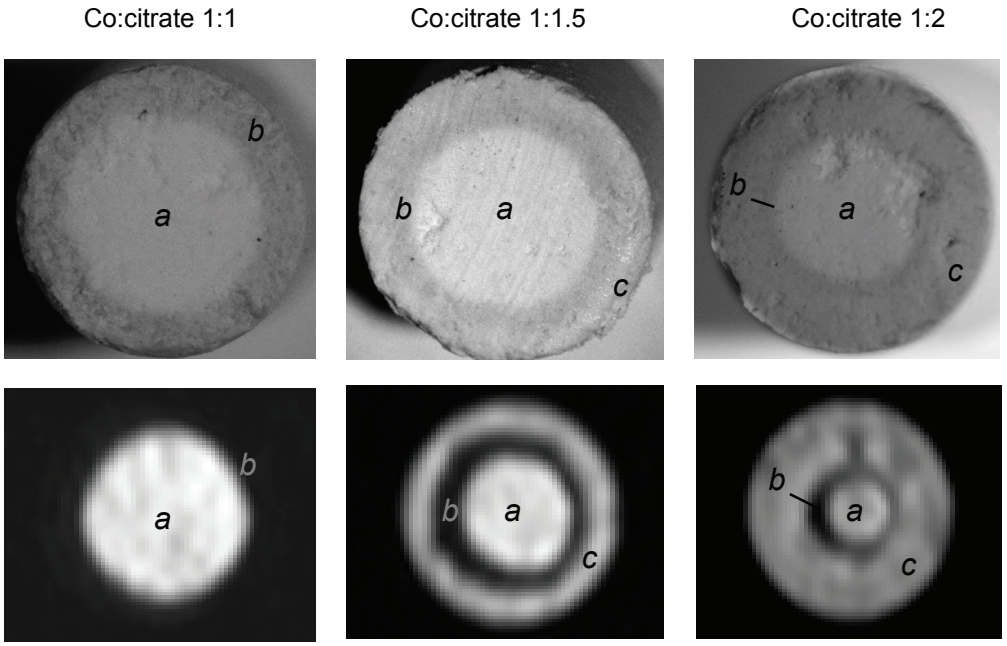

Figure 14. Photographs (top) and ^1H MRI images (bottom) recorded on Al_2O_3 extrudates 120 min after impregnation with (from left to right) 1-1-Cocitrate-pH9, 1-1.5-Cocitrate-pH9 and 1-2-Cocitrate-pH9 solutions. *For a color-version of this figure, see p. 185.*

To determine the nature of the Co(II)-complexes present in regions *a-c* inside the extrudates, UV-Vis-NIR spectra were recorded on an extrudate, bisected 120 min after impregnation with a 1-1.5-Cocitrate-pH9 solutions. The thus obtained spectra are presented in Fig 15. The positions of the measurement spots are indicated in the photograph. Bands are observed at 537 and 720 nm in all spectra recorded at positions where Co(II)-complexes are present (5,6 and 7). Only $[Co(citr)(H_2O)_3]^{2-}$ type complexes seem to be present inside the wet extrudates. The higher intensity of the d-d bands in spectra 5 and 6 shows that a slightly higher concentration of these complexes is present near the Co(II)-front. At the same time, the ^1H NMR signal at these positions is drastically decreased. Apparently, the destructive effect of $[Co(citr)(H_2O)_3]^{2-}$ complexes on the ^1H NMR signal is strongly enhanced above a certain concentration. Possibly, $[Co(citr)(H_2O)_3]^{2-}$ in solution have a much larger effect on the ^1H NMR signal than adsorbed $[Co(citr)(H_2O)_3]^{2-}$, since their paramagnetic Co(II) cations are more exposed to the water molecules. The presence of a high concentration of non-adsorbed complexes near the Co(II)-front could explain the low ^1H NMR signal observed at these positions.

The presence of additional citrate in the 1-1.5-Cocitrate-pH9 and 1-2-Cocitrate-pH9 solutions leads to a faster transport of Co(II)-complexes and the formation of a ring with higher Co-concentration near the protruding Co(II) front. When impregnation was carried out with Co(II)-

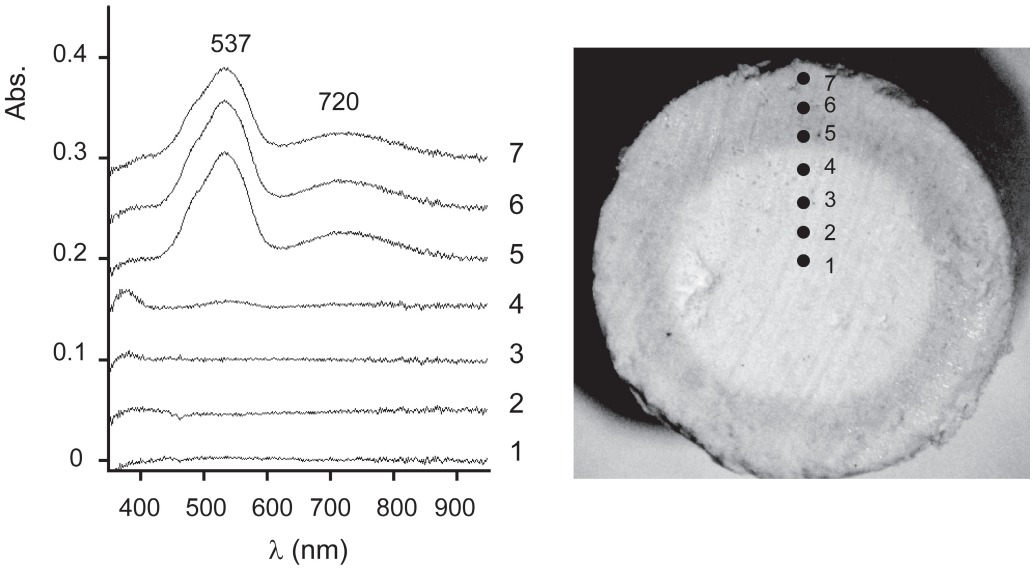

Figure 15. UV-Vis-NIR spectra recorded on an Al_2O_3 extrudate bisected 120 min after impregnation with a 1-1.5-Cocitrate-pH9 solution. The locations of the measurement spots are indicated in the photograph.

citrate solutions of pH 1 and 5, the manifestation of these phenomena could be explained by a mechanism, in which competitive adsorption takes place between citrate and Co(II)-complexes. For this explanation to be valid, $K_{ads}(citrH^{3-})$ needs to be larger than the adsorption equilibrium constants of the Co(II)-complexes, a reasonable assumption at low pH. However, at high pH, a weak interaction between citrate and the Al_2O_3 surface is reported in literature. As described in chapter 6, a homogeneous distribution of citrate was observed almost immediately after impregnation with a 0.40 M Na_3citrate solution of pH 9. This fast transport can be the result of a decrease in the number of adsorption sites available for the adsorption of citrate, rather than a decrease in $K_{ads}(citrH^{3-})$. In comparison, the 1-1.5-Cocitrate-pH9 and 1-2-Cocitrate-pH9 solutions contain a lower concentration of free citrate (Table 1). Hence, an inhomogeneous distribution of citrate may still be present in the first hours after impregnation with these solutions. Nevertheless, the occupation by citrate of a small percentage of the hydroxyl groups in the external area of the extrudates still renders the remaining hydroxyls available for the adsorption of $[Co(citr)(H_2O)_3]^{2-}$ and is unlikely to affect the adsorption of these complexes to any great extent. The situation changes when it is assumed that adsorption of citrate hinders the adsorption of $[Co(citr)(H_2O)_3]^{2-}$ on neighboring adsorption sites as well. The expected electrostatic repulsion between the adsorbed citrate and the negatively charged $[Co(citr)(H_2O)_3]^{2-}$ complex provides some justification for this assumption.

The relevant processes that occur inside an Al_2O_3 extrudate after impregnation with a 1-2-Cocitrate-pH9 solution are illustrated in a schematical manner in Fig. 16a. When competitive adsorption and blocking of $[Co(citr)(H_2O)_3]^{2-}$ adsorption sites by citrate is assumed, the distribution of citrate and $[Co(citr)(H_2O)_3]^{2-}$ complexes inside extrudates after impregnation with the different Cocitrate-pH9 solutions could be derived, using the simple model to describe impregnation. The resulting concentration profiles at 120 min after impregnation are presented in Fig. 16b.

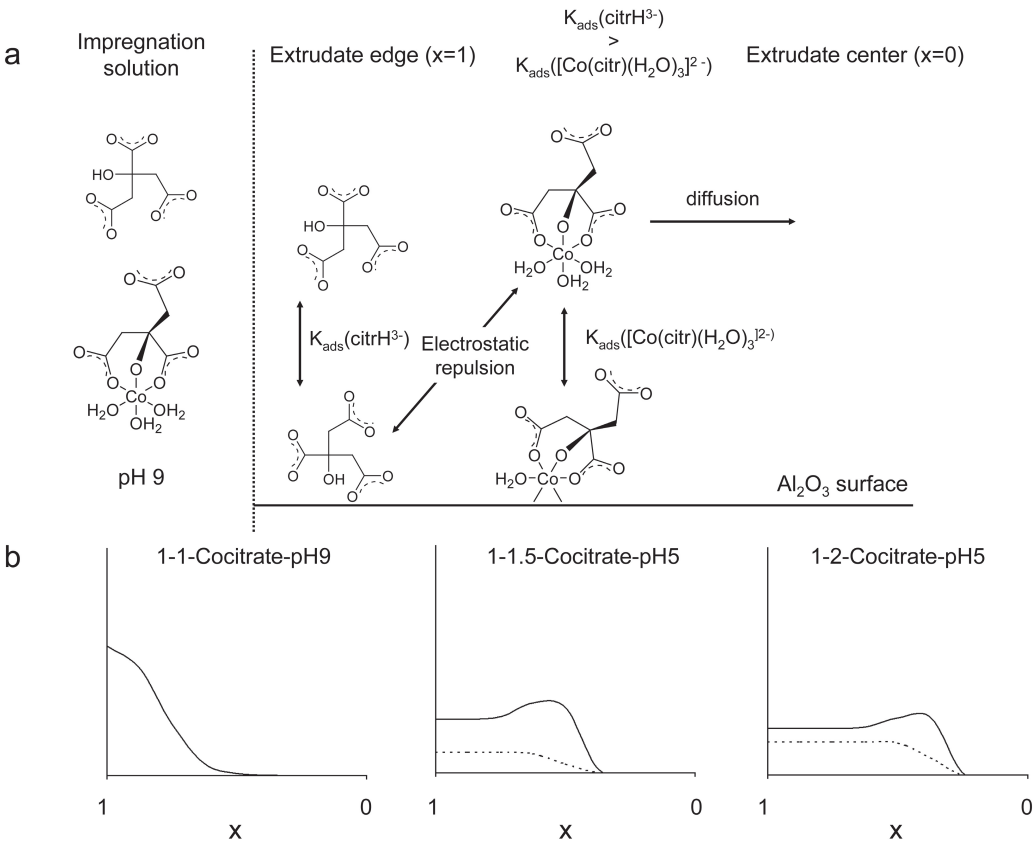

Figure 16. Schematic representation of the processes taking place inside an Al_2O_3 extrudate after impregnation with a 1-2-Cocitrate-pH9 solution (a) and the estimated distribution of $[Co(citr)(H_2O)_3]^{2-}$ (solid lines) and citrate (dotted lines) inside Al_2O_3 extrudates 120 min after impregnation with different Cocitrate-pH9 solutions.

Conclusions

The simultaneous application of UV-Vis-NIR micro-spectroscopy and MRI provided complementary information on the nature and distribution of Co(II)-complexes inside Al_2O_3 extrudates. In all cases, the obtained Co(II)-distribution inside Al_2O_3 extrudates could be derived from the ^1H MRI images, which further illustrates the potential of MRI in catalyst preparation studies. While UV-Vis-NIR micro-spectroscopy provides molecular information on the Co(II)-complexes inside the Al_2O_3 matrix, the macro-distribution of Co(II)-complexes inside the extrudates and the dynamics of the impregnation process could be envisaged by MRI.

In general, it was found that the addition of citrate to the impregnation solutions had two effects. First of all, the complexation of citrate to Co(II) resulted in a considerable increase in the interaction between the Co(II)-precursor and the support. As a result, (sharp) egg-shell Co-distributions were established after impregnation, when impregnation was carried out with solutions that merely contained Co(II)-citrate complexes. This is illustrated in the top part of Figure 17, in which a schematic representation is given of the macro-distribution of metal-ion complexes inside as a function of the adsorption strength of the complexes. Secondly, competitive adsorption between Co(II)-complexes and free citrate resulted in a faster transport of metal-ion complexes towards the center of the extrudates. The stronger interaction between free citrate and the Al_2O_3 surface led to the establishment of an egg-shell distribution of this component after impregnation. Near the exterior surface of the extrudates, fewer sites were now available for the adsorption of Co(II)-complexes and the Co(II)-complexes were found to diffuse faster to the center of the extrudates. Egg-white and egg-yolk distributions of Co were formed during ageing. The effect of the addition to the impregnation solution of a component that adsorbs strongly to the Al_2O_3 surface, on the macro-distribution of metal-ion complexes inside extrudates is schematically depicted in the bottom part of Fig. 17. By varying the pH and the citrate concentration in the impregnation solutions, the macro-distribution of Co(II)-complexes inside Al_2O_3 extrudates could be controlled.

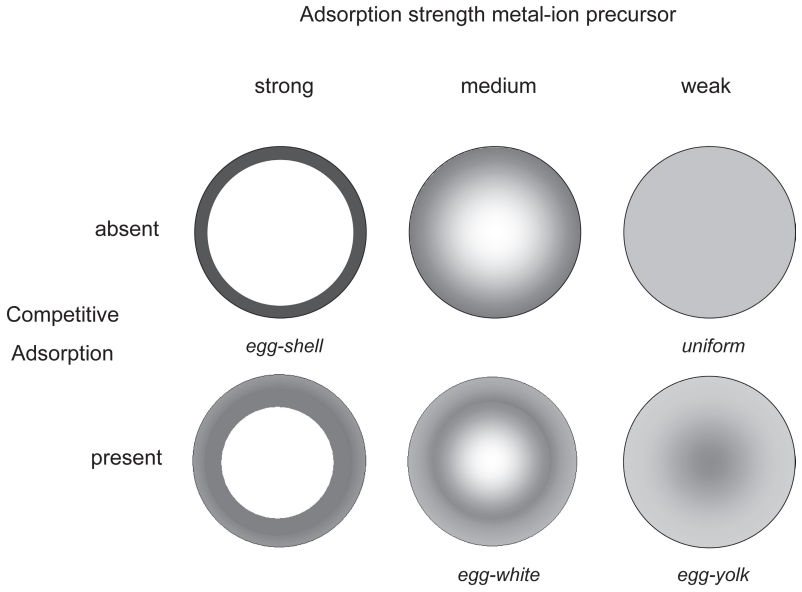

Figure 17. Schematic representation of the different types of metal-ion precursor distributions, that can be obtained inside catalyst bodies after impregnation, by varying the interaction between the metal-ion complexes and the support (horizontal) or by the addition of a competitive adsorbent (vertical).

Acknowledgments

Dr. Anna Lysova and prof. dr. Igor Koptyug of the International Tomography Center SB RAS in Novosibirsk (Russia) are kindly acknowledged for facilitating the MRI measurements and their help in interpretation of the results. Thanks to Leticia Espinosa Alonso for her help during the experiments and valuable discussions. The UV-Vis-NIR micro-scpectroscopy measurements and the photography of bisected extrudates were carried out by Danny Verboekend in the context of his master thesis. Ad van der Eerden is thanked for XRF measurements and Ad Mens for N_2-physisorption.

References

1 J. A. Fetchin, US Patent 4.409.131, **1983**.
2 H. D. Simpson, P. B. Borgens, US Patent 4.879.625, **1988**.
3 P. J. Shukis, J. D. Carruthers, V. J. Lostagio, WO Patent 9.531.280, **1995**.
4 H. D. Simpson, European Patent 0.349.223, **1989**.
5 L. van de Loosdrecht, M. van der Haar, A. M. van der Kraan, A. J. van Dillen, J. W. Geus, *Appl. Catal. A-General* **1997**, *150*, 365.
6 L. G. A. van de Water, L. G. Bezemer, J. A. Bergwerff, M. Versluijs-Helder, B. M. Weckhuysen, K. P. De Jong, *J. Catal.* **2006**, *242*, 287.
7 P. J. van den Brink, A. Scholten, A. van Wageningen, M. D. A. Lamers, A. J. van Dillen, J. W. Geus, *Stud. Surf. Sci. Catal.* **1991**, *63*, 527.
8 F. R. van den Berg, M. W. J. Craje, A. M. van der Kraan, J. W. Geus, *Appl. Catal. A-General* **2003**, *251*, 347.
9 D. J. Lensveld, J. G. Mesu, A. J. van Dillen, K. P. de Jong, *Microporous Mesoporous Mat.* **2001**, *44*, 401.
10 R. Takahashi, S. Sato, T. Sodesawa, M. Kato, S. Takenaka, S. Yoshida, *J. Catal.* **2001**, *204*, 259.
11 G. K. Bethke, H. H. Kung, *Appl. Catal. A-General* **2000**, *194*, 43.
12 S. S. Pansare, A. Sirijaruphan, J. G. Goodwin, *J. Catal.* **2005**, *234*, 151.
13 G. R. Meima, B. G. Dekker, A. J. van Dillen, J. W. Geus, J. E. Bongaarts, F. R. van Buren, K. Delcour, J. M. Wigman, *Stud. Surf. Sci. Catal.* **1987**, *31*, 83.
14 R. J. A. M. Terörde, J. W. Geus, WO Patent 9.732.813, US Patent 6.207.127, **2001**.
15 A. J. van Dillen, R. Terorde, D. J. Lensveld, J. W. Geus, K. P. de Jong, *J. Catal.* **2003**, *216*, 257.
16 J. Park, J. R. Regalbuto, *J. Colloid Interface Sci.* **1995**, *175*, 239.
17 L. G. A. van de Water, J. A. Bergwerff, T. A. Nijhuis, K. P. de Jong, B. M. Weckhuysen, *J. Am. Chem. Soc.* **2005**, *127*, 5024.
18 N. Kotsakis, C. P. Raptopoulou, V. Tangoulis, A. Terzis, J. Giapintzakis, T. Jakusch, T. Kiss, A. Salifoglou, *Inorg. Chem.* **2003**, *42*, 22.
19 J. Vakros, K. Bourikas, S. Perlepes, C. Kordulis, A. Lycourghiotis, *Langmuir* **2004**, *20*, 10542.
20 P. C. Hidber, T. J. Graule, L. J. Gauckler, *J. Am. Ceram. Soc.* **1996**, *79*, 1857.
21 P. Papageorgiou, D. M. Price, A. Gavriilidis, A. Varma, *J. Catal.* **1996**, *158*, 439.

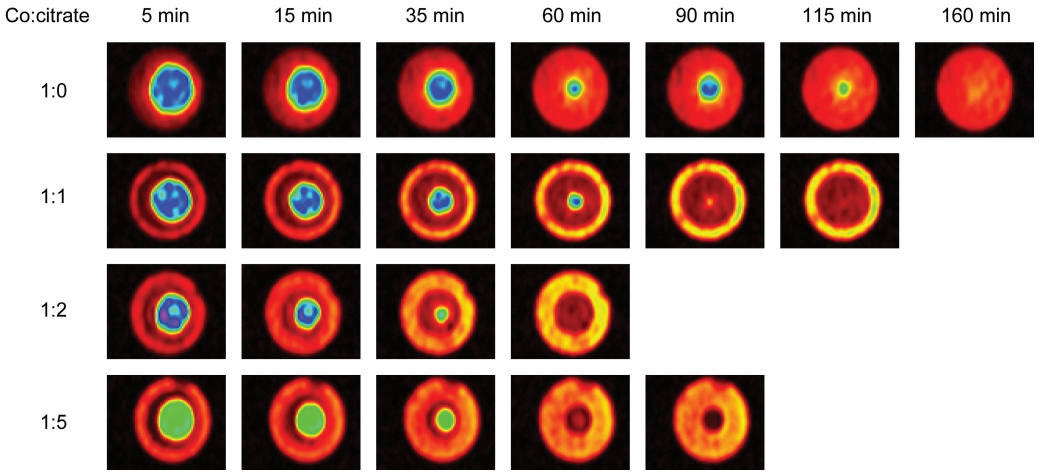

Figure 7. 4. ^{1}H MRI images recorded on Al_2O_3 extrudates after impregnation with (from top to bottom) 0.2 M $Co(NO_3)_2$, 1-1-Cocitrate-pH1, 1-2-Cocitrate-pH1 and 1-5-Cocitrate-pH1 solutions. A red color in these images represents a low ^{1}H NMR signal. A high ^{1}H NMR signal is indicated by a blue color.

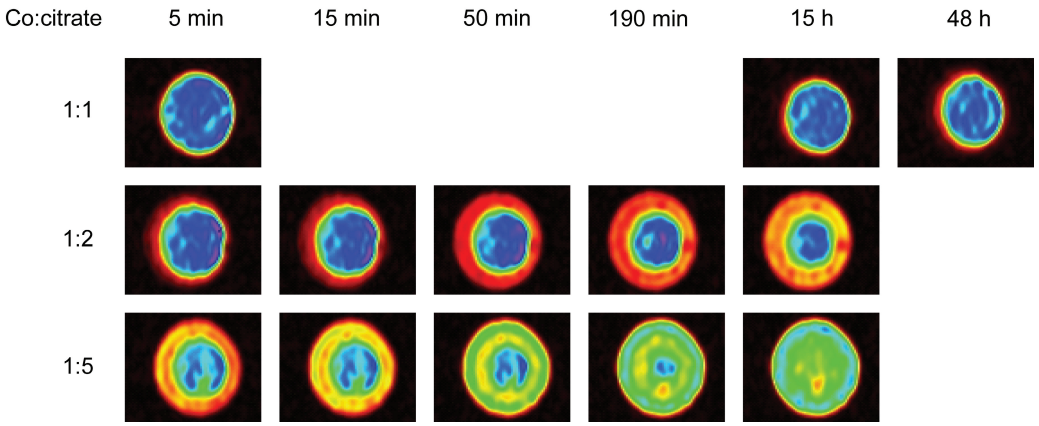

Figure 7. 8. ^{1}H MRI images recorded on Al_2O_3 extrudates after impregnation with (from top to bottom) 1-1-Cocitrate-pH5, 1-2-Cocitrate-pH5 and 1-5-Cocitrate-pH5 solutions. A red color in these images represents a low ^{1}H NMR signal. A high ^{1}H NMR signal is indicated by a blue color.

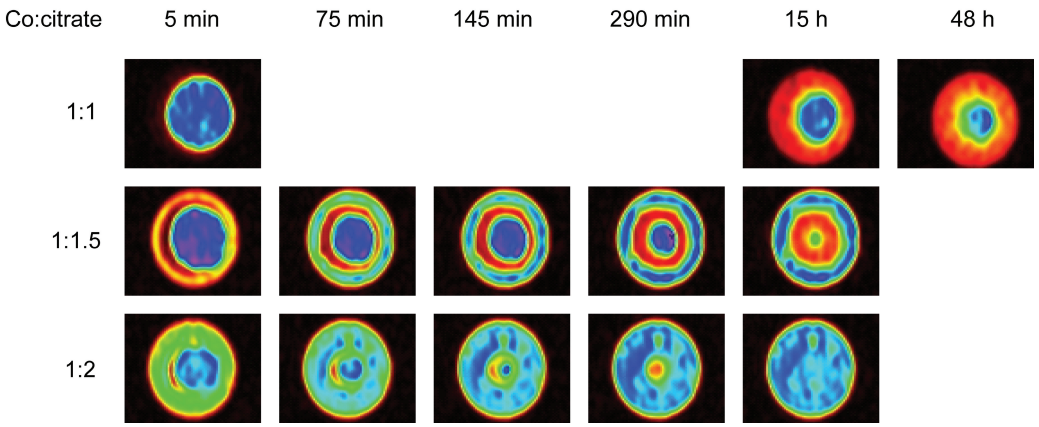

Figure 7. 12. ^{1}H MRI images recorded on Al_2O_3 extrudates at different points in time after impregnation with (from top to bottom) 1-1-Cocitrate-pH9, 1-1.5-Cocitrate-pH9 and 1-2-Cocitrate-pH9 solutions. A red color in these images represents a low ^{1}H NMR signal. A high ^{1}H NMR signal is indicated by a blue color.

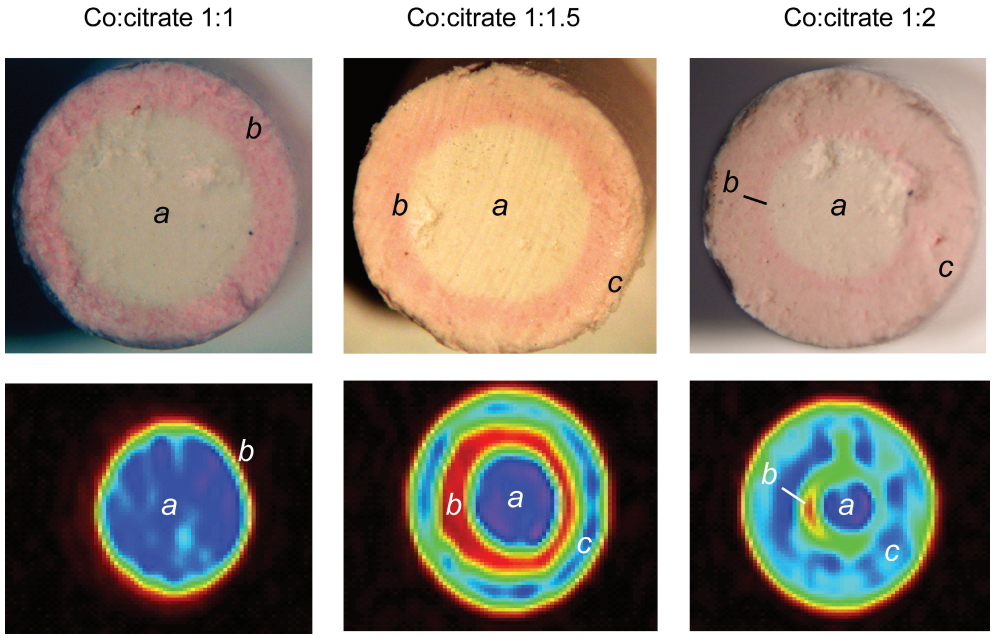

Figure 7. 14. Photographs (top) and ^{1}H MRI images (bottom) recorded on Al_2O_3 extrudates 120 min after impregnation with (from left to right) 1-1-Cocitrate-pH9, 1-1.5-Cocitrate-pH9 and 1-2-Cocitrate-pH9 solutions. A red color in these images represents a low ^{1}H NMR signal. A high ^{1}H NMR signal is indicated by a blue color.

Chapter 8A

Summary and Conclusions

The aim of this PhD-thesis was to explore the potential of spatially resolved spectroscopic techniques for the characterization of supported catalyst bodies at the different stages of their preparation process. The preparation of (Co)Mo/Al_2O_3 hydrodesulphurization catalyst extrudates was used as a showcase to illustrate the possibilities and limitations of the three different techniques under study, i.e. Raman and UV-Vis-NIR micro-spectroscopy and Magnetic Resonance Imaging (MRI).

Summary

In **chapter 2**, the use of Raman and UV-Vis-NIR spectroscopy for the characterization of Mo(VI)- and Co(II)-complexes in aqueous solution was evaluated. The speciation of these complexes was studied in the presence of citrate and phosphate as complexing agents. Reference spectra of Mo(VI)-isopolyanions, phosphomolybdate complexes and Mo(VI)- and Co(II)-citrate complexes were derived with the aid of chemometric techniques. The complexation of Co(II) by Mo(VI)-anions was found to lead to the formation of $Co_2Mo_7O_{24}$ and $H_2PMo_{11}CoO_{40}^{5-}$ complexes in CoMo-solutions.

The application of Raman micro-spectroscopy to study the preparation of Mo/Al_2O_3 catalyst bodies was the subject of **chapters 3 and 4**. In the experiments, described in chapter 3, the transport of different Mo(VI)-complexes inside 3 mm-Al_2O_3 pellets after impregnation was studied. In general, diffusion of the Mo(VI)-anions was found to be slow when impregnation was carried out with acidic solutions. Impregnation with solutions containing $Mo_7O_{24}^{6-}$ anions led to the formation of an $Al(OH)_6Mo_6O_{18}^{3-}$ precipitate on the external surface of the pellets, due to ligand-promoted dissolution of the support. The formation of $Al(OH)_6Mo_6O_{18}^{3-}$ could de prevented by the use of basic impregnation solutions or the addition of complexing agents, such as phosphate and citrate. In chapter 4, Raman micro-spectroscopy was applied as the main technique to monitor the nature and distribution of the Mo-phase in the different steps (impregnation, drying and calcination) in the preparation of industrial 1.5 mm-sized Mo/Al_2O_3

extrudates. The formation of an $Al(OH)_6Mo_6O_{18}^{3-}$ precipitate during impregnation was again observed on the exterior surface of the extrudates, resulting in the formation of bulk MoO_3 after calcination. The poor interaction between MoO_4^{2-} anions and the Al_2O_3 surface after impregnation with basic Mo(VI)-solutions resulted in the redistribution of Mo(VI)-complexes and the formation of an egg-shell distribution of Mo during the drying step. As a result of the high Mo-loading in the periphery of the extrudates, bulk MoO_3 and $Al_2(MoO_4)_3$ were formed in these areas during calcination, In both cases, the formation of crystalline oxidic phases resulted in a poorly dispersed MoS_2 phase in the final catalyst and a lower activity in hydrodesulphurization. The detrimental processes could be prevented by the addition of citric acid to the impregnation solution.

In **chapter 5**, UV-Vis-NIR micro-spectroscopy was introduced as a means to monitor the distribution of Co(II)-complexes inside $CoMo/Al_2O_3$ pellets after impregnation. Impregnation with a solution, predominantly containing $H_2PMo_{11}CoO_{40}^{5-}$ complexes, was found to lead to the disintegration of this complex inside the pellets, due to a reaction of phosphate with the Al_2O_3 surface. The $H_2PMo_{11}CoO_{40}^{5-}$ heteropolyanion could be stabilized inside the Al_2O_3 pores by the addition of extra phosphate to the impregnation solution. By varying the phosphate concentration and the ageing time, its macroscopic distribution inside the Al_2O_3 pellets could be controlled.

In the experiments reported in **chapters 6 and 7**, the application of MRI to monitor the transport of metal-ion complexes and complexing agents inside impregnated Al_2O_3 extrudates was investigated. By this non-invasive technique the dynamics of the impregnation process could be envisaged. Via the direct imaging of MRI-sensitive nuclei ^{13}C and ^{31}P, it proved possible to determine the distribution of citrate and phosphate inside Al_2O_3 extrudates as a function of time after impregnation. Through the effect of diamagnetic components on the T_1 relaxation time of water protons, the distribution of citrate could be derived in ^1H MRI experiments by the application of inversion-recovery pulse sequences. Quantitative distribution plots of Co(II) after impregnation with a $Co(NO_3)_2$ solution were obtained through the detrimental effect of paramagnetic cations on the ^1H NMR signal. This indirect imaging technique was further exploited in chapter 7 to determine the distribution of Co(II)-complexes after impregnation with Co(II)-citrate solutions of different pH and citrate concentration. The complexation of Co(II) by citrate resulted in a stronger interaction between the Co(II)-complexes and the support and the formation of an egg-shell distribution of Co after impregnation. At the same time, the presence of additional citrate resulted in competitive adsorption between citrate and Co(II)-complexes and a faster transport of Co. The macro-distribution of Co(II)-complexes

could be controlled and egg-yolk and egg-white distributions of Co could be obtained after impregnation. In all cases UV-Vis-NIR micro-spectroscopy measurements confirmed the observations made in ^{1}H MRI measurements, thus validating the use of this technique in catalyst preparation studies.

General Conclusions

As explained in the introduction (chapter 1), interaction between metal-ion complexes and the support surface can take place through a number of mechanisms, i.e. ligand exchange, electrostatic interaction and ligand promoted dissolution of the support. The molecular information obtained in Raman and UV-Vis-NIR micro-spectroscopy experiments allows one to distinguish between the different adsorption mechanisms that are operative after impregnation of catalyst bodies with solutions of different metal-ion complexes.

First of all, it was found that ligand-exchange was responsible for the adsorption of MoO_4^{2-} to the Al_2O_3-surface after impregnation with acidic AHM-solutions. A band was observed in the Raman spectra at 920 cm^{-1} that was not observed in spectra recorded on AHM-solutions. It was assigned to a molybdate covalently bound to the support surface through two bridging oxygen groups ($(Al_s)_2MoO_4$). A shift in the Co(II) d-d transition band in the UV-Vis-NIR spectra after impregnation with $Co(NO_3)_2$ solutions, pointed to a change in the coordination sphere around Co(II). This could be explained by the formation of inner-sphere surface Co(II)-complexes.

In spectroscopic studies on impregnated powdered support materials, it is impossible to distinguish between metal-ion complexes that are present in solution inside the pores or electrostatically adsorbed onto the support surface, since both have the same molecular structure and, hence, give rise to the same spectrum. Spatially resolved spectroscopic techniques offer the advantage that, besides the molecular structure of the different metal-ion complexes, their transport rate through the pore-system can be determined. This allows one to make statements on the strength of the interaction between the metal-ion precursor and the support. After impregnation of Al_2O_3 bodies with an acidic AHM-citrate solution, a slow transport of $Mo_4(Hcitrate)_2O_{11}^{4-}$ complexes was observed, as reported in chapter 3. Nevertheless, the positions of bands in the Raman spectrum of the impregnated material were identical to the band positions in the spectrum recorded on the AHM-citrate impregnation solution. Apparently, the molecular structure of the $Mo_4(Hcitrate)_2O_{11}^{4-}$ complex remained intact after impregnation. A strong electrostatic interaction between the negatively charged complexes and the positively charged surface could explain the slow transport of $Mo_4(Hcitrate)_2O_{11}^{4-}$

inside the support bodies.

A combination of low pH and a high concentration of reactive Mo(VI) complexes was found to lead to the formation of a $Al(OH)_6Mo_6O_{18}^{3-}$ precipitate on the outside of Al_2O_3 bodies after impregnation with acidic AHM-solutions, through ligand-promoted dissolution of the support (chapters 3 and 4). The formation of this phase could be demonstrated by Raman micro-spectroscopy. In characterization studies on the preparation of Mo/Al_2O_3 catalysts in the powder-form, the formation of $Al(OH)_6Mo_6O_{18}^{3-}$ has been overlooked for a long time. The resemblance in molecular structure of $Mo_7O_{24}^{6-}$ and $Al(OH)_6Mo_6O_{18}^{3-}$ makes that it is not easy to distinguish between these complexes through Raman spectroscopy. After impregnation of Al_2O_3 powder with an acidic AHM solution, both complexes are probably present in the sample, which makes the analysis even more complicated. However, the fact that the $Al(OH)_6Mo_6O_{18}^{3-}$ compound was selectively formed at specific positions in the catalyst bodies, facilitated its diagnosis and yielded additional information on its formation.

Since a combination of Raman micro-spectroscopy, UV-Vis-NIR micro-spectroscopy and MRI have been applied to study the preparation of a number of different systems, it is possible to evaluate the strengths and weaknesses of these techniques in catalyst preparation studies. The main advantage of Raman and UV-Vis-NIR micro-spectroscopy, as compared to traditional means for the analysis of catalyst bodies, such as elemental analysis, lies in the fact that molecular information can be obtained on the metal-ion complexes inside the catalyst bodies. Furthermore, wet extrudates can be analyzed, which allows one to monitor the distribution of metal-ion complexes after impregnation. Since quantification of the signal from metal-ion complexes was often cumbersome, the use of classical techniques for the reliable determination of metal-distribution profiles remains of interest. Therefore, we envisage that these techniques are to be applied alongside the conventional methods in catalyst preparation studies, as for instance illustrated in chapter 4, where SEM-EDX was used to verify the Mo-distribution profiles observed with Raman micro-spectroscopy.

The possibility to perform measurements on the distribution of components inside catalyst bodies in a non-invasive manner is the greatest asset of the MRI methods that were developed. This aspect is of specific importance when dynamic processes, such as the transport of different compounds inside impregnated catalyst bodies, are under study. The possibility to obtain quantitative information on the distribution of paramagnetic cations inside catalyst bodies is another promising feature of this technique. However, the molecular information that can be obtained through NMR-spectroscopy is most often lost when the technique is applied in

a spatially resolved mode. For this reason, the complementary use of Raman and UV-Vis-NIR micro-spectroscopy can be of great help for the interpretation of the observations made in the MRI-measurements, as was illustrated in chapter 7.

Based on the above-described results it can be concluded that micro-spectroscopic techniques can provide detailed information on the molecular structure and spatial distribution of the metal-precursors inside catalyst bodies at the different stages of catalyst preparation. This information can be used for the preparation of supported catalysts in a more controlled manner and, eventually, for the development of more active catalytic systems, as was illustrated in this PhD thesis for Mo/Al_2O_3 catalysts.

Chapter 8B

Perspectives

Most of the studies described in this PhD-thesis deal with the processes taking place after impregnation of extrudates with different impregnation solutions. In this case, well-defined metal-ion complexes were usually present in the solution inside the pores of the support. One is able to obtain a clear picture of the nature of these complexes through Raman and UV-Vis-NIR (micro-)spectroscopy by comparison to spectra of the metal-ion complexes in aqueous solution. The characterization of the surface metal-ion complexes that are formed after adsorption of these complexes to the support surface after impregnation and drying is a much more difficult task. One of the barriers that needs to be overcome is the lack of knowledge on the configuration of the oxidic surfaces.

In the characterization of calcined extrudates, the distribution and size of metal-oxide crystals are important parameters. Therefore, the application of Tomographic Energy Dispersive Diffraction Imaging (TEDDI) could yield valuable additional information. In this technique, a sample is exposed to a cylindrical collimated X-ray beam with a diameter of ~ 0.1 mm. At fixed angles to the incident beam, detectors are located to collect the X-rays in an energy dispersive way, as illustrated in Fig. 1. The thus obtained spectra contain information on the diffraction and fluorescence of X-rays in a volume defined by the intersection of the incident and diffracted beam paths, the so-called lozenge. By collimation of the diffracted beam, the dimensions of the volume from which the signal is detected can be decreased to approximately 100 μm in the directions normal to the incident beam and several millimeters in the direction parallel to the beam. The energy-dispersive spectra can be converted into 1/d diffraction patterns with the aid of Bragg's law for the diffraction of X-rays with a certain wavelength λ at a fixed angle θ as shown in Eq. 1. By translating the sample in the incident beam, information can be obtained on the distribution of crystalline phases in the material under study. The fluorescence peaks that are present in the spectra, contain information on the distribution of different elements in the sample.

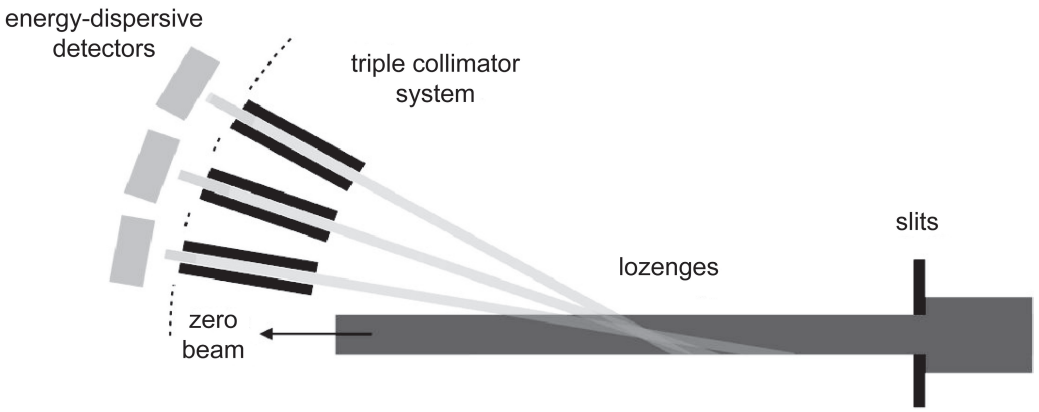

Figure 1. Schematic representation of the three-angle energy-dispersive diffractometer, as it is set up at station 16.4 of the SRS Daresbury Laboratory (UK) for the TEDDI experiments.

$$\frac{1}{d} = \frac{n\lambda}{2\sin\theta} \qquad \text{(Eq. 1)}$$

As a proof of principle, the X-ray tomography technique was applied for the analysis of a calcined Mo/Al_2O_3 extrudate of 1.5 mm diameter. The extrudate was prepared by impregnation with a 1.8 M Mo AHM-pH 6 solution, as described in chapter 4. Fig. 2 shows an energy dispersive diffraction pattern obtained from a location near the external surface of the extrudate. Peaks due to Mo K_α and K_β fluorescence are observed at 17 and 20 keV, respectively. Peaks due to reflections of bulk MoO_3 (40-50 keV) and γ-Al_2O_3 (78 keV) are present as well. An intensity map of the γ-Al_2O_3 diffraction peak (bottom left) allows one to observe the contours of the extrudate. Information on the density of the support may also be derived in this way. The distribution of the Mo-phase can be obtained through the intensity of the Mo K_β fluorescence peak for different positions (bottom middle). A rather homogeneous Mo-distribution seems to be present inside the bulk of this particular extrudate, with an accumulation of Mo on or near the outer surface. Crystalline MoO_3, on the other hand, is only present in the periphery of the extrudates, since MoO_3 reflection peaks were only observed for these positions (bottom right). These observations are in line with the results of a Raman micro-spectroscopy study on this sample. Besides the characterization of calcined material, the technique might be used to study the distribution of metal-ion complexes inside catalyst bodies after impregnation in a non-invasive manner through the fluorescence signal of the metal-atoms. Furthermore, it may be possible to study the formation of crystalline phases through in-situ studies on the drying and calcination of catalyst bodies.

In this PhD thesis, it was illustrated that micro-spectroscopic techniques can provide quantitative information on the distribution of metal-ion complexes inside catalyst bodies as a function of time after impregnation. The quantitative distribution plots of Co(II) inside Al_2O_3, obtained from MRI-measurements (Fig. 13 in chapter 6) provide in this respect the best example. No attempt was made to interpret these profiles in a quantitative manner. Nevertheless, these data would provide the perfect input for the development of models describing the adsorption and diffusion of metal-ion complexes inside catalyst bodies after impregnation. Untill now, such quantitative models were based on metal-distributions obtained after drying. The techniques that were described could be great tools for the quantitative modeling of the transport of components inside catalyst bodies after impregnation and during drying.

The analysis of bisected extrudates with Raman and UV-Vis-NIR micro-spectroscopy could be applied in an industrial context in a reasonably straightforward manner. One could envisage their use in a control system for the industrial preparation of supported catalysts. During the ageing process, individual extrudates could be removed from the product stream, to check whether a homogeneous distribution of metal-ion complexes is obtained. As a quality control of the final product, Raman-micro-spectroscopy could be used to detect the unwanted formation of crystalline phases in supported metal-oxide catalysts, while UV-Vis-NIR micro-spectroscopy could for instance be applied at this stage to signal the formation of the undesired $CoAl_2O_4$ phase in the preparation of Co/Al_2O_3 catalysts.

Acknowledgment

Simon Jacques of University College London (UK) is kindly acknowledged for the Tomographic Energy Dispersive Diffraction Imaging experiments.

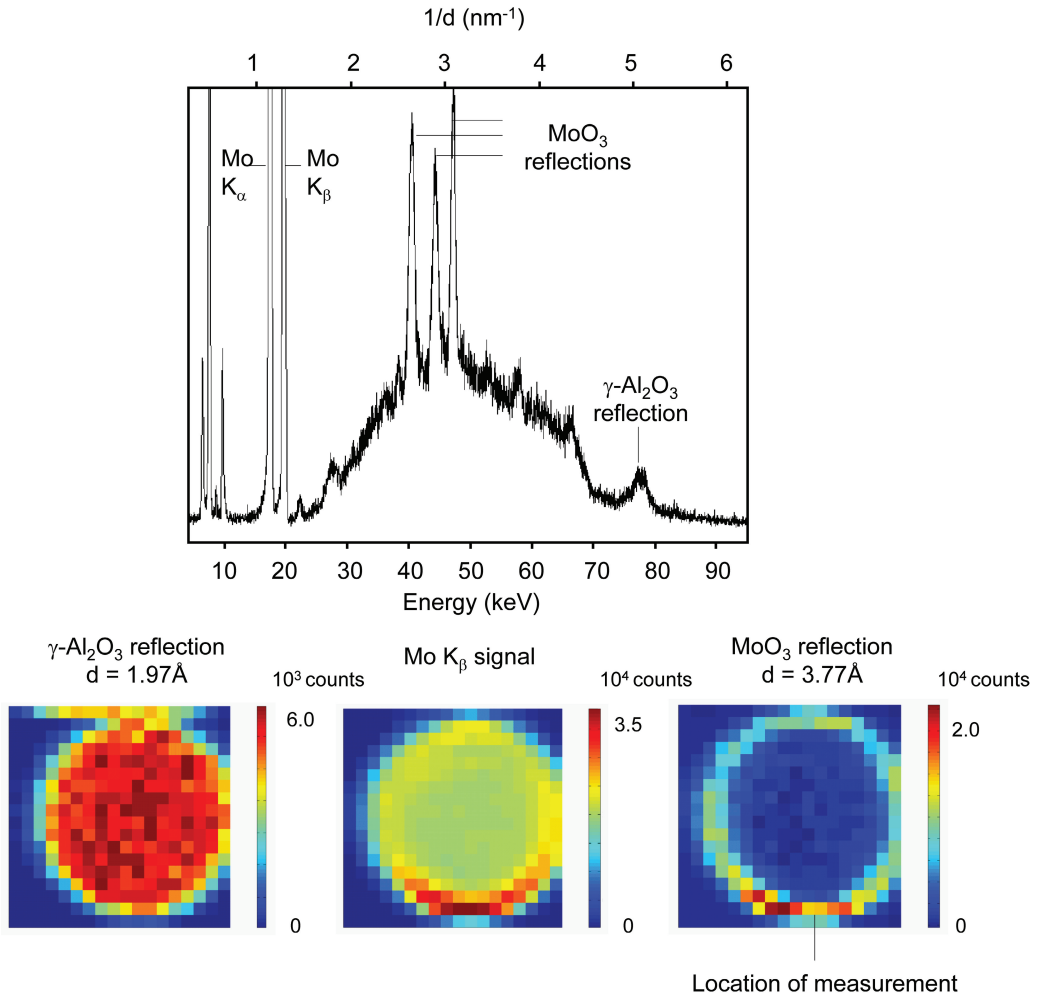

Figure 2. Energy dispersive diffraction pattern obtained on a calcined Mo/Al_2O_3 extrudate (top) and the intensity plots of the d = 1.97 Å diffraction peak of γ-Al_2O_3, the MoK_β fluorescence peak and the d = 3.77 Å diffraction peak of MoO_3 (bottom from left to right).

Hoofdstuk 8C

Samenvatting

Het voornaamste doel van dit proefschrift was het ontwikkelen van microspectroscopische technieken voor de karakterisering van gedragen katalysator lichamen, zoals extrudaten. Uiteindelijk is gebruik gemaakt van drie technieken, te weten Raman microspectroscopie, UV-Vis-NIR microspectroscopie en magnetic resonance imaging (MRI). Deze technieken maken het mogelijk om informatie te verkrijgen over de verdeling van metaalion complexen en andere verbindingen binnen een katalysatordeeltje. Deze technieken zijn toegepast om de bereiding van (Co)Mo/Al_2O_3 ontzwavelingskatalysatoren te volgen in de verschillende stappen van het bereidingsprocédé. Op deze manier werden de mogelijkheden en beperkingen van de drie microspectroscopische technieken verkend.

In **hoofdstuk 2** wordt beschreven hoe Raman en UV-Vis-NIR spectroscopie gebruikt kunnen worden voor de karakterisering van Mo(VI) en Co(II)-complexen in waterige oplossingen. Met behulp van chemometrie werden referentiespectra verkregen van Mo(VI)-isopolyanionen, fosfomolybdaat complexen, Mo(VI)-citraat en Co(II)-citraat complexen. In gemengde CoMo oplossingen, bleek dat Co(II)-kationen gecomplexeerd werden door Mo(VI)-complexen, wat leidde tot de vorming van $Co_2Mo_7O_{24}^{2-}$ en $H_2PMo_{11}CoO_{40}^{5-}$ complexen die zowel Co(II)- als Mo(IV) bevatten.

De resultaten van een Raman microspectroscopie studie naar de bereiding van Mo/Al_2O_3 katalysatoren staan beschreven in **hoofdstuk 3 en 4.** Met behulp van deze techniek werd, na impregnatie met verschillende oplossingen, de verdeling van Mo(VI)-complexen binnen Al_2O_3 extrudaten met een doorsnede van 3 mm bestudeerd. Het bleek dat het transport van de negatief geladen Mo(VI)-complexen vanaf de buitenkant van de extrudaten naar de kern na impregnatie met een zure oplossing langzaam verliep. Na impregnatie met een oplossing die $Mo_7O_{24}^{6-}$ anionen bevatte, bleek dat door de werking van dit anion, de Al_2O_3 drager gedeeltelijk oploste. Hierdoor werd er een neerslag van $Al(OH)_6Mo_6O_{18}^{3-}$ gevormd aan de buitenkant van de dragerlichamen. Dit kon worden voorkomen door citroenzuur of fosforzuur toe te voegen aan de impregnatieoplossing en zodoende stabiele Mo(VI)-citraat en

fosfomolybdaat complexen te vormen. In hoofdstuk 4 werd met behulp van dezelfde techniek de bereiding van cilindrische Mo/Al_2O_3 extrudaten met een diameter van 1.5 mm bestudeerd. De afmetingen van deze extrudaten kwamen overeen met wat gebruikelijk is in de industriële praktijk. Dit keer werd niet allen gekeken naar geïmpregneerde systemen, maar werden ook gedroogde en gecalcineerde extrudaten geanalyseerd, zodat het hele bereidingsproces kon worden gevolgd. Opnieuw bleek dat een impregnatie met $Mo_7O_{24}^{6-}$ anionen leidde tot de vorming van een $Al(OH)_6Mo_6O_{18}^{3-}$ neerslag op het buitenoppervlak van de extrudaten. Tijdens calcinatie werd deze fase omgezet in kristallijn MoO_3. Wanneer impregnatie werd uitgevoerd met een basische oplossing, die MoO_4^{2-}-anionen bevatte, resulteerde de geringe interactie tussen de Mo(VI)-complexen en het drageroppervlak in een herverdeling van de Mo-fase. Na drogen werd een verhoogde concentratie van Mo(VI)-complexen aan de buitenkant van de extrudaten waargenomen. Bij hoge MoO_3 beladingen leidde dit tot de vorming van MoO_3 en $Al_2(MoO_3)_4$ kristallen in de buitenste ring van de katalysatorlichamen. In beide gevallen had de vorming van kristallijn materiaal na calcinatie een slechte dispersie van de actieve MoS_2 fase in de katalysator tot gevolg. De activiteit van de katalysatoren in de ontzwavelingsreactie werd op zijn beurt weer negatief beïnvloed door deze verminderde dispersie. Door citroenzuur toe te voegen aan de impregnatieoplossingen, konden deze ongewenste processen worden voorkomen.

In **hoofdstuk 5** wordt een UV-Vis-NIR microspectroscopie opstelling gepresenteerd, die gebruikt kan worden om de ruimtelijke verdeling en de aard van Co(II) complexen binnen Al_2O_3 lichamen te bepalen. Met behulp van deze techniek werd waargenomen dat impregnatie van Al_2O_3 pillen met een $H_2PMo_{11}CoO_{40}^{5-}$ oplossing, leidde tot het uiteenvallen van dit complex in de poriën van de drager. Dit werd veroorzaakt door de reactie van fosfaat met het drageroppervlak. Door het toevoegen van extra fosfaat aan de impregnatieoplossing kon worden bewerkstelligd, dat hetzelfde complex gevormd werd binnen de geïmpregneerde Al_2O_3 pillen. De verdeling van $H_2PMo_{11}CoO_{40}^{5-}$ binnen de dragerlichamen kon worden ingesteld door de fosfaatconcentratie in de impregnatieoplossing te variëren.

In **hoofdstuk 6 en 7** worden experimenten besproken, die tot doel hadden om de toepasbaarheid van MRI in studies naar de bereiding van katalysatorlichamen te exploreren. Het bleek dat het transport van metaalionen en complexvormers binnen dragerlichamen uitstekend kon worden gevolgd met behulp van deze techniek. MRI heeft als voornaamste voordeel dat de diffusie van verbindingen in het poriesysteem niet wordt beïnvloed door de meting. Door de verdeling van de NMR-actieve kernen ^{13}C en ^{31}P te bepalen op verschillende tijdstippen na de impregnatie, kon het transport van citraat en fosfaat door Al_2O_3 extrudaten

worden gevisualiseerd. Diamagnetische verbindingen, zoals citraat bleken de spin-rooster (T_1) relaxatietijd van waterprotonen te verlengen. Door de T_1 relaxatietijd van protonen te bepalen op verschillende posities binnen de extrudaten kon een indruk worden verkregen van de verdeling van het citraat. Doordat paramagnetische kationen, zoals Co(II) het ^{1}H NMR signaal van water onderdrukken, kon de verdeling van deze component ook worden afgeleid uit ^{1}H MRI experimenten. Op deze manier kon kwantitatieve informatie worden verkregen over de Co(II) profielen binnen katalysatorlichamen na impregnatie met $Co(NO_3)_2$ oplossingen. In hoofdstuk 7 wordt beschreven hoe deze methode kan worden toegepast om de verdeling van Co(II)-complexen te bepalen na impregnatie van Al_2O_3 extrudaten met Co(II)-citraat oplossingen, als een functie van de pH en de citraat concentratie in de impregnatieoplossing. Complexatie door citraat leidde tot een verhoogde interactie van Co(II)-complexen met het Al_2O_3 oppervlak. Hierdoor werd het transport van deze complexen vertraagd, wat leidde tot een sterk verhoogde concentratie van Co(II)-complexen in de buurt van het buitenoppervlak van de extrudaten na impregnatie. De aanwezigheid van citraat en Co(II)-complexen in de impregnatieoplossing resulteerde in competitie tussen deze componenten voor de aanwezige adsorptieplaatsen op het Al_2O_3 oppervlak. Door een overmaat citraat toe te voegen aan de impregnatieoplossingen konden extrudaten worden verkregen met een verhoogde Co-concentratie in de buurt van de kern of in een ring binnen de extrudaten.

Op basis van de behaalde resultaten kan worden geconcludeerd dat met behulp van microspectroscopische technieken inzicht kan worden verkregen in de moleculaire structuur en de ruimtelijke verdeling van metaalion complexen binnen katalysatorlichamen in de verschillende stadia van het bereidingsproces. De toepassing van deze technieken maakt het mogelijk om gedragen katalysatoren in de toekomst op een meer gecontroleerde manier te bereiden. Een betere beheersing van het bereidingsproces kan vervolgens leiden tot de ontwikkeling van katalytische systemen met een hogere activiteit, selectiviteit en/of stabiliteit. Dat de beschreven technieken hierbij inderdaad een rol kunnen spelen, werd geïllustreerd in hoofdstuk 4, waar bleek dat Raman microspectroscopie kon worden gebruikt om nadelige processen tijdens de bereiding van Mo/Al_2O_3 katalysatoren op te sporen en zo de ontzwavelingsactiviteit van deze systemen te verhogen.

Dankwoord

Wat mij betreft het moeilijkste gedeelte van het proefschrift om te schrijven. Enerzijds is er een groot aantal mensen aan wie ik dank verschuldigd ben en wil ik niemand te kort doen. Anderzijds laat ik de omstandige, openbaar-persoonlijke bedankjes die doorgaans op deze plaats te vinden zijn liever achterwege. Specific acknowledgments are included at the end of the individual chapters.

Bert, bedankt voor het in mij gestelde vertrouwen om een aantal van je vele ideeën in relatieve vrijheid uit te mogen werken. Gelukkig blijken deze ideeën ook bij nadere inspectie vaak nog goed te zijn en was je altijd geïnteresseerd en bereid om mee te denken en bij te sturen. De ideale combinatie wat mij betreft.

Krijn, door je grote expertise was een overleg met jou altijd uitermate nuttig en leerzaam. Jouw bijdrage aan het totstandkomen van dit proefschrift was onmisbaar.

Tom, mijn promotieonderzoek begon bij jou met een pittige overhoring over de theorie van vibratiespectroscopie en eindigde met het eindeloos puzzelen boven spectra van allerlei citraatoplossingen. In de tussentijd was je altijd bereid tot het beantwoorden van vragen, het nakijken van teksten en het geven van advies. Bovenal was je met je grote relativeringsvermogen een ideale bliksemafleider en een betrouwbaar ijkpunt.

Eelco Vogt, Bob Leliveld, Jan Nieman, Sander Thoonen en Brenda Rossenaar van de vaste begeleidingscommissie vanuit Albemarle Catalysts bedankt voor jullie commentaar en suggesties.

Dymph en Monique, bedankt voor het regelen van een heleboel kleine zaken.

Thanks to all colleagues for the good time I had in the lab during the last four years. I am really going to miss your pleasant company on the workfloor and during broodjes Tricolore met tonijn, LIIT-borrels, vakgroepsuitjes and BBQ's. "Vakgroepsaanvoerder" Fouad wordt in het bijzonder bedankt voor het verdragen van de vele verwensingen tijdens als ontspanning bedoelde voetbaltoernooitjes.

Familie, vrienden en teamgenoten worden bedankt voor alle liefde, de getoonde interesse en de mogelijkheid tot ontspanning buiten het werk.

Curriculum Vitae

De schrijver van dit proefschrift werd geboren op 30 juli 1979 te Schiedam. In 1997 behaalde hij het VWO diploma aan de Interconfessionele Scholengemeenschap Westland in Naaldwijk. In september van hetzelfde jaar begon hij met de studie scheikunde aan de Universiteit Utrecht. Het doctoraal examen werd behaald in november 2002 na een bijvak bij de sectie Gecondenseerde Materie, een stage bij Synetix in Billingham (Engeland) en een hoofdvak bij de sectie Anorganische Chemie en Katalyse. Vanaf januari 2003 was hij werkzaam als assistent in opleiding in de sectie Anorganische Chemie en Katalyse aan de Universiteit Utrecht onder de supervisie van prof. dr. ir. B. M. Weckhuysen. Het promotieonderzoek werd financieel ondersteund door Albemarle Catalysts en de resultaten zijn beschreven in dit proefschrift. Het werk werd gepresenteerd op diverse internationale congressen, zoals verschillende edities van de Netherlands Chemistry and Catalysis congressen (NCCC) in Noorwijkerhout, de 226th ACS National Meeting in Philadelphia (USA), de Europacat VII Conference in Sofia (Bulgaria) en het 9th International Symposium on Scientific Bases for the Preparation of Heterogeneous Catalysts in Louvain-la-Neuve (Belgium). De schrijver van dit proefschrift ontving tijdens NCCC VI (2005) de prijs voor de beste lezing door een promovendus.

List of Publications

Refereed journals

J. A. Bergwerff, T. Visser, B. R. G. Leliveld, B. D. Rossenaar, K. P. de Jong, B. M. Weckhuysen, *Envisaging the Physicochemical Processes During the Preparation of Supported Catalysts: Raman Microscopy on the Impregnation of Mo onto Al_2O_3 Extrudates,* J. Am. Chem. Soc. **2004**, *126*, 14548.

L. G. A. van de Water, J. A. Bergwerff, T. A. Nijhuis, K. P. de Jong, B. M. Weckhuysen, *Uv-Vis Microspectroscopy: Probing the Initial Stages of Supported Metal Oxide Catalyst Preparation,* J. Am. Chem. Soc. **2005**, *127*, 5024.

L. G. A. van de Water, J. A. Bergwerff, B. R. G. Leliveld, B. M. Weckhuysen, K. P. de Jong, *Insights into the Preparation of Supported Catalysts: A Spatially Resolved Raman and Uv-Vis Spectroscopic Study into the Drying Process of CoMo/gamma-Al_2O_3 Catalyst Bodies,* J. Phys. Chem. B **2005**, *109*, 14513.

J. A. Bergwerff, L. G. A. van de Water, T. Visser, P. de Peinder, B. R. G. Leliveld, K. P. de Jong, B. M. Weckhuysen, *Spatially Resolved Raman and Uv-Visible-Nir Spectroscopy on the Preparation of Supported Catalyst Bodies: Controlling the Formation of $H_2PMo_{11}CoO_{40}^{5-}$ inside Al_2O_3 Pellets During Impregnation,* Chem. Eur. J. **2005**, *11*, 4592.

A. A. Lysova, I. V. Koptyug, R. Z. Sagdeev, V. N. Parmon, J. A. Bergwerff, B. M. Weckhuysen, *Noninvasive in-situ Visualization of Supported Catalyst Preparations Using Multinuclear Magnetic Resonance Imaging,* J. Am. Chem. Soc. **2005**, *127*, 11916.

L. G. A. van de Water, G. L. Bezemer, J. A. Bergwerff, M. Versluijs-Helder, B. M. Weckhuysen, K. P. de Jong, *Spatially Resolved Uv-Vis Micro Spectroscopy on the Preparation of Alumina-Supported Co Fischer-Tropsch Catalysts: Linking Activity to Co Distribution and Speciation,* J. Catal. **2006**, *242*, 287.

J. A. Bergwerff, M. Jansen, B. G. Leliveld, T. Visser, K. P. de Jong, B. M. Weckhuysen, *Influence of the Preparation Method on the Hydrotreating Activity of MoS_2/Al_2O_3 Extrudates: A Raman Micro Spectroscopy Study on the Genesis of the Active Phase,* J. Catal. **2006**, *243*, 292.

In Preparation

J. A. Bergwerff, A. A. Lysova, L. Espinosa Alonso, I. V. Koptyug, B. M. Weckhuysen, *Monitoring the Distribution of Paramagnetic Metal-ion Complexes inside Catalyst Bodies using Magnetic Resonance Imaging*

J. A. Bergwerff, A. A. Lysova, L. Espinosa Alonso, I. V. Koptyug, B. M. Weckhuysen, *The Influence of Citrate on the Distribution of Co(II)-Complexes inside Co/Al_2O_3 Catalyst Bodies after Impregnation: a Combined MRI and UV-Vis-NIR Micro-spectroscopy Study*

J. A. Bergwerff, T. Visser, B. M. Weckhuysen, *Spectroscopic Investigation of the Molecular Structure of Citrate, Co(II)-Citrate and Mo(VI)-Citrate Complexes in Aqueous Solution*

A. M. Beale, S. D. M. Jacques, J.A. Bergwerff, B. M. Weckhuysen, *Tomographic Energy Dispersive Diffraction Imaging of Supported Caltalyst Bodies*

Conference proceedings

J. A. Bergwerff, L.G.A. van de Water, A.A. Lysova, I.V. Koptyug, T. Visser, K. P. de Jong, B.M. Weckhuysen, *Monitoring the preparation of (Co)Mo/Al_2O_3 extrudates using spatially resolved spectroscopic techniques,* Stud. Surf. Sci. Catal. **2006**, *162*, 175.

Book chapter

J. A. Bergwerff and B. M. Weckhuysen, *Active Phase-Support Interactions: Oxide-Support Interactions* in *Handbook of Heterogeneous Catalysis, 2nd Edition* (Ertl, G., Knözinger, H., Schüth, F., Weitkamp, J., Eds.), Wiley-VCH, Weinheim, 2007, *in press*.

Appendix

Illustrations in color

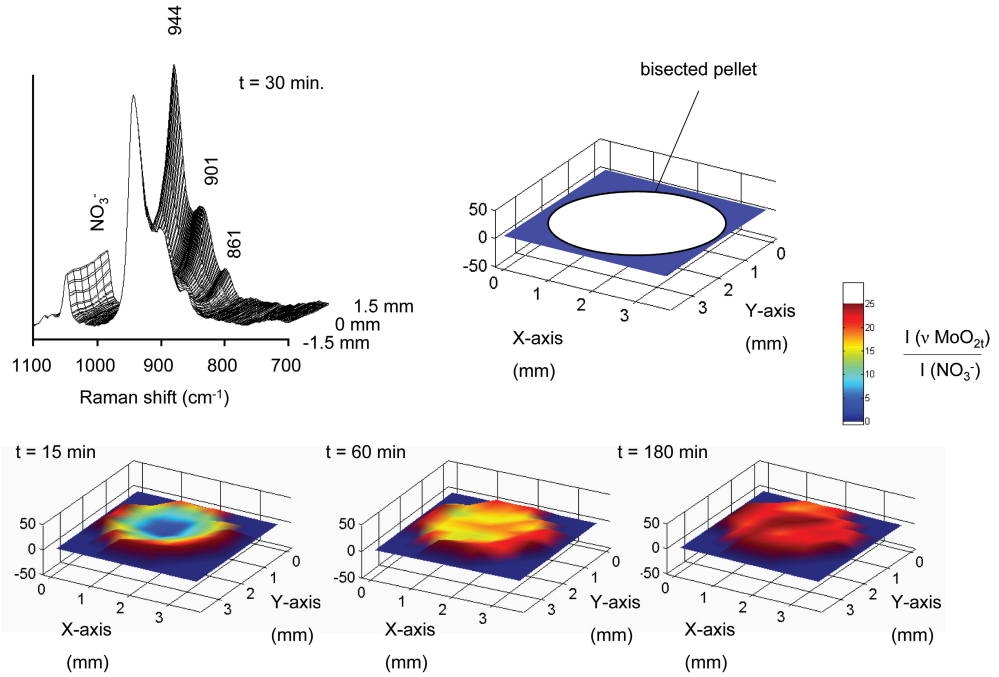

Figure 3.5. Raman spectra recorded on bisected catalyst bodies impregnated with a Mo-citrate solution, recorded 30 min after impregnation (left). Three-dimensional plots illustrating the spatial distribution of the $Mo_4(Hcitrate)_2O_{11}^{4-}$ complex in 3 mm Al_2O_3 pellets 15, 60 and 180 min after impregnation with an AHM-citrate solution (bottom). The intensity plots are obtained by referencing to the NO_3^- Raman band.

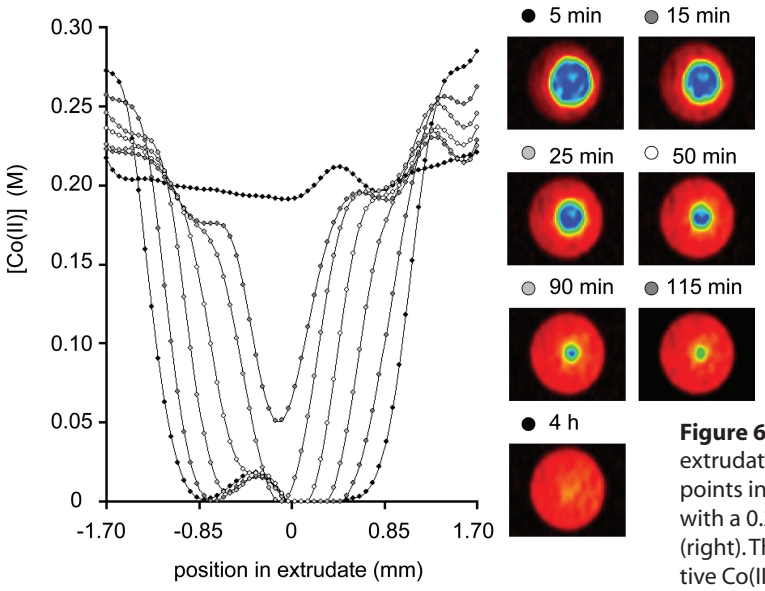

Figure 6. 14. ^1H images of an Al_2O_3 extrudate recorded at several points in time after impregnation with a 0.2 M $Co(NO_3)_2$ solution (right). The resulting quantitative Co(II) distribution plots are presented on the left. A red color in these images represents a low ^1H NMR signal. A high ^1H NMR signal is indicated by a blue color.

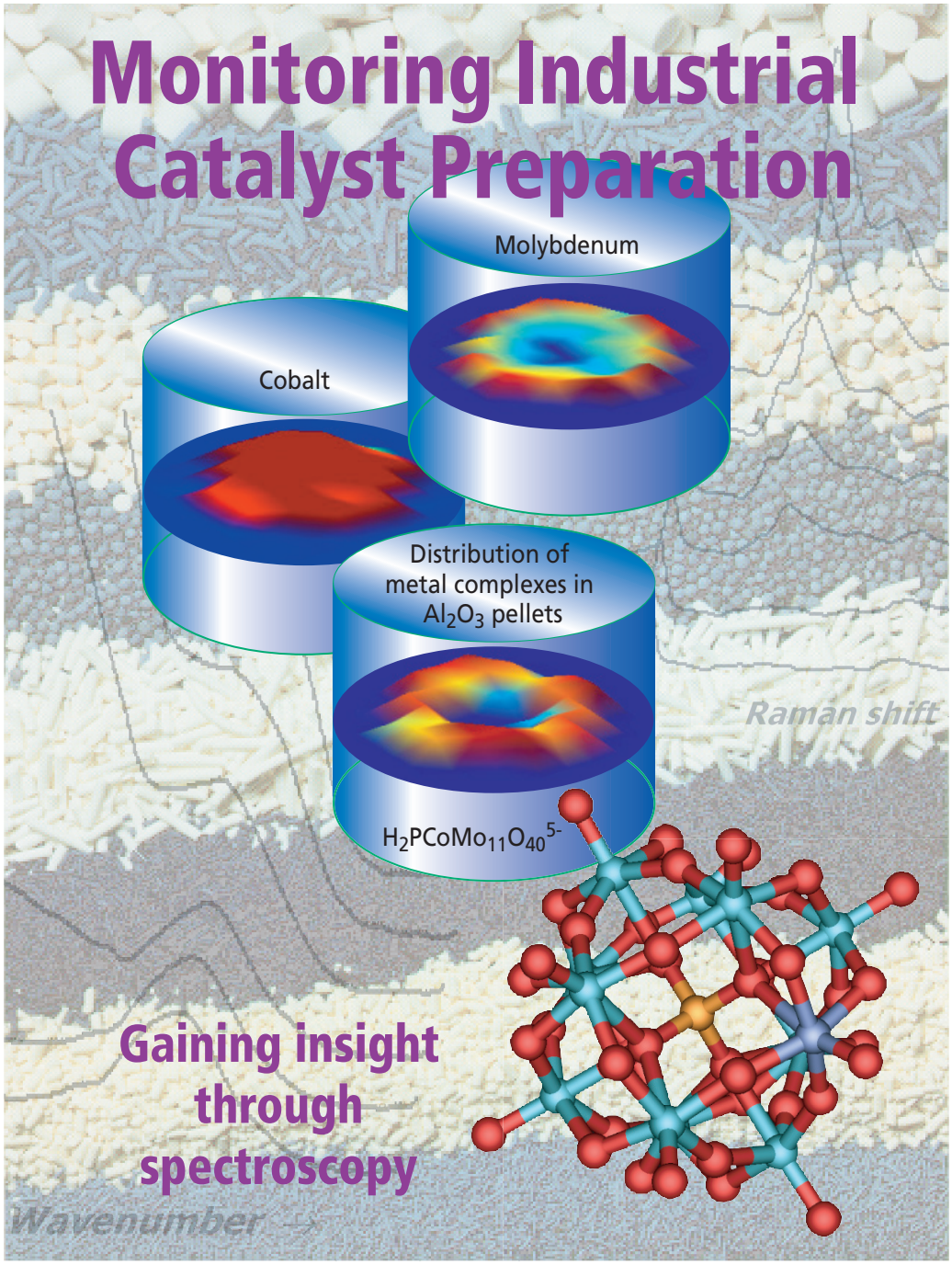

Frontispiece of J. A. Bergwerff, L. G. A. van de Water, T. Visser, P. de Peinder, B. R. G. Leliveld, K. P. de Jong, B. M. Weckhuysen, *Spatially Resolved Raman and Uv-Visible-NIR Spectroscopy on the Preparation of Supported Catalyst Bodies: Controlling the Formation of $H_2PMo_{11}CoO_{40}^{5-}$ inside Al_2O_3 Pellets During Impregnation,* Chem. Eur. J. **2005**, *11*, 4592.